Quad Polarimetric Synthetic Aperture Radar Analysis of Icebergs in Greenland and Svalbard

Johnson A. Bailey

August 2022

A thesis submitted

for the degree of Doctor of Philosophy

Biological and Environmental Sciences

School of Natural Sciences

University of Stirling

Scotland

Supervisors:

Armando Marino, Vahid Akbari, and Evangelos Spyrakos

General Abstract:

Polarimetric synthetic aperture radar (PolSAR) has been widely used in ocean and cryospheric applications. This is because, PolSAR can be used in all-day operations and in areas of cloud cover, and therefore can provide valuable large-scale monitoring in polar regions, which is very helpful to shipping and offshore maritime operations. In the last decades, attention has turned to the potential of PolSAR to detect icebergs in the Arctic since they are a major hazard to vessels. However, there is a substantial lack of literature exploring the potentialities of PolSAR and the understanding of iceberg scattering mechanisms. Additionally, it is not known if high resolution PolSAR can be used to detect icebergs smaller than 120 metres.

This thesis aims to improve the knowledge of the use of PolSAR scattering mechanisms of icebergs, and detection of small icebergs. First, an introduction to PolSAR is outlined in chapter two, and monitoring of icebergs is presented in chapter three. The first data chapter (Chapter 4) is focused on developing a multi-scale analysis of icebergs using parameters from the Cloude-Pottier and the Yamaguchi decompositions, the polarimetric span and the Pauli scattering vector. This method is carried out using ALOS-2 PALSAR quad polarimetric L-band SAR on icebergs in Greenland. This approach outlines the good potential for using PolSAR for future iceberg classification. One of the main important outcomes is that icebergs are composed by a combination of single targets, which therefore may require a more complex way of processing SAR data to properly extract physical information.

In chapter five, the problem of detecting icebergs is addressed by introducing six state-of-the-art detectors previously applied to vessel monitoring. These detectors are the Dual Intensity Polarisation Ratio Anomaly Detector (iDPolRAD), Polarimetric Notch Filter (PNF), Polarimetric Matched Filter (PMF), reflection symmetry (sym), Optimal Polarimetric Detector (OPD) and the Polarimetric Whitening Filter (PWF). Cloude-Pottier entropy, and first and third eigenvalues (eig1 and eig3) of the coherency matrix are also utilised as parameters for comparison. This approach uses the same ALOS-2 dataset, but also evaluates detection performance in two scenarios: icebergs in open ocean, and in sea ice. Polarimetric modes (quad-pol, dual-pol, and single intensities) are also considered for comparison. Currently it is very difficult to detect icebergs less than 120 metres in length using this approach, due to the scattering mechanisms of icebergs and sea ice being very similar. However, it was possible to obtain detection performances of the OPD and PWF,

which both showed a Probability of Detection (P_F) of 0.99 when the Probability of False Alarms (P_F) was set to 10^{-5} in open ocean. Similarly, in dual pol images, the PWF gave the best performance with a P_D of 0.90. Results in sea ice found eig3 to be the best detector with a P_D of 0.90 while in dual-pol mode, iDPolRAD gave a P_D of 0.978. Single intensity detector performance found the HV channel gave the best detection with a P_D of 0.99 in open ocean and 0.87 in sea ice.

In the previous two approaches, only satellite data is used. However, in chapter six, data from a ground-based Ku-band Gamma Portable Radio Interferometer (GPRI) instrument is introduced, providing images that are synchronised with the satellite acquisitions. In this approach, the same six detectors are applied to three multitemporal RADARSAT-2 quad pol C-band SAR images on icebergs in Kongsfjorden, Svalbard to evaluate the detection performance within a changing fjord environment. As before, we also make use of Cloude-Pottier entropy, eig1 and eig3. Finally, we evaluate the target-to-clutter ratio (TCR) of the icebergs and check for correlation between the backscattering coefficients and the iceberg dimension.

The results obtained from this thesis present original additions to the literature that contributes to the understanding of PolSAR in cryospheric applications. Although these methods are applied to PolSAR and ground-based radar on vessels, they have been applied for the first time on icebergs in this thesis.

To summarise, the main findings are that icebergs cannot be represented as single or partial targets, but they do exhibit a collection of single targets clustered together. This result leads to the fact that entropy is not sufficient as a parameter to detect icebergs. Detection results show that the OPD and PWF detectors perform best in an open ocean setting and using quad-pol mode. These results are degraded in dual-pol mode, while single intensity detection is best in the HV cross polarisation channel. When these detectors are applied to the RADARSAT-2 in Svalbard, the OPD and PWF detectors also perform best with P_D values ranging between 0.5-0.75 for a P_F of 0.01-0.05. However, the sea ice present in the fjord degrades performance across all detectors. Correlation plots with iceberg size show that a regression is not straightforward and Computer Vision methodologies may work best for this.

Declaration

I, Johnson Albert Bailey, declare that this thesis has been composed by myself and that it embodies the results of my own research. Where appropriate, I have acknowledged the nature and extent of work carried out in collaboration with others.

Signed: 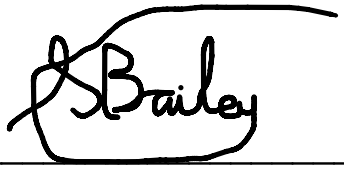 Date: 08/08/2022

Acknowledgements

This research received no external funding, but training workshops provided by the European Space Agency (ESA), and the National Aeronautics and Space Administration (NASA) contributed to the work of this thesis.

I would like to thank the source of data. ALOS-2 data were provided by the project number 1151. ALOS-2 Product-JAXA 2017, all rights reserved. RS-2 data were provided by NSC/KSAT under the Norwegian/Canadian Radarsat agreement 2016.

I would like to start with thanking my academic colleagues and contacts. Firstly, I would like to thank my primary PhD supervisor, Armando Marino for making this project possible, especially as an outsider who joined with no previous training in earth observation techniques. Additionally, thank you for the opportunities to present at international conferences, our informal chats which helped with my health and wellbeing during the last four years, and the invitation to start a new journey in Scotland. Thank you for pushing me during the most difficult times.

Secondly, to my supervisor, Vahid Akbari, thank you for providing the GIS training required for this project, as well as formal feedback and training on speckle statistics used in this work. Thank you for connecting me with other scientists from UiT The Arctic University of Norway and the Nansen Environmental and Remote Sensing Center.

Thirdly, to those who have had a minor role in this project, Vagelis Spyrakos from the University of Stirling, Anthony Paul Doulgeris and Tom Lauknes from the Arctic University of Norway, and Tao Liu from the Naval University of Engineering in Wuhan, China, thank you for the feedback on my work. A major thanks to Shane Cloude who was a guest speaker at my first day in Stirling and Eric Pottier, whose expertise from the ESA polarimetry workshop contributed to the PolSAR theory section of this work.

Fourth, to my SAR remote sensing colleagues in and out of the office, Vahid, Armando, Cristian, Morgan, Mortimer, Pedro, and Xavier, for the pub outings, and the interesting discussions. I look forward to following your work in the future. Thank you to Sam, Cristian, Mortimer and Nonglak who were my office buddies for the majority of the project.

Moving on, I would like to thank my friends and family. Firstly, to my parents for supporting me during my move to Scotland. Secondly, to my brother George for helping me understand the mathematics behind this project. Third to my other siblings, Frankie, and Saffron for your support, and fourth, to my aunt Janet for providing informal and academic support throughout this work.

Big thanks to my close friends I made here at the University of Stirling, Chloe, Caitlin, Corey, Harley, Ethan, Euan, Robyn, Jess, Lexi and Nelli. Thank you to the Stirling University Trampoline and Gymnastics Club for allowing me to add more of a balance to my study through training and competitions. Thank you to my best friends outside of university, Calum, Holly, Beth, and Lauren. The support you have all provided me throughout this project has been super appreciated.

Finally, I'd like to thank my Grandpa. You brought me and my family happiness. I hope I've made you proud.

Contents

LIST OF FIGURES

LIST OF TABLES

LIST OF ABBREVIATIONS

AVHRR – Advanced very high resolution radiometer

CFAR – constant false alarm rate

DLR – Deutsches Zentrum für Luft- und Raumfahrt (German Aerospace Center)

DMS – degrees minutes seconds

EM – electromagnetic

ESA – European Space Agency

HH – horizontal-horizontal polarisation

HV – horizontal-vertical polarisation

IIP – International Ice Patrol

IRD – Ice rafted debris

P_D – probability of detection

PDF – probability density function

P_F – probability of false alarms

PolSAR – polarimetric synthetic aperture radar

RAR – real aperture radar

RCS – radar cross section

RGB – red blue green

ROC – receiver operating characteristic

ROI – region of interest

SAR – synthetic aperture radar

SLAR – side looking aerial radar

SLC – single look complex

TCR – target to clutter ratio

UTC – universal coordinated time

UTM – universal transverse mercator

VH – vertical-horizontal polarisation

VV – vertical-vertical polarisation

WERR – windowed error reduction ratio

1.0. INTRODUCTION:

Icebergs are a large source of global freshwater formed from glaciers and ice sheets accounting for 68.9% of total freshwater on the planet (Valero *et al.*, 2002). Whilst they are important components of the cryosphere, they also carry an extensively dark history and a potentially fatal future. For one, it is well known that icebergs are a major hazard to maritime operations in the polar regions, including in both Antarctic and Arctic regions. However, as global temperatures continue to warm at an alarming rate, iceberg formation is also increasing (Rignot *et al.*, 2011), making their hazardous nature even more of a concern in these areas. The challenges that lie ahead for maritime operations such as commercial and cargo shipping, recreational water transport, fishing vessels, oil and gas sectors, coastal installations and research in the marine sciences are likely to become greater as the flux of icebergs into the polar oceans increases. Icebergs drifting into warmer oceans such as the North Atlantic Ocean have become more of a regular sighting (Sudom *et al.*, 2014), placing an enormous responsibility on these maritime operations to keep thousands of people safe, and to ensure their infrastructure is not damaged. Even more concerningly, icebergs which tend to drift into warmer oceans are a lot smaller in shape and size. Some of them are too small to be seen with the naked eye while others may be as much as 60-100 m high with wider bodies below the waterline. The ongoing effects of climate change will also influence iceberg size, as smaller icebergs are more likely to drift into important shipping lanes, rather than larger icebergs which have the potential to become grounded in enclosed regions such as fjords and bays. Rising temperatures will likely cause the trend of heavy iceberg years (i.e. increases in iceberg sightings below 48°N in the North West Atlantic) to continue (Bigg and Billings, 2014) and as the Arctic climate has warmed, world trade has also increased. In the Southern Ocean, the need for more fishing and increased polar tourism has led to more vessels entering areas with icebergs yearly (Bigg, 2015).

The story of iceberg monitoring and detection begins with the sinking of the ‘unsinkable’ ship, *RMS Titanic* in April 1912. Previous research and survivor reports suggests that the type of iceberg involved was pinnacle in shape, 15-31 m high, and about 122 m in length at the sea surface (Bigg and Billings, 2014). This would be identified as a large iceberg according to the classification criteria (Young *et al.*, 1998; Jackson and Apel, 2004). It is known that glacial ice is approximately 15% less

dense than seawater, which suggests the iceberg was around 90-185 m deep. The iceberg had drifted into the North Atlantic Ocean, south of Newfoundland, but probably had origins in the south western part of the Greenland Ice Sheet, located further north and originally had a length of 500 m. A model of the iceberg suggested that it had formed in late summer to autumn 1911 and had drifted across the Labrador Sea via the shorter routes of the Labrador Current rather than travelling around Baffin Bay (Wilton *et al.*, 2015), while at the time of the incident, the iceberg was 125 m in length at the sea surface, and between 15-17 m high. This time frame is more likely since icebergs have a short life span of a few years after calving (Bigg *et al.*, 1997). At the time of the incident, detection was primarily through the human eye, and many ships relied on radio signals given off by other ships in the proximity of their surroundings. Radio exchanges regarding the reports of ice fields (large areas of ocean with icebergs or sea ice) were known as 'ice warnings'. However, it was these ice warnings that were ignored by the lookout crew on the *Titanic*. Together with a multitude of other factors such as bulkhead placement, rivet fatigue and manoeuvrability, the ship was unable to avoid the iceberg and sank over 2 hours later. The considerable number of lives lost, and that commercial passenger ships were a revolutionary way to travel at the time meant that this event had a lot of media attention. Prior to the disaster, there were an unusual number of icebergs in the north west Atlantic shipping lanes in the spring of 1912. Because of this event, the International Ice Patrol (IIP) was set up by the US Coast Guard in 1914, and this major group is still responsible for the safety of ships in the oceans today (Murphy and Cass, 2012).

It was the IIP which began the field of iceberg detection, where icebergs were established as major marine hazards to ships. The IIP has noted that the number of icebergs passing south of 48°N between 1900-1912 averaged around 452 annually, with the bulk majority of over 1,000 occurring in 1909 and 1912. As icebergs began to grab the attention of the media, they also garnered the attention of many scientists. Icebergs soon began to be tracked with in-situ measurements. Between the years 1913-1945, ships recorded an annual average of 435 icebergs. Over 1,000 of these icebergs were recorded in 1929 and again in 1945. Collisions with water transport such as fishing boats still occurred. Later, due to large annual variations in iceberg seasons, aircraft reconnaissance between 1946-1982 counted an annual average of 273 icebergs despite the apparent increase in the number of recordings. At the same time, it was suggested that the freshwater locked up in icebergs could

be used to help alleviate the global water crisis. Ideas were proposed such as the towing of icebergs into the waters of arid coastal regions and then extracting the freshwater out of them. This technique is not feasible in areas of sea ice (Eik and Marchenko, 2010) and for larger icebergs, more powerful tugs are required. Icebergs will also melt quickly in warmer waters. In this sense, the towing of icebergs may not be a long-term practical solution, and instead attention must be turned to alleviating the pressures faced by major maritime operations.

As well as media attention and scientific interest in them, icebergs also capture the attention of other people's lives in interesting ways. Perhaps most notably the saying 'tip of the iceberg' has entered our vocabulary since 1969. Realistically, travellers flying over Arctic regions are likely to spot icebergs, as are tourists who travel on vessels in south eastern Alaska in the United States, the Antarctic Peninsula and the archipelago of Svalbard, Norway. Polar tourism began in the 1950s in Antarctica, and in 1998, flights above Greenland allowed for the viewing of icebergs from above in good air visibility. This sets the scene for the monitoring and remote sensing of icebergs, which we now turn to.

Remote sensing continues to be one of the most adaptable fields in the discipline of earth science, as technology has advanced over the past century. Earth observation is a remote sensing subject but is specific to acquiring data on observations of the physical, chemical, and biological systems, whereas remote sensing refers to broadly acquiring information from a distance. Historically, the reporting of scientific information was through ground observation and relied on telegrams and radio communication. Now the invention of computers and satellites has revolutionised the way Earth observation is carried out and disseminated. The field of remote sensing has seen major scientific progress and it continues to be a growing field of science, especially as the ongoing effects of climate change continue to shape the future of the Earth. Satellites and remote sensing of specific terrains and objects have made it possible to study remote, hostile environments where ground observations are very hard to achieve. For example, observations in heavy rainforest canopy, as well as cold, harsh Arctic climates are possible. Both these terrains are being affected by climate change and so these areas are of major interest and paramount importance to Earth scientists. Warming temperatures and human intervention are leading to deforestation and destruction of biodiversity and the melting of ice in these areas, respectively.

The detection of icebergs has seen major progress accomplished within the last few decades (Dierking and Wesche, 2013). Different detection systems have been developed as technological advance has revolutionised the scientific community. Where before, human activity was used for lookout duties on ships, now a wide number of advanced computerised detection systems, many of which originate from radars, have replaced this role. Today, field observations of icebergs are made from ships in the open ocean or in fjord environments. Between 1983-2007, various side looking radar (SLAR) on aircraft flown by the IIP recorded an average of 983 icebergs, 2,200 of which were in 1984. All these historical observations recorded by the IIP only apply to icebergs below 48°N and do not include icebergs elsewhere. Clearly, iceberg numbers have been rising. Field observations of iceberg calving events are confined to the scale of individual glaciers. The likelihood is that the accuracy of radar detection systems will continue to improve as new state of the art satellites are launched into orbit. With all this in mind, attention now turns to motivations and the novelty of this work.

1.1. Research aims and objectives

As the detection of icebergs continues to see increasing amounts of progress, rising demands on shipping and maritime activities in the Arctic are of paramount importance, particularly from the growing effects of climate change. While the IIP has significantly reduced ship to ice collisions, these still occur in modern day shipping. The technological advancement of radar polarimetry has also strongly developed over the past 30 years, with demands for more accurate models and algorithms. Remote sensing is a key contributor to the success of the Arctic shipping and maritime industries such as oil and gas. As the climate warms further, the flux of icebergs calving from glaciers in the Arctic is set to increase. Of notable concern is that icebergs intercepting shipping lanes may be smaller than 120 m in length (medium iceberg size according to classification criteria), and therefore hard to detect but still hazardous to these marine activities. It is also known that bigger icebergs can break apart into growlers and bergy bits a few metres wide, which is a challenge for even visual identification. The combination of these factors alone justifies the need to monitor and classify the icebergs in this region. Future spaceborne Synthetic Aperture Radar (SAR) missions have the potential to provide an abundance of SAR data within the next 5 years, including in the polar regions. Most crucially, research on polarimetric behaviour, and backscatter mechanisms of Arctic icebergs is lacking

when compared to other SAR applications such as ship detection. While a significant amount of research has been devoted to understanding iceberg calving, tracking, drift, and detection through various other methods, there still exists a significant gap in understanding iceberg backscatter physics, and the effects of various environmental conditions on such backscatter behaviour. Consequently, the main aim of this thesis is to contribute to overall knowledge surrounding the use of quad polarimetric analysis for Arctic iceberg detection, and classification using high resolution SAR. This is approached by processing multitemporal polarimetric SAR datasets (Chapters 4, 5 and 6), evaluating polarimetric responses to icebergs, (Chapters 4, 5 and 6) performing a multi-scale analysis of icebergs in L-band SAR data (Chapter 4), detection comparison using various detection algorithms in L-band (Chapter 5 and 6), and processing ground radar in-situ data for comparison and validation purposes of iceberg detection using C-band SAR data (Chapter 6).

A second objective is to compare detection performances in two different scenarios: open water, and sea ice floes. This will address how different environments may influence the detection ability. This is achieved in Chapter 5 with the use of novel detector algorithms that have been shown to separate icebergs from sea ice floes. The anticipation is that sea ice floes still pose a big challenge to polarimetric methods when identifying icebergs. This idea is built upon in Chapter 6, with sea ice being used to find target to clutter ratio of icebergs and open water/sea ice, in addition to target detection and backscattering coefficients.

A third objective is to determine potential classification criteria for icebergs using a range of polarimetric parameters. For example, while the Cloude-Pottier entropy has been used widely as a polarimetric parameter for ship detection, little is known how target entropy affects iceberg backscatter. Similarly, the model decomposition proposed by Yamaguchi is not designed for ice, and therefore very little is known about how this decomposition can be used to classify or detect icebergs.

1.2. Research hypothesis

The research hypothesis of this thesis is as follows:

Polarimetric analysis of Arctic icebergs for detection and classification is possible using high resolution synthetic aperture radar

The research questions associated with this hypothesis are as follows:

- What are the target characteristics of icebergs in SAR images?
- How do different environments (open water, sea ice) influence detection performance?
- Are quad-pol data important for a full analysis of icebergs?
- Is it possible to classify icebergs using a range of polarimetric parameters?
- How are backscattering mechanisms in icebergs affected by external conditions?

1.3. Statement of originality

The candidate believes that the following parts of this work constitute original contributions to the field of iceberg detection:

- A deep quad-polarimetric analysis for icebergs at L-band.
- The PolSAR classification of icebergs as aggregation of single targets.
- A quad pol multi-scale analysis of ALOS-2 PALSAR L-band SAR with understanding of how the polarimetric behaviour changes based on the scale at L-band in Greenland.
- The comparison of quad-pol iceberg detectors in L- and C-band for open ocean and sea ice in Greenland using six state-of-the-art detectors.
- Understanding of differences when looking at icebergs from satellites or ground radar. This is done using RADARSAT-2 C-band SAR and Gamma Portable Radar Interferometer (GPRI) imagery to detect icebergs in Kongsfjorden, Svalbard.

1.4. Publications

The research within this thesis has contributed to the following publications:

PAPER: Bailey, J.; Marino, A. Quad-Polarimetric Multi-Scale Analysis of Icebergs in ALOS-2 SAR Data: A Comparison between Icebergs in West and East Greenland. Remote Sens. 2020, 12, 1864.

PAPER: Bailey, J.; Marino, A.; Akbari, V. Comparison of Target Detectors to Identify Icebergs in Quad-Polarimetric L-Band Synthetic Aperture Radar Data. Remote Sens. 2021, 13, 1753.

CONFERENCE: Bailey J, Marino A, Akbari V. Determining Iceberg Scattering Mechanisms in Greenland Using Quad Pol ALOS-2 SAR Data. In2021 IEEE

International Geoscience and Remote Sensing Symposium IGARSS 2021 Jul 11 (pp. 4759-4762). IEEE.

CONFERENCE: Bailey J, Marino A, Akbari V. Comparison of Target Detectors to Identify Icebergs in Quad-Polarimetric Sar Alos-2 Images. In2021 IEEE International Geoscience and Remote Sensing Symposium IGARSS 2021 Jul 11 (pp. 5223-5226). IEEE.

CONFERENCE: Bailey J, Marino A, Akbari V. Evaluating Performance of Target Detectors for Greenland Icebergs using Quad polarimetric L-band Synthetic Aperture Radar. POLINSAR 2021, 26th April - 30th April 2021, ESA ESRIN: https://polinsar-biomass2021.esa.int/agenda/

TO BE SUBMITTED MANUSCRIPT: Bailey J, Marino A, Akbari V, Doulgeris, A P & Lauknes T. Iceberg detection with a RADARSAT-2 quad polarimetric C-band SAR in Kongsfjorden, Svalbard – comparison with ground-based radar. Journal of Selected Topics in Applied Earth Observations and Remote Sensing, 2022.

1.5. Tools

The following tools were used in the research:

- SNAP is a software product developed by the European Space Agency and is used primarily for the visualisation of SAR image data.
- PolSARpro is an ESA open-source toolbox, used for polarimetric SAR processing. This software can process quad polarisation images as well as dual polarisation images.
- Python is a programming language used for data analysis. It is popular in the fields of remote sensing and earth observation. Python libraries used in this research include numpy, pandas, seaborn, scipy, matplotlib, GDAL and rasterio.
- QGIS is an open-source map builder used for the creation and publication of maps. The software can handle numerous large datasets including from SAR missions.

1.6. Structure of thesis

This thesis focuses on polarimetric synthetic aperture radar (SAR). It shows how quad polarimetric (quad-pol) data from SAR can be used to analyse physical scattering mechanisms, effectively detect icebergs with state-of-the-art computer

algorithms, compare with data from ground-based radar, and monitor icebergs in Norwegian fjords.

Chapter 2: SAR and polarimetry

In the first half of this chapter, synthetic aperture radar is introduced. Starting broadly, electromagnetics is introduced in 2.1. The focus of this section is to introduce the reader to the background science of electromagnetic waves and microwave remote sensing that is relevant to the work in this thesis. Additionally, it will be important to explore the physical and geometrical properties of SAR data (2.2). These include the spatial resolution of SAR data and resolution cell statistics which explain how SAR data is composed of complex numbers. The principles of SAR are best laid out diagrammatically to show the basic geometry which then governs the various mathematical parameters such as swath width and incidence angle. SAR is also of statistical importance since it is prone to speckle noise. Due to the complex nature of speckle in SAR images, it is best represented using various statistical distributions. These include distributions for a complex image pixel, amplitude, phase, and intensity. Distributions become more complex when heterogeneous scenarios (such as forest and road appearing in the same pixel) are considered. In this case, the SAR image contains texture and can be modelled differently to non-textured scenarios.

In the second half of this chapter, various methods for processing SAR data are introduced (2.3). In order to be able to exploit information contained within a SAR image, the speckle noise must be filtered out. Various filters have been utilised for this purpose. A basic approach to SAR processing considers the orientation of a SAR pulse from the transmitter to the receiver. This forms the theory of polarimetry which is useful to exploit geophysical parameters of targets within a SAR image. A single target in a pixel can be characterised using the scattering matrix, while a partial target (which is a target in more than one pixel) must consider second order statistics and use either a covariance or coherency matrix based upon whether a lexicographic or Pauli scattering vector is applied. The last section of this chapter considers applications of PolSAR data which are relevant to iceberg detection and classification (2.4). Target detection consists of a sliding window that moves over a subset of a SAR image, where a detection algorithm can then be applied. This method is based on signal processing theory which involves determining the probability of detection and probability of false alarms. A false alarm refers to a target which has been

detected but is not the same target as the one relevant to the application. The black and white nature of SAR images can be exploited using a Red Green Blue (RGB) approach which is useful for classification purposes. However, to fully exploit polarimetric information about a target, decomposition theorems are preferred, depending on the nature of the target. In this section, we introduce the Cloude-Pottier and Yamaguchi theorems.

Chapter 3: Monitoring Icebergs Using SAR

The focus of this chapter is to introduce the reader to the science of icebergs and the previous work applied to icebergs for detection or classification purposes. It also introduces the reader to the application of the basic theory in this thesis. Firstly, the physics of icebergs is explored (3.1). All icebergs are composed of freshwater glacial ice, which has undergone a transformation from falling snow, to firn, to compacted ice. Air from the ice may escape as it is compacted which can affect the polarimetric behaviour of the ice body. Calving processes consider hydrostatic forces created by seawater and its properties, as well as cryostatic forces created by the movement of the ice. Once an iceberg is calved, it may either drift away from the source or it may become grounded in shallow water, until it has melted enough for it to become adrift again. This typically happens in shallow water environments such as fjords. However, drifting icebergs present a hazardous nature to all maritime operations, including commercial shipping, oil and gas infrastructure and local communities. This is set to become an even bigger problem due to the effects of climate change (3.2).

The history of remote sensing and scattering behaviour of icebergs is introduced in 3.3. After the formation of the IIP, and advances from World War II, the introduction of radar saw the implementation of aerial iceberg observations using aircraft reconnaissance. After SAR was introduced, technology now allowed these instruments to be mounted on spaceborne platforms. All radar waves that hit targets may either be reflected or scattered. Some of the energy may also be directed back to the radar receiver. This backscattered energy depends on the geophysical properties of the icebergs (3.4). A smoother iceberg surface may induce a specular reflection and result in surface scattering behaviour, while a rougher surface may have an increased amount of backscatter energy. Liquid water is very common on iceberg surfaces, including precipitation, sea spray, and saline water introduced after an iceberg has toppled over. The shadows of icebergs can also be explored.

Section 3.5 introduces the concept of iceberg detection. It is possible to visually identify icebergs in SAR images using various methods such as data extraction, target segmentation and discrimination from other targets such as ships. Previous methods of iceberg detection have ranged from iceberg drift and tracking models, iceberg ocean interaction models, and computer algorithms based on Constant False Alarm Rate (CFAR) detection. This chapter concludes by summarising key points of icebergs, their science and hazardous nature to determine motivations for the thesis (3.6). This is followed by a brief narrative (3.7) of why we choose to first exploit polarimetric characteristics and scattering physics, the comparison of various detection algorithms, and then introducing the concept of data validation through optical remote sensing, which in our work includes ground-based in-situ measurements.

Chapter 4: Quad-Polarimetric Multi-Scale Analysis of Icebergs in ALOS-2 SAR Data: A Comparison between Icebergs in West and East Greenland.

In this chapter, we investigate the geophysical properties and backscatter mechanisms of icebergs in four locations in Greenland using five ALOS-2 images. The Cloude-Pottier and Yamaguchi decompositions are used for this work. We perform multi-scale analysis using different image window sizes to determine the polarimetric information. Based on this analysis, it is possible to show that based on the scale icebergs can be identified as single, or partial targets, or multiple single targets. It is also notable that target entropy from the Cloude-Pottier decomposition changes based on meteorological and environmental conditions and is not sufficient for classification of icebergs alone. We show that overall, iceberg backscatter mechanisms in Greenland are dominated by volume scattering and surface scattering, with some double bounce scattering evident in areas of higher sea-state.

Chapter 5: Comparison of Target Detectors to Identify Icebergs in Quad-Polarimetric L-Band Synthetic Aperture Radar Data.

In this chapter, we build upon our work on polarimetric behaviour and scattering mechanisms and introduce the same ALOS-2 dataset to six state-of-the-art detection algorithms originally used with ships. These are the Dual intensity Polarisation Ratio Anomaly Detector (iDPolRAD), Polarimetric Notch Filter (PNF), Polarimetric Matched Filter (PMF), Reflection Symmetry (sym), Polarimetric Whitening Filter (PWF) and Optimal Polarimetric Detector (OPD). We perform

scenario analysis by comparing icebergs found drifting in open ocean, and icebergs embedded within sea ice floes. We also compare performances using dual-pol versions of the detectors. We show that overall, the PWF and OPD detectors provide the best detection performances.

Chapter 6: Iceberg Detection with a Time Series RADARSAT-2 C-band SAR in Kongsfjorden, Svalbard – Comparison with a Ground Based Radar

In this chapter, we introduce a time series RADARSAT-2 SAR dataset alongside a ground-based radar in Kongsfjorden, Svalbard. This is an area of high iceberg density, where icebergs break off the Kronebreen and Kongsbreen tidewater glaciers. In this work, the same iceberg detectors are applied, evaluating the detection performance of these icebergs drifting or grounded in the inner part of the fjord. We also compare iceberg detection performance with ground-based radar taken at the same time. Finally, we evaluate target to clutter ratio (TCR) and backscattering versus iceberg area (surface area of the iceberg in m^2).

Chapter 7: Discussion

In this chapter, all the major findings of the thesis are discussed. (7.1). Firstly, it is notable that target entropy using the Cloude-Pottier decomposition is not suitable as a single parameter for iceberg detection or classification. The discussion is based on the changing nature of meteorological conditions and environmental conditions, as well as the various window sizes used within the analysis. Also of notable significance is the difficulty of identifying icebergs within sea ice floes, which is still a common problem that has not been fully addressed. Backscatter signatures of icebergs are very similar to sea ice, particularly when the signal to noise ratio is low, due to a calmer sea state. Any noise contained within the energy of the SAR pulse may corrupt polarimetric information, which has a huge effect on parameters such as entropy and alpha angle. Thirdly, the imaging mode influences detection. Yet this also has major implications for the future (7.2). A quad-pol system requires twice the amount of power usage and has a huge computational burden. To account for this, the swath width of a quad-pol system is reduced. This is impractical for iceberg detection because a much larger area is required for reporting of icebergs to shipping and ice forecasts. Future spaceborne missions should consider the following recommendations: a wider swath width, a lower amount of time to acquire SAR footprint, and an appropriate frequency to increase penetration depth in icebergs.

2.0. SAR AND POLARIMETRY

2.1. Electromagnetics

The EM spectrum consists of EM radiation at given wavelengths or frequencies (Figure 2.1).

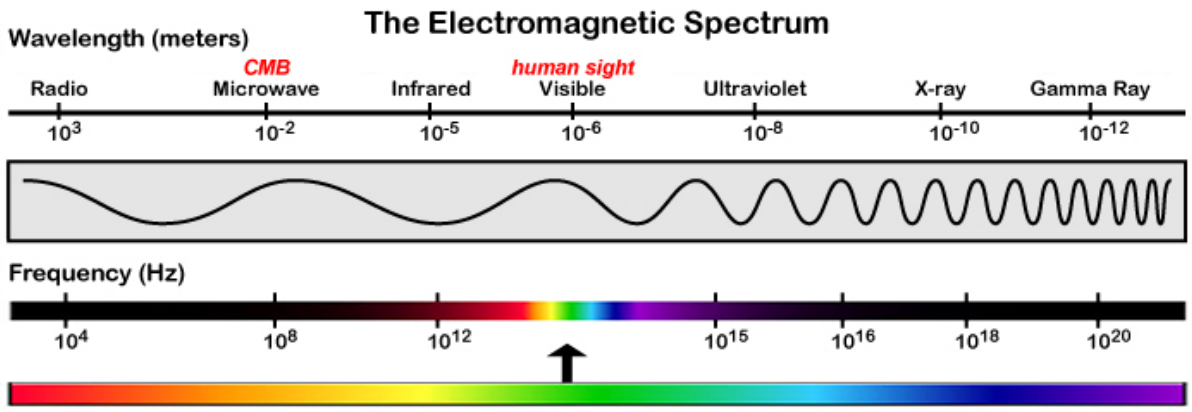

Figure 2.1*: The electromagnetic spectrum. Of interest is the microwave section, in which SAR remote sensing is based on. Longer wavelengths and a lower frequency allow microwaves to penetrate through clouds, making SAR suitable for adverse weather and night time applications. https://i.stack.imgur.com/MP8Pl.jpg*

All objects emit different forms of radiation, some of which are of interest to remote sensing scientists. Existing literature and textbooks on the field of remote sensing use different authoritative standards to define regions of the electromagnetic spectrum, for example, by wavelength, or by frequency based on the portion of the spectrum. From wavelengths of 0.38 to 3.0 µm the reflective spectrum is defined and used directly for applications of remote sensing. Visible light has obvious significance in that, additive primaries (splitting of light into three coloured segments) concern radiant energy, and subtractive primaries (mixing of coloured light) help to specify colours of any pigments and dyes used on imaging. Infrared radiation is split into near infrared and far infrared. Near infrared light has close resemblance to visible light, while far infrared is thermal radiation, extending into regions bordering that of microwave radiation. Microwaves are the longest EM waves used in remote sensing, although future systems such as BIOMASS will use P-band (around 400 MHz) which some textbooks classify as radio waves. Additionally, radio waves are used by ground penetrating radars. Microwaves can extend from those shorter wavelengths

emitted by the far infrared to longer radio wavelengths used in broadcasting (Campbell and Wynne, 2011).

Microwave remote sensing instruments can be categorised into passive sensors and active sensors. Microwave radiation is defined from frequencies of 1 GHz to 300 GHz, although active radar remote sensing also uses lower frequencies around few hundreds MHz. In terms of wavelength this corresponds to a range of 50 cm to 1 mm. The radiative absorption and emission of objects are sensitive to geophysical parameters. Such parameters include temperature and moisture. This information makes microwaves important for remote sensing and Earth observation, as will be presented further in this literature review. Passive remote sensors are often known as radiometers, while active remote sensors, which form the scope of this review, are known as RADARs, or Radio Detection and Ranging. Put simply, passive sensors rely on the detection of energy emitted by an object and originally coming from the sun, whereas active sensors utilise their own energy to illuminate the object or scene. Such energy is in the form of electromagnetic radiation. Active sensors can be categorised further into *synthetic aperture radar* (SAR) systems, weather radars, altimeters and scatterometers (Long, 2008). The latter three of these instruments are all *real aperture radar* (RAR) systems.

Radar waves that impinge on targets often behave in a manner by which only a partial amount of electromagnetic (EM) wave energy is reflected back to the radar. This energy is known as *backscattering*. Predicting the amount of backscattering continues to pose as a challenging aspect to scientists, who try to understand why such behaviour occurs.

2.1.1. SAR

To understand SAR, it is useful to briefly introduce RAR. This is a form of radar that sends a linearly frequency modulated (called a chirp) EM wave and receives the backscattered echo. The modulation is then used to gain resolution in the range directions (the directions that the waves travel from the transmitter). RAR has been in usage since the 1950s and can also be known as side looking aperture radar *(SLAR)* (Jansing, 2021) In this case, the radar travels along an azimuth direction with an EM wave transmitted from the side as shown in Figure 2.2. This type of radar was largely used before the 1950s. However, one major drawback is the low to moderate azimuth resolution that is dependent on the length of the physical antenna.

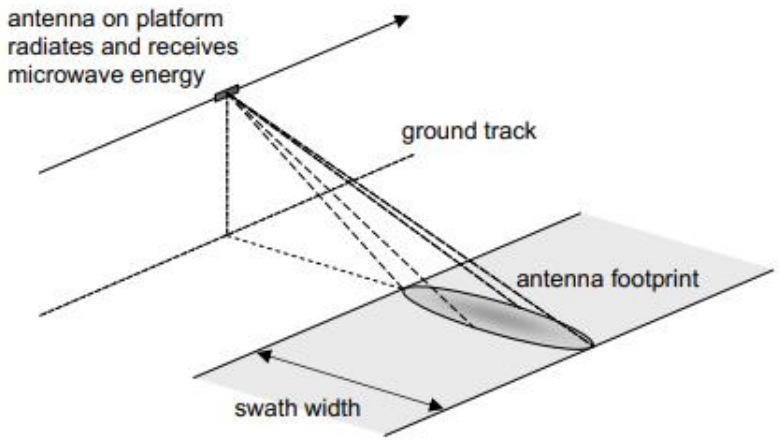

***Figure 2.2**: Geometry of SLAR, note that the system must be side looking as the incidence angle would be 0 from directly below the platform. Adapted from Richards (2009).*

With the introduction of SAR and Doppler beam sharpening in 1951, resolution greatly improved (Wiley, 1985). SAR was involved with both military and civilian applications throughout the 1970s and 80s. Today, the need for increasing the information content of data has become paramount. This might be achieved by multi-channel operation (polarimetry and multi frequency), improved range and azimuth resolution, time series involving a frequent revisit of the same area and observation angle diversity (interferometry and tomography) (Jansing, 2021).

Using a very large antenna on a SAR platform was no longer necessary, as now antennas were synthetically created. The systems travel in straight lines and make multiple transmissions over a given area at different time intervals (Lee and Pottier, 2017). Because the platform moves, there will be a Doppler shift which will modify the frequency of the backscatter echo given from an object, while the objects enter the antenna beam and subsequently leave it (i.e., while the radar passes over it). The SAR system can see this frequency shift as a linear frequency modulation (i.e., a chirp) to produce a much finer resolution image in azimuth (Jansing, 2021). Essentially the antenna length is determined, not physically, but emulated by the distance the SAR system covers that specific target in the antenna beam.

2.2. Physical and geometrical properties of SAR data

2.2.1. Resolution

The term *spatial resolution* refers to the ability of a SAR satellite to separate two scatterers that are close together. In SAR, the *range resolution* is achieved using the pulse compression technique (Chan and Lim, 2008) where pulses are linearly modulated in frequency for a set period.

Range resolution: Such linearly modulated signal is called a chirp. A 'chirp' signal is a signal at a carrier frequency of f_o created by sweeping the frequency linearly in a band B. The received echo is processed with a matched filter that compresses the long pulse into a duration equal to $\frac{1}{B}$. Slant range resolution can then be given by:

$$\delta r = \frac{c}{2B} \tag{2.1}$$

where c is the speed of light and B is the bandwidth of the transmitting signal (Jansing, 2021). The ground resolution is given by the following:

$$\delta x = \frac{\delta r}{sin\theta} \tag{2.2}$$

where θ is the incidence angle. If the incidence angle is zero, there is no spatial resolution, which explains why radars are side-looking.

The ground range resolution varies non-linearly across the swath. When two objects are illuminated by a radar beam, they both cause reflections and the echoes are received simultaneously. However, using the chirp in range and azimuth we can separate them, provided they lay in different resolution cells.

Azimuth resolution: In RAR, two objects in the *azimuth* or along-track resolution can only be separated if the distance between them is larger than the width of the beam. This means that if targets are too close together, the resulting echoes cannot be separated by the radar in the received signal, and as a result spatial resolution is degraded. This configuration is illustrated in Figure 2.3. Therefore, high resolution requires a large antenna length.

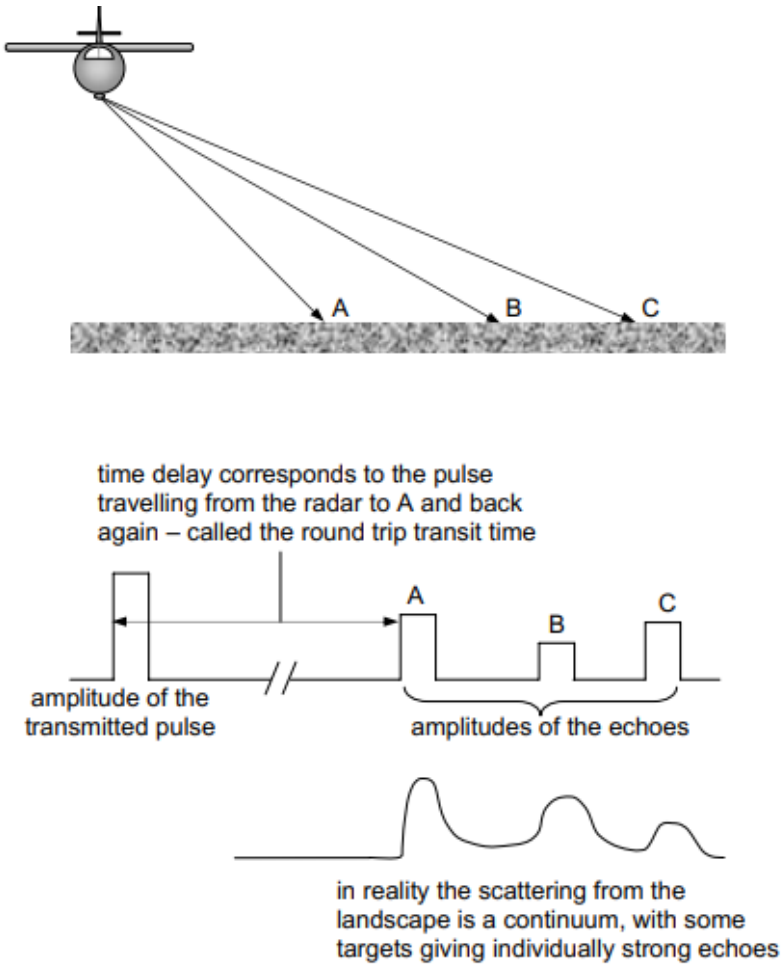

***Figure 2.3**: Spatial resolution configuration using timed echo pulses, adapted from Richards (2009)*

For SAR, a synthetic aperture length (longer effective length) of antenna is achieved by a real sensor antenna moving along a flight direction. Maximum length of the synthetic aperture is the length of the flight path between the scatterer and the antenna and is equal to the size of the antenna footprint on the ground (ΔY). Azimuth resolution thus varies for RAR, and SAR, and the following two equations give this value at a given range R_0 (Richards, 2009). The first equation shown is for RAR:

$$\delta y = \Delta Y = R_0 \theta_Y = \frac{R_0 Y}{L_Y} \tag{2.3}$$

where R_0 is the distance between platform and ground at a specific point, θ_Y is the angular beamwidth and L_Y is the length of the antenna along the azimuth direction. The second equation is for SAR (as a scatterer is coherently integrated along a flight track) and shows that azimuth resolution is directly proportional to physical antenna length.

$$\delta y = \frac{L_Y}{2} \tag{2.4}$$

A combination of both the range and azimuth resolutions creates image pixels, as shown in Figure 2.4.

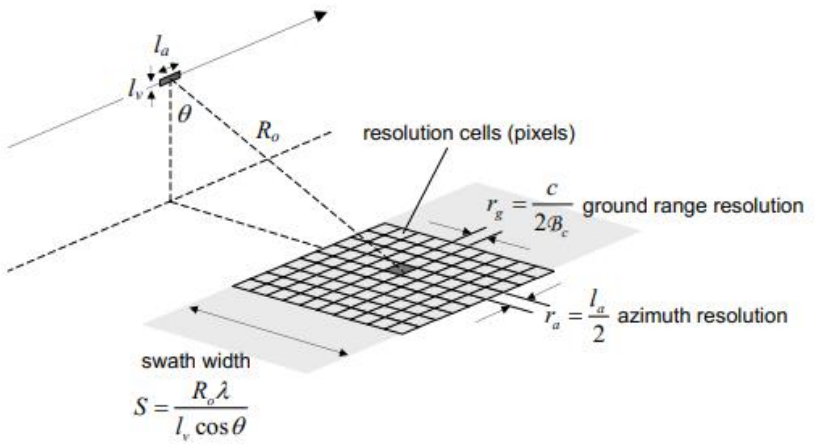

***Figure 2.4**: Spatial resolution into resolution cells, adapted from Richards (2009)*

2.2.2. Resolution cell statistics

Once a resolution cell has been created, it is now possible to determine the interaction between the electromagnetic radiation and the targets on the ground. Since the response is a wave, it has an amplitude and a phase (Woodhouse, 2005). The amplitude and phase are collected by the SAR receiver using an I/Q modulation. The result of this can be represented as a complex number, which can be written in Cartesian form with real and imaginary parts (Figure 2.5) or Euler form with amplitude and phase. The measured amplitude and phase of a single point object on the ground corresponds to one single complex number**.** However, in practice, the microwave transmitted from the radar will interact with several objects inside the resolution cell, mostly objects of the same size or bigger than the signal wavelength (Campbell and Wynne, 2011). As a result, the emitted radar pulse interacts with several objects on the ground simultaneously, and the amplitude and phase thus correspond to the coherent sum from individual objects which lead to interference. In all SAR images, the amplitude and phase responses are different in each resolution cell, which causes some targets on the ground to be brighter than others. Even in homogeneous areas small variations in the distribution of targets can affect the pattern of interference, and therefore the signal changes. This gives rise to the speckle effect, which is analysed in more detail in Section 2.7.

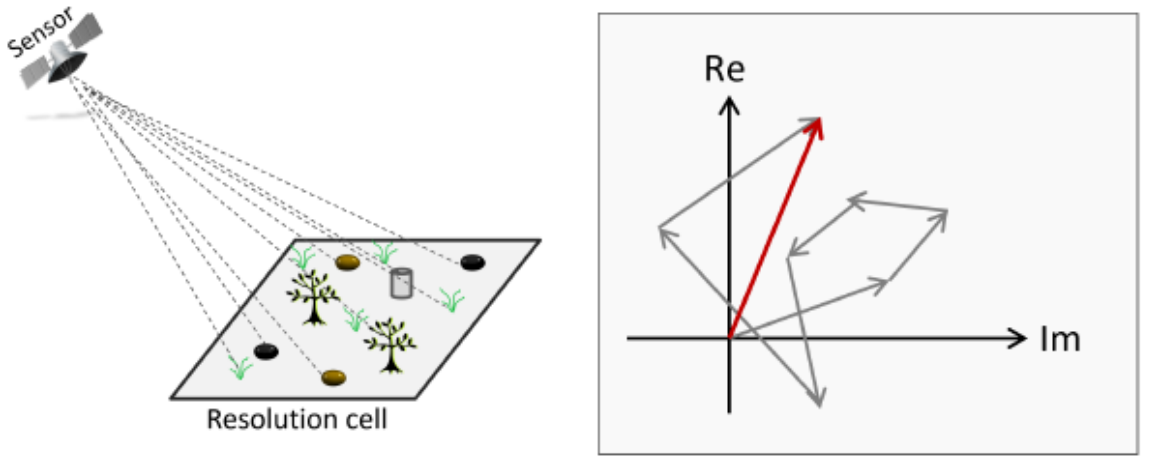

(a) Emitted EM pulse interacting with several scatterers in a resolution cell

(b) Coherent combination of responses from individual scatterers.

***Figure 2.5**: Radar wave interaction with distributed targets on the ground, and the coherent response of a resolution cell with real and imaginary parts, adapted from (Salepci et al., 2017)*

2.2.3. SAR geometry

The SAR geometry is best described visually (Figure 2.6). The first diagram is from a 2D perspective, while the second is from a 3D perspective (Figure 2.7). First, as is established, SAR is attached to an aircraft or a satellite that travels in a given line direction. This is the *flight path* or the *azimuth direction*. The distance from the ground perpendicular to the SAR is the *altitude*, while the distance the SAR beam can reach a point on the ground is known as the *slant range*. The direction on the ground perpendicular to the azimuth is called *ground range*. The *near range*, *far range* create a section on the diagram that then determines the size of the area observed by the SAR beam also called *swath width* (Jansing, 2021; Jackson and Apel, 2004).

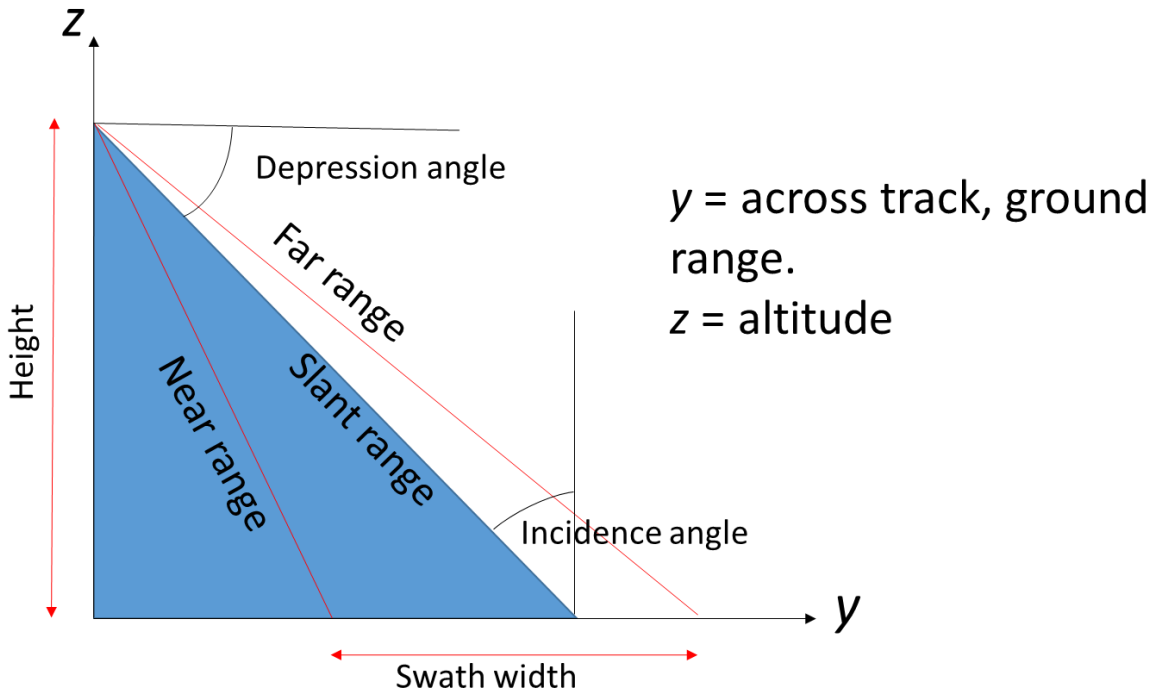

***Figure 2.6**: Principles of SAR. The point at the top of the blue triangle represents the SAR system. The diagonal red lines indicate the illumination, while the slant range is at a 45° angle to the ground.*

The angle between the slant range and the perpendicular to the ground is known as the *incidence angle*. Meanwhile the angle that is created from the slant range down to the swath width, and the ground perpendicular is known as the *depression angle*.

The diagram in Figure 2.6 is a good starter to understand SAR principles. However, it is the simplest diagram available because surface topography is disregarded, which is very often not the case.

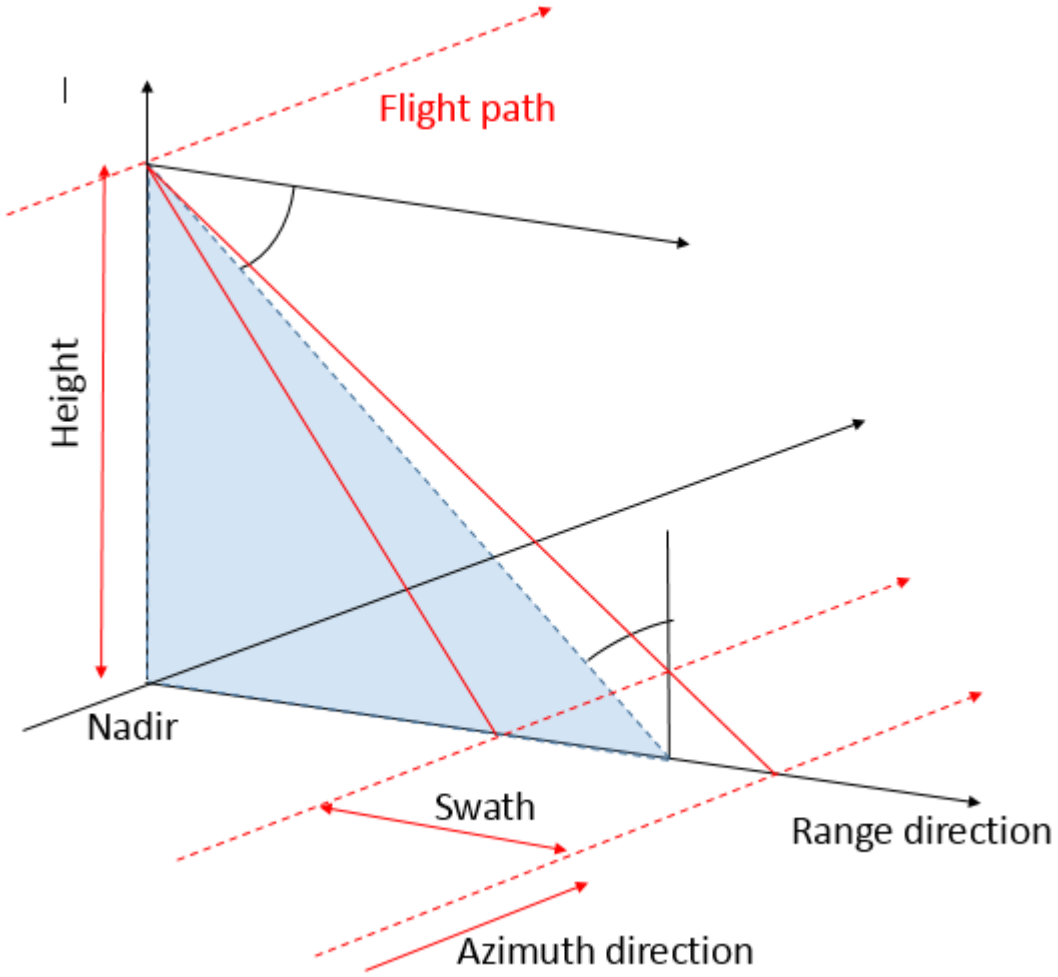

***Figure 2.7**: SAR principles from a 3D perspective. Note the depression angle, incidence angle, slant, mid and far ranges are not labelled. The SAR travels along a flight path, parallel to the azimuth direction on the ground*

2.2.4. Distortions

One disadvantage of SAR that requires processing corrections is geometrical distortions in the form of *foreshortening* (Figure 2.8), and *layover* (Figure 2.9). The diagrams below explain both, from a 2D perspective. Essentially, they are image distortions that are created from the viewing geometry of a SAR. Any mountain or tall feature appears as tilted towards the radar, so that the beam will see a smaller distance between the base of such a feature and the top. This is known as foreshortening (Richards, 2009). This effect happens because the SAR measures distance using the slant range. A topographic feature such as the one described will affect the radar beam by compressing the slope ***a*** to ***b***. Foreshortening effects will vary depending on the length of the topographical slope, and the incidence angle of the radar beam. When the radar beam is transmitted perpendicular to the slope, then

the slope, base, and top will be recorded simultaneously; this is maximum foreshortening. The slope length is reduced to zero on the radar slant range. Foreshortening often produces much brighter features on a SAR image.

.

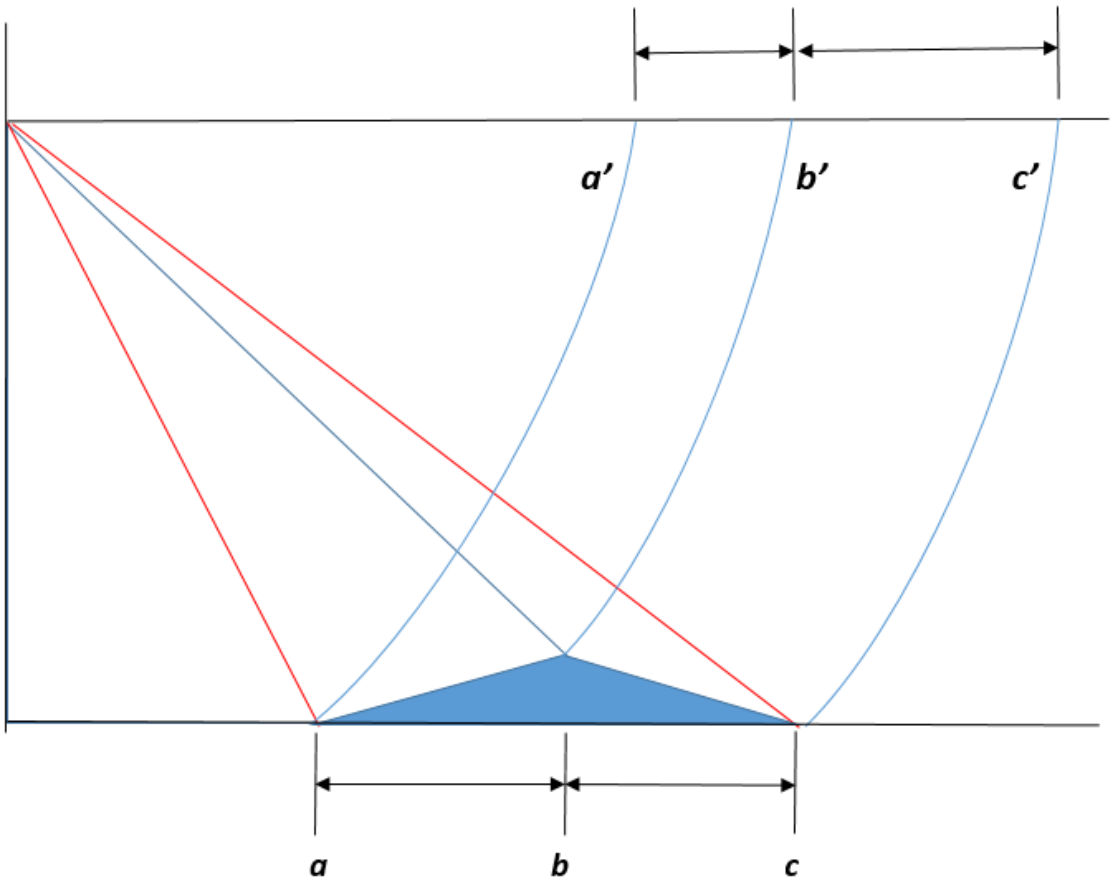

***Figure 2.8.**: Diagram showing foreshortening*

On the same lines, layover occurs when the topographic features have a much higher relief (Jansing, 2021). A transmitted SAR beam will reach the top of the tall feature before reaching the bottom. This means that the receiver of the SAR will receive the return signal from the top of the feature before receiving the return signal from the bottom. This causes displacement of the feature from the true position on the ground towards the SAR, so it 'lays over' the base of said feature. Layover therefore is an extreme case of foreshortening and they both depend on the incidence angle.

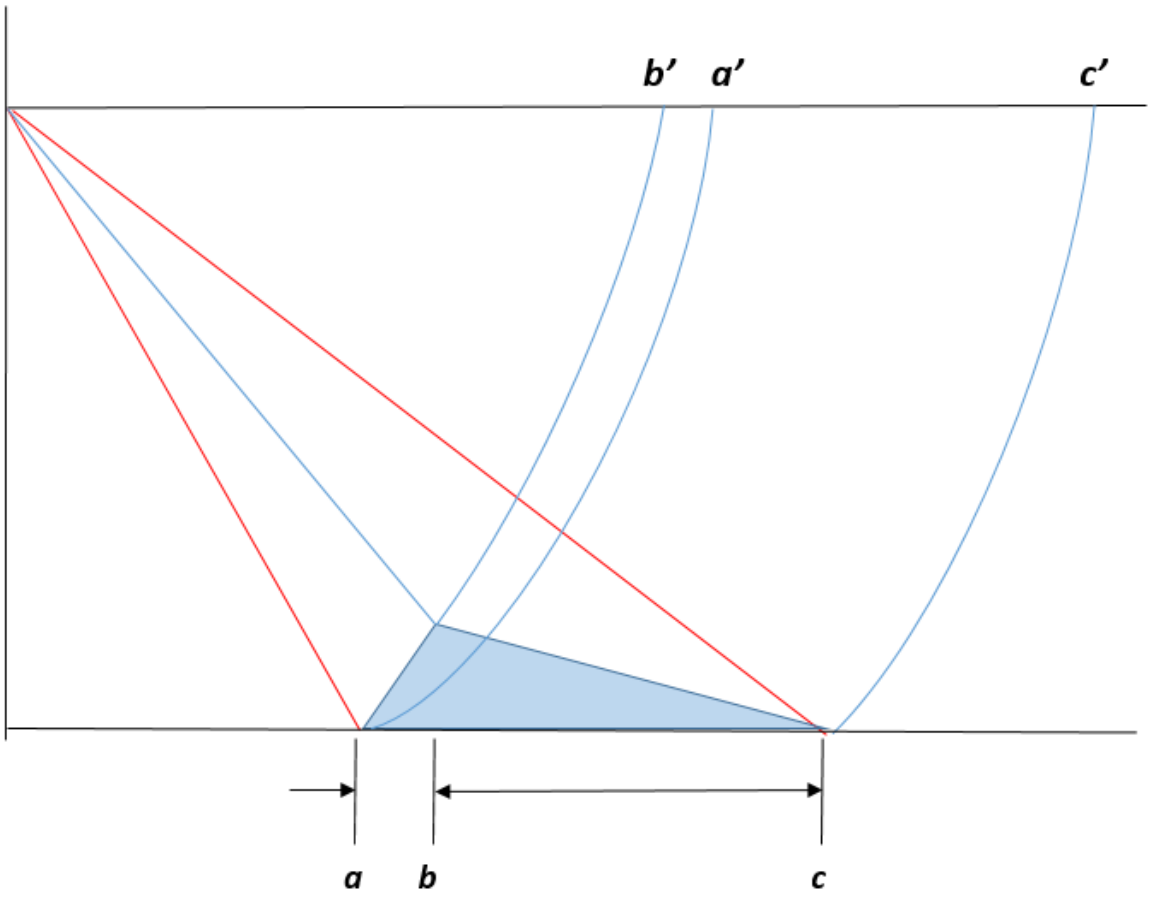

***Figure 2.9**: Diagram showing layover*

Another distortion is radar shadow, which happens when the beam from the radar cannot illuminate the ground surface of the area beyond an object. Shadows occur towards the far range, (i.e., the down range direction), behind slopes with a high relief, and vertical features. The result is that on an image, the shadowed area will appear dark because no energy is available to be backscattered back to the SAR receiver. Shadows will increase as incidence angle increases from near to far range since the beam is transmitted more obliquely to the surface.

Despite the image distortions, the geometry of the radar beam and the area being illuminated is exactly what makes radar remote sensing so useful for terrain analysis, and as this review will present later: icebergs. If effects of foreshortening and layover are not too severe, they can visually enhance the features and appearance of relief and terrain structure. Radar, then, is excellent for applications such as topographic mapping, and geologic structure identification. With the launch of several brand-new radar systems for a variety of different applications, the field of Earth observation is likely to see additional progress.

2.2.5. Speckle

SAR images differ from images produced from optical cameras. The term *speckle* refers to the noisy look of the images originated from the coherent nature of the SAR system. When a SAR system illuminates an area inside a resolution cell, the surfaces on the ground send out backscattering from several objects, called *scatterers*. An array of scatterers can add up constructively or destructively depending on the relative phase of each scattered waveform. Essentially, speckle is caused by the interference of several backscattered signals (echoes) from multiple scatterers inside the same resolution cell as they travel back to the receiver. This results in a granular appearance of objects generated on SAR images (Oliver and Quegan, 2004). In each SAR image, speckle has several consequences. The most obvious is that using a single pixel intensity value as a measure of the reflectivity of a distributed target would be erroneous (Lee *et al.*, 1994).

In radar, speckle is well known to be modelled as multiplicative noise, as opposed to other classifications such as additive noise that is found in optical images. The result of speckle generation is that the quality of a SAR image becomes degraded since the speckle gives a noisy look. Thus, image interpretation is difficult, and crucial information can be lost. Therefore, the task of despeckling in image manipulation is required to remove the speckle in the image. The first step to achieve this is by understanding statistical properties of speckle noise, so the speckle distribution is important (Lee *et al.*, 1994; Jansing, 2021).

Speckle models consider a range of different distributions which are dependent on pixel size and the number of scatterers. A probability density function (pdf) is derived from histograms showing a different distribution for various parameters. Each resolution cell of a SAR image has a random distribution of elemental scatterers.

2.2.6. Amplitude and multi-looked intensity – the Gaussian model

A good statistical model for representing the complex pixel is a Complex Circular Gaussian pdf. The pixel intensity format in a homogeneous region can be modelled with a gamma distribution. Finally, the phase of the complex pixel of a scattered wave tends to follow a uniform distribution between $-\pi$ and π (Oliver and Quegan, 2004).

Following the model of Gaussian distribution for complex pixels, we can derive that the amplitude of a scattered waveform is a *Rayleigh* distribution. The Gaussian speckle model is dependent on three conditions. First, a large number of scatterers in a resolution cell for a homogenous surface, second, the range distance is larger than many radar wavelengths and third, the surface is much rougher on the scale of the radar wavelength (Pottier *et al.*, 2005).

Let the amplitude A be defined by the following:

$$A = \sqrt{x^2 + y^2} \tag{2.10}$$

The values x and y are the real and imaginary components of the complex pixel, and both are identically and independently Gaussian distributed with a mean of zero and a variance denoted as σ^2. Amplitude A has a Rayleigh probability distribution:

$$p_1(A) = \frac{2A}{\sigma^2} \exp\left(-\frac{A^2}{\sigma^2}\right), A \geq 0 \tag{2.11}$$

where M is the mean:

$$M_1(A) = \sigma\sqrt{\pi}/2 \tag{2.12}$$

and Var is the variance.

$$Var_1(A) = (4 - \pi)\sigma^2/4 \tag{2.13}$$

The ratio of the standard deviation to mean is independent of A. The ratio equals to:

$$\sqrt{4/\pi - 1} = 0.5227 \tag{2.14}$$

This ratio is the basic characteristic of multiplicative noise.

The intensity I can be defined by the following equation:

$$I = x^2 + y^2 = A^2 \tag{2.15}$$

I can be proven to have a negative exponential distribution.

The mean:

$$M_1(I) = \sigma^2 \tag{2.16}$$

The variance:

$$Var_1(I) = \sigma^4 \tag{2.17}$$

The standard deviation to mean ratio is one, indicating that speckle would appear more pronounced in intensity images than in amplitude images. The division of the synthetic aperture length into N segments (looks) is a common approach for the reduction of speckle. Each segment is processed independently to form either an intensity or amplitude image, while the N-images are summed to form an N-look SAR image. N-look processing reduces the standard deviation of speckle by a factor of $\sqrt{N}$. However, this is only achieved at the expense of resolution, degraded by a factor of N. The intensity of N images is determined by this equation:

$$I_N = \frac{1}{N}\sum_{i=1}^{N} I_1\,(i) = \frac{1}{N}\sum_{i=1}^{N}(x(i)^2 + y(i)^2) \tag{2.18}$$

Where x and y are the real and imaginary parts of the sample. Like the Rayleigh distribution model, the real and imaginary parts are independently Gaussian distributed. It is common knowledge that NI_n has a Chi square distribution with $2N$ degrees of freedom (Lee *et al.*, 1994). So, the pdf of the N-look intensity can be described by:

$$p_N(I) = \frac{N^N N^{N-1}}{(N-1)!\sigma^{2N}} \exp\left(-\frac{NI}{\sigma^2}\right), I \geq 0 \tag{2.19}$$

This is also called a Gamma distribution.

The mean of the N-look intensity is given by:

$$M_N(I) = \sigma^2 \tag{2.20}$$

And the variance is given by:

$$Var_N(I) = \sigma^4/N \tag{2.21}$$

So, the standard deviation to mean ratio is reduced by the factor $1/\sqrt{N}$ of single look data.

The reduction of variance when averaging can be presented in the form of a histogram (Figure 2.10). Here, it can be shown that the standard deviation of the distribution has reduced, when the number of looks has increased to four.

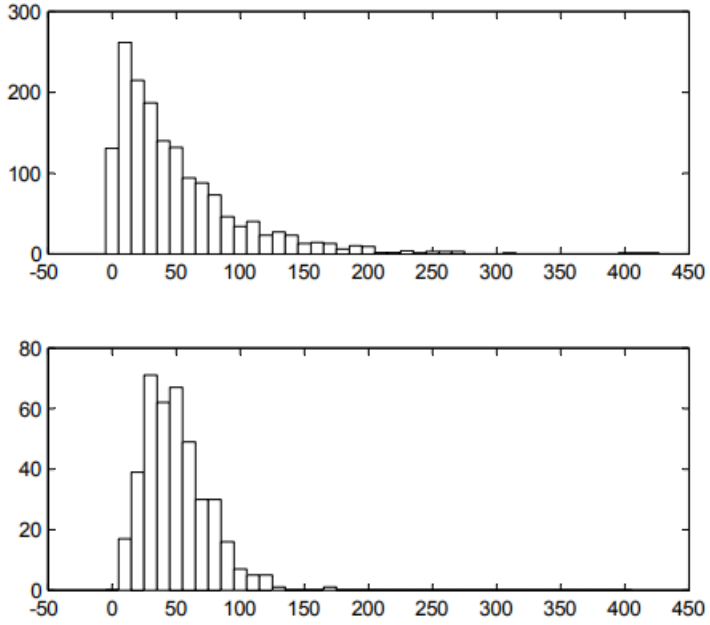

***Figure 2.10**: Histogram of exponential raw speckle on top, and a four look average gamma distribution histogram on bottom, adapted from Richards (2009)*

Speckle can be demonstrated by looking at SAR images. Figures 2.11 and 2.12 outline an ALOS-1 SAR image before and after some N-look, also called *multi-looking*. The speckle effect is very evident in the first image, making interpretation difficult. Specific targets on the scene, such as ships or icebergs are difficult to identify. After multi-looking (5 pixels by 5 pixels) the image quality seems much improved with greater capability to discern targets in the scene.

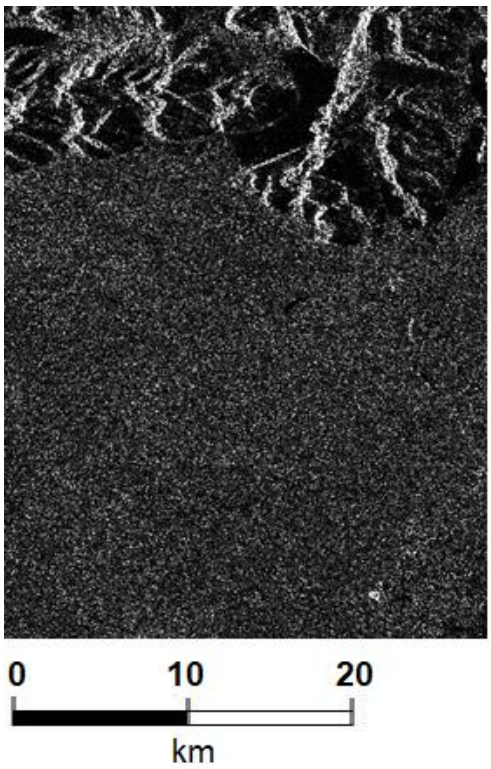

***Figure 2.11**: ALOS-2 SAR image, showing the effect of speckle.*

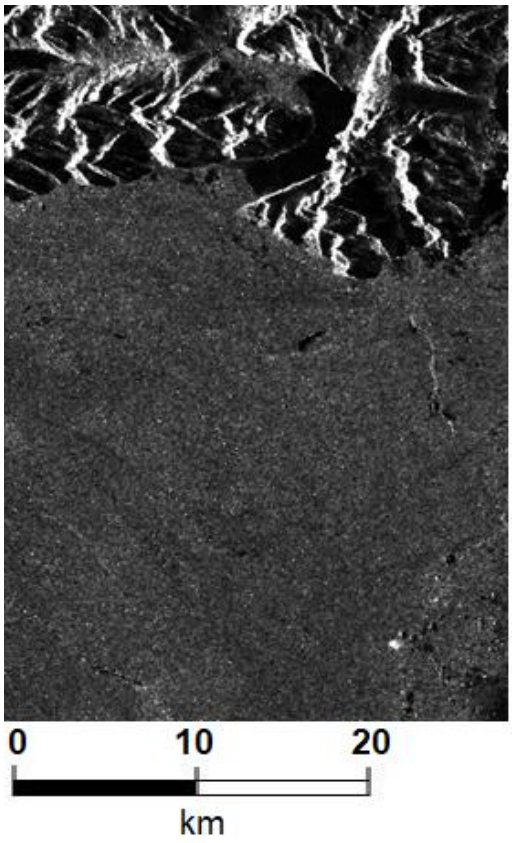

***Figure 2.12**: ALOS-2 SAR image after the speckle filter has been applied. Some of the bright objects indicate ice. We can see topographic features of mountains with glaciers. The white speck in the bottom right of the image could be an iceberg.*

2.2.7. Texture model and non-Gaussian model

While the Gaussian distribution model is good for homogeneous surfaces in coarse spatial resolution SAR images, it often fails to consider heterogeneous backscattering media by SAR with much finer resolutions. For this reason, other types of distributions including *log-normal* (Szajnowski, 1977), *Weibull* (Oliver, 1993) and *K* distributions are applied which are useful for modelling intensity statistics. The K distribution (Jakeman and Pusey, 1976) has been found to be useful since it derives from the physical scattering process, and such a distribution also reduces to the exponential distribution in the case of homogenous surfaces. Delignon and Pieczynski (2002) assumed that the random number of scatterers in each resolution cell follows a Poisson distribution, so the mean of this distribution is considered a random variable. If this random variable follows a Gamma distribution, then the intensity of the backscattered field is known to follow the K distribution.

There is evidence to suggest that real data is better modelled with texture pdf, particularly for images of the urban environment, and natural terrain such as rough sea and forests (Jin *et al.*, 2017).

2.3. Methods for processing SAR data

2.3.1. Speckle Filtering

It has been shown that speckle is problematic, but it can be mitigated using *Mutli-looking*. Multi-looking factors depend on range and azimuth resolutions. In this section, more details are provided about the different methods implemented to de-speckle images using filters (Xu *et al.*, 2008). Quality and effectiveness of such a filter depends on how the averaging is carried out. Homogeneous surfaces are far more ideal for despeckle filters because they ensure that averaging is carried out on uniform targets or terrain that have the same average radar cross section (RCS). The most simple and commonly used despeckle filter is the boxcar filter (Lee *et al.*, 1998). The boxcar filter works by simply averaging all the pixels inside one window region (a rectangle of pixels), by adding the pixel values and dividing by the pixel amount. The result is a more blurred image (Lee *et al.*, 2008).

The boxcar filter has been applied to reduce speckle in SAR and other radar images mainly because of simplicity and typically, window sizes of 3 x 3 are used as a minimum although sizes may vary by application. However, the boxcar filter is not without limitations. The first is poor resolution because of indiscriminate averaging.

This is applied to all pixels in the window that may contain different scattering mechanisms (i.e., different targets). Blurring of edges and boundaries together with the distortion of entropy values, coherence values and other polarimetric parameters are direct results of the deficiency of the boxcar filter (Lee *et al.*, 2005). Resolution is decreased as the window size is increased. Speckle filters therefore need to be adaptive; in other words, they should reduce speckle variance in homogeneous regions, but preserve boundaries and edges in non-homogeneous regions (Richards, 2009). Other types of filtering have been suggested to address this problem, such as the median filter described in Woodhouse (2005) and the Lee Sigma filter, which takes the pixels lying at two standard deviations of the central pixel's value.

2.3.2. Polarisation

Polarisation is a property of the EM wave. We refer to target polarimetry for the study of the polarisation of the EM waves after it interacts with an object. Waves which return to the receiver of the SAR system can have a defined polarisation. The receiver can measure the horizontal and vertical component of the electric field of these waves. The polarisation channels can be called *HH, HV, VV* and *VH*. HH means that the transmitted wave is linear horizontal, and the received wave is horizontal. HV is large when the original horizontally transmitted wave has been affected by the target so that it has a vertically polarised component because of its interaction at the surface. HH, HV, VV and VH are referred as polarisation channels.

Polarisation behaviour of scatterers depends on the shape, size, dielectric constant, roughness and may other factors.

2.3.3. Scattering matrix

Generally, scattered fields obey Maxwell's equations, which are linear. Therefore, postulating a linear mapping from A to B there is no loss in generality. The mapping can be represented by a *scattering matrix*. This is essentially a 2 x 2 complex matrix in which arbitrary polarisation E_i at A is mapped by the scatterer into a state E_s at B by the relationship in the following equation, where the factor in front of the matrix represents phase and amplitude variation of a spherical wave with range r, that is focused on the centre of the scattering point.

$$E_s = \frac{e^{-i\beta r}}{r}\begin{bmatrix} S_{xx\prime} & S_{x\prime y} \\ S_{y\prime x} & S_{yy\prime} \end{bmatrix}.E_i = \frac{e^{-i\beta r}}{r}\begin{bmatrix} S_{11} & S_{12} \\ S_{21} & S_{22} \end{bmatrix}.E_i \quad (2.22)$$

To relate the exchange of transmitter and receiver positions for radar, the vector reciprocity theorem for EM waves is employed. Such a theorem states that if a polarisation state P_A is transmitted from A, then the component polarised in the P_B direction at B equals the P_A component of the scattered radiation when the same object in question is illuminated from B with P_B. It is applied in any case involving a monostatic sensor or a reciprocal medium (a medium with the same polarisation properties at transmission and reception). This means that VH is equal to HV when reciprocity can be applied and the $[\boldsymbol{S}]$ matrix is symmetric. The backscatter theorem thus demonstrates that the scattering matrix is known to have three independent elements. Therefore, the reciprocity theorem is an important basic symmetry, employed in radar backscatter systems for the purpose of extracting information and system calibration (Cloude, 2010).

Every target on a coherent SAR image can be represented by a 2 x 2 Sinclair scattering matrix, shown below. This is the main scattering matrix used in the literature.

$$[\boldsymbol{S}] = \begin{bmatrix} HH & HV \\ VH & VV \end{bmatrix} \quad (2.23)$$

Here HH, HV, VH and VV are polarisation channels. This is a quad polarimetric mode with four different polarisation channels. A dual polarimetric mode uses two polarimetric channels, while a single polarimetric mode uses just one channel. A single channel can also include more than one polarisation, such as HH+VV, or HH-VV.

The four elements of the scattering matrix can also be represented by the scattering vector $\underline{k}$, which is presented as follows:

$$\underline{k} = \frac{1}{2}Trace([\boldsymbol{S}]\psi) = [k_1, k_2, k_3, k_4]^T$$

(we2.24)

Trace refers to the sum of all the elements, T refers to the matrix transpose, and ψ refers to a set of Hermitian matrices (a matrix with an equal complex conjugate transpose).

2.3.4. Covariance and coherency matrices

The *polarisation ellipse* refers to the 3D structure traced from the electric field $\underline{E}(r,t)$ in 3D space and time (Cloude, 2010). In scattering however, geometry can become a function of space/time due to either motions of particles in the scattering medium, or coherent fluctuations that are associated with speckle. A completely polarised wave is represented by two components in an orthogonal base (Jones vector) but for a partially polarised wave arising from scattering of random targets, a representation based on second order statistics (e.g., Stoke parameters) is used. For instance, the canopy of a forest is spread across multiple different image pixels and each of these pixels may have a different scattering matrix. Therefore, second order statistics need to be derived.

A more convenient representation is based on the Pauli or lexicographic scattering vectors.

In the following compact form, the 3 x 3 coherency matrix $[\boldsymbol{T}]$ is noted as follows:

$$[\boldsymbol{T}] = \begin{bmatrix} T_{11} & T_{12} & T_{13} \\ T_{21} & T_{22} & T_{23} \\ T_{31} & T_{32} & T_{33} \end{bmatrix} \tag{2.25}$$

The matrix is based on the Pauli vector representation:

$$\underline{\boldsymbol{k}} = \frac{1}{\sqrt{2}}[HH + VV,\ \ HH - VV,\ \ \ 2HV]^T \tag{2.26}$$

Hence,

$$\boldsymbol{T}_3 = \langle \underline{\boldsymbol{k}} \cdot \underline{\boldsymbol{k}}^{*T} \rangle \tag{2.27}$$

The main diagonal has real value terms (T_{11}, T_{22}, T_{33}) corresponding to the intensities of the Pauli components. The remaining elements are given by the cross-correlation between Pauli components. Another matrix, simply called a *covariance matrix* is formed with any other basis. The covariance matrix contains the second order statistics and has a useful Hermitian symmetry (Cloude, 1985; Cloude, 1986). In the following form, the 3 x 3 covariance matrix is notated as follows:

$$[\boldsymbol{C}] = \begin{bmatrix} C_{11} & C_{12} & C_{13} \\ C_{21} & C_{22} & C_{23} \\ C_{31} & C_{32} & C_{33} \end{bmatrix} \quad (2.28)$$

The matrix is generally based on the lexicographic representation which is:

$$\underline{\boldsymbol{\Omega}} = [HH \quad VV \quad HV]^T \quad (2.29)$$

Hence,

$$\boldsymbol{C}_3 = \langle \underline{\boldsymbol{\Omega}} \cdot \underline{\boldsymbol{\Omega}}^{*T} \rangle \quad (3.28)$$

An independent parameter termed *span* can be found from the total backscattering power of either the Pauli or lexicographic vector and is measured in decibels (dB). The equation for span is as follows:

$$Span = \langle |S_{HH}|^2 \rangle + \langle 2|S_{HV}|^2 \rangle + \langle |S_{VV}|^2 \rangle \quad (3.29)$$

The real value terms (C_{11}, C_{22}, C_{33}) correspond to the intensities of the co-pol and cross-pol channels. The remaining elements give the cross-correlation between two polarisation channels. To produce [$\boldsymbol{T}$] from the outer products of $\underline{\boldsymbol{\Omega}}$ it is possible to use a unitary transformation matrix to convert $\underline{\boldsymbol{\Omega}}$ to $\underline{\boldsymbol{k}}$. From here we can obtain [$\boldsymbol{T}$] as follows:

$$\underline{k} = [D_4]\underline{\boldsymbol{\Omega}} \quad (3.30)$$

where D_4 can be presented in the following form:

$$D_4 = \frac{1}{\sqrt{2}} \begin{bmatrix} 1 & 0 & 0 & 1 \\ 1 & 0 & 0 & -1 \\ 0 & 1 & 1 & 0 \\ 0 & j & -j & 0 \end{bmatrix} \quad (3.31)$$

2.4. Applications of PolSAR data

2.4.1. Adaptive target detection approach

This concept will be discussed more in the following chapters. In this section we will explain the main ideas behind adaptive processing for detection. A sliding window is used to scan an image and note the statistical nature of the area inside the

window. In adaptive processing, the local statistics of clutter are extracted using sliding kernels, which are modifications of the rectangle box.

Various pdfs can be used to model the background clutter inside the kernel which can then be used to determine a threshold by using the Neyman-Pearson (NP) Lemma to provide a Probability of Detection (P_D) and Probability of False Alarms (P_F). The complex nature of natural targets means that statistical distributions for targets can be hard to derive, and so we set the threshold based solely on the distribution of the clutter in order to keep P_F constant (Kay, 1993). This gives rise to the *Constant False Alarm Rate* (CFAR) detector. CFAR detection methods are generally used to search considerably bright pixels when compared to surrounding neighbouring pixels

A classic geometry for the kernel considers a guard window and a ring around it. A *guard window* is one in which a sliding window is nested within a training window but outside of a testing window. It has also been termed a ring window since the background between the training and the guard windows resembles the shape of a ring. The purpose of any guard window is to ensure that no pixels of an extended target are included within the external ring which acts as the training ring (Wang *et al.*, 2008; Saini *et al.*, 2020). The background clutter inside the training ring can then be used to find the threshold, and if the value of a target being tested is higher than this threshold, a detection is called.

2.4.2. Pauli RGB

The representation with the Pauli scattering vector is very useful to represent physical targets in the scene. An easy way to visualise the information in the Pauli scattering vector is by representing the components in an RGB image. For the Pauli RGB colour coding, the polarimetric channels HH+VV, HH-VV and HV are associated with the blue, red, and green colours respectively (Cloude, 2010). The same image from previous figures is now presented here in Figure 2.13, with this technique now applied.

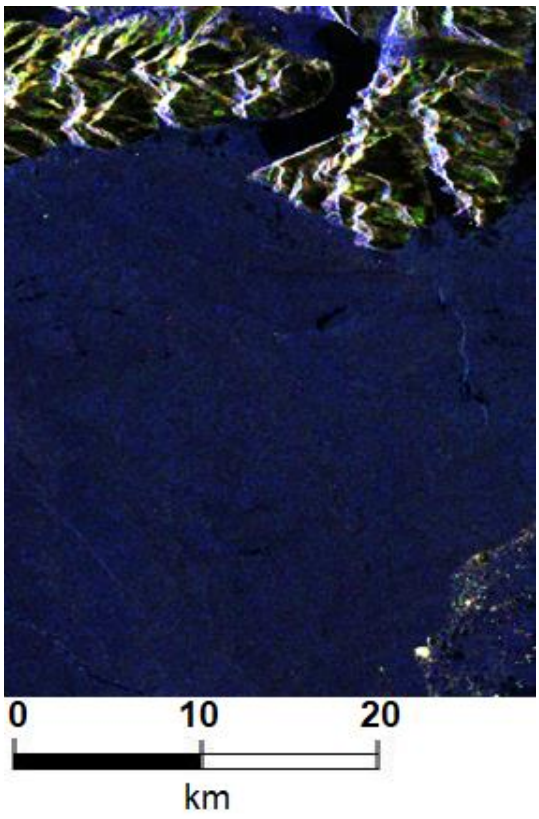

***Figure 2.13**: ALOS-2 SAR image, with Pauli RGB filtering.*

From this image, some things are quite evident. Firstly, the ocean is blue, as opposed to the mountains. There is a small green speck on the ocean, in the top left of the image, which is likely to be a vessel. There is an indication that the white speck on the bottom right of the image is an iceberg, while the white on the mountains could be glaciers. The white colour is the result of equal amplitude across all the polarimetric channels. The iceberg appears bright in the image. The most likely reason for this is because of the iceberg properties and environmental conditions such as the wetness of the icy surface. If there was any red showing in the image, this would suggest that the phase argument of HHVV* is close to π and would denote a reflection or double bounce.

The blue colour of the ocean indicates that the first polarimetric channel HH+VV has a larger magnitude compared to others. In other words, the amplitude of the HV channel is weak and the phase argument of HHVV* is very low. This symbolises scattering over a surface. The green colour shown on the mountains might indicate orientation, due to a dominant HV component. A strong HV is also due to vegetation, but we assume these mountains in Greenland do not have a significant

vegetation on top. However, while the colour coded images may provide indications on the polarimetric properties, the interpretation of colour mixture is still rather subjective. Additionally, the RGB does not consider information, regarding polarimetric cross-correlation.

The thesis now turns to discuss the exploitation of polarimetric behaviour in scattering mechanisms in more detail, beginning with the Cloude-Pottier polarimetric decomposition, and finally the Yamaguchi decomposition, which will introduce a fourth scattering mechanism.

2.4.3. Cloude-Pottier decomposition theorem

So far, a basic theory of polarimetry has been introduced. To exploit and separate scattering contributions, it is useful to apply a polarimetric decomposition to the image. Selecting the right decomposition method plays an essential role in the classification and interpretation of natural targets on the ground (Srikanth *et al.*, 2016). There are two main types of polarimetric decomposition: coherent and incoherent. A coherent polarimetric decomposition focuses only on single targets, and their corresponding scattering matrix which makes them unsuitable for situations where partial targets or a large cluster of single targets are being analysed. An incoherent decomposition requires second order statistics, and it is suited for partial targets. This thesis will focus on incoherent polarimetric decompositions. Additionally, decompositions can be categorised using a physical model or not. One model based on eigenvectors was proposed and applied to quad-pol images by Cloude and Pottier (1996) and Pottier and Cloude (1997).

Cloude (1996) discovered that it is easier to expand any depolarising system as a sum of rank-1 components. The Cloude Pottier decomposition allows for the characterisation of polarimetric targets by exploiting polarimetric information such as the alpha angle, the target entropy, and anisotropy.

After a coherency matrix is formed for each image pixel, it is now possible to decompose each pixel and exploit polarimetric information. The Hermitian nature of the coherency matrix can be expanded in terms of orthogonal eigenvectors and real eigenvalues. First the coherency matrix is presented in terms of all elements (Cloude, 2010).

$$[\boldsymbol{T}] = \frac{1}{2}\left\langle \begin{bmatrix} (S_{HH} + S_{VV})(S_{HH} + S_{VV})^* & (S_{HH} - S_{VV})(S_{HH} - S_{VV})^* & 2(S_{HH} + S_{VV})S_{HV}^* \\ (S_{HH} - S_{VV})(S_{HH} + S_{VV})^* & (S_{HH} - S_{VV})(S_{HH} - S_{VV})^* & 2(S_{HH} - S_{VV})S_{HV}^* \\ 2S_{HV}(S_{HH} + S_{VV})^* & 2S_{HV}(S_{HH} - S_{VV})^* & 4S_{HV}S_{HV}^* \end{bmatrix} \right\rangle \quad (2.29)$$

Another way of writing the dominant matrix can be as shown:

$$[\boldsymbol{T}] = \sum_{i=1}^{4} \lambda_i e_i e_i^{*T} \begin{cases} \lambda_1 \geq \lambda_2 \geq \lambda_3 \geq \lambda_4 \geq 0 \in \Re \\ e_i^{*T} e_j = 0 \end{cases} \quad (2.30)$$

From (2.30) it is possible to see that coherency matrix $[\boldsymbol{T}]$ can be expanded in terms of eigenvalues and eigenvectors:

$$[\boldsymbol{T}] = \lambda_1 \underline{e_1} \underline{e_1^{*T}} + \lambda_2 \underline{e_2} \underline{e_2^{*T}} + \lambda_3 \underline{e_3} \underline{e_3^{*T}} \quad (2.31)$$

where λ_i are eigenvalues and $\underline{e_i}$ are eigenvectors. The eigenvectors can be written as follows:

$$\underline{e_i} = e^{i\phi_i}[\cos\alpha_i \quad \sin\alpha_i \cos\beta_i e^{i\delta_i} \quad \sin\alpha_i \sin\beta_i e^{i\gamma_i}]^T \quad (2.32)$$

Here, β refers to the beta angle, which describes the orientation of a scatterer. The alpha angle α is useful to describe whether a scatterer has a single, dipole or double bounce behaviour. The target entropy is often denoted using the letter H, and is a measure of the randomness of scattering, which can tell us if there is a single dominant scattering mechanism in an image pixel. The anisotropy is denoted by the letter A and is a secondary parameter that is used when there is a high entropy, in order to work out if there are additional scattering mechanisms alongside a dominant scattering mechanism.

Four important ideas stem from this approach, including eigenvector decomposition of dominant scattering mechanisms (Cloude, 1990), eigenvector decomposition and contrast optimisation (Novak *et al.*, 1989), eigenvector decomposition and CFAR detection (Ioannidis and Hammers, 1979), and entropy/alpha decomposition which is covered in Chapter 5 (Pottier and Cloude, 1997; Cloude, 1997).

2.4.4. Yamaguchi decomposition theorem

This decomposition type is known as a model-based decomposition. Freeman proposed a decomposition for volume, rough surfaces and dihedral scattering to be applied for forests (Freeman and Durden, 1998).

Expanding upon this, (Yamaguchi *et al.*, 2005) employed a fourth scattering component: that of the helix scattering mechanism. Although it is not commonly used in cryosphere applications, the model is presented for the first time in Chapter 4 with an application to icebergs. Generally, helix scattering tends to be found in urban environments, particularly around the tops of buildings and skyscrapers rather than natural scatterers. However, the model is used in this work because it expands on the reflection symmetry condition that cross polarisation and co polarisation correlations are close to zero.

For each component, the individual scattering matrix is as follows:

$$horizontal\ dipole = \begin{bmatrix} 0 & 0 \\ 0 & 1 \end{bmatrix} \tag{2.33}$$

$$vertical\ dipole = \begin{bmatrix} 1 & 0 \\ 0 & 0 \end{bmatrix} \tag{2.34}$$

$$horizontal\ diplane = \begin{bmatrix} 1 & 0 \\ 0 & -1 \end{bmatrix} \tag{2.35}$$

$$vertical\ diplane = \begin{bmatrix} -1 & 0 \\ 0 & 1 \end{bmatrix} \tag{2.36}$$

$$single\ scatterer = \begin{bmatrix} 1 & 0 \\ 0 & 1 \end{bmatrix} \tag{2.37}$$

$$left\ helix = \begin{bmatrix} 1 & j \\ j & -1 \end{bmatrix} \tag{2.38}$$

$$right\ helix = \begin{bmatrix} 1 & -j \\ -j & -1 \end{bmatrix} \tag{2.39}$$

So far in this thesis, the basic concepts of SAR and polarimetry have been introduced. Attention now turns from the theory to the application. In Chapter 3, the physics, and effects of icebergs are introduced as well as an extensive review on the literature surrounding the detection of icebergs in the past and present, and future trends of iceberg activity as a result of climate change.

3.0. MONITORING ICEBERGS USING SAR

3.1. Iceberg physics

3.1.1. Morphology

Freshwater is estimated to make up around 2.5-2.75% of water sources on Earth. Of that percentage, only 0.3% of freshwater comes from surface sources such as rivers and lakes. Another 30.8% comes from groundwater sources. But the main source of freshwater (68.9%) is from glaciers, which this review is focused on since the melting of glaciers generates the formation of icebergs when glacier tongues reach the sea. In this section, icebergs are introduced, classified by size, and shape, and the description of iceberg properties is established.

Icebergs are specifically defined by their shape and size. Essentially, they are large chunks of ice serving as sources of freshwater which have calved from a glacier tongue, ice sheet or ice shelf (Young et al., 1998). The definition adopted by the World Meteorological Organisation (WMO, 2014) is “a floating ice mass extending more than 5 m above the sea surface, which has carved from a glacier or ice shelf”. This differs from sea ice, which forms from the surface of seawater itself and so is a source of saltwater. Classification of icebergs is available (Young *et al.*, 1998; Wesche and Dierking, 2012) but there is no universally accepted size classification for certain types based on location and some schemes are inadequate for use. As shown in Figure 3.1, icebergs have different shapes and sizes. Sizes range from growlers (0-5 m long, ~1m high), bergy bits (5-15 m long, 1-5 m high), small iceberg (15-60 m, 5-15 m high), medium iceberg (60-120 m long, 16-45 m high), large iceberg (120-220 m long, 46-75 m high), very large iceberg (>220 m long, >75 m high), and giant iceberg (>18 km long).

Iceberg shapes are categorised into tabular, non-tabular, domed, wedge, dry dock, pinnacle and blocky (Wesche and Dierking, 2012). Tabular icebergs are defined as flat sheets of floating ice with a length/height ratio of ≥ 5:1. Non tabular icebergs have an average width, length, draught ratio of roughly 1:1:6 (Bigg *et al.*, 1997) where the term *draught* refers to the depth of the iceberg below the ocean surface. Height to length ratios can be found in Hotzel and Miller (1983). Iceberg observations for the purposes of classification have been carried out. Dowdeswell (1989) used aerial photography and data collected from 60 MHz radio-echo sounding

equipment to investigate icebergs calved from glaciers in Svalbard. Additionally, Dowdeswell and Forsberg (1992) described observations of icebergs made directly from inner transects in the inner part of Kongsfjorden, Svalbard. They found that iceberg calving was mostly dominated by large numbers of small icebergs.

Table 3.1 summarises the size and shape classification of icebergs, respectively. Icebergs are of interest to scientists because they pose major marine hazards to marine traffic. One example is iceberg drift, which has been the topic of various studies to monitor ocean currents (Gutt and Starmans, 2002). In addition to the RMS Titanic collision, there have been other documented ship collisions with icebergs. A database for these collisions is available in (Hill, 2000)

***Table 3.1**: Iceberg size classification*

Growler	Bergy bit	Small	Medium	Large	Very large
0-5 m	5-15 m	15-60 m	60-120 m	120 -220 m	>220 m

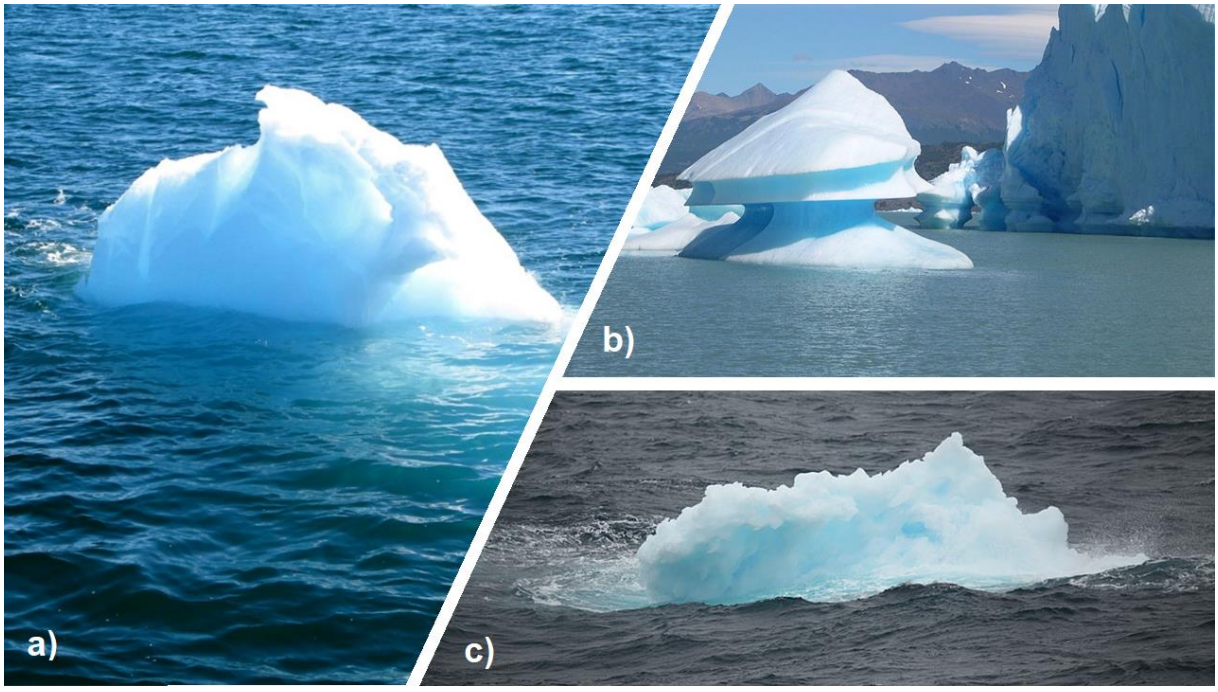

***Figure 3.1**: a) an iceberg classified in size as a growler, b) an iceberg classified in shape as a wedge, c) an iceberg classified in size as a bergy bit*

3.1.2. Formation

An iceberg is a product of freshwater ice formed when a mass of ice calves off the tongue of a glacier or ice shelf. In ice shelves, seaward movement is between 0.3 and 2.5 km/year. Factors such as ocean currents and ocean swell cause stresses on the seaward front of a shelf and leads to eventual fracturing. Fracturing is evident along cracks and crevasses in the ice. On mountain glaciers or narrow ice streams, the stresses on the ice are greater and so these glaciers tend to be heavily crevassed, and calving frequencies are higher. Tidewater glaciers are grounded and slow moving and produce a relatively small iceberg flux. Fracturing occurs by wave action or crevassing. Tabular icebergs tend to form from behind the front of an ice shelf as rifts develop and rupture on a regular basis, but because long sections of ice are floating, the stresses are reduced so fracturing happens further apart in time and space.

Whilst glaciers tend to calve smaller, more irregular icebergs in the Arctic, the nature of the glacier ice mass and the mechanism that fractured them is also of importance. A glacier floating at the terminus will yield different icebergs to a glacier grounded and stationary. Smaller icebergs calve off glaciers that are not afloat at their termini. Grounded glaciers such as the Columbia Glacier have been studied extensively (Brown *et al.*, 1982). It is full of crevasses, and calving happens as a result of shear fracturing and on a seasonal basis. However, a glacier with a floating terminus will generally calve icebergs with a width equal to the thickness (Reeh, 1968). Two calving forcing mechanisms are evident in glaciers with floating termini, and ice shelves, firstly, the stresses within the ice and low hydrostatic pressure, and secondly, buoyancy forces from the ocean or storm surges.

The movement of icebergs from their source is also considered important. For example, in fjords, there is a down-glacier wind that prevents the build-up of sea ice or icebergs within the region at the front of the glacier. Icebergs can also become grounded as they move towards the mouth of the fjord. Only when they have melted enough to float again, will they continue moving down fjord. Grounding may happen based on two factors. Firstly, there may be submarine, or aerial deltas created by side ice streams. Secondly, there may be shallow former moraines created down fjord, from fjord exit sills, and valleys (Bigg, 2015). Icebergs in other environments such as open water may not be restricted by such factors.

The formation and morphology of glaciers can be examined in full detail in Haykin *et al.* (1994). When snowfall exceeds loss due to evaporation/melting, a basic glacier is created in the mountains. Fresh accumulation of snow (Murphy, 2014) has a density of between 0.06-0.08 g/cm^3 due to trapped air between hexagonal snow crystals. The time for the conversion of snow to ice is dependent on temperature. When glaciers are at a constant pressure melting point (temperate glaciers) delicate snow melts quickly, and crystals become spherical in shape, increasing density to about 0.2 g/cm^3. Denser snow takes a granular form. In contrast, melting and compression in subpolar and polar glaciers may take years. Ice crystals grow larger and join together, eliminating the space between crystals. Eventually, as this compaction process continues, compression recrystallisation, freezing and thawing further increases the density to a point at which snow becomes firn. Firn is the intermediate stage within the conversion of snow to ice, at a density of 0.4-0.55 g/cm^3. But as the density increases through recrystallisation and the sealing of air passages between ice grains, the firn becomes glacial ice, typically at around 0.8-0.85 g/cm^3 (Haykin et al., 1994). Literature on the density of icebergs varies. Murphy (2014) documents icebergs from the Greenland area to be 0.917 g/cm^3, while some upper portions of tabular icebergs in the Antarctic are compacted snow, which is permeable, and thus these bergs have a lower density (Weeks and Mellor, 1978).

In Greenland glaciers glacial ice forms as air in the firn is trapped in atmospheric gas bubbles or forced out through cracks and fissures in the ice. An increase in density is a result of trapped air under pressure within these gas bubbles, making glacial ice impermeable to water. Tiny air bubbles that have been distributed throughout the ice are responsible for the visual white colour of ice. When white ice is placed in water, gas bubbles pop under the pressure release, and fizzing occurs. Louder crackling sounds of the ice occur under stress fracturing of smaller pieces. Bubble size ranges between Greenland and Antarctic ice. Scholander and Nutt (1960) reported diameters of 0.02-0.18 mm and lengths of 4 mm for bubbles in Greenland icebergs. Gow (1968) examined Antarctic glaciers and found bubble sizes ranged between 0.49-0.33 mm; the size would decrease with depth, but density was independent of depth. (Gammon *et al.*, 1983) reported round, ellipsoidal shaped bubbles, with elongation ranging a few tenths of millimetres. These studies suggest that typical values of bubble sizes in glacial ice range in the order of 0.1-0.5 mm. In visual contrast to white ice, ice that appears blue indicates no bubbles. Blue ice is some of the oldest ice, and far more hazardous than that of white ice. Because the

air bubbles have been squeezed out by the pressure, and the ice crystals have increased in size, density is higher.

The final density of glacial ice may exceed 0.9 g/cm^3. Once this ice breaks off into seawater, about six-sevenths of the freshwater ice will be submerged, because the density of seawater is 1.0 g/cm^3. This is echoed by Haykin et al. (1994) stating that approximately one seventh of the iceberg mass rests above the surface. Therefore, studies such as Ardhuin *et al.* (2011) show that approximately 90% of an iceberg's volume is underwater.

3.1.3. Calving processes

There is no one universal model of iceberg calving within the literature. The calving processes of iceberg in the Arctic and Antarctic are incredibly complex, and involve several environmental factors such as wind speed, ocean wave oscillation, glacial speed and flow, and geomorphology of glacial environments such as fjords. Several authors discuss these processes in more detail (Benn *et al.*, 2007; Bassis, 2011). The mechanisms behind iceberg calving are identified by Kristensen (1983). These are: creep failure, reeh type calving, hinge-line calving, vibrational calving, and iceberg collisions with ice shelves. In creep failure, lateral/horizontal stresses are induced by the spreading of the glacier tongue or ice shelf. In Reeh type calving (Reeh, 1968), fracturing occurs at the point where the distance from the ice edge is equivalent to the ice thickness, due to creeping of the ice. Hinge-line calving is caused by storm waves causing ice to fracture at the grounding line. Vibrational calving refers to deforming of an ice shelf due to swell, storm surge or tsunami waves. Collisions with icebergs and ice shelves happen in Antarctica, where ice shelves are a common feature of the cryosphere.

The forces that govern the calving of icebergs are hydrostatic forces from the ocean, and cryostatic forces caused by the slow movement of the glacier or ice shelf. These forces are balanced at the base of floating ice, but become unbalanced towards the ice surface, and above the ocean level. This produces a tensile force from the top that pushes the ice towards the water, and a bottom buoyancy force that acts on the base section of landward ice, effectively compressing the ice body and resulting in a large shear stress, usually at a distance equal to the ice thickness (Reeh, 1968). It is also noted by Benn *et al.* (2007) that the strain rate may be a main factor of calving, particularly when the surface of the ice is present with crevasses which vary spatially according to the velocity of ice movement. There are also

second-order processes such as fracture propagation which occurs in response to imbalances in stress close to the front of the glacier. A glacier terminus might also be subject to melting at or below the ocean waterline, which also leads to undercutting and stress imbalances. Or at the grounding line of the glacier and water, bending of a glacier tongue may occur. Third order processes include the fracturing of submarine platforms below the ocean surface.

According to Bigg (2015), three major factors that determine calving environment can be outlined. The first factor relates to the strength of the ice itself, which is governed by the subglacial hydrology and from crevassing processes. Examples include crevasses which fill with water as opposed to those that are dry, the speed of the ice movement over slopes, and the runoff of meltwater down crevasses away from the glacier. Secondly, the temperature of the ocean water has an effect on the submarine melting of ice below the surface. A partial increase in freshwater melting into the ocean will affect the local temperature and salinity profiles, although this effect is partial when compared to the overall temperature of the water. The last factor relates to the ice melange: a sea ice and iceberg mix at the front of the glacier. If a large ice melange is not present, calving is more likely to occur under normal conditions. Sometimes downslope winds at the glacier front can carry this ice melange away from the terminus. But, if present, ice melanges alter the force balance at the terminus, and lead to less calving. In Greenland, all three of these factors result in iceberg calving, but this has changed over the past century (Bigg *et al.*, 2014).

The characteristics of all icebergs occur primarily because of calving processes, while some processes that occur after calving may also have an impact. Most tidewater glaciers that are grounded and have high ice cliffs will be heavily crevassed. Here, the stresses produced by the glacier movement over the changes in topography towards the ocean, and ocean wave swell interaction result in local fracturing at the glacier front, which produces an imbalance in the hydrostatic and cryostatic forces. Secondary factors that can cause cryostatic pressure to become too great can include wind velocity which drives wave motion. Local fracturing can also occur as a result of undercutting at the base of the ice cliff. As a result, icebergs calved in this manner are smaller in size, usually irregular in shape and may also be subject to further processes as they drift away from the glacier (Bigg, 2015). It is noted that on mountain glaciers, there is a correlation between iceberg flux and the

width of an ice stream or fjord, which produces greater local shear stresses. Crevassing is even more local, and smaller icebergs occur. In contrast, large tabular shape icebergs form from large ice shelves, or from wider fjords. Here, the dominant factor of calving is not the flow speed of the ice, but rather the buoyancy force of the ice shelf or ice section (in a fjord) on the ocean surface. This reduces the shear stresses considerably and leads to fracturing further apart in time and space. Ice shelves tend to produce icebergs around 20-30 km in diameter, while ice in wider fjords can lead to more medium to large icebergs (Bigg, 2015).

From recent work conducted by Bassis and Walker (2012), it is now known that the thickness of the ice stream entering the water plays a role in iceberg calving. The horizontal stress of the ice S_{xx} is determined by the difference in the weight of the ice and the water and air column of the same height in front of it.

$$S_{xx} = \frac{1}{2} p_i g H \left[1 - \left(\frac{p_w}{p_i}\right)\left(\frac{D}{H}\right)^2\right] \tag{3.1}$$

Here, p_w and p_i are the densities for water and ice, respectively, D is the depth of water from the ocean surface to the base of the ice, and H is the ice thickness. This model proves that the ice can fail when both crevasses that form from the top of the glacier downward, and crevasses that form from the bottom upward are present. The shear stress S_{xx} exceeds that of the critical stress τ_c of the ice which leads to eventual fracturing. Considering the maximum thickness, where S_{xx} exceeds τ_c, and if the fraction of the ice thickness dominated by crevasses is r, the upper bound of the ice front thickness H_{max}can be found and is as follows:

$$H_{max} = \frac{(1-r)\tau_c}{p_i g} + \sqrt{\left(\frac{(1-r)\tau_c}{p_i g}\right)^2 + \frac{p_w}{p_i} D^2} \tag{3.2}$$

Overall, this model shows that a glacier which is more deeply crevassed has a lower ice thickness that is stable for a given water depth, and calving becomes more likely if the ice thickness increased because of upstream effects. If the depth of the water is higher, calving is also more likely as the ice is floating, and floating ice is only stable if not deeply crevassed. In fjords, ice is not normally floating on the water, and so any crevassing happens as a result of other ablation processes that occur before the ice reaches the calving zone (Bassis and Walker, 2012).

Generally, the annual discharge of icebergs calved from tidewater glaciers can be calculated as follows:

$$Q_{total} = Q_{flux} - Q_{v\,loss} \quad (3.3)$$

where Q_{flux} is the volume of ice discharge at the tidewater glacier terminus, and $Q_{v\,loss}$ is the loss of ice volume due to tidewater outlet glacier terminus changes in position (Burgess *et al.*, 2005). Q_{total} can only be determined through knowledge of the cross-sectional area, average cross-sectional velocity at the terminus of each glacier, and any history of terminus advance/retreat.

3.1.4. Grounding processes

In fjord environments, it is not only the calving of icebergs that determine the final characteristics of iceberg shape and size. As noted above and in Bigg (2015), one factor affecting iceberg calving is the ice melange. In fjords, the ice melange also determines the rate at which iceberg movement down the fjord can take place. In some glaciers, strong winds that move downstream can keep the region in front of the terminus free from sea ice and icebergs, while in others, a thicker melange can trap newly calved icebergs and only allow for their movement down fjord over long periods of time, up to months and years (Mugford and Dowdeswell, 2010). It is also well known that icebergs can become grounded within fjords. The sides of a fjord are often steep, because of rapid flowing palaeo ice streams which will have led to more erosion of the landscape over time. Yet, despite this, the grounding of icebergs can still occur where the ice streams have formed submarine or aerial deltas. In some fjords, the fjord sill at the exit can also result in icebergs becoming grounded if the depth of the ice body scours the surface of the sill. If this happens, the icebergs will remain grounded until they have melted sufficiently to float once more, which could take months or even years (Bigg, 2015).

Grounding also occurs outside of fjords, particularly in shallow seas. Icebergs from east Greenland can become grounded in the continental shelf regions south of Baffin Island, across the Labrador Sea and down towards the Grand Banks of Newfoundland. These waters are less than 200 m deep, which when combined with icebergs where ~85% could be submerged down to 200 m, is a recipe for iceberg grounding (Marsh *et al.*, 2015). While iceberg grounding in open water is not necessarily a hazard to ships or fixed marine platforms, over time, as the iceberg melts enough to sufficiently float again, they can be problematic. As a result,

grounded icebergs are also of importance, particularly in areas causing the greatest disruption to human society. For example, local communities along the east coast of Canada. But the grounding and scouring of these icebergs off Labrador and east Newfoundland may also be partly responsible for increased iceberg numbers south of 48°N in the spring months according to recent modelling (Wilton *et al.*, 2015).

The grounding and scouring of icebergs also explain why they are a major indicator of climate change, as they carry and deposit ice rafted debris (IRD) along the sea floor. In some areas, however IRD can also be deposited from sea ice. So other ways to look for climate change proxies in icebergs involve looking at scouring marks on the sea bed caused by iceberg contact. Sediment can be left behind in grounded icebergs as they melt, and these deposits are called iceberg contact deposits (Benn and Evans, 2014). They also pick up sediment from the sea floor as they push through the sea floor sediments. This sediment freezes to the base of the iceberg, which also can occur under glaciers and ice shelves. Additionally, iceberg collisions with the sea floor can also lead to earthquakes which are detectable from long distances (MacAyeal *et al.*, 2008). As a final note, collisions cause damage to marine benthic ecosystems.

Attention now turns away from the physics of icebergs, processes, and movements towards their hazardous nature and thus, the novelty of the work carried out in this thesis.

3.2. Icebergs as hazards

The nature of icebergs is of importance to remote sensing scientists. Glaciers are smaller in size compared to massive ice sheets such as those found in the Antarctic (Dowdeswell and Jeffries, 2017). Icebergs less than 120 m in length are incredibly hard to see in SAR systems (Wesche and Dierking, 2012) or may not be picked up at all. Additionally ship operators may find these types of small icebergs very hard to spot. Given that numerous shipping routes are in operation in the Arctic for commercial and maritime purposes, these icebergs are major hazards to their operation and navigation (Marino *et al.*, 2016b). In east Greenland, the direction of travel for icebergs is mostly southward on the East Greenland Current until they reach Cape Farewell at 60°N. They then drift north-east, travelling in the West Greenland Current towards Melville Bay or they can turn west in Davis Strait before drifting south (Robe, 1980). In Greenland alone, the Jakobshavn Glacier produces at

least one tenth of the total iceberg flux from the Greenland Ice Sheet (Robe, 1980). These icebergs drift around Baffin Bay in an anti-clockwise direction before travelling south in the Labrador Current. Only around 400-800 icebergs drift as far south as 48°N off Newfoundland.

It is not only shipping that icebergs present a hazard to, but also stationary marine platforms such as oil rigs and costal installations (Bigg, 2015). Additionally, icebergs can carve channels through sea sediment which can pose a risk to undersea cables and pipelines. The IIP provides real time data on iceberg movements in the north Atlantic and Arctic Oceans. Bigg (2015) documents that iceberg numbers in the north west Atlantic Ocean have increased significantly in the last two decades. That number may now be even higher at the time of writing. Incidents in the Atlantic still occur, although they do not lead to sinking, but do lead to damage. The past record of 200 years shows that 26% of 371 (96) vessels sank or were abandoned after a collision, and 90% of these collisions occurred in low visibility (Hill, 2006). However, encounters between fishing vessels and icebergs are notable (Hill, 2000; Hill, 2006). In December 2011, the most recent incident, an iceberg tore a hole in a fishing vessel off the Antarctic coast.

Icebergs also present hazards to other maritime operations. The difference between these and ships is that ships can move out of the way at low speeds or respond to alerts of ice in the vicinity. However, fixed installations such as oil rigs are also at risk of iceberg collision, such as off the coast of Newfoundland (Barry and Gan, 2022). It is known that very heavy icebergs have the capability of exerting forces greater than 10^7 N which makes the potential force an iceberg can exert on a fixed platform enormous. Despite this, the threat of collision is low. Fixed platforms such as offshore wind farms are not currently located in areas of high iceberg activity. Additionally, fixed platforms like this and oil rigs are only connected to the sea bed at a depth of around 30 metres, which means only smaller icebergs could reach the platforms without becoming grounded. But despite these observations, even a small iceberg could exert a force equivalent to a cargo ship, making these fixed platforms still vulnerable to collisions. It is oil and gas rigs that carry some of the greatest risk, especially as polar exploration for hydrocarbons remains necessary to supply the global economy. Icebergs have been observed since 1992 (Hawkins *et al.*, 1993) in the vicinity of the area around the Falklands which has been proposed as a drilling site since 2015.

These incidents all demonstrate the need to monitor and detect icebergs to increase maritime safety. The remote sensing of icebergs is therefore of paramount importance, a topic to which is now introduced.

3.3. Remote sensing and scattering of icebergs

3.3.1. Remote sensing of icebergs

SAR plays an important role in iceberg detection. It is useful to describe how it was introduced using the example of the IIP as above. The record improved during World War II with the introduction of air patrols all the way through to the 1950s, as this provided an opportunity to track icebergs in good weather. Ships were then used to focus more on oceanographic missions, and ship-board radar was introduced (Christensen and Luzader, 2012), which had 24-hour operation. Radar was also attached to aircraft as well as patrol ships. However, the threat of bad weather still prevented this technology from reporting icebergs in poor visibility due to wave reflection in high sea states (Bigg, 2015). Thus, until 1983, the common method of iceberg detection was through visual identification using rotating scanning radars. These were soon found to have difficulties with detecting at long-range due to a coarser azimuth resolution. Side looking radar (SLAR) made a breakthrough in that year and improved the discrimination of icebergs and ships even further and was also the first time that radar could perform in all weather conditions. With the exception of SeaSAT and Kosmos used for demonstration missions before 1990, in 1993, the concept of SAR was used for iceberg detection (Christensen and Luzader, 2012) which is now the most used method for iceberg detection and used by many groups such as the IIP.

Satellites with SARs on board such as ERS-1, ERS-2 and Envisat and Sentinel-1 have a high spatial resolution of 30 m. This allows for the detection of smaller icebergs with an edge length of approximately 100 m (Wesche and Dierking, 2012). This means that SAR can detect from the higher range to medium bergs. Detection of icebergs smaller in size is, therefore, more complicated, and problematic.

One other difficulty in observing icebergs is to understand whether or not each new observation was a new iceberg, or one already observed prior. This led to the IIP introducing a model drift of icebergs in 1979 which become far more sophisticated over time (Smith, 1993).

While it has been clarified that these remote sensing systems are not yet capable of detecting smaller iceberg sizes, it has not been established how physical and environmental conditions of icebergs induce backscattering. Similarly, Murphy (2014) found that while radar scatterometers are useful for iceberg tracking, knowledge of high radar backscatter from SAR remains unknown.

3.3.2. Backscattering of icebergs

Modelling backscatter continues to pose a challenge to scientists in the field of remote sensing. In the case of SAR in iceberg detection, certain parameters of an iceberg are thought to induce backscatter depending on several conditions. In Bayer *et al.* (1991) the backscattering of terrain is analysed. A terrain may have different brightness depending on factors such as the slope angle and relief aspect relative to the direction of illumination. In the case of icebergs, this study suggests that the geometric properties of icebergs would influence the image created by SAR.

Shoshany *et al.* (2000) takes the question of SAR backscatter further since there is a relationship between this behaviour and soil moisture and surface roughness. In the case of icebergs, the roughness would be of paramount importance to determining the behaviour of SAR backscatter.

It is now useful to introduce the three most common types of scattering behaviour which a PolSAR can exhibit and how these are related to iceberg scattering. This will also be referred to when examining polarimetric decompositions (see Section 4.3). Here, the basic scattering behaviour of surface, volume and double bounce is described (Figure 3.2).

Every medium or surface has a dielectric constant, which refers to the relative permittivity, or the ratio of permittivity of a medium and the one of free space. The strength of *surface scattering* is determined by its dielectric constant, as well as the roughness of the surface. Here we refer to roughness compared to the wavelength used. Surface scattering can be defined as a scattering behaviour which occurs when there is a large discontinuity in dielectric constant, such as from air to water.

When the surface is very smooth, a radar wave that hits that surface will not reflect much energy back to the receiver. Most of it will be transmitted in a forward direction as for a mirror, also called specular reflection (Richards, 2009).

As the surface of the medium becomes rougher, the scattering behaviour changes and now begins to occur in all directions, including back to the radar. A

small level of roughness results in small backscattering and the specular component will be larger than the backscattered component. However, a very rough surface decreases this specular component considerably. Additionally, as the scattering is now happening in all directions, more backscatter is received by the radar, resulting in a lighter appearance of the medium on SAR imagery. Various models of surface backscatter exist, but a notable one which can be used to model the sea surface is the Bragg model (Plant, 1990), defined as the sum of two components of specular (coherent) behaviour and non-specular (incoherent) behaviour

The second major scattering mechanism happens because of many individual scatterers which all contribute backscatter to the radar. Numerous discontinuities in dielectric constant give rise to *volume scattering*, and such examples include tree canopies, and pipe and lenses in icebergs/glaciers.

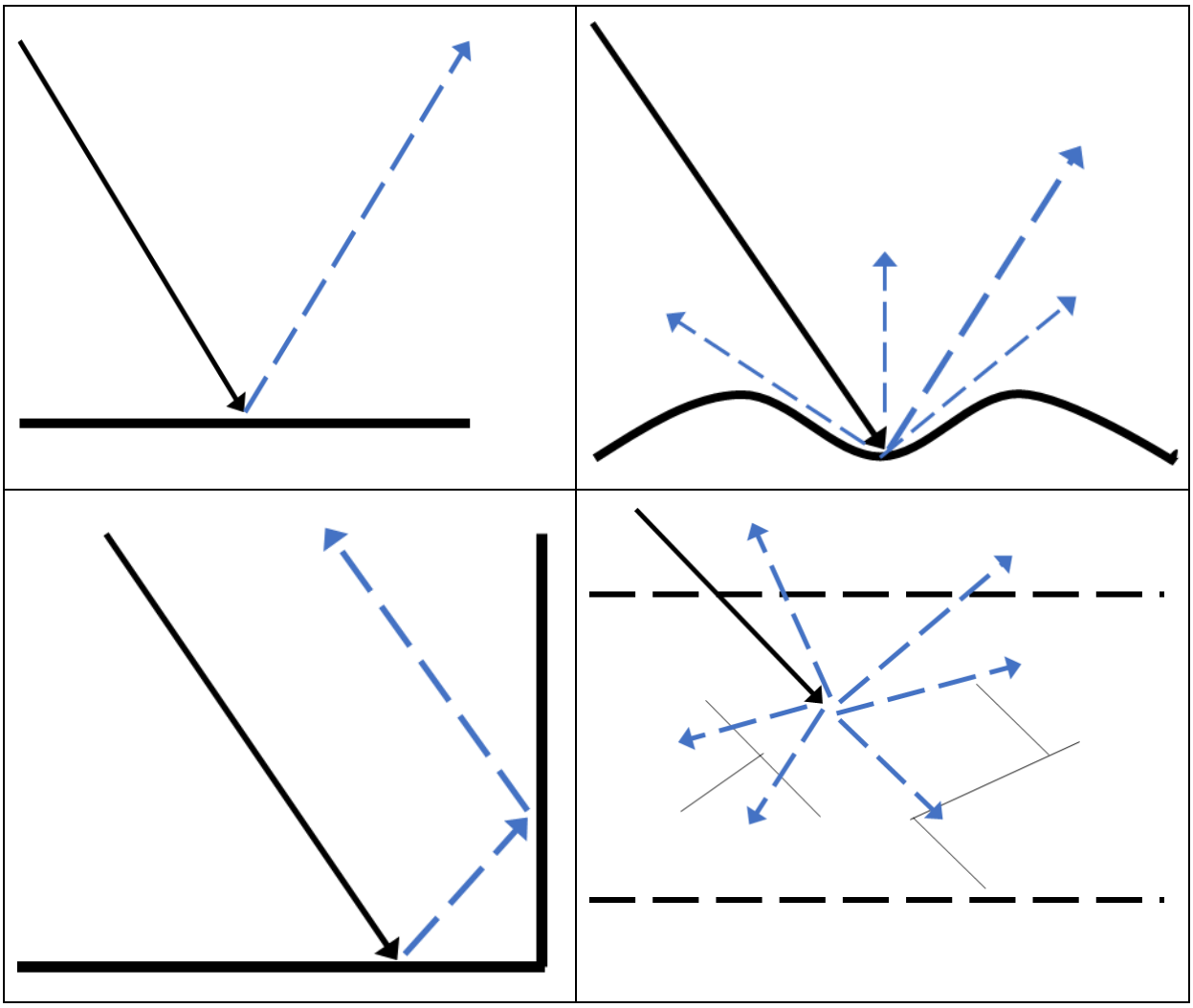

***Figure 3.2**: basic scattering mechanisms found in nature, a) single surface scattering, b) rough surface scattering, c) double bounce scattering from a corner reflector, d) volume scattering within an upper and lower boundary, black arrows indicate incident radar wave, blue arrows indicate scattered waves, note in rough surface scattering, the specular component is most prominent*

So far, only a horizontal dimension has been considered, as is the case for surface scattering. But for volume scattering, the vertical dimension must also be included, such as the upper and lower boundary of an iceberg body, or the layers of a tree canopy. Using the example of icebergs, the energy of a wave must continue to scatter across multiple different layers in the ice body until the wave is attenuated or the lower boundary of the iceberg is reached. When an iceberg topples over, the dielectric constant properties of the ice body will change, and the resulting scattering behaviour will also change as a result. Areas which have been immersed in seawater will have a higher dielectric constant compared to drier areas.

The third type of scattering considers a horizontal plane and a vertical surface. In this instance, the travelling wave reaches the vertical surface, bounces away towards the horizontal plane, and is then backscattered back to the radar. The path with opposite direction also happens. This is termed *double bounce scattering* or simply, double bounce. In the case of icebergs, the vertical surface of the ice body rests upon a horizontal sea surface, and as a result, the edges of icebergs may have a large double bounce scattering component, if this dihedral corner is oriented directly towards the radar. If oriented completely away from the radar, then depending on such an orientation, the double bounce component will decrease in nature.

In addition to the dihedral corner reflector, double bounce scattering also occurs from a facet, which is a term used to describe a flat surface composing the target. In the case of icebergs, irregularity in the shape of the ice body will determine the nature of multiple bounce behaviour from corner reflectors or facets. A tabular iceberg has obvious corner reflectors and will have a stronger double bounce component if facing the radar, whilst an irregular shaped iceberg will have a combination of corner reflectors and facets, which may not necessarily face the radar, resulting in a weaker response. It is also important to note that if the EM radiation penetrate the ice, we do not expect the side wall to produce double bounces. However, if the ice is wet and the penetration is reduced by surface water, then we could have more reflections from the ice body.

3.4. Iceberg detection

3.4.1. Visually identifying icebergs in SAR images

One of the most important studies which quantified iceberg radar backscattering coefficients in the Weddell Sea was carried out by Wesche and Dierking (2012). It was established that the backscattering coefficient of icebergs was the sum of surface and volume scattering contributions. Backscatter intensity influences the brightness of an iceberg on an image. The higher the coefficient, the brighter the target. In the case of icebergs, some can stand out distinctly from the background clutter in high resolution SAR images. However, brightness is also affected by other factors such as high wind speeds, precipitation/surface liquid water and higher incidence angles.

In this work, iceberg visualisation is determined using a five-point segmentation model which is described below (Figure 3.3). The following figure is the one we developed in this thesis and is applied in the following chapters.

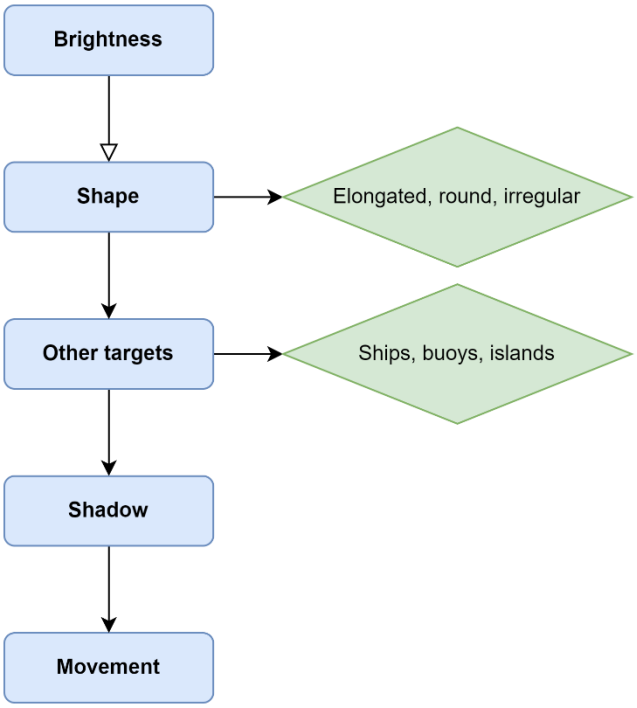

***Figure 3.3**: Iceberg segmentation visualisation model. Blue boxes indicate steps, green diamond boxes indicate examples.*

The first step is to evaluate the brightness of the target. It is important that the target is not yet determined to be an iceberg at this stage. This step involves examining any large bright spots on a SAR image after all other image processing is

complete. A very bright target would indicate a high backscattering intensity. The position of the bright spot in relation to other areas of the image can then be evaluated. An iceberg would be far more likely if the bright spot were situated outside of a glacier terminus, for example. However, even in high resolution SAR images, just one or two very bright pixels can be mistaken for sea ice.

The next step is to evaluate the shape of the target. It is well known that icebergs in Antarctica tend to be flat and tabular in shape, so there should be little sign of any irregularity. However, in the Arctic, irregularity is more important. The shape of the target is more likely to be an iceberg if it can be shown clearly that it is irregular. It is important to remember that other targets have very distinct shapes, so these need to be removed. For example, in ship detection, a much more elongated target is likely to be a vessel. Small islands, or smaller targets like buoys can also be mistaken for icebergs. Separating targets from islands is possible using land masking.

As in Section 3.11, looking for shadows is also an ideal step in iceberg segmentation. If the target is very bright, has a good shape, and now also has a dark shadow beside it, the chances are now more likely it is an iceberg. However, as noted in Wesche and Dierking (2012) ‘dark’ icebergs can happen when the volume scattering component is reduced by surface liquid water, wet snow, or temperatures above the melting point. Another difficulty comes from icebergs embedded within sea ice. Sometimes the iceberg might be too small amongst the sea-ice floes, or the incidence angle of the image may not be high enough to distinguish a shadow. However, sometimes icebergs can be identified within sea-ice floes visually. The darker edges of these icebergs can sometimes appear on images.

The last indicator that a target may be an iceberg is movement. For a time-series dataset, it is possible to study the past location of a bright target and whether it has drifted any particular distance. A smaller iceberg will drift faster due to a lower mass. A larger iceberg may drift more slowly. Using this model, it may be possible to visually distinguish icebergs in images. However, it is important to note that when not backed up by validation data, icebergs visualised by eye are subject to human biases. In this work, care has been taken during the visualisation process to ensure all targets are identified as icebergs.

In our study we obtained Figure 3.4 which shows the result of the eigenvector decomposition on an ALOS-1 SAR image. Using the maximum eigenvalue, clearly the shadows of icebergs within the region can be distinguished, since they appear much darker than the icebergs themselves, which are brighter (in this case, yellow).

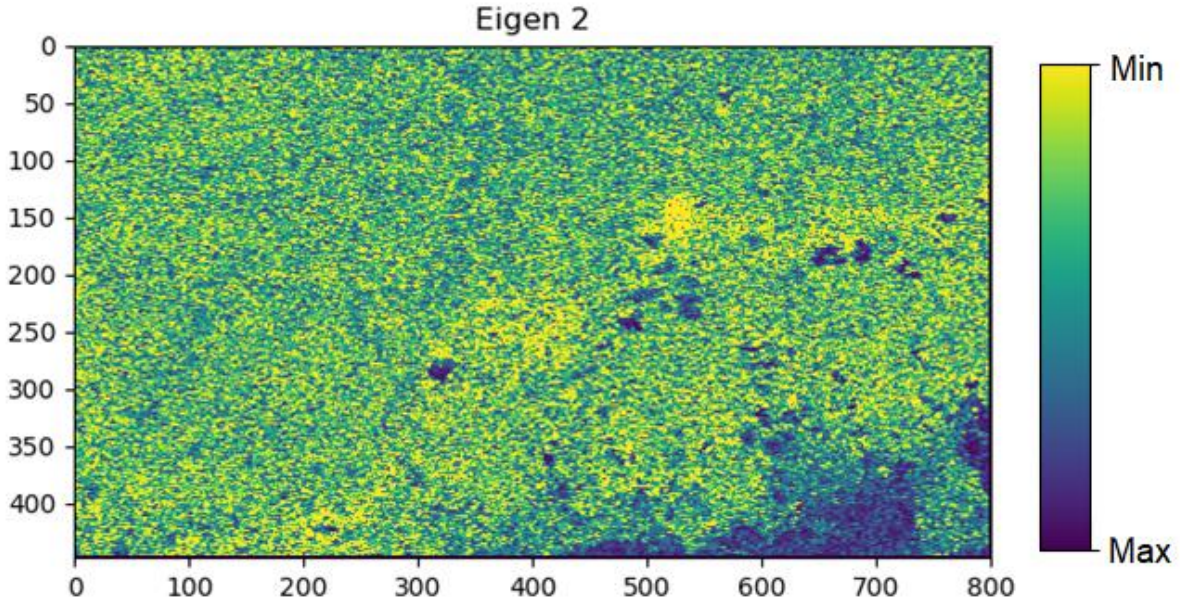

***Figure 3.4**: Effect of eigenvector decomposition on an ALOS SAR image, large yellow dot with dark areas indicates icebergs and iceberg shadows. Colour bar indicates min to max eigenvalue,*

3.4.2. Detection history

One of the first segmentation iceberg detection models was proposed by Williams *et al.* (1999). The authors used the ERS-1 SAR satellite with a 30 m spatial resolution from the European Space Agency (ESA). This model focused on the technique of pixel bonding, which can help to delineate iceberg edges on SAR images. An 8 x 8 pixel window scans the image and calculates the mean and standard deviation based on the intensity of backscatter, which gave a pixel size of 100 m x 100 m. Usually because of the stronger contrast between the ice body and the open ocean/sea ice background, a 3 × 3 pixel window is more suitable for icebergs than a 5 x 5 pixel window used for intensity estimates in sea ice floes, but in the case of Williams, (1999), the level of speckle was high. Iceberg edges are also sharper than those of sea ice floes. Finally, a 3 x 3 boxcar is justified as the smallest possible filter to detect icebergs down to a few pixels in length. The model assumes a threshold value above which a certain pixel neighbourhood is classed as heterogeneous. The results of this model showed an ability to detect icebergs more

than six pixels in size. This technique has been extended to sea-ice floes and has been used with C-band and X-band SAR instruments (Hall *et al.*, 2012). A downside to this approach is that it is currently semi-automatic, requiring the confirmation of each selection of tracked icebergs.

Later, the first computer-based model for the tracking and identification of icebergs less than 200 metres in length was proposed by Silva and Bigg (2005) and tested on ERS and ENVISAT SAR data. This study was an important breakthrough for identifying small to medium iceberg shapes and using them for tracking purposes. This model has an online processing time of 10-15 minutes for iceberg identification and less than 5 minutes for tracking applications. Limitations to this work included pixel distances of 100 metres, and increased speckle noise found on higher resolution images. This model, alongside many other traditional models applied in the literature is based on backscatter intensity. This work was built upon even further by Denbina and Collins (2012) who applied circular polarisation to this technique (compact polarimetry) and has promised higher identification rates. This method expands upon traditional polarimetry which uses linear polarisation. They tested linear data and compact polarimetry to detect icebergs in the Labrador Sea and found that the compact pol data missed fewer targets.

Despite the improvement of iceberg monitoring over the past few decades, the background risk of icebergs remains (Christensen and Luzader, 2012). Any immediate risk is managed through daily iceberg charts and bulletins by the North American Ice Service using information from the IIP, but longer-term risk still carries the potential of iceberg collisions, and thus will affect the planning of marine operations and use of North West Atlantic shipping routes (Bigg *et al.*, 2021). Seasonal forecasts of iceberg numbers require knowledge on annual variations in iceberg numbers. Bigg *et al.* (2014) and Wilton *et al.* (2015) attempted to solve this problem using ocean-iceberg modelling. In this approach, a circulation model was proposed to study the ocean circulation and the iceberg drift and melting from variations in climate over the whole of the twentieth century. A second approach was also proposed which uses a Windowed Error Reduction Ratio (WERR) control systems identification model (Zhao *et al.*, 2016). This approach involved the design of a polynomial regression system and results showed that three environmental variables modulated the iceberg production, trajectory and melt rate. In both models, the correlation ranged between 0.83 and 0.84, and it was established that icebergs

which reach 48°N have calved from Greenland the year before. More recently, Bigg *et al.* (2021) used the WERR model to forecast the 2018 iceberg season up to 8 months in advance and predicted a high iceberg season for 2017-2018 with 71% confidence. They found that 2017 and 2018 each had iceberg numbers above average for all predictions. These models demonstrate the feasibility to produce long-term iceberg risk shipping forecasts for marine planning months in advance.

There exist numerous studies on using Constant False Alarm Rate (CFAR) detectors on icebergs. Previously, CFAR detection has already been proven useful for ship detection (Scharf and Demeure, 1991; Vachon *et al.*, 1997; Gill, 2001). More recently it has been applied to icebergs (Power *et al.*, 2001; Gill, 2001). The CFAR detector has been used in the following ways: differentiation of icebergs from vessels (Howell *et al.*, 2004), studies of iceberg frequencies in Greenland (Buus-Hinkler *et al.*, 2014) and more recently, iceberg detection with TerraSAR X Stripmap images (Frost *et al.*, 2016). CFAR detectors are not without limitations, however. When applied in areas of high iceberg density, high wind velocity and high sea-state, this method alongside other thresholding methods fails as soon as backscatter intensities are higher than or match those of open water.

Attempts to detect smaller iceberg sizes are evident in the literature. Some studies show that 10 m spatial resolution for different types of SAR imaging data, such as quad pol data has been used to detect icebergs of approximately 100 m diameter. Marino *et al.* (2010c) used SAR polarimetry and perturbation analysis to develop an algorithm enhancing the detection of ships and icebergs. Marino *et al.* (2016b) enhance this work, proposing a new dual-polarisation radio anomaly detector (DPolRad) algorithm to detect smaller icebergs. It is established in Marino (2018) that richer information could be obtained if the use of quad-pol data was implemented.

Finally, the tracking of icebergs in SAR images was also attempted. One of the most well-known trajectory models is proposed by Bigg *et al.* (1997). The authors establish a three-dimensional ocean circulation model based on the thermodynamics and dynamics of icebergs for the Arctic and North Atlantic oceans and tests the model with observational data on iceberg motion. They found that the major force balance in iceberg motion is advection from the water, and water resistance. One significance of this study is that it demonstrates the importance of time and size of iceberg calving from individual glaciers. The authors also suggest that iceberg studies have the potential to address future geophysical and climatic questions.

3.5. Iceberg properties

3.5.1. Topography

No single iceberg is of the exact same shape. Because ice can form at cold temperatures, and melt at warm temperatures, the composition of the iceberg is always changing. The topography of the iceberg plays a very important role in SAR detection. These undulations within icebergs can be detected with remote sensing radars. One study from Zakharov *et al.* (2013) summarised how multi resolution and frequencies of SAR can lead to a more coherent knowledge of iceberg topography. Although interferometric data is often used to reconstruct icebergs using topographical computer models, the heights of shadows can also be used to analyse surface topography. Generally, the darker shadows indicate more of a pinnacle topography, whilst icebergs that are smoother classified as tabular will appear much brighter (Herdes *et al.*, 2012).

Similar studies have been done to estimate heights of icebergs, in addition to reflectance. Viehoff and Li (1995) employed the use of Advanced Very High Resolution Radiometer (AVHRR) and used ERS-I SAR data to identify areas of high backscatter on icebergs. The shadows created by tabular icebergs were then used to estimate heights and corresponding draughts of the icebergs. However, these papers contained no information regarding smaller icebergs, which have been harder to detect.

A third and more recent study (Frost *et al.*, 2016) employed the use of high-resolution X-band SAR to detect icebergs. This study highlighted how topography can affect the detection performance. Because icebergs have topographic differences, scatterers generate a lot of variation during SAR processing. However, this study identified major limitations regarding the backscattering intensity of icebergs because they were found to overlap with intensities of the surrounding ocean. Intensity of backscatter in open water depends on surface roughness. A higher wind speed will generate a rougher sea. Once intensities overlap with those induced by icebergs, thresholding methods fail. Filtering techniques were used to separate iceberg intensities from open water intensities.

3.5.2. Wetness/liquid water

In the Arctic, the weather is constantly changing. Snow is prone to melting, and rainwater may fall from clouds within warmer areas of water that may contain

icebergs. As a result, when the snow cover melts on icebergs, or when rainfall strikes the top of icebergs, a wet layer is produced. The wetness of the iceberg surface is another property that can affect the detection by SAR satellites. One study (Gray and Arsenault, 1991) documented the reflections of L-band SAR in icebergs and found that surface wetness (a thin layer) may decrease the ability for SAR pulses to penetrate and backscatter from the iceberg.

The research literature also documents how SAR backscatter is very sensitive to surface wetness. A flooded surface (with liquid water on top) may appear dark on a SAR image. Changes in surface wetness occur over long periods of time (Herdes *et al.*, 2012). The explanation as to why wet surfaces appear dark on a SAR image is given in Wesche and Dierking (2012). In regions where summer temperatures are at, or above the melting point, the water or wet snow on an iceberg surface significantly reduces the volume scattering contribution, so that icebergs stand out as dark targets on SAR images. This is pointed out in Mazur *et al.* (2017) emphasising that backscatter is significantly decreased.

3.5.3. Shadows

Another method of iceberg detection is through identification of shadows. On a SAR image, these will appear as regions of very low brightness. The shadows are cast by the icebergs because of the slant angle of incidence of the SAR signal. The shadows show up as darker strips along the side of an iceberg, making it useful to distinguish between icebergs and multi-year ice floes. Additionally, as has been previously mentioned, shadows could be used for estimating iceberg heights and hence iceberg thickness (Viehoff and Li, 1995) but errors may be significant.

The Cloude Pottier decomposition theorem may be applied to provide a better detection method for shadows (See Section 3.4.1).

3.6. Motivations for thesis

As it has been shown in these first three chapters, remote sensing of icebergs is extremely important. Icebergs in the Arctic are hazards not only as a result of their irregular shape, but also due to how small their sizes are compared to the icebergs in Antarctica. Additionally, the calving rate of icebergs in Greenland as a result of climate change is approximately 10,000-30,000 annually (Frost *et al.*, 2016). Not only does this mean the potential for more icebergs abundant within shipping routes, but also these icebergs may be a lot smaller in size, as melting rates increase and

reduce their lifetimes. As of the present day, the current consensus is that icebergs less than 120 metres in length are too small for SAR instruments to detect and identify. When compared with the need for increased shipping routes, this can become a global problem.

In the future SAR satellite will acquire images at higher resolution, maybe using constellations already present such as ICEYE or Cappella. ESA is also planning higher resolution SAR with ROSE-L. Additionally, the future systems will likely be equipped with quad pol capabilities.

The threat of climate change is evident; rising global temperatures are projected to reach above 1.5°C by 2050 according to the IPCC 6th Assessment report in 2020 (Zhai *et al.*, 2021). Icebergs are a major indicator of climate change; in the North West Atlantic iceberg sightings below 48°N have occurred in almost every year of the last three decades and the flux of icebergs calving from Greenland has also increased (Csatho *et al.*, 2008). The Arctic ice extent and thickness has been in major decline. Warming temperatures will accelerate the rate of melting of ice sheets and speed up glacier movements towards their termini. Changes in ice gradient along the periphery of the ice sheets will also speed up the flow of ice. These changes are consistent with iceberg calving. A rise in ocean temperatures is also linked to increased melting under ice shelves, decreasing the thickness of the ice, and weakening it substantially to cause fracturing and eventually calving. These processes are set to intensify under climate change (Straneo *et al.*, 2013; Bigg *et al.*, 2014). However, some previous observations may challenge the idea of increasing iceberg flux. Firstly, in Greenland, mass loss has mostly been driven through melting rather than calving; in 2010, the ratio of mass calving to melting was about 1:2 (Rignot et al., 2011). Secondly, as glaciers retreat, their termini no longer contact seawater, and therefore become terrestrially terminating glaciers. It has already been reported that calving flux has been decreasing because of marine to terrestrial termination in two glaciers at 64°N on the west coast and around the east coast from the Geikie Plateau. Warmer temperatures are leading to higher precipitation in Greenland, but causing melting more than calving (Hanna *et al.*, 2012). It is Antarctica where ice discharge could increase because of increased snowfall which is suggested to rise by a factor of three by 2500 (Winkelmann *et al.*, 2012). Therefore, the likelihood of iceberg flux in Antarctica is only set to increase (Bigg, 2015).

Despite the long-term effects of iceberg discharge in Greenland, the short-term effects point towards increased iceberg flux, and this is why icebergs will continue to be hazards for years to come in the Arctic regions, and why the work of remote sensing scientists who monitor, detect, identify, and classify icebergs is paramount to the safety of all maritime operations. This forms the main motivation behind this thesis. As glacier terminuses retreat in fjord environments, it is expected that iceberg flux could double by 2200 (Nick *et al.*, 2013). Only beyond this period, the glaciers will have retreated far enough from marine to terrestrial settings, which will result in a rise of melting as opposed to calving.

So far, in this thesis, this chapter and the previous chapter have covered literature reviews on the history and importance of iceberg detection, introduction to SAR remote sensing, polarimetry and iceberg science. Attention now turns from these areas of iceberg detection using PolSAR, to addressing the research gaps outlined in these reviews in Chapters 4, 5 and 6.

3.7. Narrative in following chapters

Iceberg backscatter models are lacking in the literature, and do not consider various polarimetric characteristics. For polarimetric decompositions such as Cloude-Pottier, very few applications on icebergs are known or tested on high resolution SAR data in areas of major iceberg activity. These methods have however been applied to ships (Touzi *et al.*, 2004; Li *et al.*, 2009; Liu *et al.*, 2020), and various other applications such as oil spills (Jones *et al.*, 2011). It is well known that a vessel is a partial target, but little information exists on the classification of icebergs as polarimetric targets. This will be assessed using multi-scale analysis of L-band quad pol data on icebergs in Greenland (Chapter 4).

Perhaps most importantly, it is well known that polarimetric targets exhibit different backscattering mechanisms (Cloude, 2010). Beside speculation, little is known on backscatter mechanisms in icebergs. In this work, we assess two polarimetric decompositions, Cloude Pottier, and Yamaguchi, to determine the backscattering mechanisms of icebergs (Chapter 4).

As detection methods become more advanced, the focus has turned on the application of these methods on larger datasets. Despite the abundance of literature on quad-pol methods applied to vessels, the literature for these same methods applied to icebergs is lacking, aside from a notable few (Marino et al., 2012, Frost et

al., 2016; Soldal et al., 2019). Additionally, it is not known if quad-pol iceberg detector algorithms perform any differently in various environments. In this thesis, attention is given to icebergs standing alone in open ocean, and icebergs embedded within sea ice. In Chapters 5 and 6, the detection capabilities in two location and two frequency bands are addressed. Here, detector algorithms are tested and evaluated on ALOS-2 L-band data and RADARSAT-2 C-band data for the first time.

So far, we have considered the polarimetric behaviour and the detection capabilities of icebergs. When compared to satellite data, ground-based radar provides two advantages to iceberg detection research. Firstly, they provide validation data, and secondly, they provide this data in time periods of minutes, allowing for a real time comparison of both satellite and ground radars where available. Therefore, the last data chapter (Chapter 6) considers this application in a Norwegian fjord setting. Not only are iceberg data collected using the same detection methods as in Chapter 5, but now we apply a ground-based radar to validate the data, and to test detection performance.

4.0. QUAD POLARIMETRIC MULTI-SCALE ANALYSIS OF ICEBERGS IN ALOS-2 SAR DATA: A COMPARISON BETWEEN ICEBERGS IN WEST AND EAST GREENLAND

This chapter is also available as a journal paper within Remote Sensing. We introduce the concept of multi-scale analysis on icebergs using ALOS-2 SAR data, by employing two types of polarimetric decomposition: model and eigenvalue/eigenvector based to evaluate the potential of PolSAR to provide good iceberg classification.

Bailey, J.; Marino, A. Quad-Polarimetric Multi-Scale Analysis of Icebergs in ALOS-2 SAR Data: A Comparison between Icebergs in West and East Greenland. Remote Sens. 2020, 12, 1864.

Abstract:

Icebergs are ocean hazards which require extensive monitoring. Synthetic Aperture Radar (SAR) satellites can help with this; however, SAR backscattering is strongly influenced by the properties of icebergs, together with meteorological and environmental conditions. In this work, we used five images of quad-pol ALOS-2/PALSAR-2 SAR data to analyse 1332 icebergs in five locations in west and east Greenland. We investigate the backscatter and polarimetric behaviour, by using several observables and decompositions such as the Cloude–Pottier eigenvalue/eigenvector and Yamaguchi model-based decompositions. Our results show that those icebergs can contain a variety of scattering mechanisms at L-band. However, the most common scattering mechanism for icebergs is surface scattering, with the second most dominant volume scattering (or more generally, clouds of dipoles). In some cases, we observed a double bounce dominance, but this is not as common. Interestingly, we identified that different locations (e.g., glaciers) produce icebergs with different polarimetric characteristics. We also performed a multi-scale analysis using boxcar 5 × 5 and 11 × 11 window sizes and this revealed that depending on locations (and therefore, characteristics) icebergs can be a collection of strong scatterers that are packed in a denser or less dense way. This gives hope for using quad-pol polarimetry to provide some iceberg classifications in the future.

4.1. Introduction

Climate change is increasing the formation of new icebergs due to rapid melting and speeding up of glacial ice (Vincent, 2020; Xie *et al.*, 2019). Remote sensing techniques, such as Synthetic Aperture Radar (SAR), have routinely been used to detect and analyse large icebergs (Akbari *et al.*, 2016b; Zakharov *et al.*, 2013), however, the understanding of the scattering mechanisms for iceberg backscattering is still a topic of research (Hannevik, 2017). It is known that physical properties of icebergs may induce different backscattering behaviours (Ferdous *et al.*, 2020).

Greenland and the Arctic are currently warming rapidly due to climate change (Hanna *et al.*, 2012). Many of Greenland's glaciers are melting and icebergs are calving into the ocean much more rapidly (Fettweis *et al.*, 2008). These icebergs can drift into the Atlantic and into important shipping lanes. For this reason, monitoring the iceberg behaviour is critical to ensure the safety of maritime activities. Arctic iceberg sizes can be relatively small with a few tens of metres outside the water. This presents a challenge for monitoring (Soldal *et al.*, 2019). Studying the scattering behaviour of icebergs is therefore important in order to identify smaller icebergs via PolSAR analysis.

4.1.1. Icebergs in SAR

Satellites with SARs on board such as ERS-1, ERS-2, Envisat and Sentinel-1 have a high spatial resolution of around 30 m, but this varies depending on the acquisition mode. Recent work has also been carried out using COSMO-SkyMed X-band imagery (Nunziata *et al.*, 2018; Parmiggiani *et al.*, 2018). For classification purposes, SAR can detect from the higher range of medium icebergs. Detection of icebergs smaller in size is, therefore, more complicated and problematic (Marino, 2018). Although there are studies proposing backscattering models of icebergs, it is not clear how physical (e.g., shape, structure) and environmental (e.g., temperature, surface liquid water) conditions of icebergs can modify these backscattering models.

Backscatter from icebergs can be rather similar to the clutter background when sea ice surrounds the iceberg. Indeed, several papers have outlined the difficulty of detecting icebergs embedded within sea ice (Marino, 2018). When sea ice has an irregular or rough shape, such as the presence of ridges or hammocks, the backscattering from sea ice can become very bright and resemble the one from icebergs producing several false alarms (Soldal *et al.*, 2019).

Iceberg surface roughness plays a very important role in SAR detection, especially when the iceberg is melting. Open water backscatter intensities sometimes have a stronger backscattering than small icebergs (Wesche and Dierking, 2012). Iceberg radar backscattering coefficients are the sum of surface, multiple reflections, and volume contributions of an iceberg. Backscattering intensity depends on iceberg shape, surface roughness and ice volume (fraction, shape, size of cracks, air bubbles and impurities) (Willis *et al.*, 1996). Smaller iceberg sizes may also be a result of image speckle lowering the spatial resolution. As a result, targets in single pixels are much harder to detect than those in multiple pixels (Soldal *et al.*, 2019).

The application of quad-pol SAR data can be used to increase our ability to distinguish between icebergs and sea ice (Dierking and Wesche, 2013). This is due to the capability to identify multiple scattering mechanisms and avoid focusing on a fixed scattering mechanism, where the iceberg may be very weak, or the background may be very strong.

In Greenland, snow is prone to melting and rainwater may fall from clouds within areas of warmer water where the iceberg may drift. Additionally, when an iceberg topples over, it may show the bottom part which is covered in high-dielectric constant saline ice (Wesche and Dierking, 2015).

Tabular icebergs that have been freshly calved also appear brighter, indicating that any surface wetness is a result of later events, such as snow melt or other precipitation (Williams *et al.*, 1999). Icebergs that stand out as dark targets are a result of reduced volume scattering and radiation being reflected specularly on top of wet surfaces (Wesche and Dierking, 2012).

Backscatter intensities have been recorded on icebergs in the Weddell Sea using ERS-1 C-band SAR. It has been documented that they have an intensity range of −6 to −4 dB (Young *et al.*, 1998). The surrounding clutter may produce an intensity of less than −10 dB (Young *et al.*, 1998). However, these figures were dependent on seasonal variation. An image taken in the summer is likely to show a different scattering intensity to an image taken in winter. In this work, we use SAR images taken in both summer and winter.

Generally, icebergs which are smaller in size and embedded within sea ice, prove difficult for SAR detection. Accurate iceberg identification is dependent on the ability to distinguish them from open water, sea ice and other polar targets, all under

a range of interchangeable environmental and meteorological conditions. Properties of icebergs along with their surrounding conditions determine the brightness and reflectivity when interpreted on a SAR image. Significantly, paucity of data surrounding backscatter behaviour is limited. In this work, we apply a range of polarimetric parameters to icebergs shown in SAR images to try to address this limitation.

4.1.2. Aims and Objectives

The aim of this work is to analyse backscatter and polarimetric behaviour based on a series of polarimetric parameters. These include the Cloude–Pottier decomposition (Cloude and Pottier, 1996), the Yamaguchi decomposition, Pauli RGB and an overall intensity operator (span). These PolSAR methodologies can shed some light on the understanding of the different scattering mechanisms contributing to the iceberg backscattering. Our hypothesis is that icebergs exhibit a combination of different scattering mechanisms. It is hoped that this will lead to the improvement of future iceberg classification.

4.2. Materials and Methods

Each SAR image was taken from the PALSAR-2 instrument aboard the ALOS-2 radar satellite over east, north and west Greenland. These data were collected under an open JAXA Announcement of Opportunity. A total of five images were selected for analysis, processed via calibration, construction of a covariance matrix, boxcar filtering and finally, PolSAR parameters. We then performed a multi-scale analysis using two window sizes. In this section, we specify the materials and methods carried out for the analysis. A description of the SAR data is presented in Table 4.1.

Table 4.1. *ALOS-2/PALSAR-2 JAXA properties. Centre DMS coordinates are selected for latitude and longitude. Incidence angle range is min, centre and max. Note the ground resolution is for ALOS-2/PALSAR-2 quad-pol mode. Time is UTC.*

Image ID	**Location**	**Lat/Lon (DMS)**	**Resolution (m)**	**Incidence Angle Range (°)**	**Date/Time**
ALOS2066231360-150815	Blosseville Coast N	68°02'13.2"N 30°19'58.8"W	4.3 × 5.1	37, 39, 41.5	15/08/2015 01:26
ALOS2064761430-150805	Nuugaatsiaq	71°25'26.4"N 53°26'52.8"W	4.3 × 5.1	37, 39, 41.5	05/08/2015 02:48
ALOS2064461300-150803	Isortoq	65°07'08.4"N 39°13'37.2"W	4.3 × 5.1	37, 39, 41.5	03/08/2015 02:07
ALOS2057951350-150620	Blosseville Coast S	67°19'1.2''N 32°37'33.6''W	4.3 × 5.1	29, 31, 33.6	20/06/2015 01:26
ALOS2191031530-171206	Savissivik	75°52'19.2''N 62°10'48''W	4.3 × 5.1	29, 31, 33.6	06/12/2017 02:52

4.2.1. SAR Processing and Iceberg Detection

In this section, we outline the procedure carried out to process the SAR dataset in order to evaluate the polarimetric information from the icebergs. A summary of steps is presented in Figure 4.1.

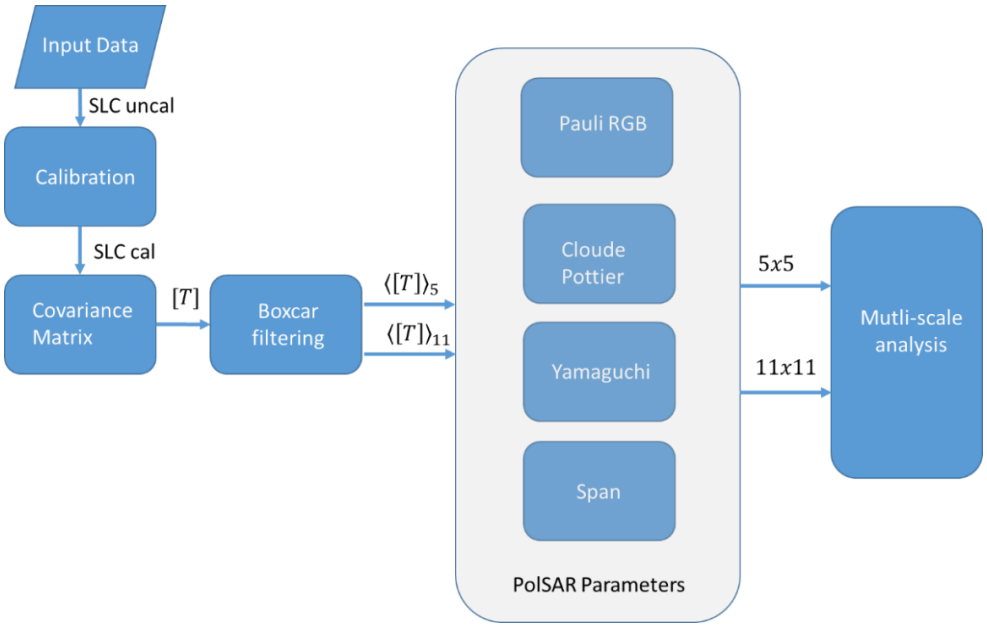

Figure 4.1. *Block diagram outlining the methods of the study. The covariance matrix was built before main multi-scale analysis. Note that Pauli RGB refers to the RGB image and without it, the other steps would not have been carried out.*

The first step was to input ALOS-2 quad-pol data and calibrate them into the appropriate SAR real and imaginary parts for each image. The radiometric calibration we applied on all images simply removes the output scaling applied by the SAR focusing processor and formatting as sigma naught (normalised radar cross section). However, it does not convert data in dB since we are interested in the Single Look Complex (SLC) format. The next step in processing the quad-pol data was to derive the structure of the covariance matrix, which will reveal the second order statistics of the partial target once the averaging is applied. We applied averaging using two filters either of 5 × 5 (which corresponds to 25.5 × 21.5 m) or 11 × 11 (which corresponds to 56.1 × 47.3 m). After the filtering, the data (in covariance matrix format) are ready to be processed for extracting decomposition parameters (Cloude–Pottier, Yamaguchi) or other observables (Pauli RGB and span). A list of all the polarimetric parameters used is in Table 4.2

Table 4.2. *Polarimetric parameters. Note the Yamaguchi parameters had their orientation removed and the span is a separate parameter that was deduced independent of a decomposition.*

Parameter	Type	Notes
Alpha	Cloude–Pottier Decomposition	-
Entropy	Cloude–Pottier Decomposition	-
Beta	Cloude–Pottier Decomposition	-
Anisotropy	Cloude–Pottier Decomposition	-
Span	Observable	-
Y Double	Yamaguchi Decomposition	Orientation removed
Y Helix	Yamaguchi Decomposition	Orientation removed
Y Surface	Yamaguchi Decomposition	Orientation removed
Y Volume	Yamaguchi Decomposition	Orientation removed

All these parameters are used to evaluate the polarimetric and brightness behaviour of icebergs. Please note, some of the parameters such as the Yamaguchi components are expressed in dB to ease the visualisation. The dB was applied to the outcome of the Yamaguchi.

The final step used here is the identification of icebergs, which feed in the iceberg analysis. To do this, we used the RGB images with large zooms (500 × 500 pixels) where we could adjust the contrast accordingly. The RGB images were composed with the intensities of the Pauli components: HH + VV for red, HH-VV for green and 2 HV for blue. An iceberg was selected if it represented an anomaly in backscattering with one (or all) of the following features: it was very close to the glaciers, it had a dark shadow in the looking direction (far range side), it had a bright rim in the direction of the sensor, it showed signs of breaking the sea ice surrounding it by being grounded and not able to move as the rest of the sea ice.

To keep a more conservative approach, other targets such as ships identified by a characteristic elongate shape were removed from the analysis. The same approach removed charter rocks or targets very large in size and with visual characteristics similar to islands.

Each target identified as an iceberg on the image was pinpointed by identifying the middle pixel in radar coordinates. Since we performed filtering, the middle pixel will be significant for an area of the iceberg, either 25.5 × 21.5 m or 56.1 × 47.3 m. Identification of the middle pixel was done because one of the running hypotheses of our analysis is that icebergs are a composite of different scattering mechanisms and if we would have averaged all the points together, we would not have been able to check for this. Only by keeping the area smaller were we able to perform multi-scale analysis.

It is important to point out that as we are missing in situ validation data, we are restricting our analysis to icebergs we can identify by visual analysis. The ones that cannot be visualised because of a small size or a wet surface (and therefore, very dark) are extremely challenging for the analysis, since they will require extensive in situ observations.

4.2.2. Geographical Location and Meteorological Data

The icebergs used in our analysis are all situated within the Greenland area. Greenland is influenced by various weather patterns, as well as the Gulf Stream and East Greenland Current, which affects temperatures on the east and west sides. Blosseville Coast runs along the southeast of Greenland down towards Isortoq. Nuugaatsiaq sits on the west coast and Savissivik sits on the far northwest coast.

Figure 4.2 shows the locations of the ALOS-2/PALSAR-2 images, while Tables 4.1 and 4.3 include the dates of each acquisition.

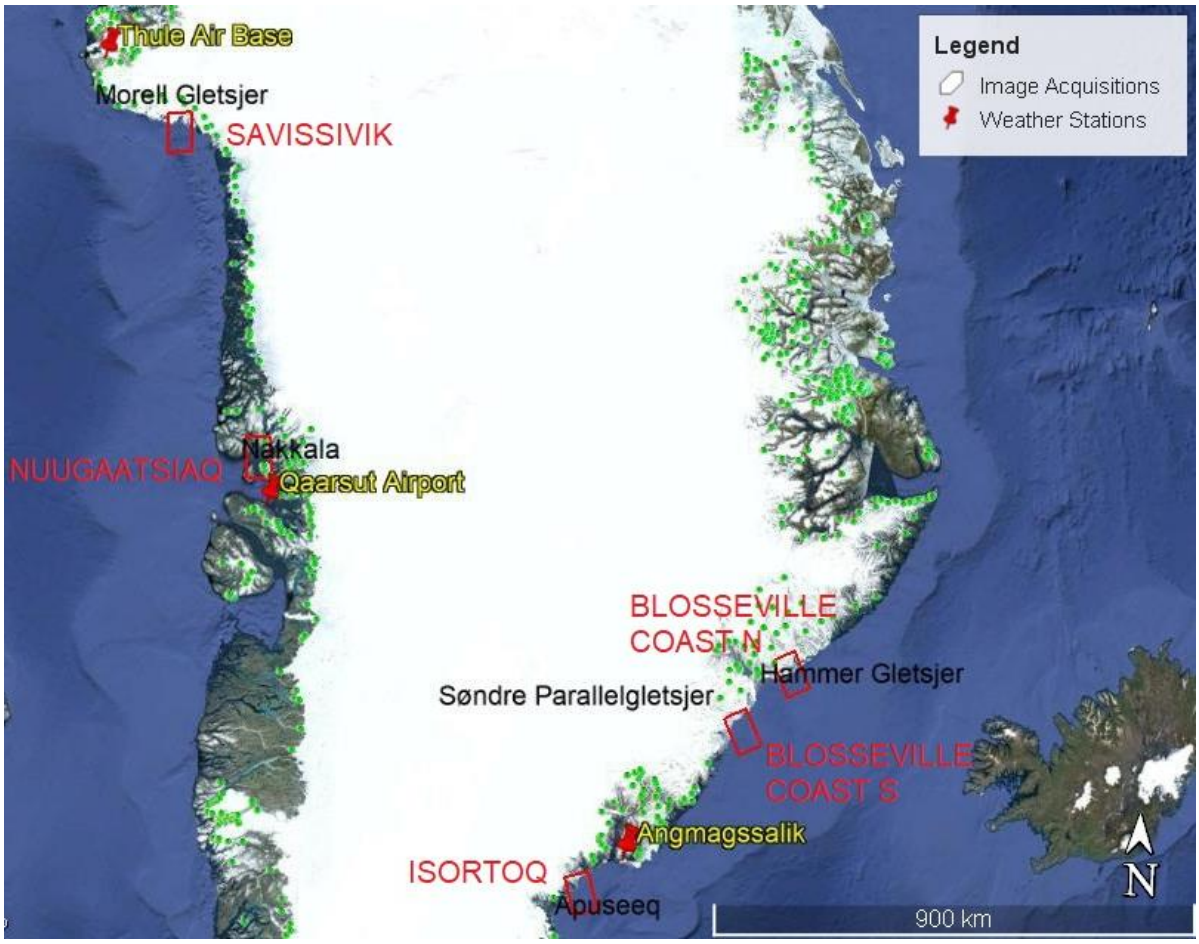

Figure 4.2. *Google Earth image of data acquisition. Red pinpoints indicate the weather observation stations, with names shown in yellow labels. Red boxes indicate the image footprints. Red labels indicate footprint locations. Green dots indicate GIS data for Greenland glacier locations. Glaciers names are in black. White compass point indicates north. 900 km indicates the scale of the image.*

Because backscattering behaviour may be dependent on environmental factors such as the presence of surface liquid water, (besides size and shape of the icebergs) meteorological information such as temperature and precipitation were collated for the nearest available weather stations. These data were also collected according to monthly data trends from 2015 and 2017. Please note, we are only using a monthly average for meteorological conditions simply due to the paucity of data available. We were unable to find daily wind, temperature, and precipitation data for the locations in the given time period.

Three weather stations were investigated: Angmagssalik near to both Blosseville Coast, and Isortoq in east Greenland, Thule Air Base near to Savissivik in

north Greenland and Qaarsut Airport near to Nuugaatsiaq in west Greenland. There is no weather data for the two Blosseville Coast locations, and we approximated these data using the closer Angmagssalik station.

4.2.2. Meteorological Conditions

The meteorological conditions in east, north and west Greenland, including temperature and precipitation levels, were also examined according to the locations of the three images. A record of the temperature and precipitation levels for Isortoq, Savissivik and Nuugaatsiaq corresponding to the dates of the image creation are shown in Table 4.3.

Table 4.3. *Average Greenland meteorological conditions for images taken. Each location is a weather observation station. Note the image taken near Savissivik is acquired in December 2017, while the images taken near Isortoq and Nuugaatsiaq are taken in August 2015. Average data represent the month of image acquisition. Temperature is monthly averaged minimum.*

Location	**Min Temperature (°C)**	**Average Rainfall (mm)**	**Average Wind Speed (km/h)**	**Date Taken**
Angmagssalik	−3	5.44	6.9	03/08/2015
Angmagssalik	−4	25.18	7.6	20/06/2015
Angmagssalik	−3	5.44	6.9	15/08/2015
Qaarsut Airport	1	78.94	6.2	05/08/2015
Thule Air Base	−18	4.83	11.7	06/12/2017

Due to the time of day the SAR images were taken (between 01:26 and 02:50 a.m.), minimum temperature was chosen for each location. There is a 19 °C difference between the locations. Average precipitation showed only rainfall for this period, with Nuugaatsiaq on average receiving 73.5 mm more than Isortoq. Average wind speeds did not very much, being around 6.5 km/h. The exception is Savissivik, which had a wind speed higher than that of the other two stations. Although we do not know the exact temperatures when the images were taken, these data are useful in showing that in some locations, such as Isortoq and Nuugaatsiaq, it is possible to observe the temperatures at which ice will melt.

Due to the effect of the Arctic polar days and nights, it is likely that in all of the images (with the exception of Savissivik) the iceberg surfaces may have been subject to solar radiation. This is because these images were acquired during summer months (Table 5.1). Radiation may have led to surface melting, in which the top of icebergs may have some surface liquid water. The opposite is likely for Savissivik, as this image was taken in December and the effect of 24 h darkness together with a high wind speed and a very low temperature would have decreased the likelihood of surface liquid water present on the icebergs.

4.2.3. Glaciers that Calved Icebergs

Classification data of glaciers in Greenland are publicly available (Bjørk *et al.*, 2015). In this section, we have taken the approximate locations of each glacier and characteristics of icebergs that may have calved from them.

Table 4.4 outlines glacier names and geophysical parameters. The calving rates are based on an estimated retreat (Ultee and Bassis, 2020). Glacier names are based on the dataset from Bjørk *et al.* (2015) and the glacier tongue widths are calculated with distance tools in GIS software using images taken on 31 December 2016. Iceberg sizes are evaluated on SAR images and based on the classification detailed in Young *et al.* (1998) and approximates from each image.

In the following, we will investigate if the different size has an effect on different backscattering behaviour. Based on what we observe from SAR images, the tongue width does not seem to be easily related to the iceberg size. We also expect that the East Greenland Current could be having a significant effect on iceberg drift.

One important consideration is that icebergs small in size may be more prone to toppling over. This will show the saline ice surfaces that will be much less penetrable by the radar radiation. This effect is expected to be similar to having surface liquid water and it can result in making the iceberg less bright in images.

Table 4.4. *Glacier geophysical parameters. Note that the tongue widths, calving rates and iceberg sizes are estimates. Glacier names are taken from a database of known Greenlandic glaciers.*

Name of Glacier	**Tongue Width (km)**	**Estimated Calving Rate (km/yr)**	**Location**	**Iceberg Size**
Hammer	16	<5	Blosseville Coast N	Small
Nakkala	15	<5	Nuugaatsiaq	Medium
Apuseeq	4	<5	Isortoq	Small
Søndre Parallelgletsjer	12	<5	Blosseville Coast S	Large
Morell	10	<5	Savissivik	Small

4.2.4. SAR Dataset

All the SAR data are quad-polarimetric, with a mean incidence angle of 34.9, an ascending mode and a right observation direction. A total of 1332 icebergs were identified in this paper. The way we identified the icebergs is by looking at small targets which stand out from the background. The main metric was to look at brightness, shape, presence of shadow (when visible) and the effect that the icebergs are not surrounded by sea ice (if grounded). This means that the analysis will be inherently restricted to icebergs, which are visible in images. The smallest icebergs we identified were only a few pixels across, while the largest were a few tens of pixels. Clearly the size of the iceberg can be bigger than the part that is visible in SAR images, and therefore, these values are only indicative of the iceberg part that is scattering substantially, but it is very likely that the whole iceberg is much bigger than this. This leads to a minimum visible size of around 10 × 10 m and a maximum of 215 × 255 m.

4.3. Results

4.3.1. Preliminary Image Analysis

Figure 4.3 presents the Pauli RGB image for Blosseville Coast N. The RGB Pauli component represents the elements of the Pauli vectors in linear scale. Since the scale does not allow us to see details, Figure 4.4 presents a visual close-up identification of an area of the image with an abundance of icebergs. The figure also includes the corresponding alpha and entropy for both averaging window sizes. Looking at the Pauli RGB, it is easy to identify icebergs in the channel area. The

image was acquired in August. The sea area seems to be a mix of open ocean, thin sea ice (bluish areas), small floes and icebergs. Please note how the bright points (generally with shadow features) appear to generally have a low alpha angle and a rather low entropy, which would suggest surface scattering mixed to volume scattering. Comparing 11 × 11 and 5 × 5, we can see the feature seems to be mostly consistent in these images, but the following plots will show that some differences exist.

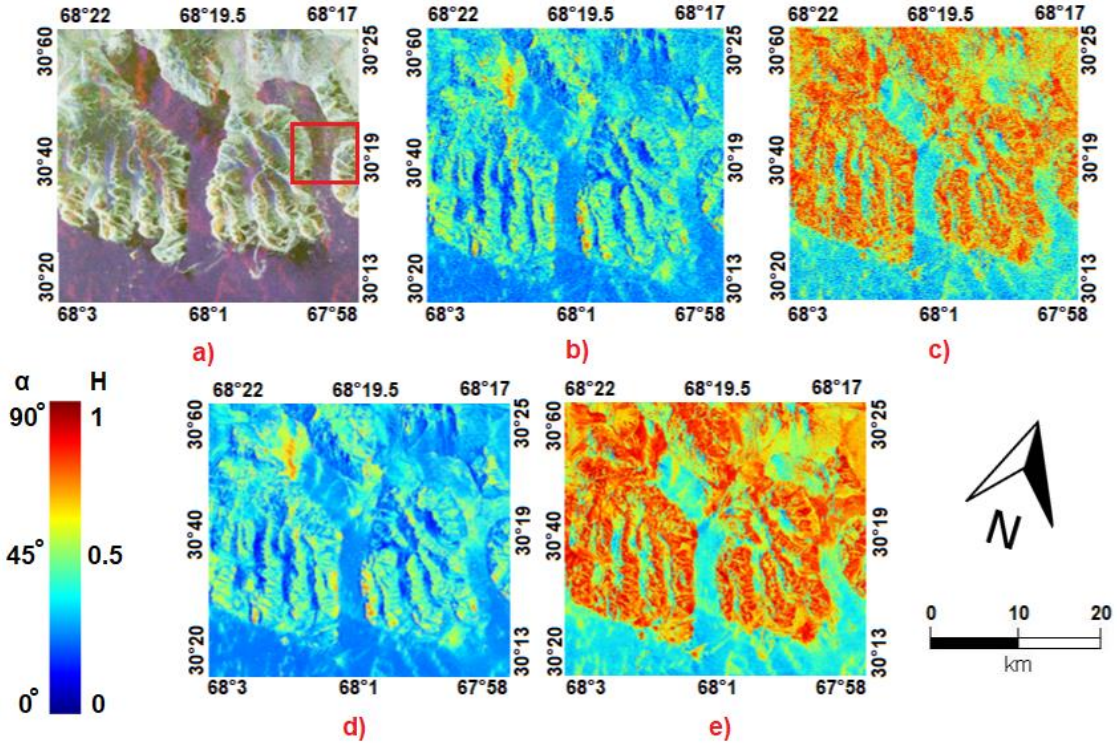

Figure 4.3. *Output images for Blosseville Coast N, 15/08/2015 01:26, (**a**) Pauli RGB image, (**b**) alpha image in a 5 × 5 window, (**c**) entropy image in a 5 × 5 window, (**d**) alpha image in an 11 × 11 window, (**e**) entropy image in an 11 × 11 window. Red box indicates extent of Figure 4.4. Numbers on the edges of images indicate image DMS coordinates. The sea ice situation is a mix of ice floes and open ocean.*

Figure 4.5 presents the Pauli RGB images with a corresponding alpha and entropy image for the 5 × 5 window for Nuugaatsiaq and the visual analysis of icebergs. This acquisition was also done in August and the sea appears mostly as open ocean. Again, icebergs are relatively easy to identify in the alpha image as low values with surface scattering and a medium entropy.

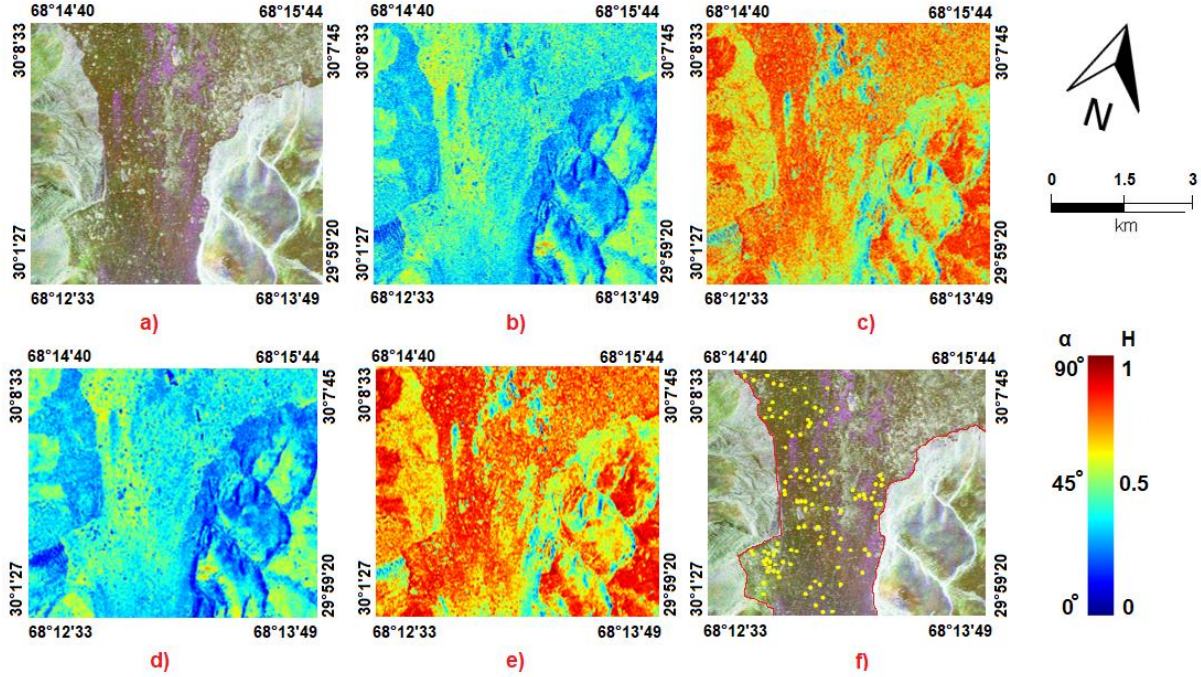

Figure 4.4. *Output close-up images for Blosseville Coast N, 15/08/2015 01:26, (**a**) Pauli RGB image, (**b**) alpha image in a 5 × 5 window, (**c**) entropy image in a 5 × 5 window, (**d**) alpha image in an 11 × 11 window, (**e**) entropy image in an 11 × 11 window, (**f**) visual analysis of icebergs (in yellow) and coastline (in red). Numbers on the edges of images indicate image DMS coordinates. The sea ice situation is a mix of ice floes and open ocean.*

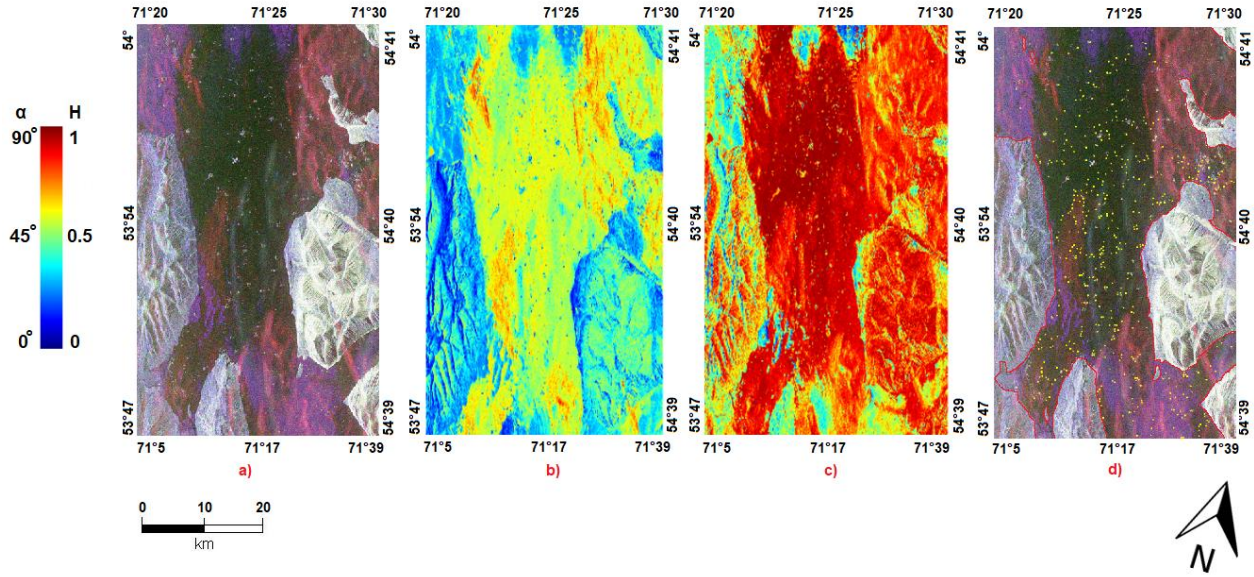

Figure 4.5. *Output images for Nuugaatsiaq, 05/08/2015 02:48, (**a**) Pauli RGB, (**b**) alpha image in a 5 × 5 window, (**c**) entropy image in a 5 × 5 window, (**d**) Pauli RGB visual analysis of icebergs. Yellow dots show icebergs. Red outline indicates coastline. Numbers on the edges of images indicate image DMS coordinates. The sea ice situation is mostly open ocean.*

Figure 4.6 presents the Pauli RGB images with a corresponding alpha and entropy image for the 5 × 5 window for Isortoq as well as the visual analysis of the icebergs. This is also an August image, and the sea region is a mix of open ocean (bluish area) and small floes (grey areas).

Finally, Figure 4.7 presents the Pauli RGB for Blosseville Coast S and Savissivik and the visual analysis of the icebergs in each. The first was acquired in June and the other in December. The area here is clearly covered by sea ice.

Note that in some images, there are red spots and stripes in the sea regions. These are due to bright azimuth ambiguities from the mountains near the coastline. In all the Pauli images, icebergs appear as bright points, mostly white (due to saturation in visualisation). In some images, sea ice can be rather bright and appear in grey. The lack of colour is likely to be due to unpolarised scattering where the three components of the Pauli are similarly weighted. This can happen in ice with large deformation features or (more likely in our case) with very small floes with high rims (as pancakes).

Although most of the icebergs appear as blue spots (showing surface scattering), a few, especially in Blosseville Coast N, appear as red spots showing double bounce.

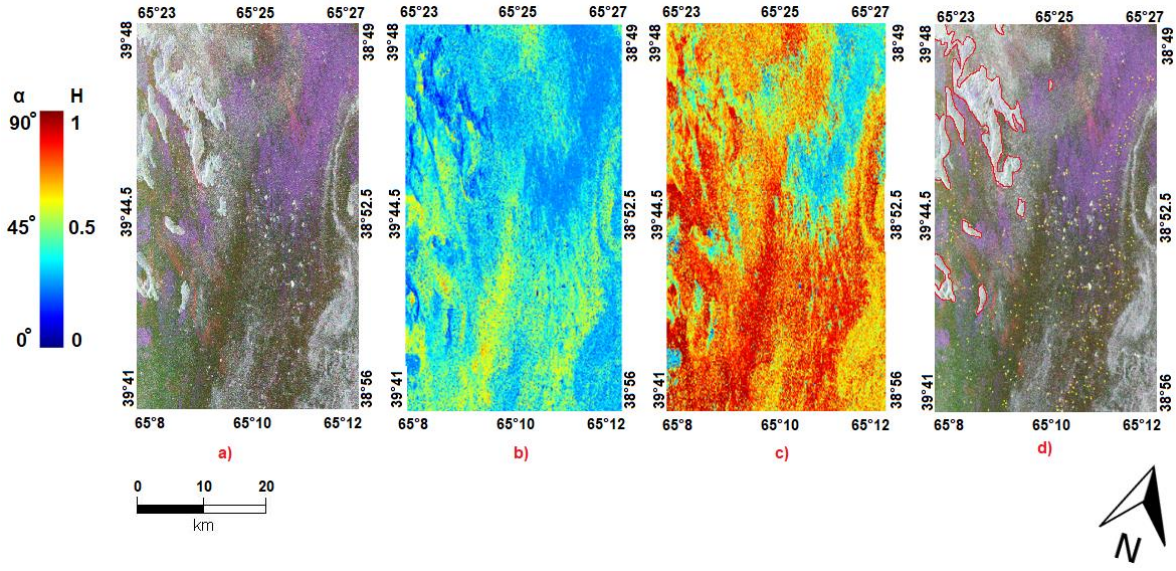

Figure 4.6. *Output images for Isortoq, 03/08/2015 02:07, (**a**) Pauli RGB, (**b**) alpha image in a 5 × 5 window, (**c**) entropy image in a 5 × 5 window. (**d**) Pauli RGB visual analysis of icebergs. Yellow dots show icebergs. Red outline indicates coastline. Numbers on the edges of images indicate image DMS coordinates. The sea ice situation is a mix of open ocean (bluish area in the RGB) and small flows (grey areas).*

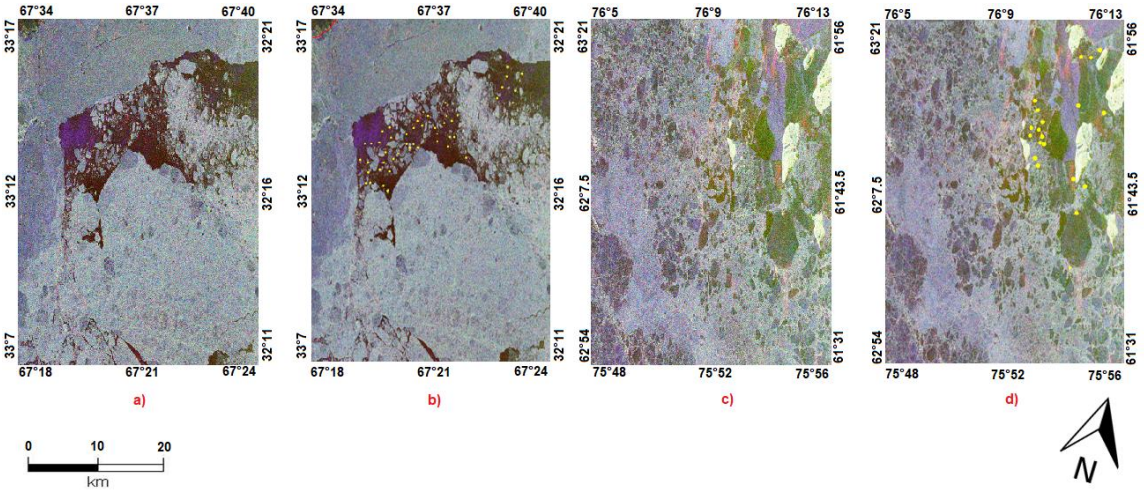

Figure 4.7. *Output images for (**a**) Blosseville Coast S Pauli RGB image 20/06/2015 01:26, (**b**) Blosseville Coast S visual analysis, (**c**) Savissivik RGB image 06/12/2017 02:52, (**d**) Savissivik visual analysis. Yellow dots show icebergs. Red outline indicates coastline. Numbers on the edges of images indicate image DMS coordinates. The sea ice situation is mostly pack ice with several leads.*

In Blosseville Coast S, we were able to clearly observe icebergs only in the open water region. There are few large icebergs in Savissivik with smaller icebergs in the surroundings.

4.3.2. Polarimetric Behaviour

This following quantitative analysis will show that icebergs are more commonly showing either surface or volume scattering and only rarely, double bounce. In this section, we present plots to extract information about the polarimetric behaviour of icebergs and to compare this across the different locations. The colours in the images represent the different locations of icebergs (i.e., the five images). Please note, we have presented these results graphically rather than statistically. This is because analysis of these results using statistics would be too complicated, as numerically finding a metric or an operator to check the differences in polarimetric parameters would not be easy to interpret.

In order to assess how spatially packed the scatterers are in icebergs, we performed a multi-scale analysis where two moving windows were used, a 5 × 5 and an 11 × 11. One of the objectives is to understand if icebergs properly fit the model of partial targets (where the single target components are uniformly distributed) or if they are a composition of single targets located in proximity to each other.

4.3.2.1. Cloude–Pottier

In this section, we present the Cloude–Pottier boxplots and scatter plots for analysis. The first parameter we want to analyse is the entropy. An important factor when evaluating the entropy is to check its relation to the overall brightness, since this is also an indicator of the presence of dominant scatterers or the closeness of the backscattering to the noise floor (which will increase the value of entropy).

The boxplots for the entropy are presented in Figure 4.8, where the two subplots show the change in values with increasing window size. It is very interesting to notice that icebergs present a wide range of entropy values. The 11 × 11 window, which is the most commonly used for this, shows that we have low entropy (single targets) for the icebergs in Savissivik, Blosseville Coast N and S, while other locations present mid to high levels of entropy. Isortoq presents relatively high entropy and lower backscattering, suggesting that there are no dominant scatterers in those icebergs.

Please note how the values change when modifying the window size. This will be discussed in the following section.

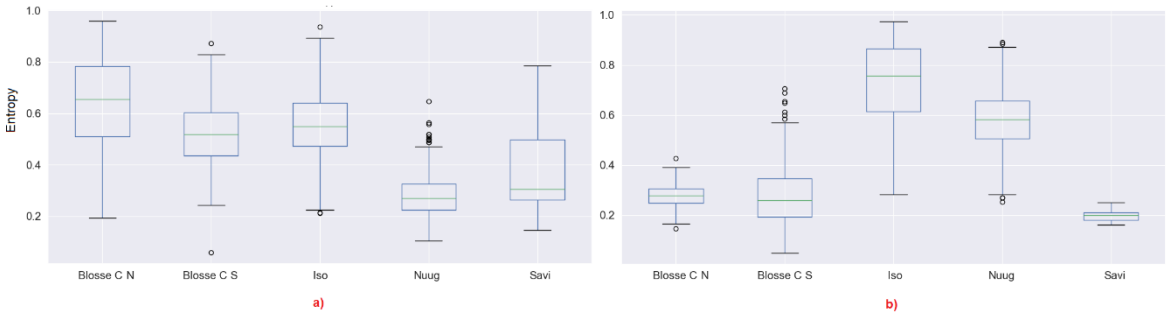

Figure 4.8. *(**a**) Iceberg entropy boxplot 5 × 5 window, (**b**) 11 × 11 window. Large entropy changes are most significant in Blosseville Coast N and Savissivik. Dots indicate outliers.*

The value of the entropy can be influenced by the span, and therefore, we first present the boxplot of the span in Figure 4.9, and then, in Figure 4.10, we show the span against entropy in a 5 × 5 averaging window and an 11 × 11 window. We can see that lower values of span (below −20 dB) have generally higher values of entropy (above 0.5). This is in line with the fact that darker icebergs are closer to the noise floor, which adds depolarisation.

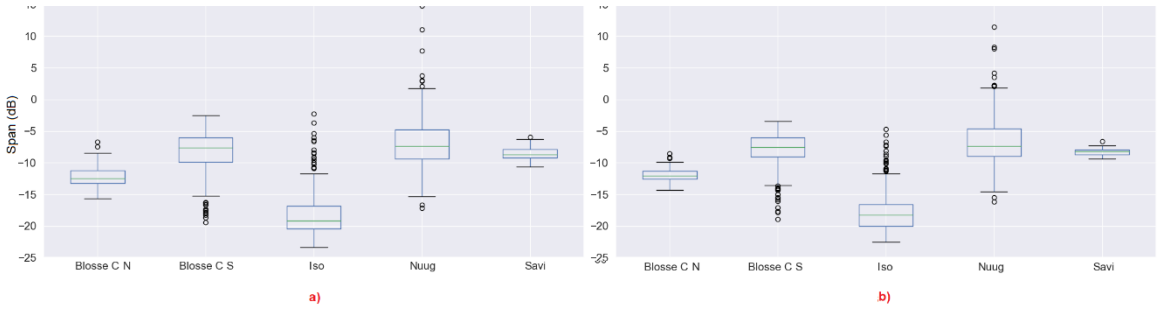

Figure 4.9. *(**a**) Iceberg span boxplot 5 × 5 window, (**b**) 11 × 11 window. Changes in span are minimal. Dots indicate outliers.*

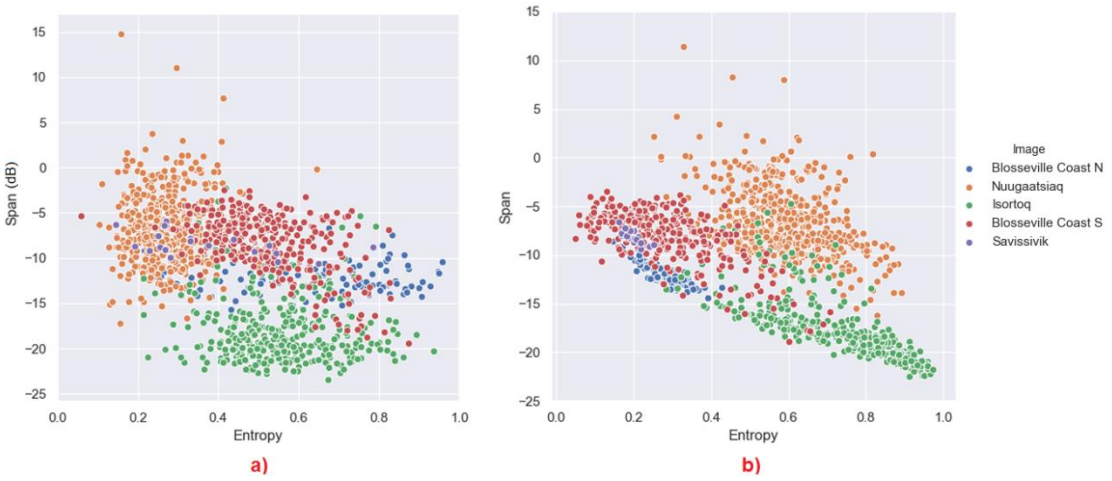

Figure 4.10. *(**a**). Iceberg entropy, span plot 5 × 5 window, (**b**) 11 × 11 window. Note the negative values for span. Dots indicate icebergs.*

We can now proceed analysing alpha. The boxplots for the averaged alpha are presented in Figure 4.11, where again, the two subplots show the change in values with modifying window size. In order to have a more meaningful interpretation of the alpha values, Figure 4.12 shows the averaged alpha angle against entropy in a 5 × 5 window and an 11 × 11 window. The average alpha is quite low when the entropy is low. However, there are few points where the alpha reaches high values. Clearly, when the entropy increases, the alpha is forced toward 60°.

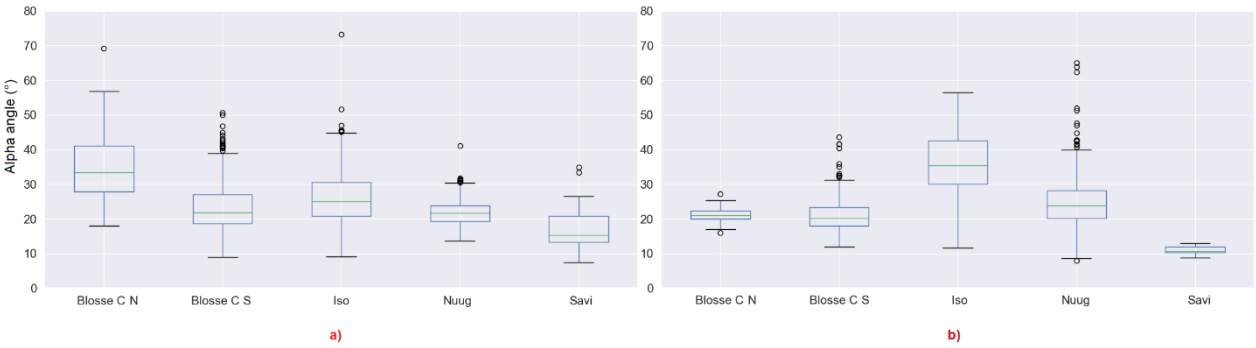

Figure 4.11. *(**a**) Iceberg alpha boxplot 5 × 5 window, (**b**) 11 × 11 window. Significant changes in alpha are evident in Blosseville Coast N and Savissivik.*

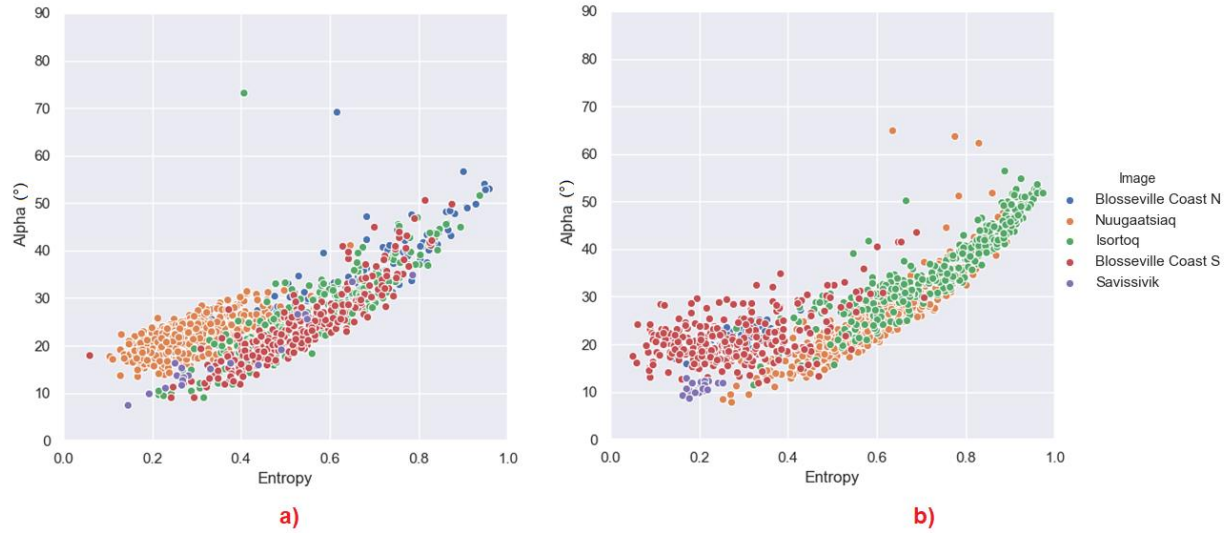

Figure 4.12. *(**a**) Iceberg alpha, entropy plot 5 × 5 window, (**b**) 11 × 11 window. Dots indicate icebergs.*

Figure 4.13. shows that there is no pattern between alpha and span, beside the fact that Isortoq has low values of span, which leads to a higher entropy, and therefore, a higher alpha.

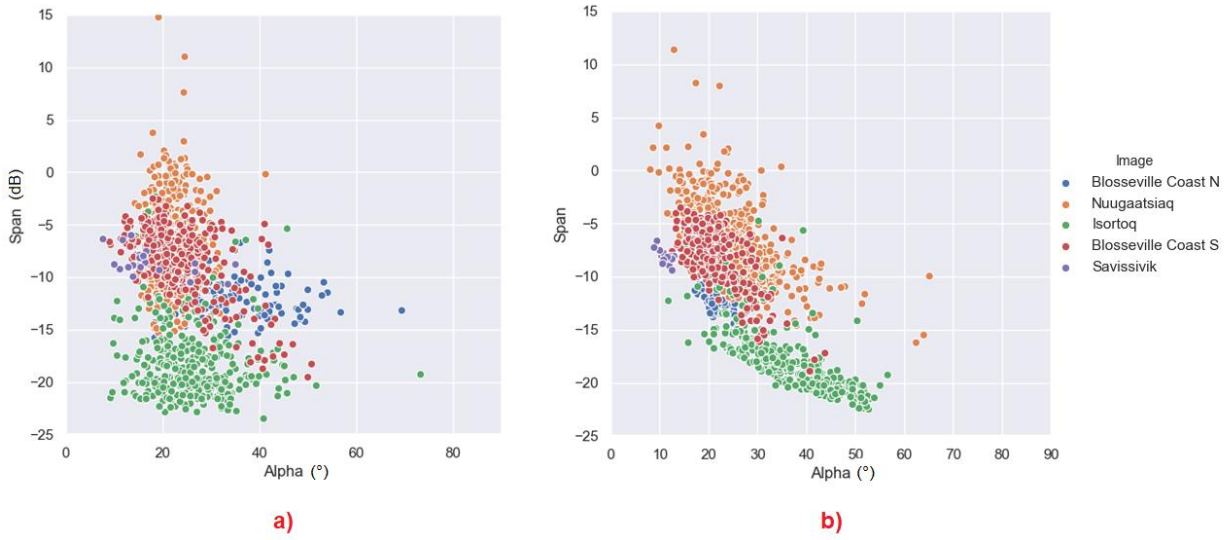

Figure 4.13. *(**a**) Iceberg alpha, span plot 5 × 5 window, (**b**) 11 × 11 window. Dots indicate icebergs.*

Another parameter of interest is beta. The boxplot of beta is presented in Figure 4.14, while the plots in Figure 4.15 show the average beta against alpha angle for 5 × 5 and 11 × 11. Interestingly, we can see that ordinarily there is no preferred beta value. However, for some locations and window sizes, the beta angle is closer to zero, indicating horizontally oriented scatterers. Since the scattering is mostly surface, the impact of beta angle (present in the second and third element of the Pauli vector) is possibly noisy and more difficult to interpret.

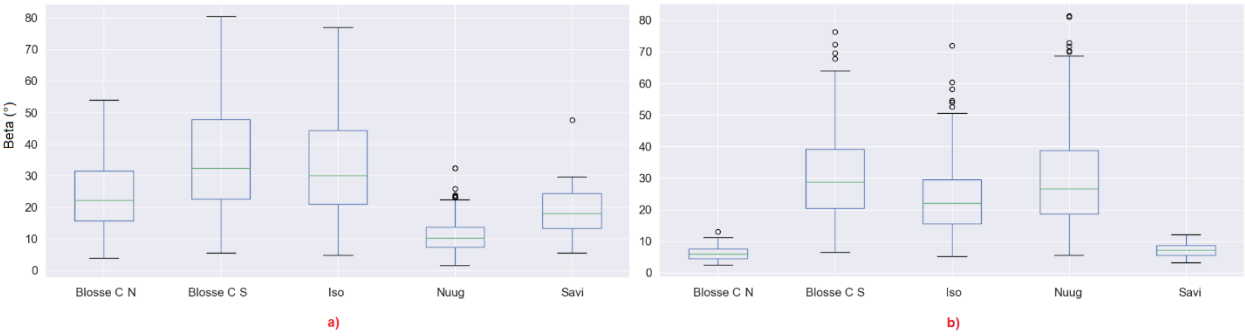

Figure 4.14. *(**a**) Iceberg beta boxplot 5 × 5 window, (**b**) 11 × 11 window. Significant changes in beta are evident in Blosseville Coast N, Nuugaatsiaq and Savissivik.*

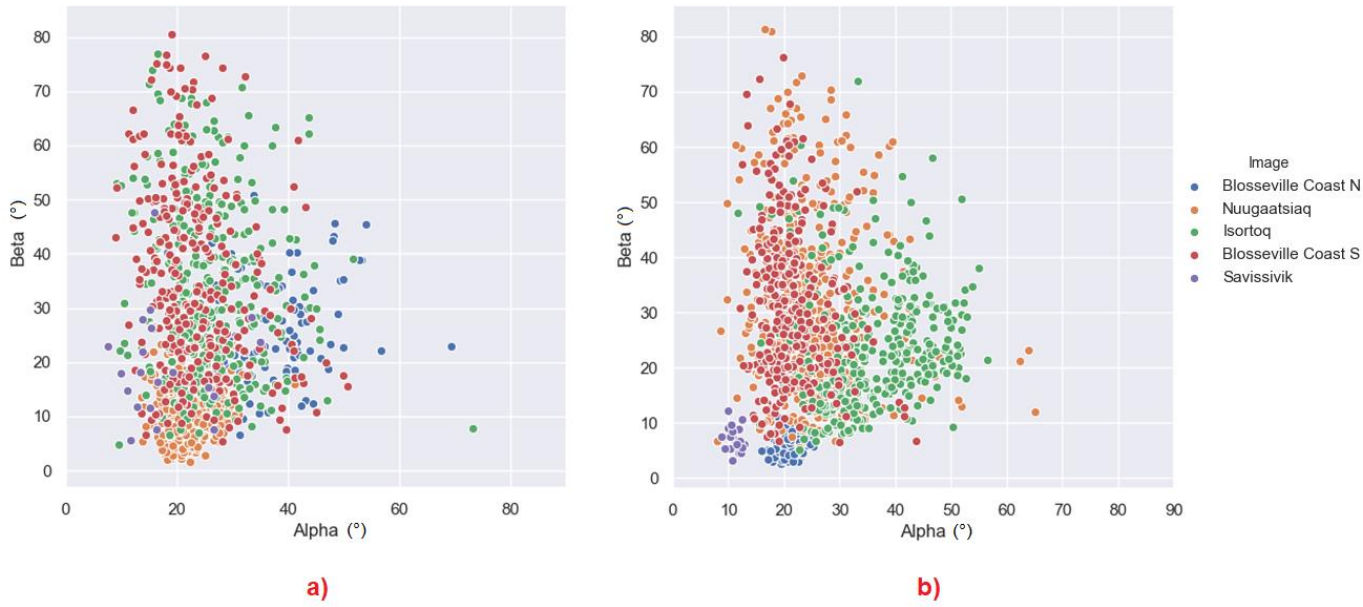

Figure 4.15. *(**a**) Iceberg alpha vs. beta plot 5 × 5 window, (**b**) 11 × 11 window. Dots indicate icebergs.*

Figure 4.16 shows the entropy against anisotropy. This is important to evaluate if there is only one or more scattering mechanisms besides the dominant one. A scatter plot for anisotropy is shown in Figure 4.17

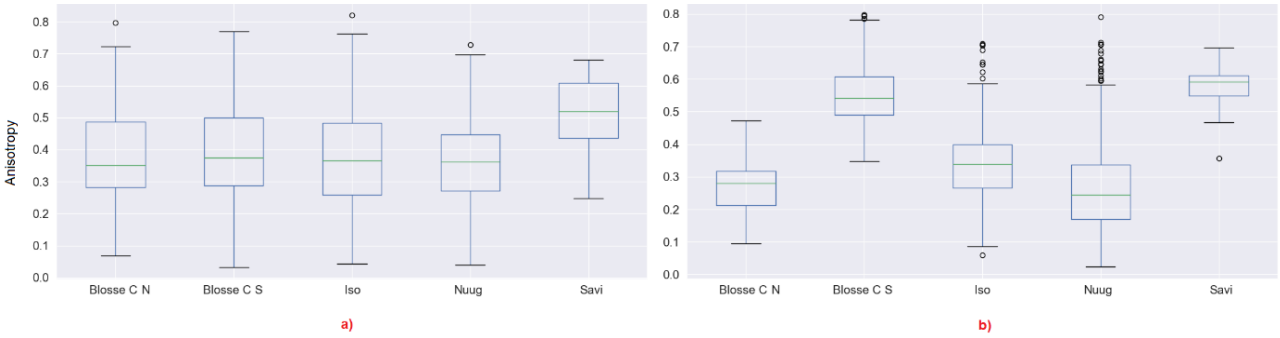

Figure 4.16. *(**a**). Iceberg entropy, anisotropy boxplot 5 × 5 window (**b**) 11 × 11 window. Slight changes in anisotropy are evident in Blosseville Coast N, Blosseville Coast S, Isortoq and Savissivik.*

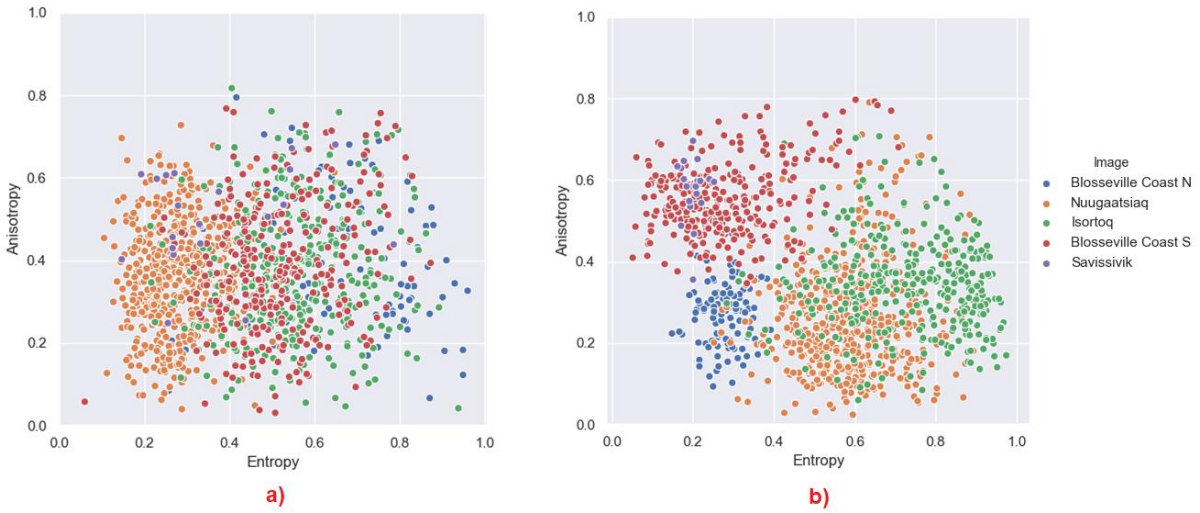

Figure 4.17. *(**a**) Iceberg anisotropy plot 5 × 5 window, (**b**) 11 × 11 window. Dots indicate icebergs.*

No evident trend appears here. However, the change with window size will be discussed later.

We also tested a four component scattering model devised by Yamaguchi *et al.* (2005). The four components are double bounce, surface, volume, and helix scattering. Here, we present the Yamaguchi boxplots for analysis (Figures 4.18 to 4.21). From Figure 4.18, surface scattering changes minimally for Blosseville Coast N and S with a higher window size, while in other locations it generally changes significantly, sometimes increasing, and other times decreasing. The increase may be due to the inclusion of edge pixels which show strong double reflection effects while the reduction may be due to averaging out some small scatterers within the ice body.

For this task, we also produced scatter plots. In Figures 4.22–4.27, we show dB plots between the different four components. A red line bisects through each graph, helping to distinguish if one of the two components is dominant. Please note, the algorithm we used avoids instability by clipping low values to the lowest value in the image. This is the reason we can see repeated lowest values in the plots.

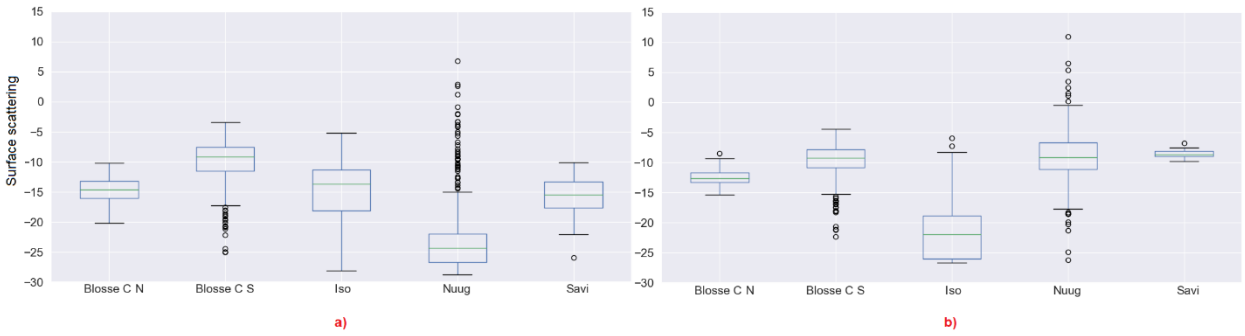

Figure 4.18. *(**a**). Iceberg surface scattering boxplot 5 × 5 window, (**b**) 11 × 11 window. There are significant changes in surface scattering in Savissivik.*

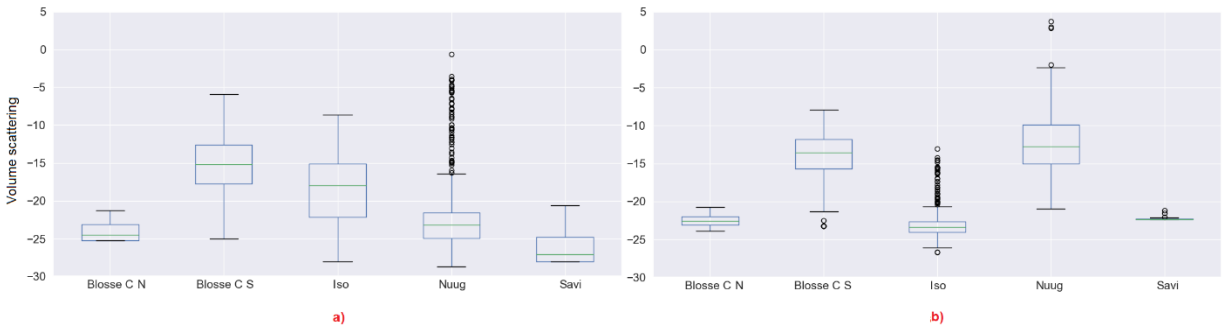

Figure 4.19. *(**a**). Iceberg volume scattering boxplot 5 × 5 window, (**b**) 11 × 11 window. There are significant changes in volume scattering in Isortoq and Savissivik.*

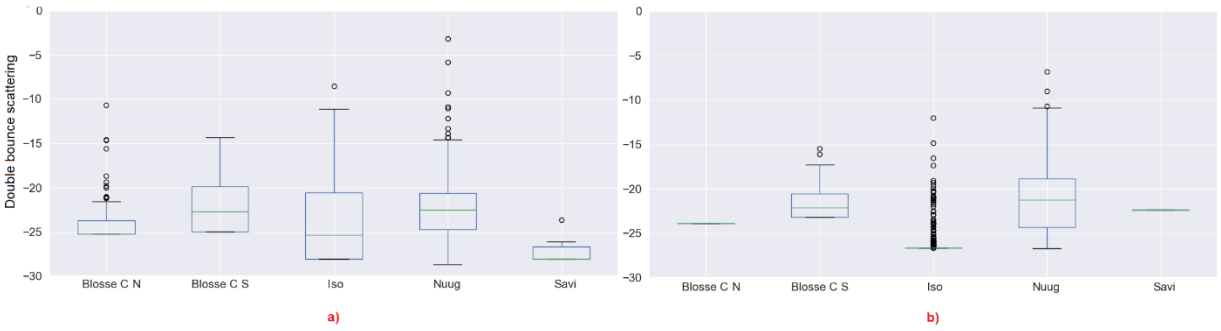

Figure 4.20. *(**a**) Iceberg double bounce scattering boxplot 5 × 5 window, (**b**) 11 × 11 window. There are significant changes in Blosseville Coast N, Isortoq and Savissivik.*

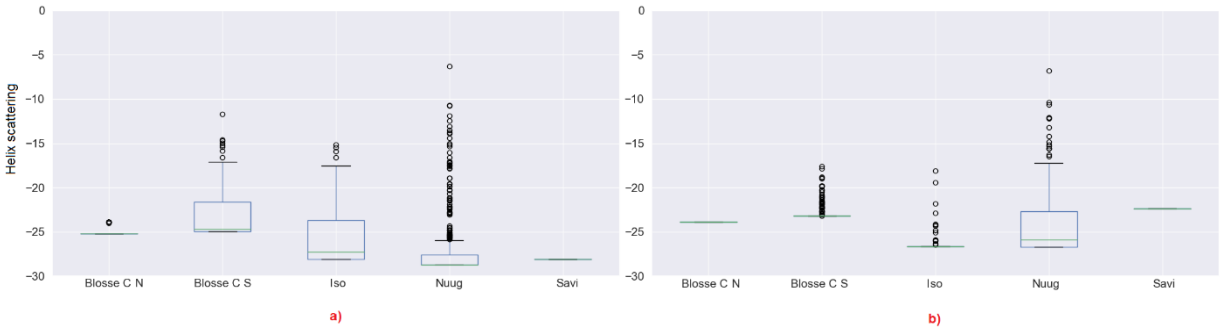

Figure 4.21. *(**a**) Iceberg helix scattering boxplot 5 × 5 window, (**b**) 11 × 11 window. There are significant changes in helix scattering in Blosseville Coast S, Isortoq and Nuugaatsiaq.*

From Figure 4.22, we can see that for icebergs in almost all scenarios, when the backscattering is high enough, surface scattering is larger than the volume scattering. This is also corroborated by the previous plots. However, when the signal is low, the difference is less evident. This may indicate that the volume scattering, although present, may not be the dominant mechanism for these icebergs at L-band.

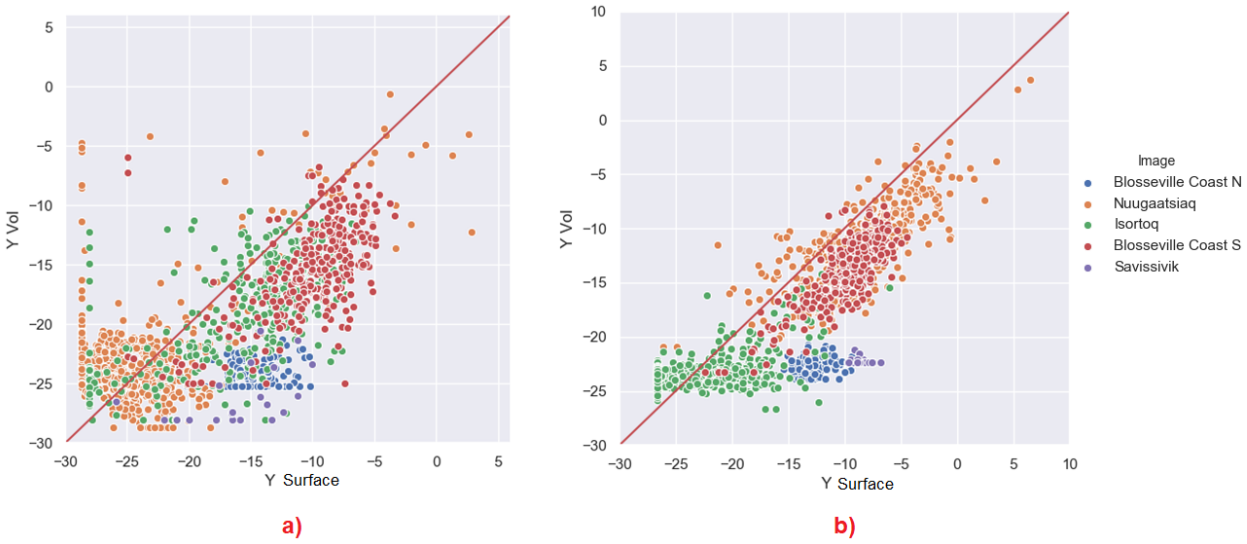

Figure 4.22. *(**a**) Iceberg volume scattering, surface scattering plot in a 5 × 5 window, (**b**) 11 × 11 window. The majority of icebergs show surface scattering. Dots indicate icebergs. All values are in dB.*

Figure 4.23 shows the comparison in backscatter between volume and double bounce. We can observe that by using an 11 x 11 window, there is more volume scattering than double bounce. With a 5 x 5 window, this information is site related, but nonetheless, the volume appears to be stronger in most of the cases.

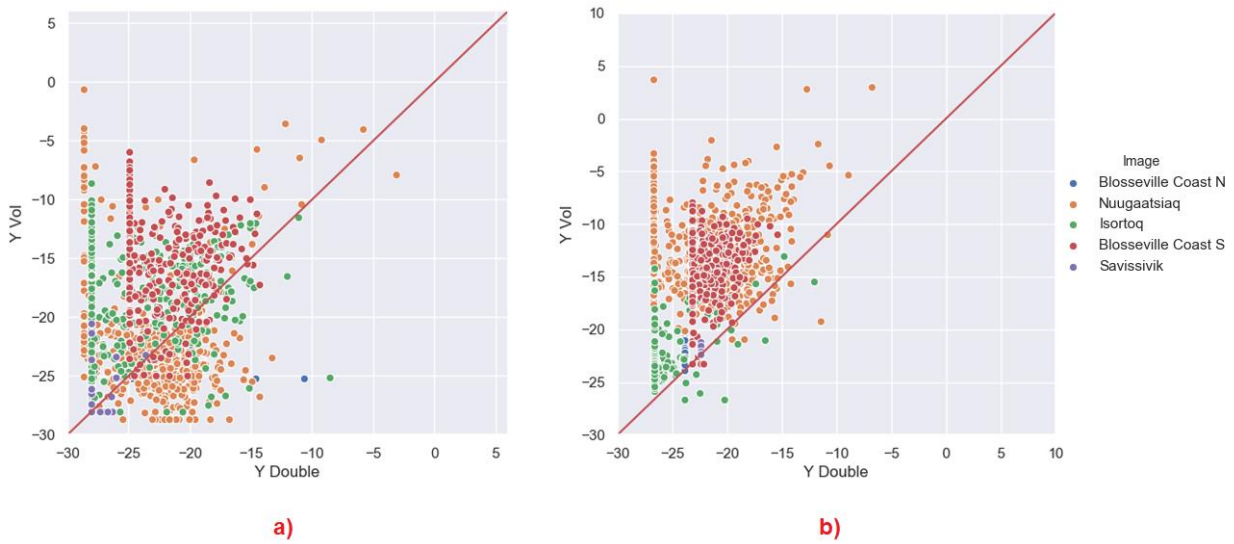

Figure 4.23. *(**a**) Iceberg double bounce scattering, volume scattering plot in a 5 × 5 window, (**b**) 11 × 11 window. The majority of icebergs show volume scattering. Dots indicate icebergs. All values are in dB.*

If we look at Figure 4.24, we compare the double bounce with surface. It appears as surface is again dominant in most of the icebergs with 5 × 5, except a few exceptions where the double bounce is stronger. Double bounce seems to be dominant only in a limited number of icebergs.

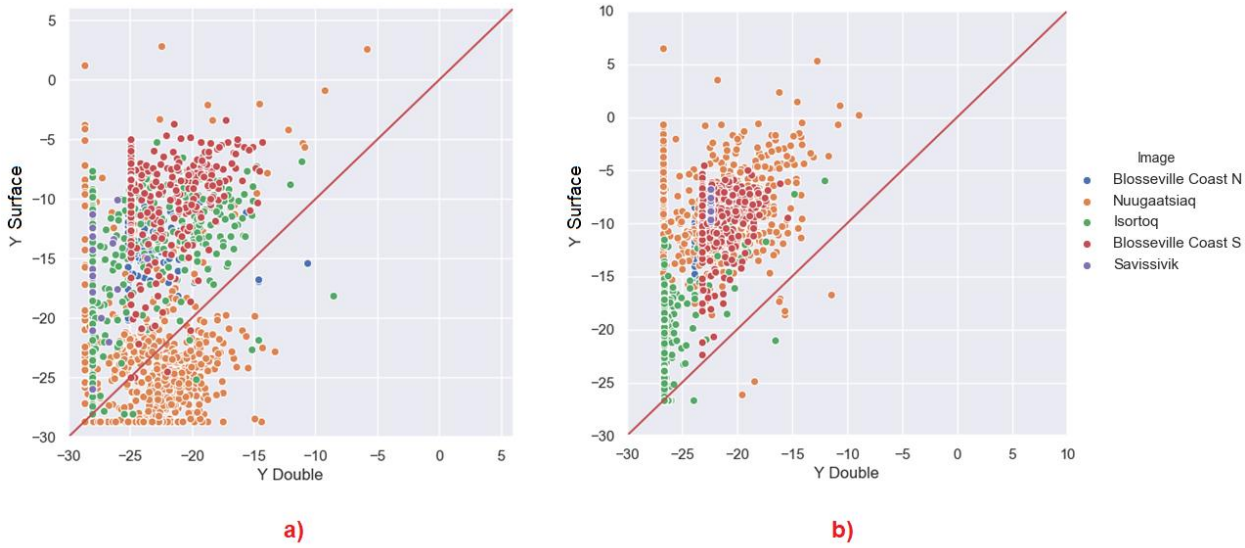

Figure 4.24. *(**a**) Iceberg double bounce scattering, surface scattering plot in a 5 × 5 window, (**b**) 11 × 11 window. The majority of icebergs show volume scattering. Dots indicate icebergs. All values are in dB.*

The following three plots in Figures 4.25–4.27 compare the helix scattering. We can see that helix scattering is generally not dominant compared to any other

scattering mechanisms in all the locations. There are some exceptions for a few icebergs, but normally, the helix is not expected to be strong. It is showing a scattering behaviour which is reflection symmetric.

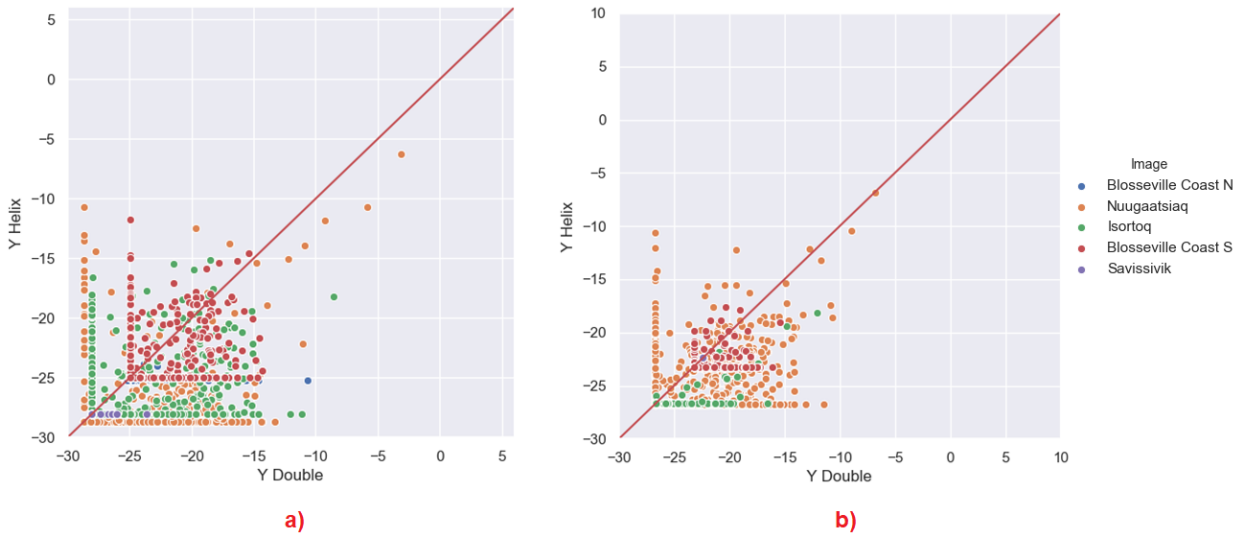

Figure 4.25. *(**a**) Iceberg double bounce scattering, helix scattering plot in a 5 × 5 window, (**b**) 11 × 11 window. The majority of icebergs tend to show significant double bounce. Dots indicate icebergs. All values are in dB.*

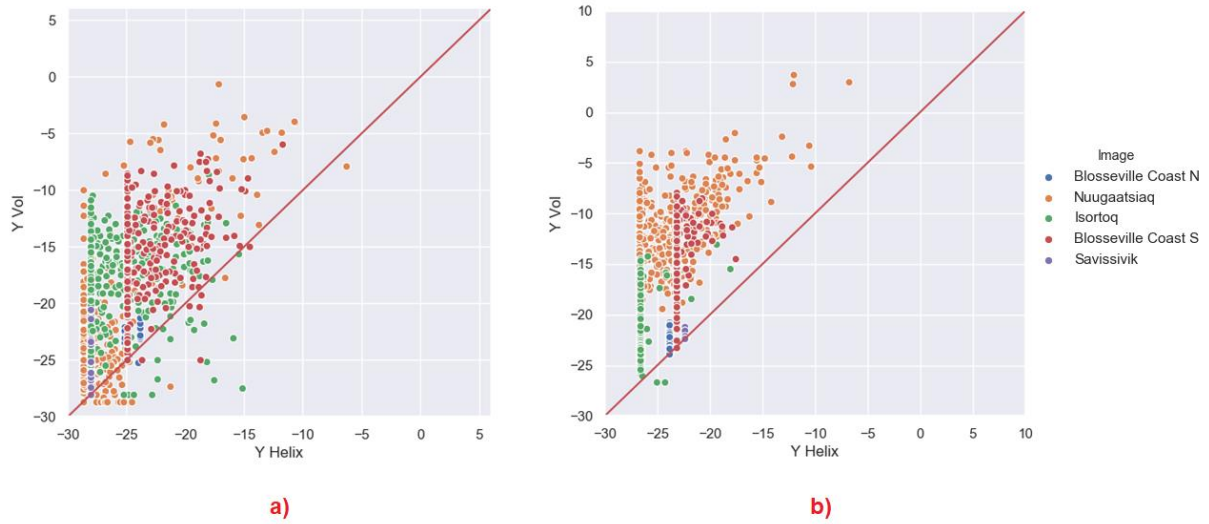

Figure 4.26. *(**a**) Iceberg helix scattering, volume scattering plot in a 5 × 5 window, (**b**) 11 × 11 window. The majority of icebergs show more volume scattering. Dots indicate icebergs. All values are in dB.*

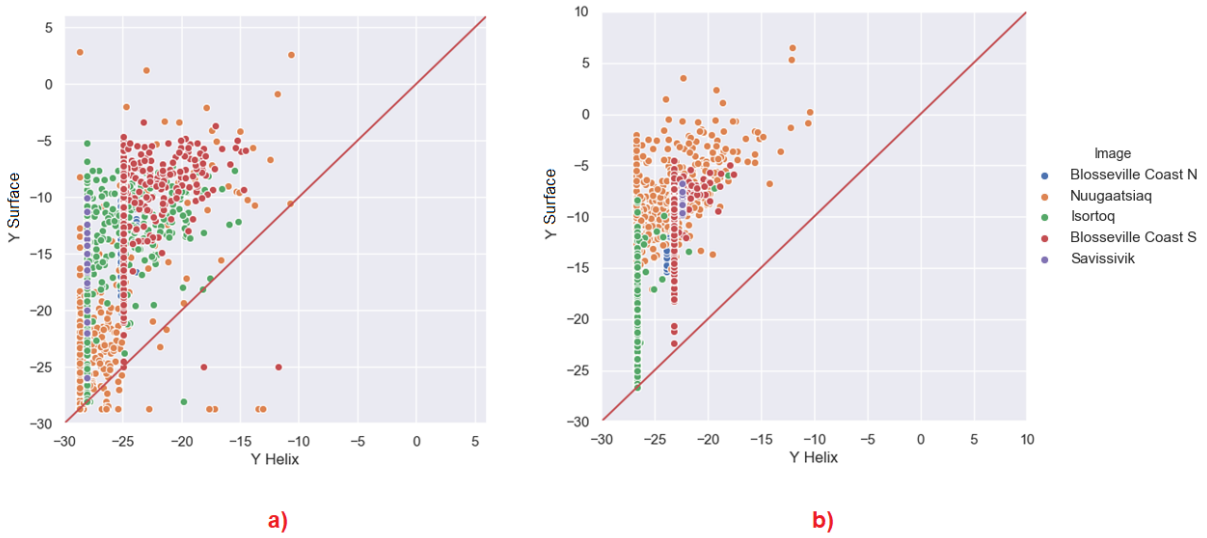

Figure 4.27. *(**a**) Iceberg helix scattering, surface scattering plot in a 5 × 5 window, (**b**) 11 × 11 window. The huge majority of icebergs show surface scattering. Dots indicate icebergs. All values are in dB.*

4.4. Discussion

The analysis of 1,332 icebergs in Greenland showed that there are several commonalities in the scattering behaviours, but also differences. In the following, we identify the main highlights of this analysis.

4.4.1. Depolarisation

Entropy values on any given stationary target captured by SAR give a good indication of the variety of scattering mechanisms present within the target. The icebergs analysed seem to have a large variety of entropy values. We also performed a multi-scale analysis to check if icebergs can be approximated as (a) partial targets with a uniform distribution of scattering mechanisms, (b) single targets with a single scattering mechanism or (c) a mixture of single targets in close proximity. Looking at the differences in entropy, when the window was changed from 5 × 5 to 11 × 11, we can conclude that icebergs can be included in all the three categories. Even more interesting, the geographical location seems to suggest in which category they are. If the target is a fully uniform partial target, then the entropy should not change, except that when selecting very small windows (e.g., 3 × 3), we may have a bias toward smaller values.

Interestingly, we can see two patterns when reducing the window size to 5 × 5:

(a) We may expect that by reducing the window, the entropy may tend to increase because in a smaller window, we expect that it is less likely to have lots of dominant scatterers. This is the case for instance for Nuugaatsiaq and partially for Isortoq. This is an indicator that dominant scatterers in these icebergs are not packed uniformly and very close to each other. When we use a smaller window, we include less dominant scatterers and increase the entropy. Considering the window sizes, we may expect strong scatterers being located no closer than a few tens of metres. This may represent some topographic features of the iceberg. From a more theoretical point of view, it indicates that scattering from those icebergs is not well approximated by a partial target with fully developed speckle. A uniform distribution of scatterers is slightly more realistic for Isortoq, where the reduction is not very large, although the values are already quite high to start with due to the low backscattering and the effect of noise.

(b) Blosseville Coast N and S and Savissivik are an interesting case, since several icebergs reduce their entropy when increasing the window. Inspecting the images, we observed that these are smaller icebergs and when increasing the window, we included the edge pixels, which are generally brighter. We therefore included in the window other dominant scatterers that increase the entropy. Please note, we used the middle pixels of the icebergs because we are interested in the scattering behaviour of the ice body, in order to improve our understanding of icebergs. If we had to include the edges for all the icebergs, we may have masked the inner behaviour. Nevertheless, when the icebergs are small, excluding the edge is simply not an option. This is also true for detection studies in which iceberg edges could be critical to identify icebergs (Williams *et al.*, 1999).

This analysis shows an important finding. Entropy cannot be used on its own to detect icebergs, regardless of the behaviour of the background (which may also have high entropy). For instance, one may think that icebergs are characterised by high entropy. However, if there is a dominant scatterer and we use larger windows as for Blosseville Coast N or Savissivik, the entropy may be quite low. Entropy alone will not be effective and extra information needs to be considered.

The proximity and distribution of dominant scatterers is a physical parameter for icebergs. In the future, we will investigate how we could use this for classifying different typologies of icebergs.

The difference in temperature and possibly of wet conditions seems to not affect the entropy significantly. The reason may be that there was not much liquid water during acquisition. However, it seems that for Blosseville Coast N and Savissivik (the coldest images), the span is generally among the highest and the entropy is reducing when increasing the window size. However, the latter can just be due to the edge effect. We could therefore conclude that surface liquid water is not largely present here or not impacting much.

4.4.2. Target Characteristics

The total backscattering varies greatly with the lowest values around −28 dB. This is especially visible in Isortoq. In actual fact, the icebergs in Isortoq were floating in an area of very low sea backscattering. This corroborates the fact that open water backscattering signals may be stronger than backscatter signals from smaller icebergs (Wesche and Dierking, 2012). Normally, these icebergs would be masked by the clutter background. Besides Isortoq, most of the icebergs are above −10 dB, showing a relatively strong backscattering in L-band. In terms of topography, higher backscatter signals could indicate smoother icebergs, and therefore, less volume scattering, which is supported by Viehoff and Li (1995).

When the entropy increases, this forces the average alpha to increase towards 60°. If there is a dominant mechanism in an iceberg, this seems to be a mix of surface or dipole scattering. Dipole scattering can be generated by the ice body, and therefore, this suggests volume scattering. However, in a few icebergs there is a dominant double bounce contribution, which seems to be the exception more than the norm. Additionally, the edge effect for Blosseville Coast S seems to increase the value of alpha, but it does not bring it to anything closer to dihedral scattering. In its nature, it still seems to be mostly surface scattering (probably due to surface in layover) mix to a dihedral component, which can produce something that resembles a dipole.

The anisotropy values for the 5 × 5 window are mostly spread. This is most likely due to the fact that anisotropy requires a large average in order to be estimated properly. The results obtained in Figure 4.17 are therefore not to be taken as very

significant. Once the window gets larger, some patterns become evident. For instance, in Blosseville, the icebergs north and south of the glaciers seem to have different values of anisotropy. This is possibly due to different temperature effects with some presence of surface liquid water. Although, it is unlikely that icebergs in Blosseville Coast N are very wet because looking at the entropy and span, this seems to be a minor difference. Interestingly, this minor difference is visible when examining the two less dominant scattering mechanisms by using the anisotropy. Specifically, the colder condition in Blosseville Coast S produces a higher entropy, which means that the second scattering mechanism is much stronger than the third. This is in line with the idea that the radiation may have a bigger penetration in the ice body and the surface scattering is accompanied by some dipole/volume scattering within the iceberg. More data will be needed on other glaciers to support this idea.

The alpha angle varies significantly for different icebergs going mostly from surface to dipoles. This suggests that icebergs can appear in images with a polarimetric behaviour which will resemble mostly a surface or volume scattering. Interestingly, the alpha angle seems to be correlated with the locations and possibly the iceberg geometry. Also of interest, we can observe differences between icebergs in Blosseville Coast N and S, although they are mostly calved by the same glacier. Again, the fact that Blosseville Coast S (the colder image) has an entropy higher than Blosseville Coast N is an indicator that we may have a larger penetration in the ice body due to less presence of surface liquid water (Wesche and Dierking, 2015).

4.4.3. Model Based Analysis

The Yamaguchi decomposition allows us to evaluate the polarimetric scattering of icebergs compared to a model considering surface, volume (of randomly oriented dipoles), double bounce and helix. Some caution must be taken when analysing these results. The volume component of the Yamaguchi model (Yamaguchi *et al.*, 2005) was not designed for ice, and therefore, the four basic scatterers may not be the most appropriate to analyse ice bodies. If a model is not perfectly fit to the scattering behaviour, it means that the true targets on the ground will project on the theoretical targets of the model introducing misinterpretation. In practice, this tells us that trends that we see cannot be trusted blindly but need to be interpreted in light of what other observables tell.

On first glance, in the volume vs. surface plot (Figure 4.22), when the backscattering signal is high, surface scattering seems to be dominant. Volume

scattering becomes more dominant when the backscattering gets lower, maybe due to an increased penetration which will result in a reduction in surface scattering and an increased loss in the iceberg body. This also indicates the presence of features in the ice (cracks, crevasses, air bubbles, impurities and other features within the ice body) (Kirkham *et al.*, 2017; Willis *et al.*, 1996). These results may indicate that the volume scattering, although present, may not be the dominant mechanism for these icebergs at L-band. In the surface vs. double bounce plot (Figure 4.24), it appears that surface scattering is again dominant in most of the icebergs with 5 × 5, except a few exceptions where the double bounce is stronger. Double bounce seems to be dominant only in a limited number of icebergs. However, when we compare double bounce to volume (Figure 4.23), the latter seems to be stronger in most cases. This shows that the pure double bounce reflection is again uncommon, and icebergs tend to have either surface or volume scattering, or a combination between surface and multiple reflections.

Our results showed a very minimal effect of helix scattering for all icebergs. In all the plots, helix seems to be the lowest scatterers. We can therefore conclude that helixes are not the most appropriate targets for observing the type of icebergs present in these scenes.

Finally, regarding eventual effects of surface liquid water, observing the volume vs. surface plot (Figure 4.22) for Blosseville Coast N and S, we can again notice that the percentage of surface against volume is reducing when the conditions are colder. That is to say, the Blosseville Coast S points are closer to the line than the one for the N. This corroborates an increased ice penetration when the conditions are colder.

4.4.4. Summary

The general results show that volume scattering seems to be more important when backscattering is low. However, the plots tell us that the dominant scattering mechanism is surface scattering, followed by volume. This is true for icebergs which show a higher backscattering signal. These Yamaguchi results seem to corroborate with the Cloude–Pottier results.

We also investigate trends of polarimetric behaviour with temperature and eventually surface liquid water. We could compare icebergs in two close areas (Blosseville N and S), one taken in August (N) and one in June (S). Temperatures

were likely to be both sub-zero. However, the solar radiation may have produced some surface liquid water on icebergs in Blosseville Coast N. Interestingly, we notice that icebergs in Blosseville Coast S (colder) generally present a higher alpha (mixture of surface and dipole scattering) and a higher anisotropy (indicating there is a second strong scattering mechanism). Additionally, the Yamaguchi decomposition also returned that the amount of volume scattering is more present in the colder image (Blosseville Coast S). We believe this may be linked to less surface liquid water, which produces a larger penetration in the ice body showing a larger volume scattering. To be finally proven, this would require a much larger dataset with more locations.

4.5. Conclusions and Further Work

Icebergs in the Arctic are subject to various backscattering behaviours during SAR image acquisition. This behaviour is dependent on iceberg properties, such as shape and size, as well as environmental and meteorological factors such as surface wetness, surface roughness and cracks/crevasses. In this study, we used five ALOS-2/PALSAR-2 L-Band SAR images to extract polarimetric information based on the backscattering behaviour of icebergs. We applied the Cloude–Pottier eigenvalue/eigenvector decomposition and Yamaguchi model decomposition by processing the average pixel values of each image. We also performed a multi-scale analysis of the images using 5 × 5 and 11 × 11 window sizes to determine the differences in polarimetric scattering behaviour and to understand if icebergs can be approximated as single targets, partial targets, or a combination of single targets. In the wider scope, it is important to produce accurate iceberg detectors to ensure the enhanced safety of maritime activities, particularly due to climate change. Therefore, by performing this analysis, we also examined the potential for icebergs to be classified based on polarimetric behaviour and geographical location. Our results show that icebergs exhibit a mix of all three polarimetric targets, but with predominance of surface and volume scattering. In some instances, double bounce can dominate the scattering, but this is rather rare. An important finding from this work is that entropy alone will not be sufficient for iceberg classification from SAR imagery.

Many icebergs exhibit a variety of characteristics depending on their locations (i.e., the glacier from which they were calved). Additionally, we could observe differences between icebergs in similar locations but at different times of the year.

This suggests that colder conditions may produce more volume scattering. The analysis shows that polarimetry at L-band has potential for classifying iceberg geometry and presence of liquid water. However, to attempt classification, we would need a validation dataset where images of each iceberg structure are present, and this is currently not available.

Further work within this field includes a comparative analysis showing more iceberg locations and times of the year in the Arctic. Additionally, investigating the link between shape of icebergs via other reference data and applying PolSAR scattering models developed for glaciers. We will also investigate and compare different PolSAR detectors to identify the methodologies that seem to be more suited for detection. We also recommend estimation of the anisotropy using a large average.

Contributions

Conceptualization, J.B.

Methodology, J.B., and A.M.

Software, J.B.

Validation, J.B., and A.M.

Formal analysis, J.B.

Investigation, J.B.

Resources, A.M.

Data curation, J.B.

Writing—original draft preparation, J.B.

Writing—review and editing, J.B., and A.M.

Visualisation, J.B.

Supervision, A.M.

Project administration, J.B.

5.0. COMPARISON OF TARGET DETECTORS TO IDENTIFY ICEBERGS IN QUAD POLARIMETRIC ALOS-2 SAR IMAGES

This chapter is also available as a journal paper within Remote Sensing. We now turn our attention to the detection of icebergs using ALOS-2 SAR data. We introduce six state of the art detectors, and three polarimetric parameters as detectors to evaluate detection performance.

Bailey, J.; Marino, A.; Akbari, V. Comparison of Target Detectors to Identify Icebergs in Quad-Polarimetric L-Band Synthetic Aperture Radar Data. Remote Sens. 2021, 13, 1753.

Abstract:

Icebergs represent hazards to ships and maritime activities and therefore their detection is essential. Synthetic Aperture Radar (SAR) satellites are very useful for this, due to their capability to acquire under cloud cover and during polar nights. Additionally, polarimetry has been proven to improve the detection capability. In this work, we compared six state-of-the-art target detectors to test their performance and ability to detect small sized icebergs in four locations in Greenland. These were the polarimetric notch filter (PNF), polarimetric match filter (PMF), multi-look polarimetric whitening filter (MPWF), optimal polarimetric detector (OPD), reflection symmetry detector, and the dual polarisation anomaly detector (iDPolRAD). We used four single look complex (SLC) ALOS-2 quad-pol images from JAXA. The data were calibrated and processed. We produced the covariance matrices of each image before applying a testing and training window for detection. We also included a guard window to reduce false alarms. Our results show that the multi-look polarimetric whitening filter and optimal polarimetric detector perform better in quad and dual pol mode detection. We tested two scenarios: open ocean and sea ice. The analysis shows that overall, quad pol detectors have the best detection performance. If we fix the false alarm to 10^{-5} the probabilities of detection are 0.99 in open ocean and 0.90 in sea ice. Dual pol or single pol detectors show an overall reduction of performance, but this degradation is not very large when the value of false alarms is relatively high (i.e., we are interested in bigger icebergs, as they are easier to detect). However, the differences between quad- and dual- or single-pol detectors became more evident

when we fixed the false alarm value for low detection probabilities 10^{-6} (i.e., smaller icebergs). Here, the HV channel showed accuracies of 0.62 for open ocean and 0.26 for sea ice, compared to values of 0.81 (open ocean) and 0.77 (sea ice) obtained with quad pol detectors.

5.1. Introduction

Iceberg detectors have been proposed based on the polarimetric behaviour of targets. Different detectors include iDPolRAD (Marino *et al.*, 2016b), PNF (Marino, 2013), PMF (Novak *et al.*, 1989), symmetry (Nunziata *et al.*, 2010), MPWF (Chaney *et al.*, 1990) and OPD (Novak and Burl, 1989). Several papers have introduced new detection algorithms for ice bodies (Marino *et al.*, 2016b), (Marino *et al.*, 2016a), (Marino *et al.*, 2015a), (Akbari and Brekke, 2017b). These include icebergs and sea-ice. A new detector (iDPolRaD) (Marino *et al.*, 2016b), was proposed to address the problem of detecting small icebergs embedded within sea-ice (Soldal *et al.*, 2019). Most iceberg detectors apply methodologies previously developed to detect ships. In general, vessels show a different backscattering behaviour compared to open ocean, where they appear brighter than the background (Marino *et al.*, 2015b; Wackerman *et al.*, 2001; Jackson and Apel, 2004). Previous work found that there is a large degree of dihedral scattering present between vessels and open water (Iervolino *et al.*, 2015). This is due to the signal reflecting off the sides of ships (particularly if the target is facing in the azimuth direction) and then the sea clutter.

The clean sea polarimetric characteristic at C- and L-band can be mostly modelled using a Bragg surface (Crisp, 2004). In contrast, ships as well as icebergs show different polarimetric characteristics (Dierking and Wesche, 2013). Work carried out by Dierking and Wesche (2013) showed that icebergs strongly exhibit volume scattering. This was echoed by work carried out by Bailey and Marino (2020) on icebergs in Greenland which showed that targets exhibit a mix of volume, and surface scattering with minimal dihedral behaviour. This is likely due to the effects of these irregular shaped icebergs toppling over. Smaller icebergs are larger hazards to ships, and detection ability is paramount to ensure the safety of maritime shipping. In papers focused on scattering behaviour, it is common that pixel sizes are smaller (1-4 pixels) and so multi-analysis is required in different window sizes (Bailey and Marino, 2020; Dierking and Wesche, 2013). However, this does not negate the inability of detectors to identify icebergs at these pixel sizes. The aim of this chapter is to compare six different detectors on ALOS-2 PALSAR data for iceberg detection in

Greenland. Since icebergs have been shown to exhibit a combination of scattering mechanisms, it is expected that this will affect the detection performance. These aims will be achieved by reviewing the literature of previous detection methods that have originally been applied to ship detection and extending their use with L-band data on icebergs. In order to compare detection performance, we consider two scenarios: icebergs found in open water, and icebergs embedded within sea ice. It is expected that performance will be lower in sea ice due to similar backscatter signals.

The chapter is organised as follows. Detection methodologies are presented in Section 5.2. The dataset and results are given in Section 5.3. Discussion and conclusions are outlined in Sections 5.4 and 5.5.

5.2. Methods

In this section, we determine and discuss various target detectors and review the previous research surrounding them. Some (but not all) of these state-of-the-art detectors have been validated only with ships. This work extends the analysis to icebergs and to the use with L-band.

5.2.1. IDPolRAD & DPolRAD

These detectors have been designed to identify icebergs embedded within sea ice. The detection procedure is based on the intensity of the cross and co polarisation channels, *HH* and *HV* (or *VV*, *VH*) (Marino *et al.*, 2016b). Due to volume scattering and multiple reflection icebergs are expected to have a cross-polarisation which is higher than the surrounding sea or sea ice (Marino *et al.*, 2016b). The detector therefore identifies an increase in depolarisation. The algorithm consists of two boxcar filters in two window sizes within the *HV* and *HH* intensity images.

$$\Lambda = \frac{\langle |HV|^2 \rangle_{test} - \langle |HV|^2 \rangle_{train}}{\langle |HH|^2 \rangle_{train}} > T_{\Lambda} \quad (5.1)$$

The two window sizes $\langle\rangle_{test}$ and $\langle\rangle_{train}$ are spatially averages, as is the case for boxcar filters (Lee *et al.*, 1994) The training window is larger than the testing window. T_{Λ} is a threshold. An extensive derivation of the formula is available in Marino *et al.* (2016b). We tested this detector for performance on the iceberg dataset.

In general, a detection is triggered if an iceberg of the right size is found in the test window, which increases the value of Λ. An iceberg that is much larger than the test window will not trigger a detection. If the surface is homogeneous, then the

detector is equal to zero and if there is a reduction in volume, the detector becomes negative. The complex nature of icebergs and sea ice unfortunately does not allow for the discrimination of icebergs with respect to other large sea ice features such as hummocks.

The detector was tested using Sentinel-1 dual pol data (Marino *et al.*, 2016b). The detector improved the contrast between icebergs and sea ice clutter by up to 75 times, greatly increasing the probability of accurate detection. The average sea ice-clutter was found to reduce by a factor of 35. Here, the detector is tested on L-band ALOS-2 data for the very first time.

More recently, work tested the detector on Sentinel-1 EWS C-band data (Soldal *et al.*, 2019). Here, results showed that incidence angle did not affect the output of the detection filter, and the consensus is that not all icebergs show a strong backscattering with HV polarisation. Several other papers test the detector on ship detection and found similar performances better than that of the CFAR method (Chen and Reed, 1987; Marino *et al.*, 2015b; Marino and Iervolino, 2017).

We also try for the first time a different version of the iDPolRAD, which exploits quad-pol data:

$$\Lambda = \frac{\langle |HH-VV|^2 \rangle_{test} - \langle |HH-VV|^2 \rangle_{train}}{\langle |HH+VV|^2 \rangle_{train}} \quad T_\Lambda \tag{5.2}$$

The intensity dual polarisation anomaly detector (iDPolRAD) is similar to the DPolRAD, with the difference being that the cross channel *HV* is multiplied as two boxcar filters are applied over the *HV* and *VV* intensity images. Here, the scattering properties between the clutter and the target are exploited. The detector can detect anomalies depending on if the target is producing an increase of volume scattering or multiple reflections. The detector is written as follows:

$$I = \frac{\langle |VH|^2 \rangle_{test} - \langle |VH|^2 \rangle_{train}}{\langle |VV|^2 \rangle_{train}} \sigma^0{}_{HV} = \Lambda \sigma^0{}_{HV} > T_\Lambda \tag{5.3}$$

The data are calibrated as normalised radar cross sections (RCS), shown by σ^0. Λ is a term that can be written as follows:

$$\Lambda = \rho_{ring} \frac{1+c}{R_\rho{}^{-1} + cRVH^{-1}} - \rho_{train} \tag{5.4}$$

Where ρ is known as the depolarisation ratio and used to determine if the estimation is performed in the training window or the area between the testing and training window (ring). RVH, c and Rρ are derived from the following:

$$RVH = \frac{\langle |VH|^2 \rangle_{test}}{\langle |VV|^2 \rangle_{ring}}$$

$$c = \frac{N_{train}}{N_{test}} \tag{5.5}$$

$$R\rho = \frac{\rho_{test}}{\rho_{ring}}$$

where N_{train} and N_{test} are the number of pixels inside the training and testing windows. The detector was tested in a case study in which SAR images were acquired from the Sentinel-1 satellite.

5.2.2. Polarimetric Notch Filter

This method is based on the fact that ships and the sea have different polarimetric properties. It is based on the Geometrical Perturbation analysis proposed in Marino (2012), and Marino *et al.* (2010a). It considers the full polarimetric information (phase or intensity) (Marino, 2013; Marino *et al.*, 2015b), and assumes that the surrounding sea is homogeneous (has a similar scattering behaviour). The final expression for the GPPNF is presented here, but the reader is referred to the papers Marino and Walker (2011) and (Marino *et al.*, 2010b) for a detailed analysis.

$$\gamma_n = \frac{1}{\sqrt{1 + \frac{RedR}{\underline{t}^{*T}\,\underline{t} - |\underline{t}^{*T}\,\underline{t}_{sea}|^2}}} > T_n \tag{5.6}$$

Where $\underline{t}$ is the partial feature vector (a six dimensional complex vector obtained stacking the independent elements of the covariance matrix) for the test area, T_n is the threshold and *RedR* is set as a constant for the minimum target to be detected and avoids numerical errors when computing the detection mask. The sea clutter $\underline{t}_{sea}$ is the normalised partial feature vector for the sea background. As this algorithm is quite general, it can also be used for the detection of other polarimetric targets, such as icebergs. In some cases, acquiring four polarisations is not feasible, and thus a dual polarimetric detector was proposed based on the GP-PNF (Marino *et al.*, 2013b). For the sake of brevity, the final detector expression is shown:

$$\gamma_{dn} = \frac{1}{\sqrt{1+\frac{RedR}{\underline{t_d}^{*T}\,\underline{t_d} - \left|\underline{t_d}^{*T}\,\underline{\hat{t}}_{dsea}\right|^2}}} > T_n \tag{5.7}$$

where $\underline{\hat{t}}_{dsea}$ refers to the dual polarised partial feature vector of the sea.

5.2.3. Polarimetric Match Filter

The Polarimetric Match Filter (PMF) was proposed by Novak and optimises the contrast between targets and the clutter (Novak *et al.*, 1989). The difference with the GP-PNF is that in the PMF, we apply an optimisation of the contrast, whereas the PNF considers mean information. In particular, the highest contrast is achieved through selecting the specific scattering mechanism $\underline{\omega}$ that optimises this. In other words, the detector processes the polarimetric return to provide maximum target-to-clutter ratio. The expression is as follows:

$$\Lambda_m = \max_{\omega \epsilon C^2} \frac{\underline{\omega}^{*T}|C_t|\underline{\omega}}{\underline{\omega}^{*T}|C_{sea}|\underline{\omega}} > T_m \tag{5.8}$$

For the PMF, we present the maximum and minimum eigenvalues as sigma1 and sigma3.

5.2.4. Reflection Symmetry

The reflection symmetry detector is derived on the basis of scattering reflection symmetry and was proposed by Nunziata *et al.* (2010). The detection is built using the complex values of *HH* and *HV*, with a cross-correlation evaluated in the element C12 of the covariance matrix (Marino *et al.*, 2013a). In theory, C12 should be equal to zero if the scenario is reflection symmetric. From this assumption, the C12 element should equal zero for the sea as a homogeneous surface, whereas targets such as ship and icebergs should return a higher C12 value, since heterogeneous asymmetric scatterers compose them. The equation is as follows:

$$XC = |\langle \boldsymbol{S}_{HH}\boldsymbol{S}_{HV}^{*}\rangle| \tag{5.9}$$

5.2.5. Optimal Polarimetric Detector

The optimal polarimetric detector (OPD) was proposed by Novak, and is based on the likelihood ratio test (LRT) under complex Gaussian statistics (Novak and Burl, 1989; Novak *et al.*, 1989). The LRT can be given when both the target and

clutter distributions are known. The optimal polarimetric detector takes into account both the target to clutter ratio (TCR) and the speckle reduction.

$$\underline{X}^{*}\Sigma_{c}^{-1}\underline{X} - \left(\underline{X} - \overline{\underline{X}}_{t}\right)^{*}(\Sigma_{t} + \Sigma_{c})^{-1}\left(\underline{X} - \overline{\underline{X}}_{t}\right) > T \tag{5.10}$$

In the case of icebergs, it is difficult to say what the covariance matrix of a general iceberg is. Therefore, in the following we will use a scaled identity matrix assuming icebergs are fully depolarised. This is a gross approximation, which may limit the detector performance. We leave this as future work to find a better approximation of the covariance matrix of icebergs.

5.2.6. Polarimetric Whitening Filter

The polarimetric whitening filter (PWF) is a detector that is designed to maximally reduce the speckle variation (Chaney *et al.*, 1990). It has been shown that in some circumstances the PWF provides a similar performance to the OPD in PolSAR images (Liu *et al.*, 2019). The PWF was also extended to multi-look scenarios (Liu *et al.*, 1998) and this is the version we will use in this work. Performance of the PWF depends on the quality of estimating the clutter. If the estimation of the clutter covariance matrix is closer to the real one, then we get the best performance. The formula of the PWF is as follows.

$$\underline{X}^{*}\Sigma_{c}^{-1}\underline{X} > T \tag{5.11}$$

However, the PWF has been extended for use in multi-look estimation by Liu *et al.* (1998), and Lopes and Séry (1997). The output for the MPWF is as follows:

$$z = \frac{1}{L}\sum_{i=1}^{L} y_{i}^{*}\,\Sigma^{-1}y_{i} = tr(\boldsymbol{r}^{-1}\boldsymbol{Y}) \tag{5.12}$$

Here, tr(.) is a trace operator, *y* is the speckle and *L* is the number of independent samples. It is suggested that the term *z* is known to obey the Gamma distribution (Khan and Guida, 2013). However, it is difficult to say if the probability density function (pdf) of the scatterers in icebergs obey the Gamma distribution and in future work we will compare histograms to see which pdf best fits the scatterers. Since there is an absence of texture, the covariance matrix obeys the Wishart distribution (Novak *et al.*, 1989). In the case of a textured scenario, the MPWF is rewritten as:

$$z = \frac{1}{L}\sum_{i=1}^{L} k_i^* \, \Sigma^{-1} k_i = tr(\Sigma^{-1}\boldsymbol{C}) = \frac{t}{E\{\tau\}} tr(\boldsymbol{r}^{-1}\boldsymbol{Y}) = \tilde{\tau} x \quad (5.13)$$

Where τ is a unitary texture variable, k is the scattering vector and $x = tr(\boldsymbol{r}^{-1}\boldsymbol{Y})$. When L = 1, the gamma distribution is presented in the single look complex (SLC) case. ***C*** is the multi look covariance matrix and sigma represents the statistical mean of multi-look covariance matrix ***C***. The covariance matrix for the Gaussian speckle is represented by ***r***, and ***Y*** is a random matrix that is only affected by speckle (Liu *et al.*, 2019). Here, the statistics of *z* are unknown under texture models.

5.2.7. Dataset

All ALOS-2 data were collected under a JAXA Announcement of Opportunity, in four locations in Greenland. Areas surveyed were in close proximity to named Greenlandic glaciers; data for which is available (Bjørk *et al.*, 2015). This meant the abundance of icebergs was high. Two scenarios were considered: firstly, two locations in which targets were located in open ocean, and secondly, two locations in which targets were embedded within sea ice, and ice floes. All data are quad-polarimetric, with an ascending mode and Single Look Complex (SLC) format with an average incidence angle of 35 degrees. The resolution in ground range is 4.3 m whereas the azimuth resolution is 5.1 m. In our previous paper (Bailey and Marino, 2020) we focused on the polarimetric behaviour of icebergs. In this work, we focus on target detection. The dataset is the same as in section 4.2. The only difference is the Blosseville Coast S location is not used (see Table 4.1). For an illustration of the study area, please see Figure 4.2

5.2.8. ROC curves

In this work, we use receiver operating characteristic (ROC) curves to show detection results. Previous work on CFAR detection also utilise ROC analysis. However, it should be noted that CFAR averaging requires an analytical probability density function (pdf) of the detector. The reason we do not use CFAR here is because this changes the focus of the work from the best detection performance to the best assumption of the pdf. Since modelling pdfs is very complicated, it requires substantial work. A ROC curve is independent of this assumption as it does not require an equation for probability of false alarms. Instead, we apply a trial and error based approach where the threshold is tweaked until the best ROC curve results are achieved. In doing so, we make an assumption of the pdf for each detector, which allows for a fairer comparison.

5.3. Results

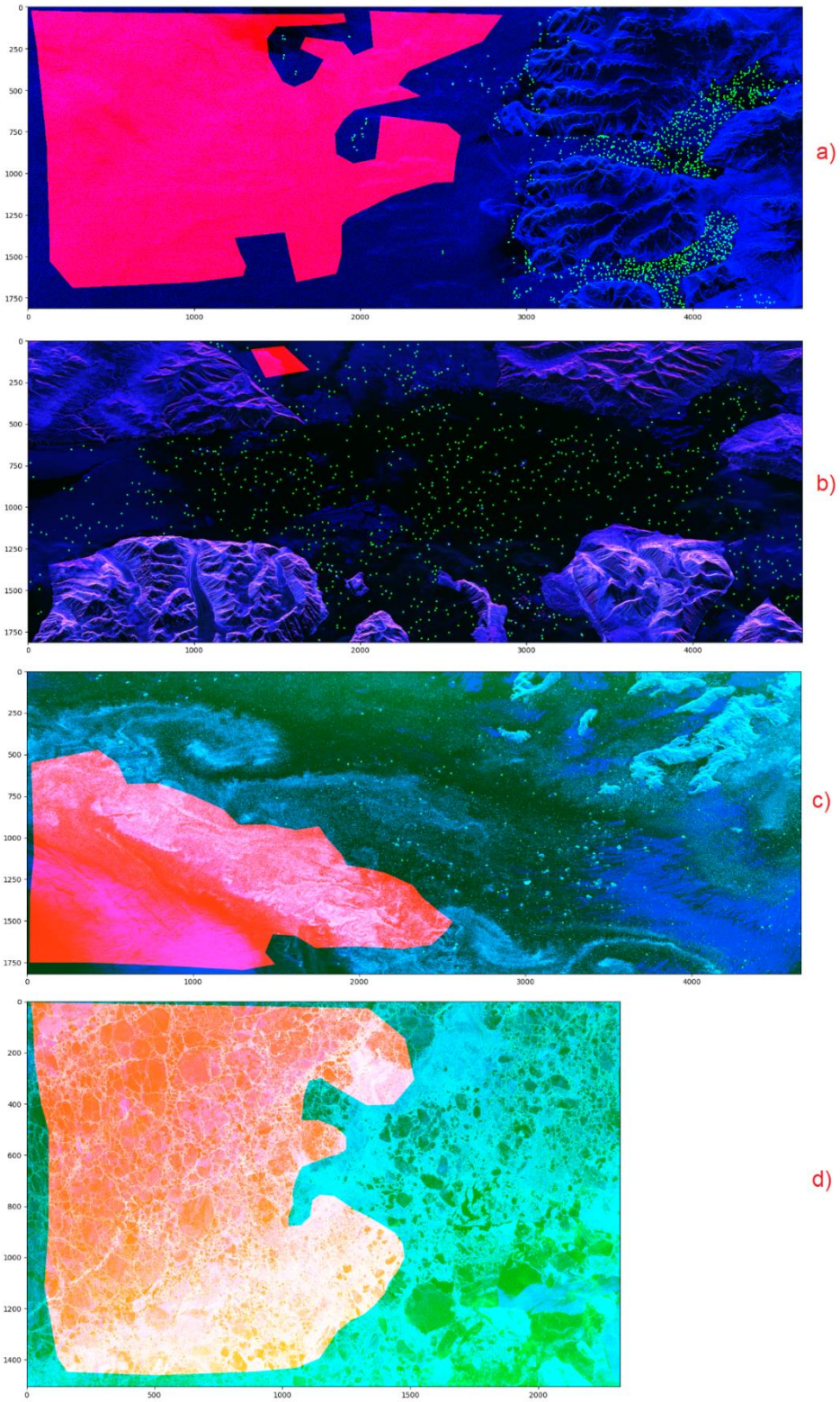

***Figure 5.1. a**) Target and clutter mask for Blosseville. Scenario is a mix of open ocean, and glacier tongues. Azimuth ambiguities are present in the middle of the image. **b**) Nuugaatsiaq. Scenario is a mix of open ocean, and islands. **c**) Isortoq. Scenario is a mix of sea ice and ice floes. **d**) Savissivik. Scenario is mainly sea ice, with embedded targets. Yellow dots in all images indicate icebergs. Red polygon indicates clutter*

5.3.2. Identifying targets and clutter

Icebergs were visually identified in images using RGB images in which the contrast could be adjusted accordingly. In order to evaluate the statistics for probability of false alarms (P_F), we considered areas inside images that were presenting either open ocean or sea ice. Figure 5.1 shows the clutter area as a red polygon and icebergs as green dots for Blosseville. Nuugaatsiaq and Isortoq, and Savissivik. As we can see, the clutter in Blosseville and Nuugaatsiaq is open ocean, while in Isortoq and Savissivik it is sea ice.

5.3.3. Preliminary detection comparison

Here, we show the comparison of the different detectors in three polarimetric modes, quad-pol, dual-pol, and single-pol. We will first present the detector images for a qualitative assessment over a zoomed area and after that, the receiver operating characteristic (ROC) curves for a quantitative assessment. All detection images have been created using a window size for the test area or 5 x 5 and (when required) a training area of 105 x 105 pixels using a guard window of 35 x 35. Figure 5.2 represents the guard window approach we used. In the following, we will also test changes in this windows configuration.

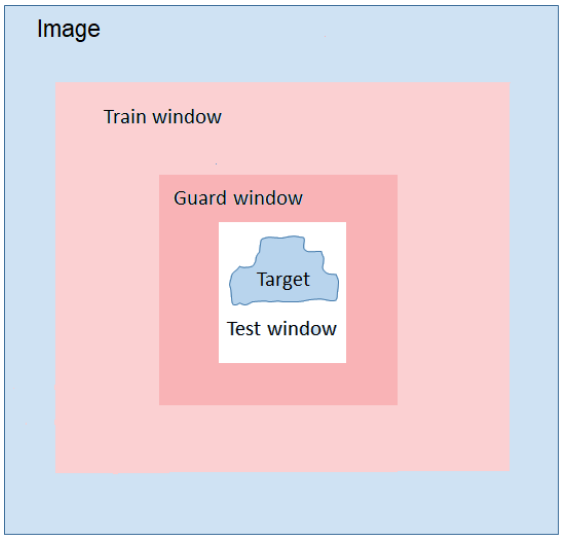

Figure 5.2. *The guard window approach. The blue area represents an image with pixels, the light pink area represents the train window, the dark pink area represents the guard window, to eliminate background clutter from the test window (white), in the case of this analysis, the target is an iceberg.*

5.3.4. Detection images

Figure 5.3 shows the iDPolRAD, DPolRAD, Notch filter and symmetry detection images for Blosseville. Please note, land (bottom and top of the image) will be detected too but we can exclude it using land masks.

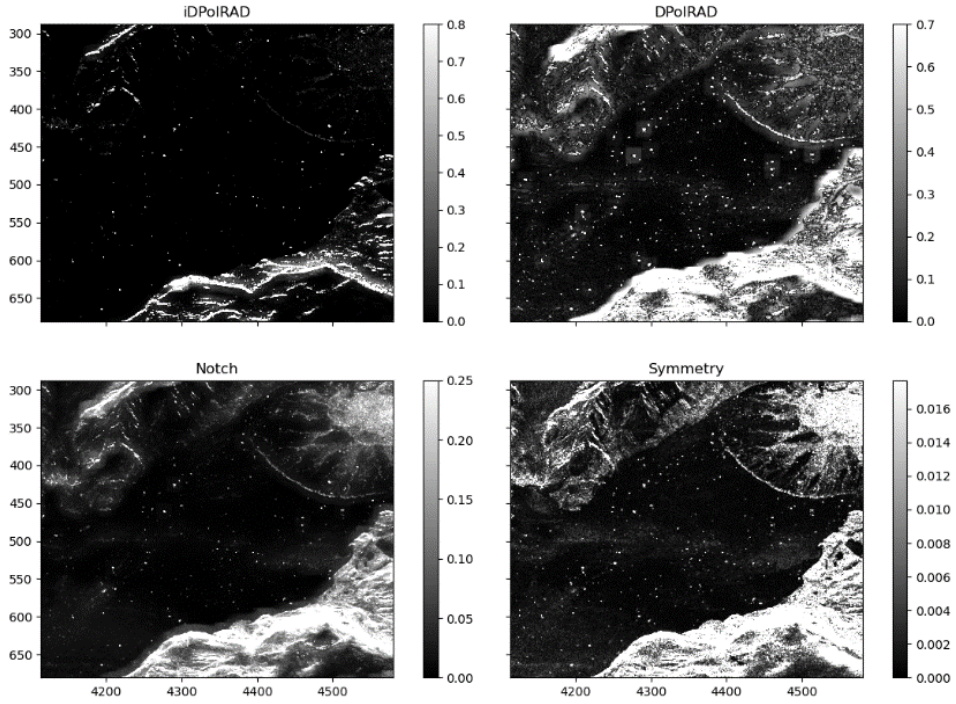

Figure 5.3. *Iceberg detection iDPolRAD, DPolRAD, Notch filter and symmetry for Blosseville. Image size is 350 x 500 pixels. Colormaps indicate detection intensity.*

If we look at the images, we seem to have the clearest detection using the reflection symmetry followed by the Notch filter and the DPolRAD close behind. The next images in Figure 5.4 show parameters from the Cloude-Pottier decomposition with alpha, entropy, first eigenvalue (lambda1) and third eigenvalue (lambda3) (Cloude, 2010).

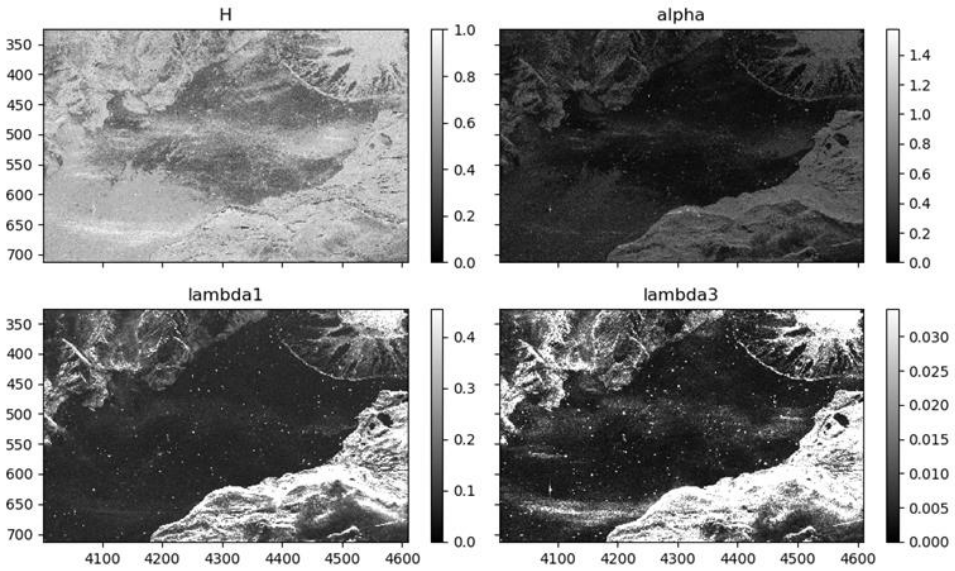

Figure 5.4. *Iceberg detection entropy H, alpha, lambda1 and lambda 3 for Blosseville. Image size is 350 x 600 pixels. Colormaps indicate detection intensity.*

From the images, it is clear that the alpha and entropy are not perfect detectors. Rather they are better to show classification of sea ice as in Section 5.3.6. The eigenvalues seem to be more suited for the detection task.

The images in Figure 5.5 show the first (sigma1) and third (sigma3) eigenvalues from the PMF, then the PWF and OPD.

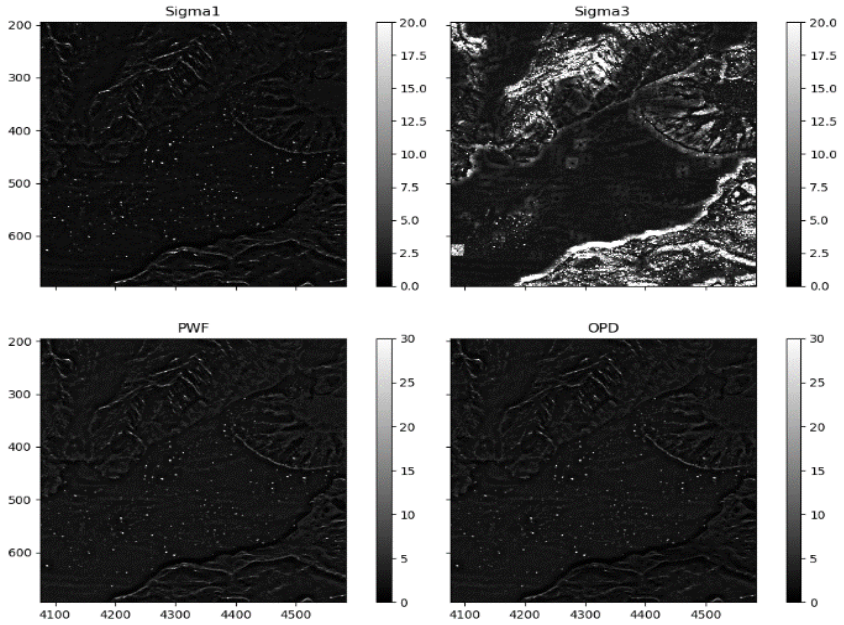

Figure 5.5. *Iceberg detection sigma 1, sigma 3, PWF, OPD for Blosseville. Image size is 400 x 600 pixels. Colormaps indicate detection intensity.*

From the images, it is clear that sigma1, PWF and the OPD detectors tend to give the visually best performance while sigma3 is missing many icebergs.

Detector output show similar trends in other locations. It is clear that a quantitative analysis is needed to evaluate the performance in a better way. This follows in the next section.

5.3.6. ROC curve detection analysis

In this section, we present the ROC curves. These are plot of probability of detection (P_D) against probability of false alarms (P_F). We first present the quad-pol results, then move to dual-pol and single-pol results. We will first show the ROC curves and then summarise them in tables in the next section. The ROC curves can also be used to aid the selection of P_F. Previous work shows that in ship detection, it is a common requirement for P_F to be < 10^{-4} (Marino *et al.*, 2015b) or 1 over 10,000 pixels. Therefore, in this analysis, we select $P_F = 10^{-5}$ and $P_F = 10^{-6}$ to analyse the detector performance.

5.3.6.1. Quad-pol ROC curves

Figure 5.6 presents a ROC curve for the case of open ocean clutter (Blosseville and Nuugaatsiaq) using a test window size of 5 x 5 and a train window size of 105 x 105.

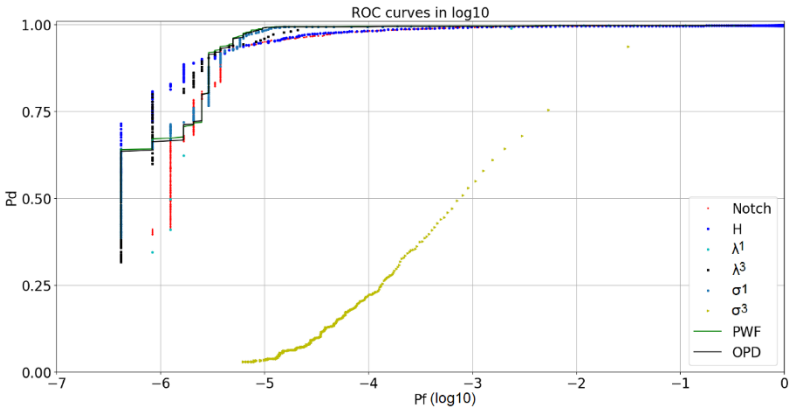

Figure 5.6. *Iceberg detection ROC curves for open ocean, test size 5 x 5, train size 105 x 105. Notch means polarimetric notch filter, H means entropy, λ^1 and λ^3 are the first and third eigenvalues of the covariance matrix, σ^1 and σ^3 are the first and third sigma values of the polarimetric match filter, PWF means polarimetric whitening filter, and OPD means optimal polarimetric detector.*

From Figure 5.6, we can see that in case of open ocean, the third eigenvalue of the PMF does not perform properly. This is expected since icebergs are brighter than the background in most open ocean conditions. Other detectors provide similar performance, but we can see some differences when we consider different levels of false alarm rates.

1) $P_F = 10^{-5}$

Here, we can see that the PWF and OPD both seem to provide the best performance (0.990) followed by sig1, notch filter, entropy, eig3 and eig1. The worst performance is sig3 of the PMF with a P_D of 0.034.

2) $P_F = 10^{-6}$

Here, the best detector is the entropy (0.808) followed by the eig3, PWF, sig3, OPD, and the notch filter. The worst performance is the first eigenvalue (0.345)

Figure 5.7 presents a ROC for the case of sea ice (Isortoq and Savissivik). Interestingly, we can see that in Figure 5.7, the entropy performance declines, which is most likely due to the number of scatterers present in the sea ice, which increases their entropy. Other adaptive detectors (e.g., PMF, PWF, PNF) also show a decreased performance in sea ice, since they are detecting heterogeneity of the sea ice.

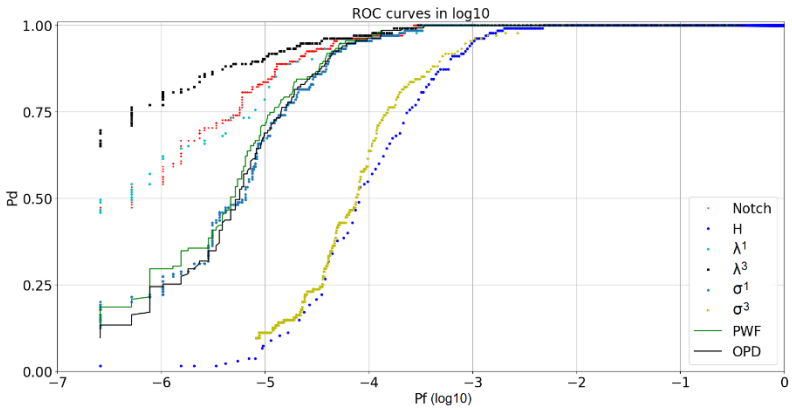

Figure 5.7. *Iceberg detection ROC curves for sea ice, test window 5 x 5, train window 105 x 105. Notch means polarimetric notch filter, H means entropy, λ^1 and λ^3 are the first and third eigenvalues of the covariance matrix, σ^1 and σ^3 are the first and third sigma values of the polarimetric match filter, PWF means polarimetric whitening filter, and OPD means optimal polarimetric detector.*

2) $P_F = 10^{-5}$

The best detector is third Cloude-Pottier eigenvalue eig3 with P_D equal to 0.770. This is followed by the notch filter, eig1, PWF, OPD, sig1 and sig3. The worst performance is the entropy (0.074).

2) $P_F = 10^{-6}$

Here, the performance degrades, but the eig3 remains the best detector with a P_D of 0.770. This is followed by the eig1, notch filter, PWF, OPD, sig1, with no result for sig3. The entropy shows the worst overall performance with a P_F of 0.015.

We want now to test in a different training window. We show the quad-pol ROC curves with a test window of 15 x 15 and a train window of 255 x 255 window, including a guard of 205 x 205 pixels (Figures 5.8 and 5.9). It is interesting to see that by using a larger window, the performance has been reduced. This is because the icebergs analysed here are particularly small and a larger window seems to impede detection. For instance, in open oceans some of the smaller icebergs can only be detected with probability of false alarms proximal to 1.

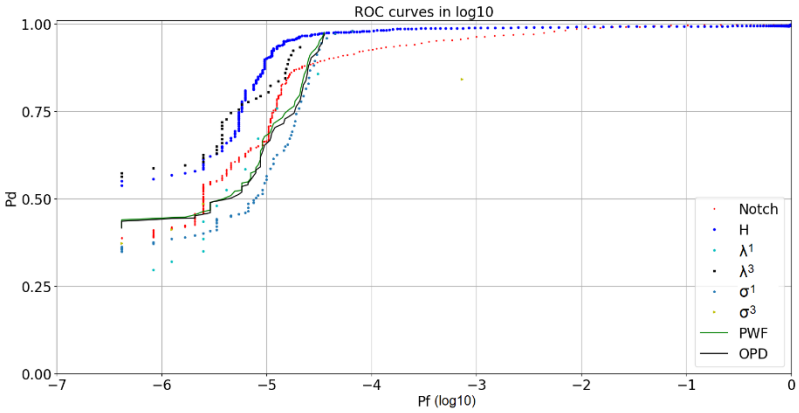

Figure 5.8. *Iceberg detection ROC curves for open ocean, test window 15 x 15, train window 255 x 255 with a guard window of 205 x 205. Notch means polarimetric notch filter, H means entropy, λ^1 and λ^3 are the first and third eigenvalues of the covariance matrix, σ^1 and σ^3 are the first and third sigma values of the polarimetric match filter, PWF means polarimetric whitening filter, and OPD means optimal polarimetric detector.*

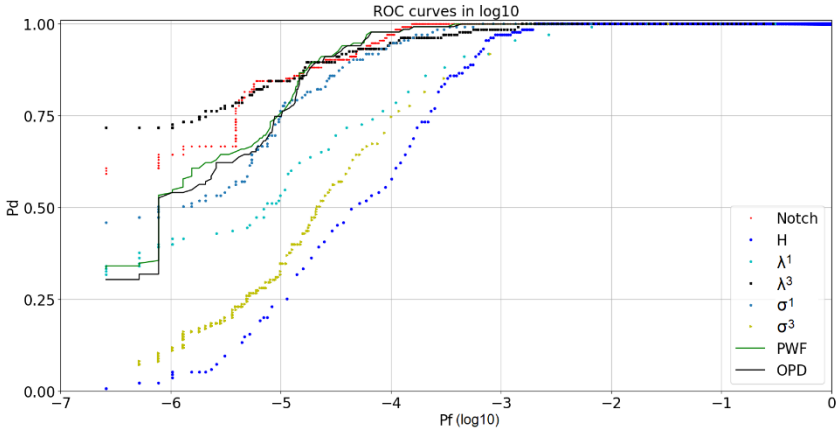

Figure 5.9. *Iceberg detection ROC curves for sea ice, test window 15 x 15, train window 255 x 255 with a guard window of 205 x 205. Notch means polarimetric notch filter, H means entropy, λ^1 and λ^3 are the first and third eigenvalues of the covariance matrix, σ^1 and σ^3 are the first and third sigma values of the polarimetric match filter, PWF means polarimetric whitening filter, and OPD means optimal polarimetric detector.*

Finally, we want to show the effects of NOT using a guard window for the detectors that need training. These detectors may be simpler to implement. This is in Figures 5.10 and 5.11. The performance is again clearly reducing, showing the importance of using a guard window for training.

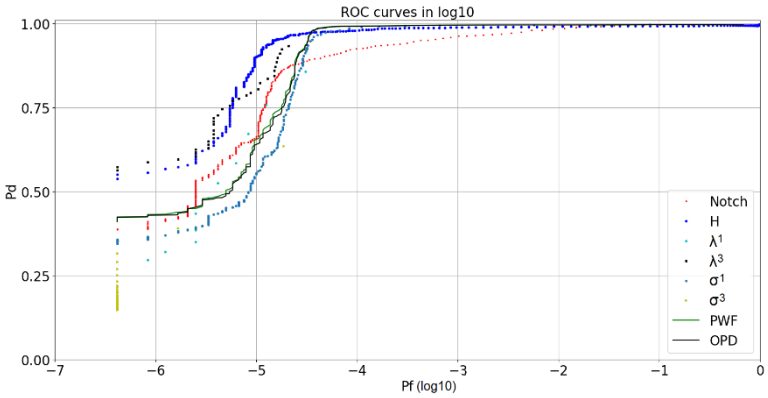

Figure 5.10. *Iceberg detection ROC curves for open ocean, test window 5 x 5, train window 105 x 105 with no guard window. Notch means polarimetric notch filter H means entropy, λ^1 and λ^3 are the first and third eigenvalues of the covariance matrix, σ^1 and σ^3 are the first and third eigenvalues of the covariance matrix, PMF1 and PMF3 are the first and third sigma values of the polarimetric match filter, PWF means polarimetric whitening filter, and OPD means optimal polarimetric detector.*

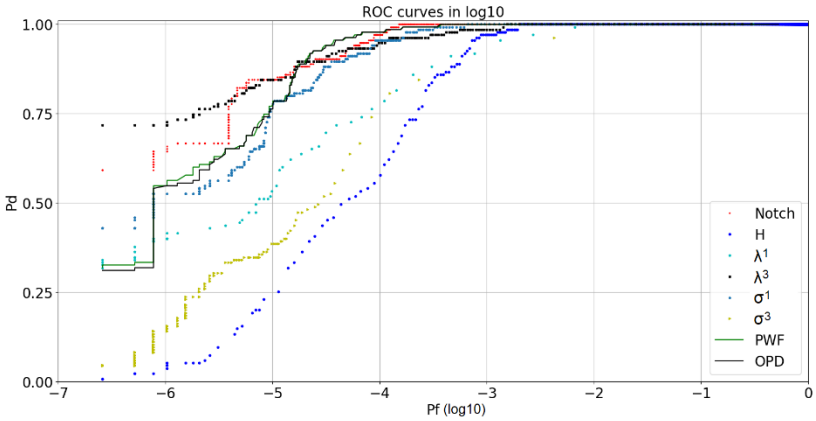

Figure 5.11. *Iceberg detection ROC curves for sea ice, test window 5 x 5, train window 105 x 105 with no guard window. Notch means polarimetric notch filter, H means entropy, eig1 and eig3 are the first and third eigenvalues of the covariance matrix, PMF1 and PMF3 are the first and third sigma values of the polarimetric match filter, PWF means polarimetric whitening filter, and OPD means optimal polarimetric detector.*

5.3.6.2. Dual-pol ROC curves

For the dual-pol ROC curves, we present the same window size with a guard window, but this time we are only considering three elements of the covariance matrix C11, C22 and C12 for analysis. This means that only the images HH and HV are used. Figure 5.12 shows a dual-pol ROC curve with a 5 x 5 test window, a 35 x 35 guard window size and a 105 x 105 train window size.

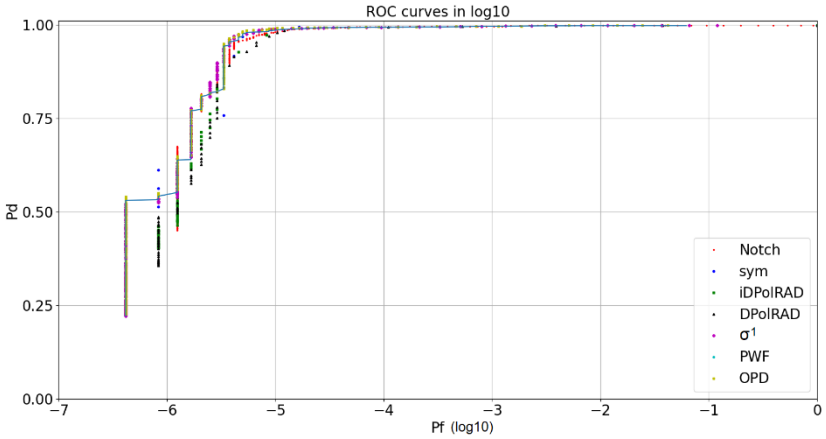

Figure 5.12. *Iceberg detection dual-pol ROC curves for open ocean, 5 x 5, train size 105 x 105. Sym means symmetry detector. iDPolRAD and DPolRAD mean dual intensity polarisation ratio anomaly detector, σ^1 is the first eigenvalue for the polarimetric match filter.*

All the dual pol detectors tested provide relatively similar performances. Again, we want to analyse performances using two different levels of false alarm rates.

1) $P_F = 10^{-5}$ The PWF provides the best performance (0.990) followed by sig1, OPD, notch and both the DPolRAD and iDPolRAD. The symmetry has the worst performance (0.969). No performance is shown from sig3 because in dual pol, we do not have the third eigenvalues.

2) $P_F = 10^{-6}$ When compared to the quad pol results, we can see a substantial difference in P_D values. The symmetry detector becomes the best detector (0.612) followed by the PWF, OPD, sig1, DPolRAD, iDPolRAD and notch filter with the worst performance (0.451).

Figure 5.13 presents the same result with sea ice clutter. Note that we can see differences between quad and dual for all levels of P_F.

1) $P_F = 10^{-5}$ - Here, we can see that the DPolRAD provides the best performance (0.874) followed by the symmetry, iDPolRAD, PWF, sig1, OPD. The notch filter has the worst performance (0.793).

2) $P_F = 10^{-6}$ – Here, we can see that there is a range of P_D values for all the detectors. The DPolRAD and iDPolRAD show the best performance (0.593). This is followed by the notch filter and sig1, PWF and symmetry. The OPD detector appears to show the worst performance with a P_D value of 0.313.

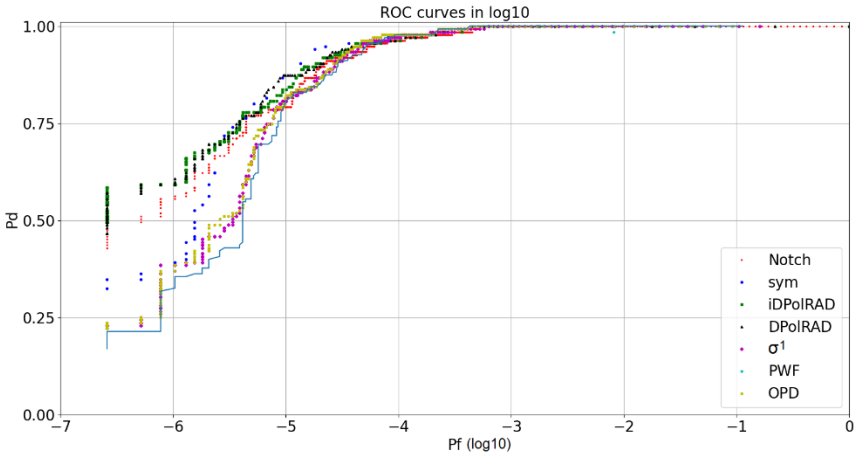

Figure 5.13. *Iceberg detection dual-pol ROC curves for sea ice, test window 5 x 5, train window 105 x 105. Sym means symmetry detector. iDPolRAD and DPolRAD mean dual intensity polarisation ratio anomaly detector, σ^1 is the first eigenvalue for the polarimetric match filter.*

The first thing to notice from Figures 5.12 and 5.13 is that the notch filter gives an improved performance in sea ice, to the quad pol version, which helps understand how the improved power of some adaptive detectors may produce several false alarms when there is sea ice. Performance between other detectors is also similar, with, PWF showing the best performance (0.990) in open ocean when P_F is 10^{-5}. The DPolRAD slightly outperforms with a P_D of 0.874 in sea ice when P_F is 10^{-5}.

As an important finding, we show that the dual pol performance is overall lower than the quad pol performance.

5.3.6.3. Intensities ROC curves

In this section, we investigate detectors set with intensity of backscattering when a specific scattering mechanism is used to see the projection of the scattering matrix. These certainly include the single-pol detectors when we use the co-pol or cross-pol channels on their own. But they also include quad pol detectors when we consider coherence combinations of co-pol channels. We show ROC curves in Figures 5.14 and 5.15 using C11, C22 and C33, plus T11 and T22 images. We apply to a window of 5 x 5.

Again, we want to analyse performances using two different levels of false alarm rates.

1) $P_F = 10^{-5}$ The HV cross channel seems to provide the best performance (0.989) followed by HH, HH+VV and HH-VV. The VV channel gives the worst performance (0.851). In open ocean, there is not a significant difference in performance compared to the dual pol results.

2) $P_F = 10^{-6}$ Here, the performance degrades and HH-VV shows the best performance (0.822) followed by HH, and HV with the worst performance (0.624). Now the difference is much more apparent in all the channels except HH-VV, but this requires quad-pol analysis as above.

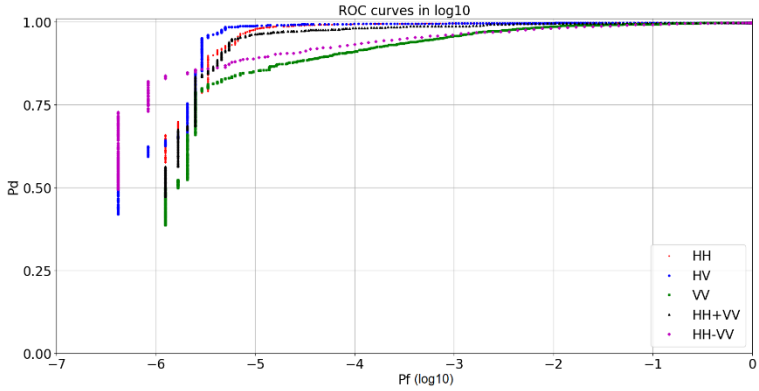

Figure 5.14. *Iceberg detection intensity ROC curves for open ocean, 5 x 5, train window 105 x 105. C11 is a HH polarisation, C22 is a cross polarised HV polarisation, C33 is a VV polarisation, T11 is a HH + VV polarisation and T22 is a HH – VV polarisation.*

Figure 5.15 shows the ROC performance in sea ice clutter. Again, we want to analyse performances using two different levels of false alarm rates.

1) $P_F = 10^{-5}$ Here, we can see that the VV channel provides the best performance (0.719) followed in order by HV, HH + VV and HH-VV with the worst performance (0.561). No matter what P_F value, the performance has declined.

2) $P_F = 10^{-6}$ The performance here has degraded, with HH-VV providing the best performance (0.334) followed only by HV (0.255).

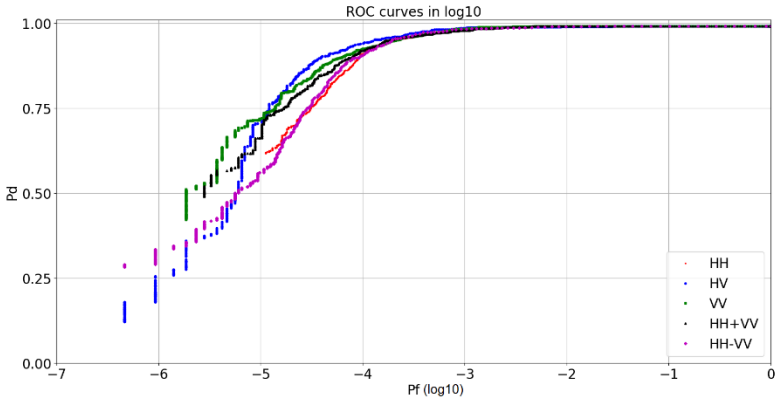

Figure. 5.15. *Iceberg detection intensity ROC curves for sea ice, 5 x 5, train window 105 x 105. C11 is a HH polarisation, C22 is a cross polarised HV polarisation, C33 is a VV polarisation, T11 is a HH + VV polarisation and T22 is a HH – VV polarisation.*

5.3.7 Best detectors

Table 5.1 summarises the quad-pol results and reveal that the best detectors for quad-pol appear to be the PWF, OPD, H and Eig3 detectors, with the worst performance from the PMF3 in open ocean, and entropy in sea ice. Table 5.2 summarise the dual-pol results and shows that the best detectors for dual pol again appear to be the OPD and PWF in open ocean. However, for sea ice, the best detector appears to be the iDPolRAD and DPolRAD. Finally, Table 5.3 shows that the best detection intensity appears to be the HV channel when the detection is easier and HH-VV in more complex environments.

***Table 5.1**: Probabilities of detection for quad-pol data*

	Eig1	Eig3	H	PNF	PMF1	PMF3	PWF	OPD
Open ocean								
$P_F=10^{-6}$	0.345	0.800	**0.809**	0.412	0.668		0.671	0.663
$P_F=10^{-5}$	0.799	0.944	0.948	0.950	0.983	0.034	**0.990**	**0.990**
Sea ice								
$P_F=10^{-6}$	0.570	**0.770**	0.015	0.541	0.222		0.296	0.244
$P_F=10^{-5}$	0.785	**0.904**	0.074	0.837	0.674	0.111	0.711	0.689

***Table 5.2**: Probabilities of detection for dual pol data*

	iD	D	PNF	PMF1	Sym	PWF	OPD
Open ocean							
$P_F=10^{-6}$	0.462	0.487	0.451	0.535	**0.612**	0.551	0.542
$P_F=10^{-5}$	0.972	0.970	0.978	0.988	0.969	**0.990**	0.985
Sea ice							
$P_F=10^{-6}$	**0.593**	**0.593**	0.556	0.385	0.363	0.370	0.313
$P_F=10^{-5}$	0.837	**0.874**	0.793	0.808	0.867	0.815	0.800

***Table 5.3**: Probabilities of detection for single-pol intensity data*

	HV	HH	VV	HH+VV	HH-VV
Open ocean					
$P_F=10^{-6}$	0.624	0.782			**0.822**
$P_F=10^{-5}$	**0.989**	0.977	0.851	0.962	0.890
Sea ice					
$P_F=10^{-6}$	0.255				**0.334**
$P^F=10^{-5}$	0.706		**0.719**	0.663	0.561

5.4. Discussion

In this section, we outline and evaluate the results of the analysis.

Using a test window of 5 x 5 and training window 105 x 105, the ROC curves suggest that the best performance for detecting icebergs in open ocean provides a P_D of 0.99 with a P_F of 10^{-5} using the PWF and OPD, or 0.81 for P_F 10^{-6} using the entropy. When we compare with iceberg detection in sea ice, with the same false alarm rate, we have a detection accuracy of 0.9 and 0.77 respectively using eig3; indicating detection in sea ice is more complex. This can be explained by the fact that sea ice can trigger false alarms, especially in more powerful detectors (Marino *et al.*, 2016b).

Interestingly, we can see that performance evaluation in dual pol shows a reduction of P_D for small values of false alarms. For instance, fixing P_F to 10^{-6} the accuracy is 0.61 in open ocean and 0.59 in sea ice. This is in line with the fact that by reducing the number of polarisation channels, our discrimination capability is reduced. However, when the detection task is easier (in open ocean), and we use larger values of P_F then the difference in performance between dual and quad detection is very limited.

Results from detectors based on intensities, show again that in easier scenarios where $P_F=10^{-5}$ and the setting is open ocean, the difference is minor with *HV* reaching accuracies of 0.985 (compared to 0.99 of quad). However, if we choose scenarios that are more complex, the performance of *HV* degrades and a quad pol

detector performs better. For instance, with $P_F=10^{-6}$ in open ocean we have *VV* going at $P_D=0.78$ (compared to 0.99 of quad), and within sea ice we have accuracies of 0.71 for $P_F=10^{-5}$ (compared to 0.90 of quad) and 0.25 for $P_F=10^{-6}$ (compared to 0.77 of quad).

To summarise, when the detection scenario is easier because we are looking at larger icebergs in open ocean, a single polarisation channel will perform relatively similar to a quad polarimetric one. However, when detecting icebergs in sea ice or we are interested in smaller icebergs (smaller false alarm rate) then adding polarimetric information will help. Finally, we saw that when we increase the test window to 15 x 15 and train window to 255 x 255, the P_D value reduces. This is in line with the fact that when we have a bigger window, we include more pixels and thus smear the target and decrease the probability of detection (Marino *et al.*, 2015b). Moreover, when we do not use ring windows then we have degradation of performance. The absolute values for the accuracies need to be taken with care since we only restricted the analysis to the icebergs that are clearly identifiable. However, the relative comparison of detectors should still be preserved if less bright icebergs in the images were introduced.

5.5. Conclusion

In this work, we tested an ALOS-2 dataset with six state-of-the art detectors, most of them designed to be used for ship detection. The detectors are the dual intensity polarisation ratio anomaly detector (iDPolRAD), polarimetric notch filter (PNF), polarimetric match filter (PMF), reflection symmetry, multi look polarimetric whitening filter (MPWF) and optimal polarimetric detector (OPD) We estimated detection performance over four ALOS-2 quad-pol single look complex SAR images, in four locations in Greenland. To compare the performances of each detector, we performed the analysis using two scenarios. Two of the images had icebergs in an open ocean setting, and two showed icebergs embedded within sea ice. In total we considered 3,242 icebergs in this analysis.

We show that overall, the quad pol detectors OPD and PWF provide the best detection performance with a PD of 0.99 in open ocean when the false alarm is set to 10^{-5}. However, in sea ice, the eig3 shows the best performance (0.90). For dual pol performance, we conclude that the PWF gives the best performance in open ocean (0.90). In the sea ice, the best detector is DPolRAD (0.978). Finally, we test the data

in single pol mode, showing that the best performance is *HV* in the open ocean (0.99) and in the sea ice (0.87).

The differences between quad- and dual- or single-pol detectors are more evident when we go for low detection probabilities 10^6; when compared to the *HV* channel; quad pol detectors increase the P_D from 0.62 to 0.81 for open ocean and from 0.26 to 0.77 for sea ice.

Contributions

Conceptualisation, J.B., and A.M.

Methodology, J.B.

Software, A.M., and J.B.

Validation, J.B., A.M., and V.A.

Formal analysis, J.B.

Investigation, J.B

Resources, A.M.

Data curation, J.B.

Writing—original draft preparation, J.B.

Writing—review and editing, J.B., and V.A.

Visualisation, J.B.

Supervision, A.M.

Project administration, J.B.

6.0. ICEBERG DETECTION WITH A RADARSAT-2 QUAD POL C-BAND SAR IN KONGSFORDEN, SVALBARD – COMPARISON WITH GROUND BASED RADAR

This chapter is a journal article that has to be submitted to the Journal of Selected Topics in Applied Earth Observation and Remote Sensing (JSTARS). Here we expand on our iceberg detection work by introducing ground-based radar.

Abstract:

Satellite monitoring of icebergs in the Arctic region is paramount for the safety of shipping and maritime activities. The potential of PolSAR data in enhancing detection capabilities of icebergs under interchangeable and challenging conditions is explored in this work. We introduce RADARSAT-2 quad-pol C-band data to detect icebergs in Kongsfjorden, Svalbard. The location contains two tidewater glaciers and is chosen because multiple processes are present in this region such as ice formation and its relationship with the glaciers and freshwater discharge. Six state-of-the-art detectors are tested for detection performance. These are the dual intensity polarisation ratio anomaly detector (iDPolRAD), polarimetric notch filter (PNF), polarimetric match filter (PMF), symmetry, polarimetric whitening filter (PWF), optimal polarimetric detector (OPD). Additionally, we also tested the Cloude-Pottier parameters. In this study, we make use of a ground-radar for validation and comparison of satellite images with ground-based images. We show that in calm sea-state conditions, the OPD and PWF detectors give high Probability of Detection (PD) values of 0.7-0.8 when the Probability of False Alarm (PF) value is 0.01-0.05, compared to choppy sea conditions where the same detectors have degraded in performance (PD = 0.5-0.7). Target to clutter ratio (TCR) values for each polarisation channel are also extracted and compared to the icebergs' dimensions. Ground-based images show higher values in TCR, compared to satellite images. These findings corroborate previous work and show that sea ice activity, surface roughness, incidence angle, weather and sea state conditions all affect the sensitivity of the detectors for this task.

6.1. Introduction:

In this chapter, target detection algorithms are applied to three RADARSAT-2 images of an area of iceberg and sea-ice cover in the Kongsfjorden in Svalbard, Norway. In Kongsfjorden, icebergs are calving off the Kronebreen and Kongsbreen tidewater glaciers, and becoming embedded within sea-ice floes (Gerland and Renner, 2007).

The detection of icebergs using SAR data often employs conventional constant false alarm rate (CFAR) methods using a sliding window. Targets are discriminated by looking at the differences in the backscattering when comparing the value of a target window over a clutter window (Oliver and Quegan, 2004). The threshold is set using statistical tests and any target brighter than the threshold triggers a detection. Thus, this technique helps identify bright targets in darker clutter background. However, numerous problems arise. Firstly, it is very common for the ocean clutter window to become contaminated by nearby targets (Tao *et al.*, 2015). In areas of high iceberg density such as at the edge of glacier tongues, the large presence of icebergs can disrupt the statistical modelling of clutter, causing severe reduction in CFAR detection performance and increasing the false alarm rate. This is known as the capture effect (Li *et al.*, 2020). Secondly, the meteorological and oceanographic conditions, including presence of sea ice, can increase the backscatter from the sea, causing heterogeneous clutter and thus, higher false alarm rates. This is known as the clutter edge effect (Tao *et al.*, 2016). Thirdly, the size of the window being used is important; bigger windows can include more image pixels, causing diluting targets during averaging while smaller windows can exclude pixels of iceberg edges. Attempts to address these problems have included the implementation of a guard window in between the testing and training windows, which has been shown to increase performance (Bailey *et al.*, 2021). Another limitation to these iceberg detection methods is that even in areas such as open ocean, numerous rocks and small islands can increase the number of false alarms. This is addressed by including an initial stage in image processing in which a land mask is applied before detection can begin (Crisp, 2004). It is important to note that land masking may still include small, unmapped rocks.

It is well known that polarimetric synthetic aperture radar (PoLSAR) can help target classification and therefore the discrimination between icebergs and background. Multiple papers highlight the importance of cross-polarisation; icebergs

tend to be detected easier in a HV channel compared to co-polarisation channels HH and VV (Karvonen *et al.*, 2021; Dierking and Wesche, 2013; Marino *et al.*, 2016b). This finding was first concluded by Dierking and Wesche (2013) and as a result, many CFAR methods used for iceberg detection exploit this property.

Previous work undertaken in Kongsfjorden has utilised C-band PolSAR. Akbari and Brekke (2017a) proposed a near-real-time (NRT) processing chain for iceberg detection in non-homogeneous areas of sea clutter. An iceberg segmentation algorithm was tested on quad-pol RS2 images and found to handle various different sea states and areas of high iceberg density without the need for local training windows. However, it should be noted that the frequency at C-band may not be low enough to further discriminate between iceberg backscatter profiles and sea-ice backscatter profiles. This is because C-band frequencies will not penetrate far enough to reveal internal features of iceberg bodies, such as cracks, and crevasses (Dierking and Wesche, 2013).

Previous work has been carried out on icebergs of a similar size and shape in east and west Greenland (Bailey *et al.*, 2021) using ALOS-2 L-Band SAR images. Here, several detectors, were tested for two scenarios: icebergs in open ocean, and icebergs embedded within sea-ice floes. More recently, (Himi *et al.*, 2021) concluded that icebergs off the coast of Newfoundland exhibit a high volume scattering component in open ocean, compared to surface scattering in sea ice. With the calving of 30,000 icebergs a year estimated in the Arctic regions (Frost *et al.*, 2016; Karvonen *et al.*, 2021), attention now turns to areas situated at glacier termini.

The main aims of this chapter are the following:

a) To apply six state-of-the-art detectors to a RADARSAT-2 dataset in Kongsfjorden, Svalbard to determine overall detection performance for this environment. These detectors are the same used in Chapter 5 and are applied to this data for the first time. We also make use of Cloude-Pottier entropy for comparison purposes.
b) to validate the satellite detection results using data acquired from Ku-band ground-based radar.

One of the novelties of this work is the comparison with a ground radar: the Gamma Portable Radio Interferometer (GRPI) (Werner *et al.*, 2008; Werner *et al.*, 2012). The ground and satellite images were acquired at the same time allowing

comparison. This allowed a validation of satellite data for smaller icebergs and to compare the backscattering of the two very different systems. GPRI also provides insights about the more general topic of iceberg detection with radar. We show the potential of using portable radar systems for the validation of satellite SAR detectors.

The chapter is organised as follows. Methods are reviewed in Section 6.2, a background to the dataset is introduced in Section 6.3. Results are presented in Section 6.4. A discussion is outlined in Section 6.5. Conclusions and further work are summarised in Section 6.6.

6.2. Methods:

We use quad-pol Synthetic Aperture Radar RADARSAT-2 images to identify icebergs in surrounding sea ice clutter. The iceberg detection system in this paper consists of the following processing steps:

6.2.1. Preprocessing

Firstly, the raw RADARSAT-2 data are extracted and calibrated as sigma nought. We produced the covariance matrix elements of each acquisition and converted them into a coherency matrix by using a unitary transformation matrix. Geocoding is applied to the elements of the coherency matrix.

6.2.2. Masking

To reduce the possibility of false alarms caused by radar backscatter returns from islands and rocks in the fjord, a land mask is applied by using a land boundary map or shoreline layer. However, land masking is not always fully accurate due to multiple factors. These include geocoding errors, errors in recording coastline, unmapped rocks, erosion of coastline and variations in tide activity (Brusch *et al.*, 2010). The land mask we use here was provided by the Norwegian Polar Institute.

6.2.3. Preparing validation dataset

In order to validate the detectors, we identified areas of open-ocean, sea-ice and icebergs in both satellite and ground images. The creation of the validation dataset is achieved by extracting the ground-based images created from optical imaery, and then in both the satellite and ground datasets, applying polygons to each set of pixels that are visually identified as an iceberg. Icebergs are selected if they appear very bright in the image, cast a shadow to the side, and are not elongated in

shape (which may indicate a vessel). We extract the centre coordinates for each iceberg.

In the following, we produce a shapefile of clutter polygons as a secondary layer, and then merge and stack layers together. We also produce target and clutter masks from the RS2 scenes (Figure 6.4). Finally, all the satellite and ground raster data were stacked together to form a final cube. The final raster cube consists of all three acquisitions, the masks for target, clutter and land mask, and ground image raster data.

6.2.4. Target-to-clutter ratio (TCR)

In order to detect icebergs in SAR images, a significant level of contrast between target and background clutter is required. Here, we use target-to-clutter ratio (TCR) to evaluate the contrast between icebergs and background clutter for different polarimetric channels and detectors. The TCR of each iceberg was calculated by taking the maximum value of an iceberg pixel and dividing either by the average (referred to as mean TCR) or the maximum (referred to as maximum TCR) value of the closest clutter area. It is important to note that the TCR requires polygons to be convex to avoid computational errors. The diagonal axis of each polygon is extracted using geometrical properties. Previous work has used TCR to assess detector performance (Akbari *et al.*, 2016a; Cristea *et al.*, 2017). Please note the concept of TCR requires a ratio or power and therefore it cannot be easily extended to other detector observables. This is because the detector observables often receive a removal of scaling which make them not comparable with power measurements.

The maximum TCR values for all icebergs and clutter in each scene are presented in eq (6.1) and (6.2). It is important to note that the TCR is affected by factors such as the number of pixels used for the estimation. In this work, we use a maximum of a 3x3 window to evaluate TCR statistics against iceberg area (defined as the surface area of the iceberg in m^2).

$$Max\ TCR\ =\ target_{max}\ /\ clutter_{mean} \tag{6.1}$$

$$Mean\ TCR\ =\ target_{mean}\ /\ clutter_{mean} \tag{6.2}$$

6.2.5. Visual identification of icebergs

In the following there is an explanation of the rules we used to perform the visual identification of icebergs.

Brightness: Icebergs in SAR images represent higher brightness than the surrounding ocean. However, sea ice backscatter intensities can be similar to icebergs (Himi *et al.*, 2021). Using brightness alone is not sufficient to identify all icebergs within a high-density region of sea-ice cover. To avoid errors in iceberg identification, it is useful to add information about the geometry and shape.

Longitudinal axis: We focused on smaller icebergs of less than 120 m in longitudinal length, since these are the one that are harder to detect. The size of the target visually identified must not exceed this threshold.

Shadow: Targets which are bright on an image, with a darker region next to it are considered as potential icebergs. In sea-ice, icebergs can often be identified by their shadow, even if the pixel brightness of both the icebergs and the sea ice is the same.

Shape: Targets with regular elongated shapes are considered to be vessels and are eliminated from the analysis.

If all the above discrimination features fall within the ranges we specified, the target is considered to be an iceberg. Clearly, when performing this visual identification, we mostly select icebergs surrounded by relatively low sea or sea-ice level. The ones embedded in high clutter areas (high sea state and deformed ice) are just not visible with enough confidence. However, the ROC curves and TCR compare icebergs with clutter areas that are not necessarily surrounding the iceberg and therefore can have larger intensity.

The icebergs are then polygonised so that geometrical properties such as area, shape, major and minor axis are made available in tabular form. The area is calculated by counting the pixels that make up each iceberg and multiplying by pixel spacing. The position of an iceberg is determined using the coordinates of the iceberg polygon centroid, which can be converted into latitude and longitude using the geocoded information of the PolSAR image.

6.3. Study Area and Dataset

In this section we introduce the dataset and summary tables of the satellite and ground radars.

All data were acquired over Kongsfjorden in Svalbard, where iceberg calving is prominent. Kongsfjorden is situated on the west coast of Spitsbergen in Ny Alesund at roughly 79°N and 12°E (Figure 6.1). Radar backscatter is affected by the changing conditions in the fjord, since the Konebreen and Kongsbreen glaciers produce an abundance of iceberg calving. This is in addition to freshwater discharge and wind, which in turn affects sea-ice activity and changing sea states. Sea-ice activity is most prevalent from September to June, usually in the inner part of the fjord, while the outer part is usually open sea or contains drift-ice. Typically, icebergs can be found embedded and frozen within the sea-ice during winter months and drifting in open ocean during the summer months (Svendsen *et al.*, 2002). The location is also in close proximity to a Norwegian Polar Institute (NPI) research station on the south side of the fjord, which aids in logistics for fieldwork.

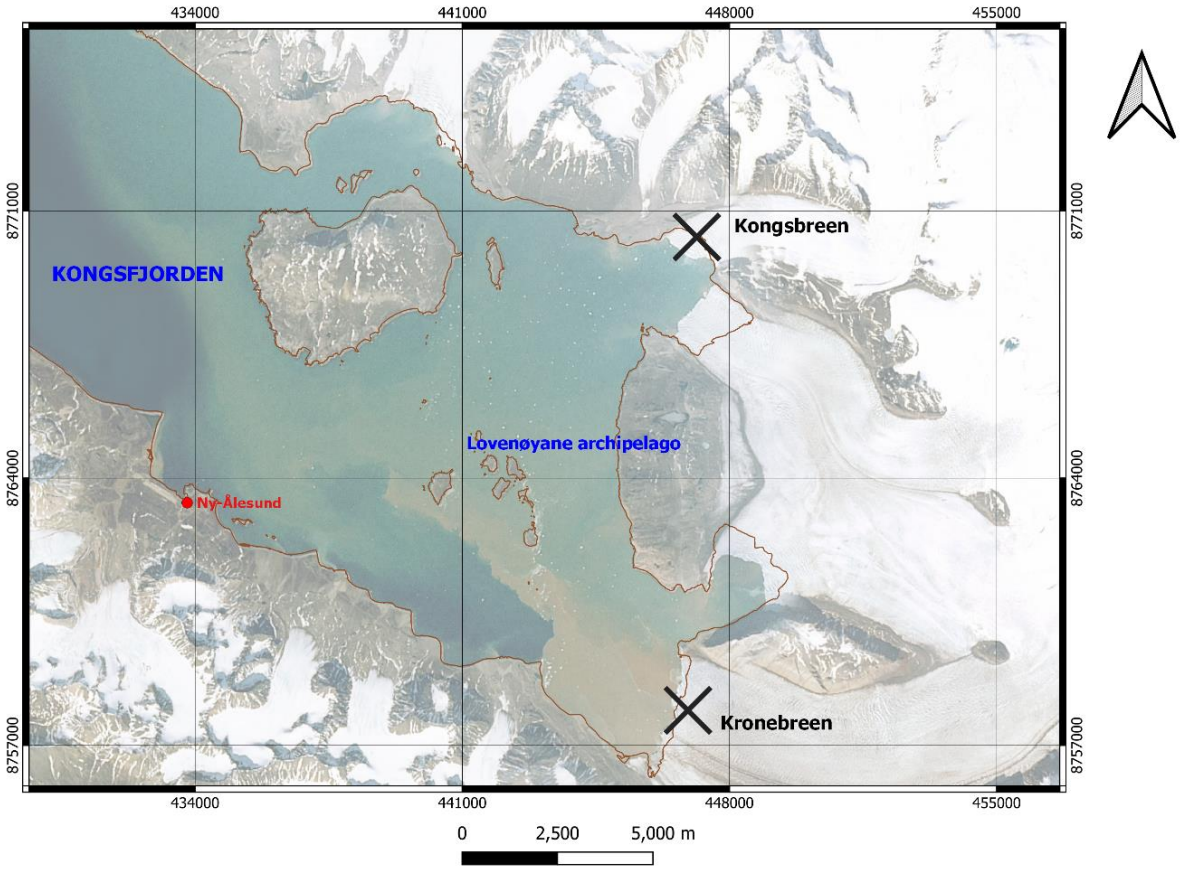

***Figure 6.1**: Study area showing Kongsfjorden in Svalbard, Norway. Black crosses indicate tidewater glaciers, red text indicates settlements, blue text indicates the Kongsfjorden and the Lovenøyane archipelago, brown line indicates land masking.*

Icebergs can also group and become clustered or grounded within fjords, an area where at least 20% of the coastline is dominated by tidewater glaciers (Dowdeswell and Forsberg, 1992). Notable iceberg sizes range from growler to bergy bit. Studies on the size and frequencies of icebergs in the fjord have found that the largest iceberg was 30 m in width, although it was an extreme outlier. Although this work focuses on icebergs from two tidewater glaciers, the fjord is fed by five glaciers (Liestøl, 1988). However, sea-ice floes are also present in the fjord, which makes distinguishing the smallest icebergs from sea ice floes very difficult. Another significance of Kongsfjorden is that it is incredibly shallow in areas where icebergs are drifting. 26% of an inner bathymetric section of the inner fjord has a depth >20 m. Therefore, icebergs can become grounded, and end up melting in the fjord in less than a month. It is also suggested that most of the icebergs come from Kronebreen, as it is a relatively fast flowing glacier and is also highly crevassed, which suggests more smaller size calving of irregular shape icebergs (Dowdeswell, 1989).

For this analysis, a total of 92 icebergs were selected for analysis using satellite data, and a total of 60 icebergs were selected for data validation using ground-radar.

6.3.1. RADARSAT-2

The satellite data in this paper consist of three multi-looked quad-pol C-band SAR time-series images in fine beam mode acquired from the RADARSAT-2 satellite launched by the Canadian Space Agency (Livingstone *et al.*, 2006). As listed in Table 6.1, the SAR scenes were taken over a range of ascending and descending orbits with an incidence angle range of 23° to 46°. The original resolution of RADARSAT-2 single look complex (SLC) is 5.2 m in range and 7.6 m in azimuth, respectively. They cover the time span between 15-17 April 2016. In this work, we did not access the SLC, but images that were calibrated multi-looked and geocoded to a Universal Transverse Mercator (UTM) grid to produce multi-looked images with 20 m pixel spacing. Therefore, the final resolution for our images is 20 x 20.

Figure 6.2 shows the geocoded Pauli RGB (R = HH-VV, G = HV, and B = HH+VV) of the acquisitions. The scene collected on April 15th (Figure 6.2a) shows a relatively calm sea-state with sea-ice activity present west of the Lovenøyane archipelago. The open sea north of the archipelago has an extremely low radar backscatter, representing a very calm sea-state, and this is where the icebergs are more visible. The scene collected on April 16th (Figure 6.2b) appears to show a more

heterogeneous sea-state due to higher wind conditions. This is evident through brighter areas of radar backscatter in the surrounding sea clutter. When compared with Figure 6.2a, icebergs north of the Kronebreen glacier appear to be drifting north west. Brighter iceberg backscatter signatures are also visible. The scene collected on April 17th (Figure 6.2c) shows a relatively calmer sea. The sea appears calmer than in Figure 6.2b as shown by less bright radar backscattering. The icebergs west of the Kongsbreen glacier appear to show higher backscatter in addition to the surrounding terrain. This can be attributed to a higher incidence angle in comparison to the first two scenes. In all images, icebergs are situated slightly north to north east of the archipelago, while the outer part of Kongsfjorden appears to be free of icebergs.

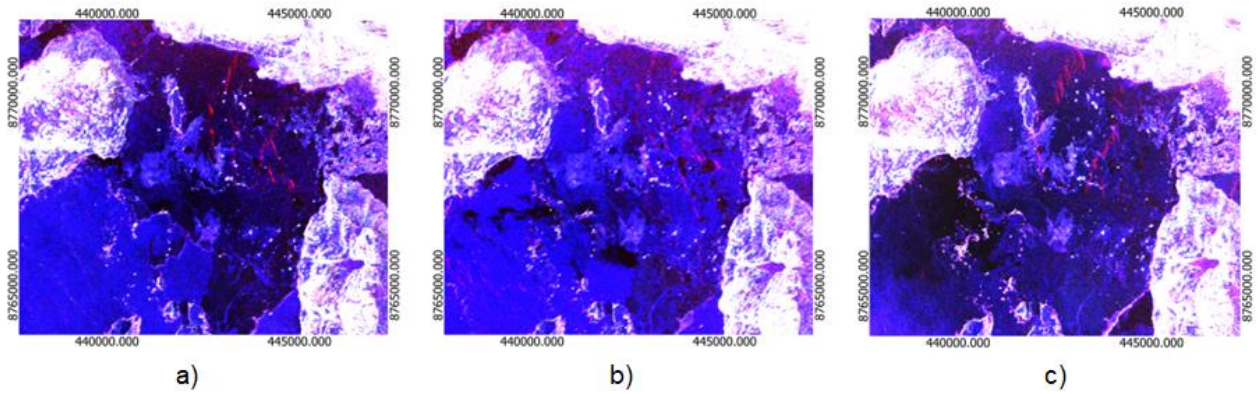

***Figure 6.2**: Pauli RGB of each image acquisition with GIS coordinates **a**) 15th April, **b**) 16th April, **c**) 17th April. Red = intensity of HH-VV; Green = intensity of HV; Blue = intensity of HH+VV*

***Table 6.1**: RADARSAT-2 image acquisitions, note that the latitude and longitude is for the centre coordinate of each scene*

Scene	***ID***	***Date***	***Time (UTC)***	***Lat/Lon***	***Beam***	***Incidence Angle (°)***	***Orbit***
20160415	*470697*	*15th April 2016*	*15:39*	*12.340636, 78.924756*	*FQ13*	*32-34*	*Asc*
20160416	*470930*	*16th April 2016*	*15:10*	*12.328320, 78.932074*	*FQ5*	*23-25*	*Asc*
20160417	*471190*	*17th April 2016*	*15:10*	*12.175653, 78.896132*	*FQ25*	*38-40*	*Asc*

6.3.2. GPRI

Ground-based data in this paper consist of three single real aperture Ku-band (1.74 wavelength) Gamma Portable Radar Interferometer (GPRI) image acquisitions with a ground azimuth resolution of roughly 7 m (in the location of the icebergs) at 1 km distance from the sensor and a range resolution of roughly 1 m. Beginning on 15th April at 15:15 (UTC time), the instrument conducted a sweep every two minutes with only one interruption of 4 hours on the morning of 16th April, and continued until 19th April at 08:00. The three images in question were collected on 15th April until 17th April and have corresponding times with the RS2 data. The GPRI data are used in two ways: a) as ground-truth in tandem with the satellite data to visually identify icebergs, b) to compare the detectability of icebergs in the two systems.

The large extent of the images generated from the GPRI, together with the high frequency and quality of the intensity images demonstrate the potential of using ground-based radar observations to identify and characterise icebergs and growlers. The GPRI data are greatly beneficial for ground truthing, allowing for the ability to track icebergs and growlers over time, as well as monitoring size and shape like in ship observations.

Figure 6.3 shows the ground radar scene from 15th April, together with a smaller region of interest (ROI) from each acquisition to zoom on a smaller area where we can visually identify icebergs. The bright backscatter signatures can be attributed to a higher incidence angle in each scene, with icebergs being identified visually north to north east of the archipelago. It is important to note that due to differences in incidence angle between ground and satellite images, icebergs that are visible in ground images may not be visible in satellite images.

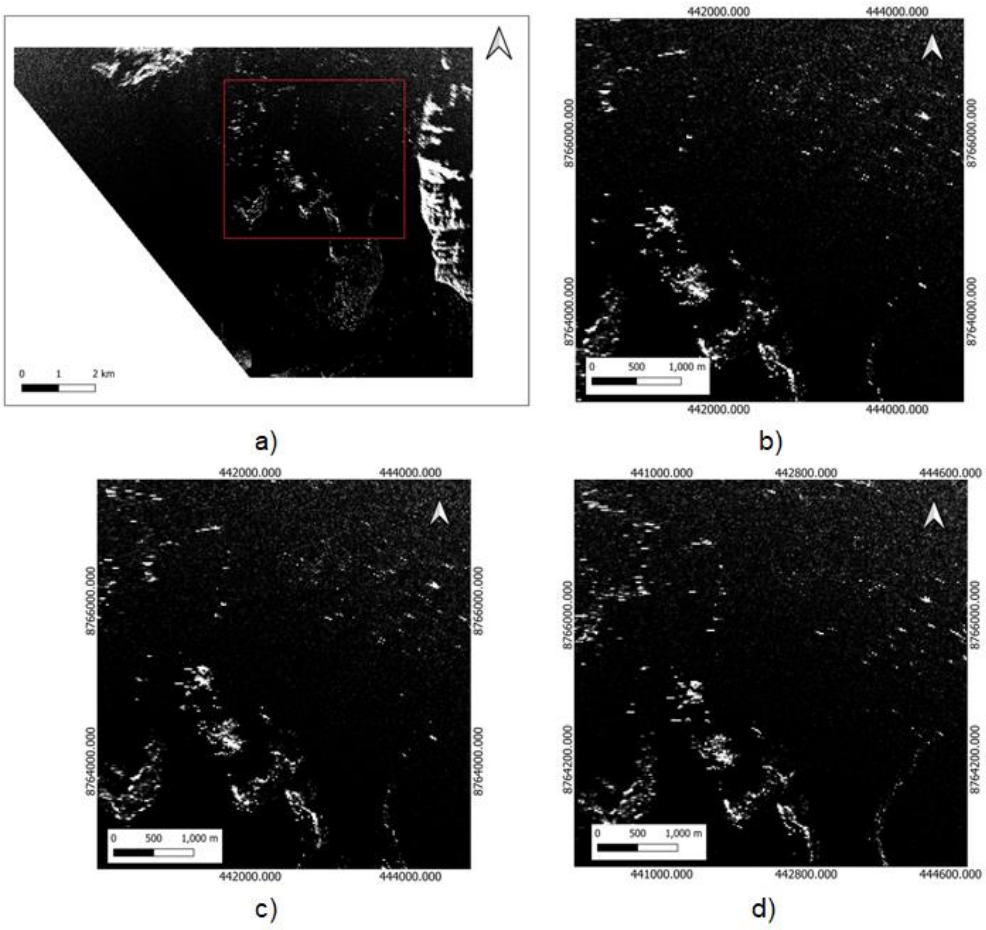

***Figure 6.3**: GPRI scene acquisition GIS coordinates **a**) full image, **b**) zoom 15th April, **c**) zoom 16th April, **d**) zoom 17th April*

***Table 6.2**: GPRI specifications*

Frequency (GHz)	***Operational Range (m)***	***Range Resolution at 1km distance (m)***	***Azimuth Resolution at 1km distance (m)***	***Transmit bandwidth (MHz)***	***Time span***
17.1-17.3	20-10,000	0.95	6.8	200	15-17 April

6.3.3. Meteorological Conditions

Meteorological data covering temperature, wind speed and direction can be found in Table 6.3. Data are taken from the nearby Ny-Ålesund weather station, and all data corresponds to the date and time of each image acquisition.

***Table 6.3**: Meteorological data from Ny-Ålesund weather station. Full coverage of data is available from YR, a service from the Norwegian Meteorological Institute and NRK (https://www.yr.no/nb)*

Image	Temperature (°C)	Wind Speed (m/s)	Wind Direction
20150415	-10	5.4	SE
20150416	-7.5	1.7	SSE
20150417	-7.1	7.3	ESE

6.4. Results:

6.4.1. Preliminary image analysis

Figure 6.4 shows the target and clutter masks we used for performing validation in each acquisition. Please note, some of the icebergs drifted and therefore we needed to derive their masks in different acquisitions.

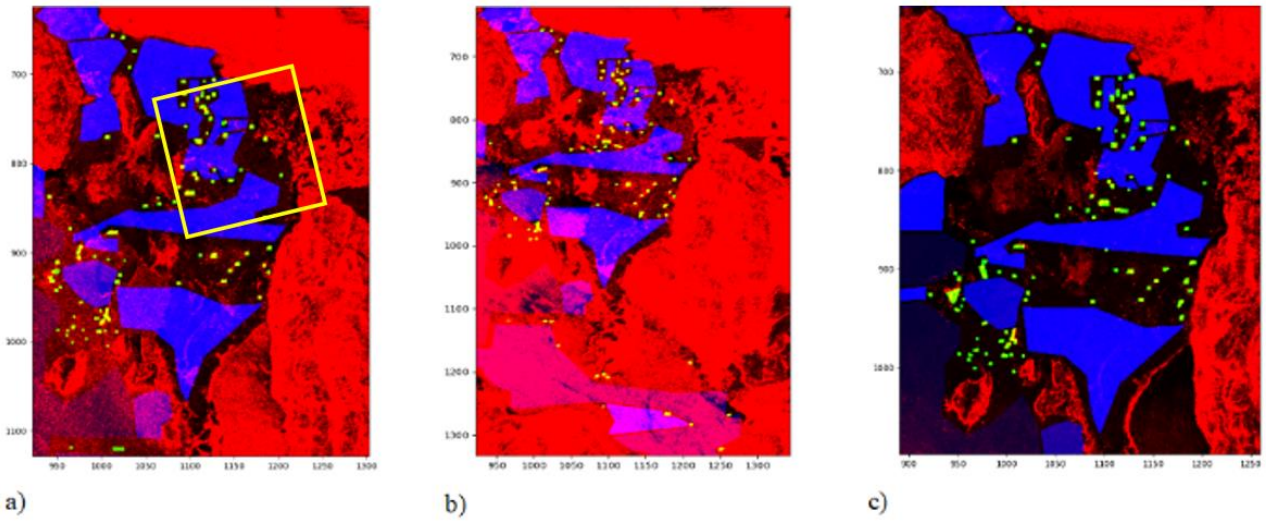

***Figure 6.4: a**) target and clutter mask ROI 15th April, **b**) target and clutter mask ROI 16th April, **c**) target and clutter mask ROI 17th April, blue areas mark clutter, green/yellow polygons indicate icebergs, yellow box indicated detection ROI.*

The SAR images clearly show that the icebergs are drifting in the fjord. The majority of the icebergs are densely concentrated just north of the archipelago, while some clusters are also found further east, and north-east.

6.4.2. Detector images.

The following figures show the detectors in a chosen region of interest (ROI). These images have been produced before thresholding is applied, in order to visualise the detection maps. In this way, it is easier to present a qualitative analysis of detection performance. Figure 6.5 depicts the iDPolRAD, DPolRAD, PNF and symmetry. Figure 6.6 shows detection image outputs for entropy, alpha, lambda1 and lambda2 which are the eigenvalues of coherency matrix **[T]**. Figure 6.7 shows the detection image outputs for OPD, PWF, and PMF. Please note, all the figures of each detector do not contain units.

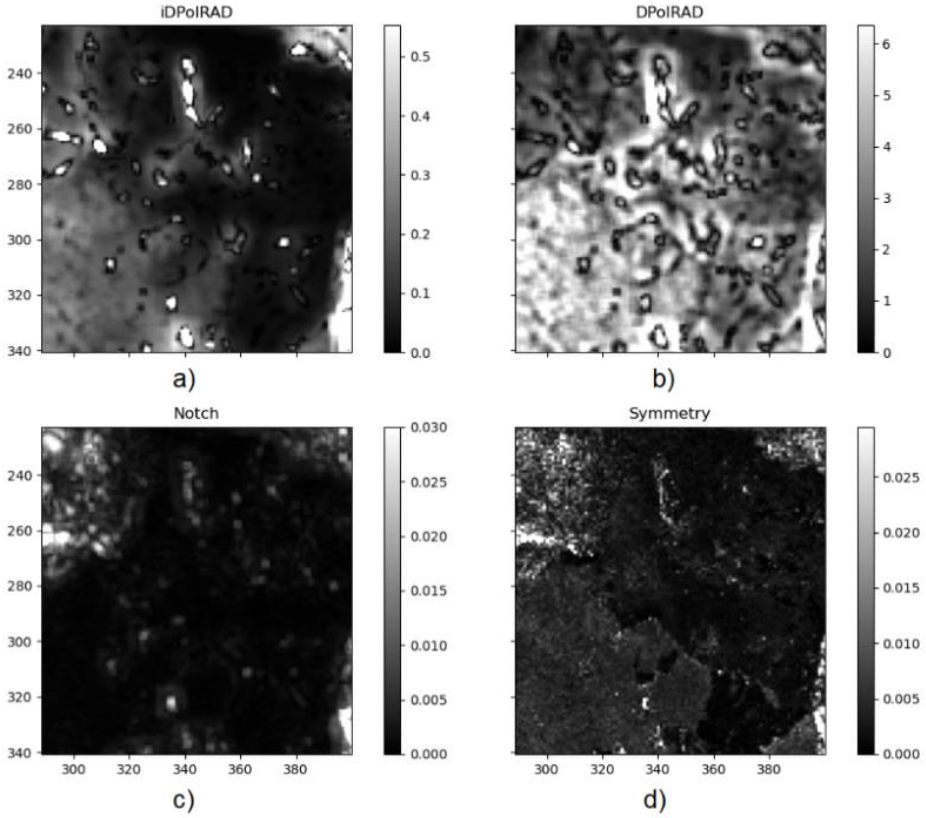

***Figure 6.5**: detection image outputs for ROI, April 15th, **a**) iDPolRAD, **b**) DPolRAD, **c**) polarimetric notch filter, **d**) reflection symmetry*

From Figure 6.5 we can see that the iDPolRAD and symmetry detectors tend to discriminate icebergs from the surrounding clutter best, followed by the DPolRAD and notch filter. In the DPolRAD and symmetry detectors, areas of sea-ice can also be observed, and it is likely that the number of false alarms will reflect this. However, it is possible to see that some of the icebergs seem to be missing.

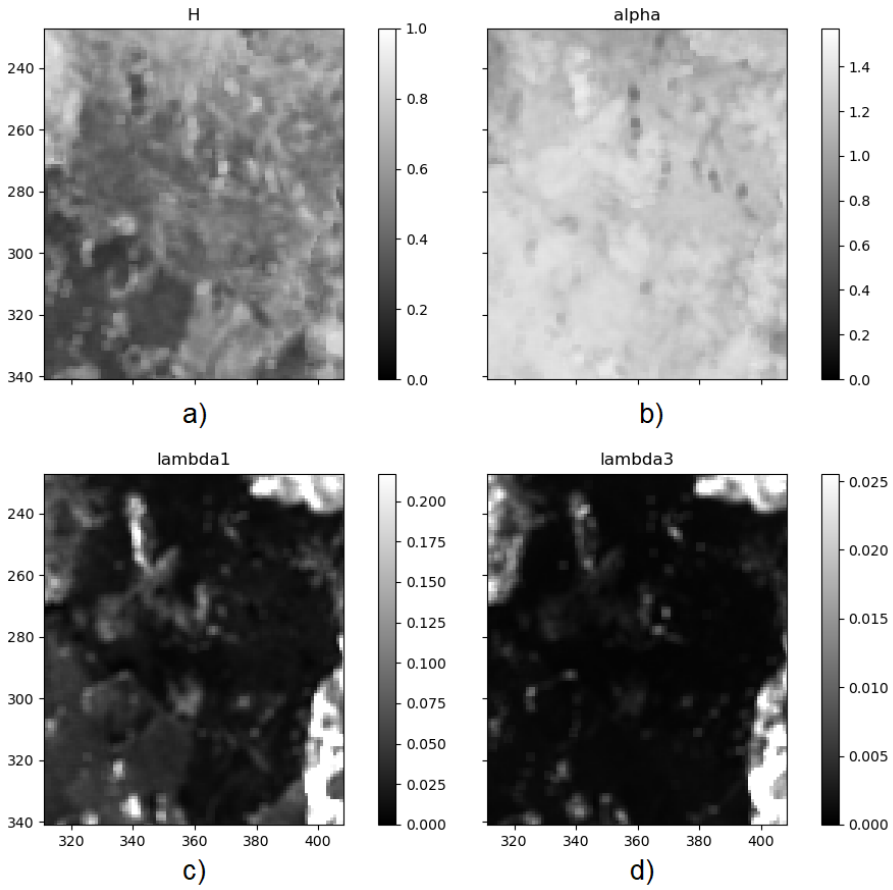

***Figure 6.6**: detection image outputs for ROI, April 15th, **a**) entropy, **b**) alpha, **c**) lamdba1, **d**) lambda2*

From Figure 6.6, initially it is evident that detection performance is weaker. In fact, it is very difficult to see icebergs in the entropy image and the alpha image, whereas lambda1 and lambda3 are able to distinguish some icebergs, though this appears brighter in lambda3. Since entropy and alpha are not really used for detection, it is only being used for comparison purposes.

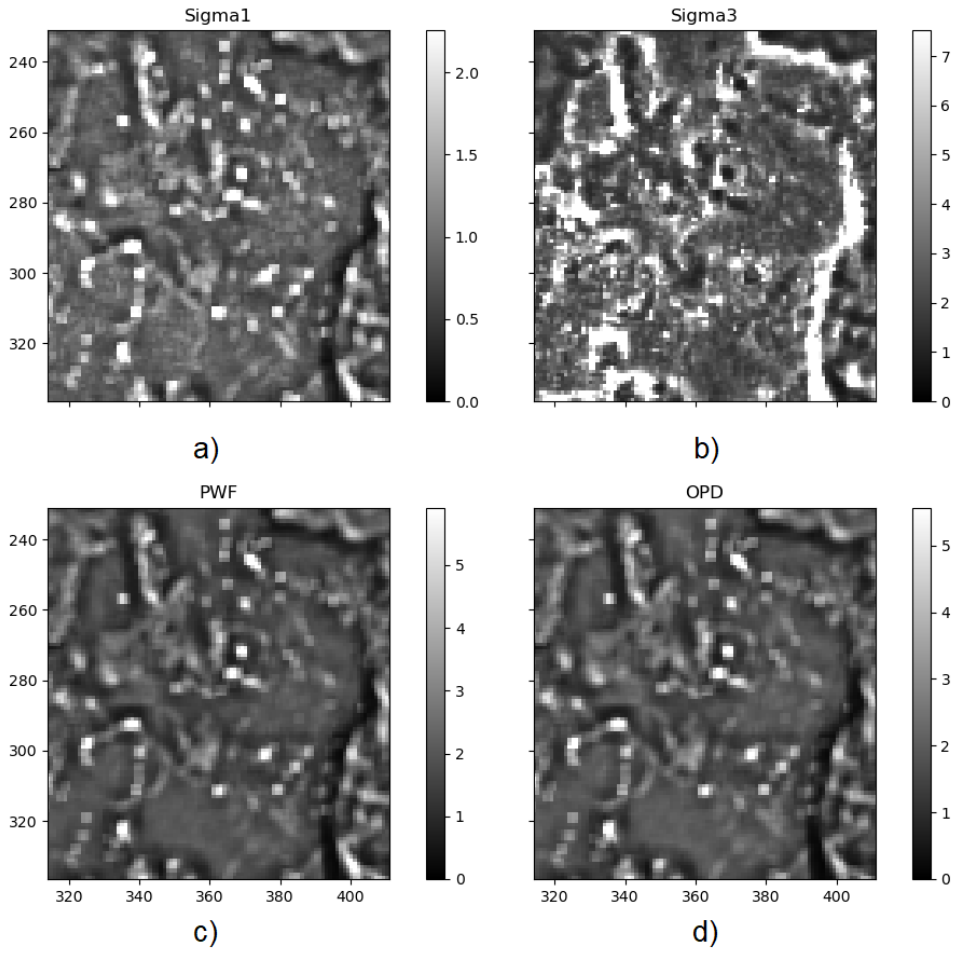

***Figure 6.7**: detection image outputs for ROI, April 15th, **a**) sigma1, **b**) sigma3, **c**) polarimetric whitening filter, **d**) optimal polarimetric detector*

In Figure 6.7, performances appear remarkably similar, particularly within sigma1, PWF and OPD. Here the detection is focused more on contrast enhancement, and icebergs are clearly visible in contrast to the surrounding clutter, although some sea-ice backscatter is bright within sigma1, making detection difficult. Visually it can be seen that the PWF and OPD seem to be better in isolating bright targets and making the background quite homogeneous. Also please note that the operations of the PWF, PMF, PNF and OPD present an unscaled observable, which is somehow normalised. This may show a flatter image to the eye, but the importance when it comes to detection theory is also the variation of target and clutter which impact their separability.

6.4.3. Detector performance ROCs

In this section, we present the ROC curves which show the Probability of Detection (P_D) against the Probability of False Alarms (P_F) for each scene. Figures

6.8-6.10 represents a ROC curve for the scene collected 15th April, 16th April, and 17th April respectively.

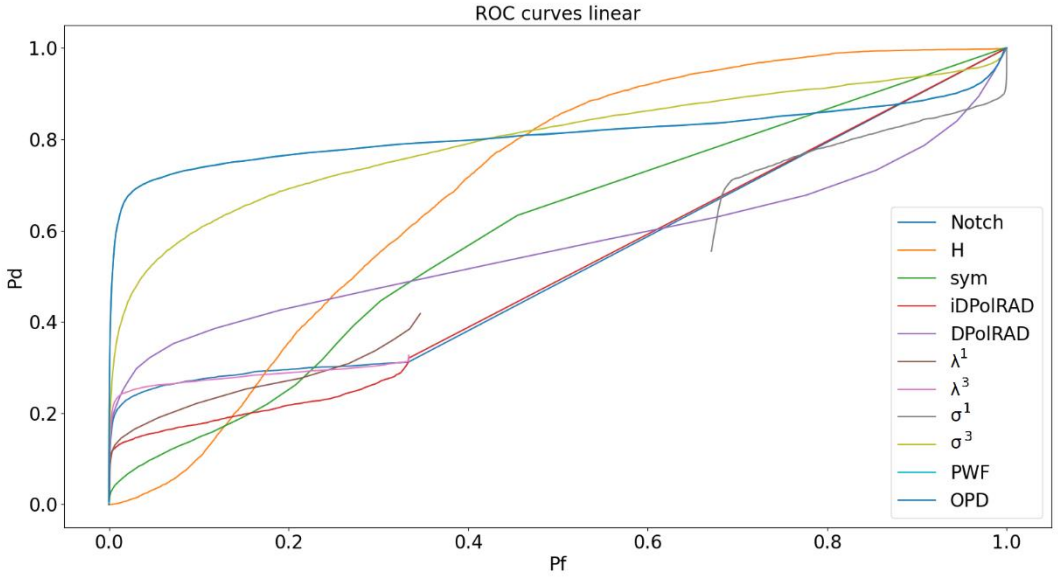

***Figure 6.8**: ROC curves for scene collected 15th April, note that Notch is polarimetric notch filter, H is entropy, λ^1 and λ^2 are the first and third eigenvalues of covariance matrix C, σ^1 and σ^3 are sigma1 and sigma3 of the polarimetric match filter, iDPolRAD is the dual intensity polarisation ratio anomaly detector, sym is reflection symmetry, PWF is polarimetric whitening filter and OPD is optimal polarimetric detector*

From Figure 6.8 we can clearly see that the detection performance is variable across all detectors. The behaviour of the detectors is different depending if we focus on low or high value of probability of false alarms. Please note that the PWF and OPD are showing the exact same ROC curve.

a) Low P_F: The PWF and OPD detectors perform very similarly with P_D values ranging between 0.5 and 0.7 for P_F between 0.01 and 0.1.

b) High P_F: when we relax the value for the false alarms to an unrealistic 0.5, the entropy shows the greatest detection performance.

Entropy cannot be used as a detector because sea-ice and dark open ocean are showing large values of entropy. In the case of the former this is due to the presence of several scattering mechanisms, for the latter due to the proximity of the noise floor. However, the entropy is also sensitive to the presence of smaller icebergs because these increase the number of scattering mechanisms in the

averaging cell. Therefore, if we move to practically unusable level of false alarms entropy is the only detector that spots the very small icebergs.

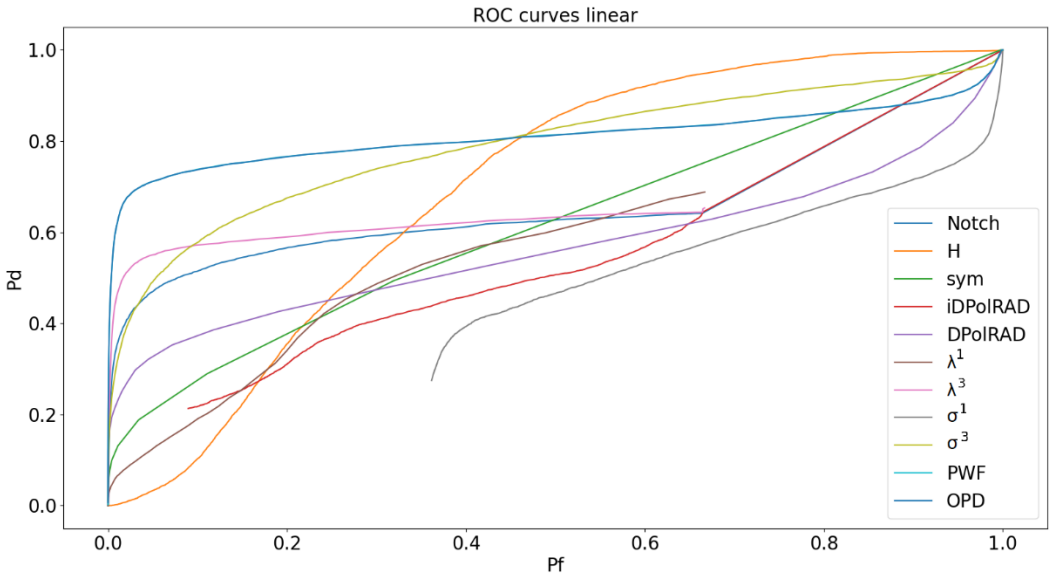

***Figure 6.9**: ROC curves for scene collected 16th April, note that Notch is polarimetric notch filter, H is entropy, λ^1 and λ^2 are the first and third eigenvalues of covariance matrix C, σ^1 and σ^3 are sigma1 and sigma3 of the polarimetric match filter, iDPolRAD is the dual intensity polarisation ratio anomaly detector, sym is reflection symmetry, PWF is polarimetric whitening filter and OPD is optimal polarimetric detector*

Figure 6.9 presents the ROC for the 16th April acquisition. Interestingly, the detection performance of the PWF have significantly improved with a P_D value of roughly 0.75 for P_F of 0.01 when compared to the scene collected on 15th April. However, performances of the other detectors, especially of the polarimetric match filter, notch filter, symmetry, eig1 and eig3 have substantially degraded. This is possibly a consequence of a higher sea-state condition on 16th April, producing a more heterogenous sea surface, and increasing the false alarm rate. Since the PWF detector is not based on contrast enhancement and target-to-clutter-ratio, but rather speckle reduction, it performs well to the surrounding clutter, suggesting good clutter estimation. A higher increase of sea-state activity and the presence of sea-ice explain the degraded performances in the iDPolRAD and DPolRAD detectors, which have low P_D values < 0.4.

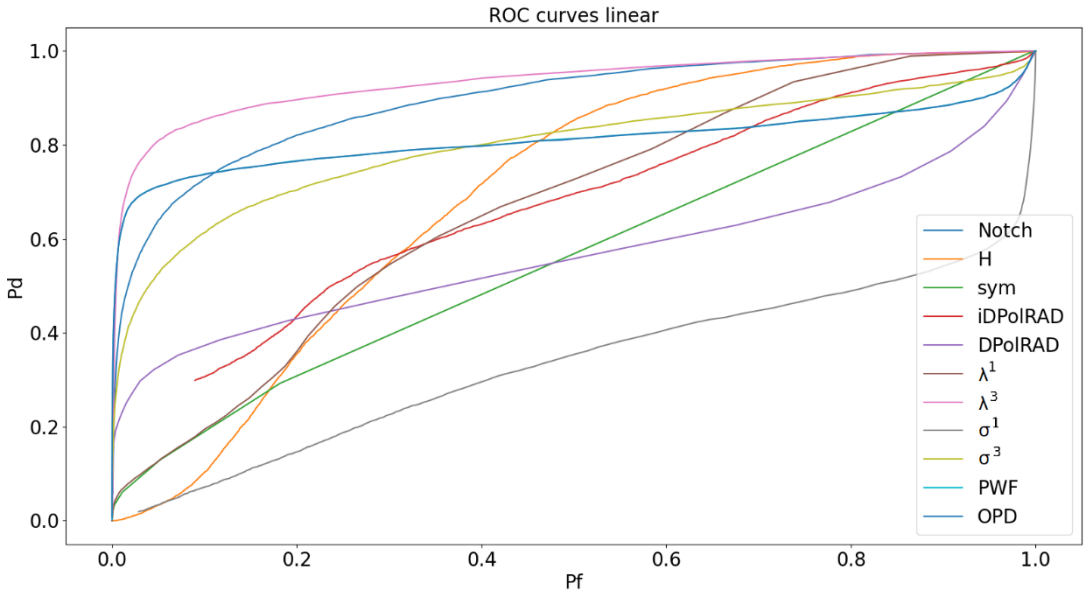

***Figure 6.10**: ROC curves for scene collected 17th April, note that Notch is polarimetric notch filter, H is entropy, λ^1 and λ^2 are the first and third eigenvalues of covariance matrix C, σ^1 and σ^3 are sigma1 and sigma3 of the polarimetric match filter, iDPolRAD is the dual intensity polarisation ratio anomaly detector, sym is reflection symmetry, PWF is polarimetric whitening filter and OPD is optimal polarimetric detector*

Figure 6.10 presents the ROC for the 17th April acquisition. Like in the previous scenes, the OPD and PWF detectors have a similar performance, giving P_D values of roughly 0.7. This is followed by PMF1 and eig1. Here, the iDPolRAD is among one of the top detectors with a P_D of roughly 0.75 when P_F is 0.15.

6.4.4. GPRI detection

As a preliminary analysis, in each ground radar scene, we consider a few examples of three icebergs and compare to the satellite data to look for evident differences. Figures 6.11, 6.12, 6.13, 6.14 and 6.15 represent ground and satellite images of a particular region of interest (ROI) from the same scene.

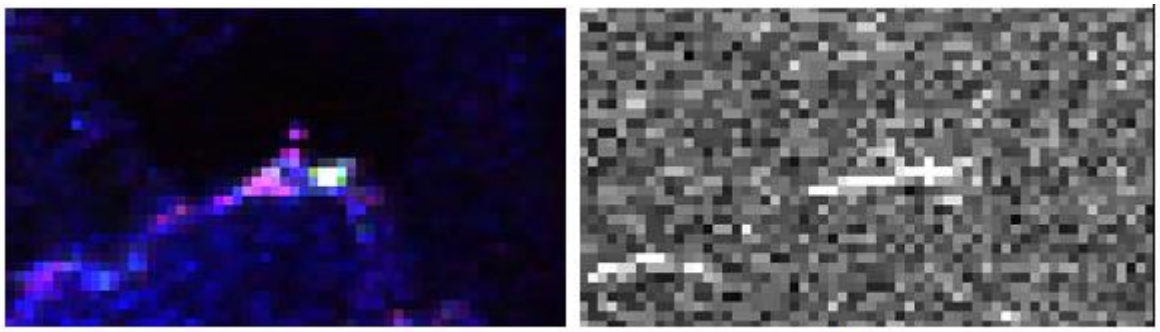

***Figure 6.11**: Iceberg backscattering comparison a) satellite, b) ground radar, coordinates for iceberg centre are 441411, 8766881.2, scale is 1:4105, and coordinate reference system is EPSG 32633*

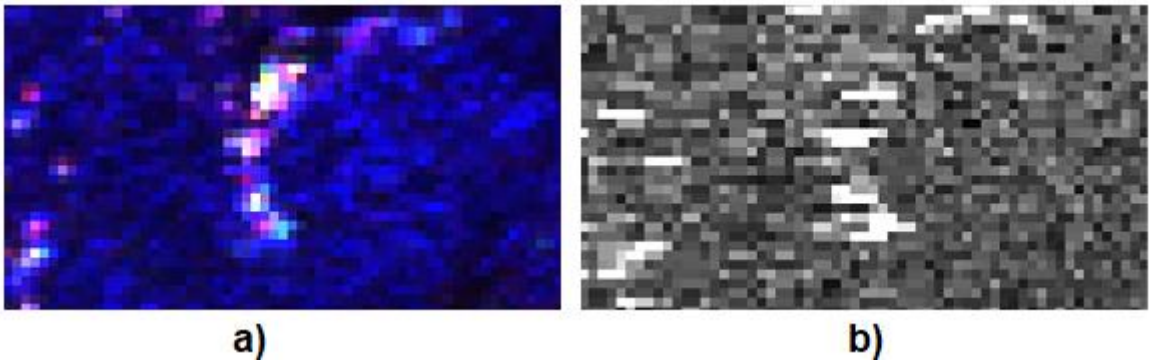

***Figure 6.12**: Iceberg detection comparison a) satellite, b) ground radar, coordinates for iceberg centre are 440732.4,8766551.8, scale is 1:4105, and coordinate reference system is EPSG 32633*

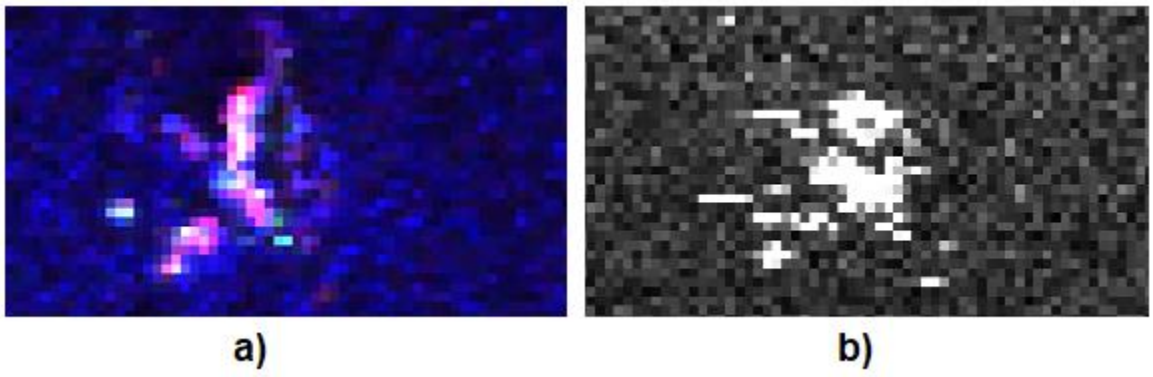

***Figure 6.13**: Iceberg detection comparison a) satellite, b) ground radar, coordinates for iceberg centre are 441331.1,8765102.4, scale is 1:4105, and coordinate reference system is EPSG 32633*

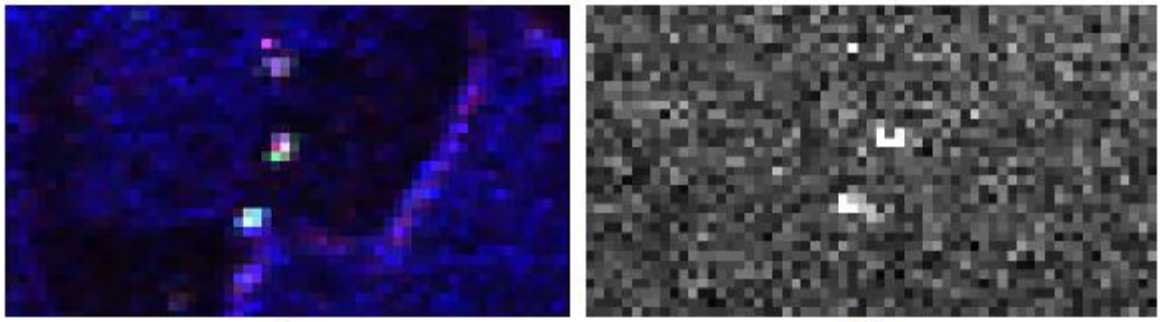

***Figure 6.14**: Iceberg detection comparison a) satellite, b) ground radar, coordinates for iceberg centre are 441552.3,8765779, scale is 1:4105, and coordinate reference system is EPSG 32633*

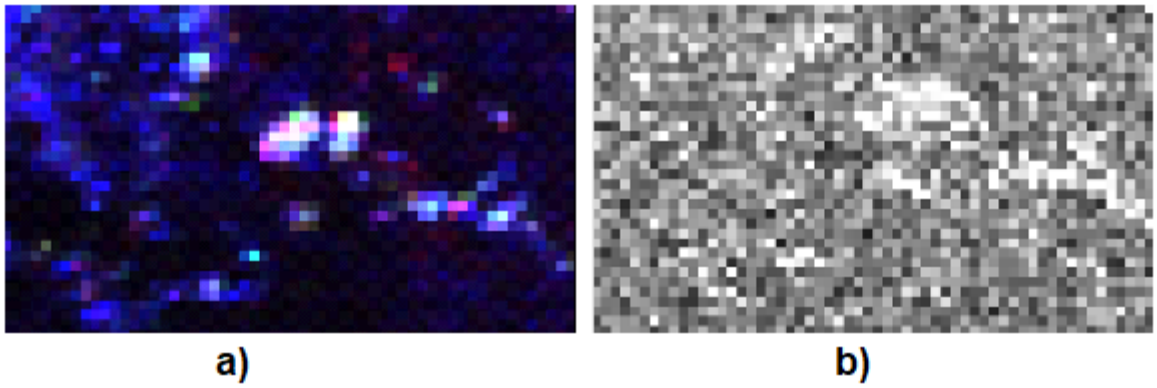

***Figure 6.15**: Iceberg detection comparison a) satellite, b) ground radar, coordinates for iceberg centre are 443131.2,8767761.9, scale is 1:4105, and coordinate reference system is EPSG 32633*

In all the corresponding ground radar images, we can see that the targets are more elongated and stretched in shape when compared to the icebergs in the satellite images. The icebergs in the ground image are also a lot brighter than the ones in the satellite images. This can be attributed to a series of causes:

a) higher (grazier) incidence angle in the ground images: a higher incidence angle may increase the iceberg backscattering by producing more double bounces and on the other side reduce the clutter scattering. However, this will not work if the iceberg is not significantly above sea level.

b) the across range (the equivalent azimuth for a moving platform) resolution of the ground radar is much larger than the range resolution. This makes the icebergs show as more elongated in shape due to focusing issues.

In the next section we perform a more quantitative comparison between the two systems evaluating the target-to-clutter-ratio.

6.4.5. Target-to-clutter ratio and backscattering

Boxplots are presented for analysis to show the difference in variation between mean and max TCR values for satellite images (Figures 6.16, 6.17 and 6.18) and ground images (Figure 6.19). In addition to this we also plotted backscatter values against the area of the icebergs to evaluate if larger icebergs are prone to have larger backscattering. A selection of the scatter plots is presented in Figure 6.20. Here we only show scatter plots where the correlation coefficient is bigger than 0.5. The plots also show a linear regression, to aid the visual interpretation of the data. However, we do not suggest using linear regression to estimate size of icebergs from backscattering due to the low R squared values. The value for the correlation is presented in Table 6.3.

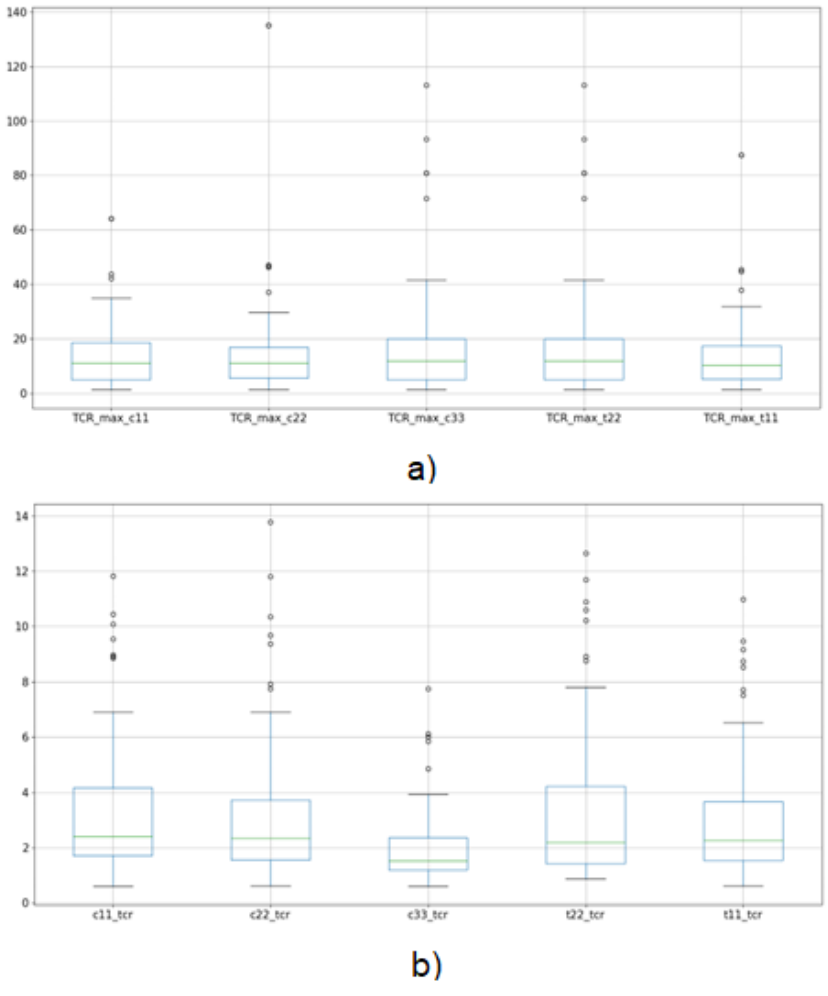

***Figure 6.16**: Satellite TCR mean and max boxplots 15th April, plots from left to right: C11 channel, C22 detector, C33 channel, PWF detector, OPD detector, T22 channel. Small circles indicate outliers, green line indicates average value, the box shows the interquartile range*

From Figure 6.16 no distinguished pattern appears for mean TCR, but variation is apparent in max TCR as well as numerous outliers. The C33 channel appears to remain constant between mean and max TCR, indicating no real change in TCR during this date.

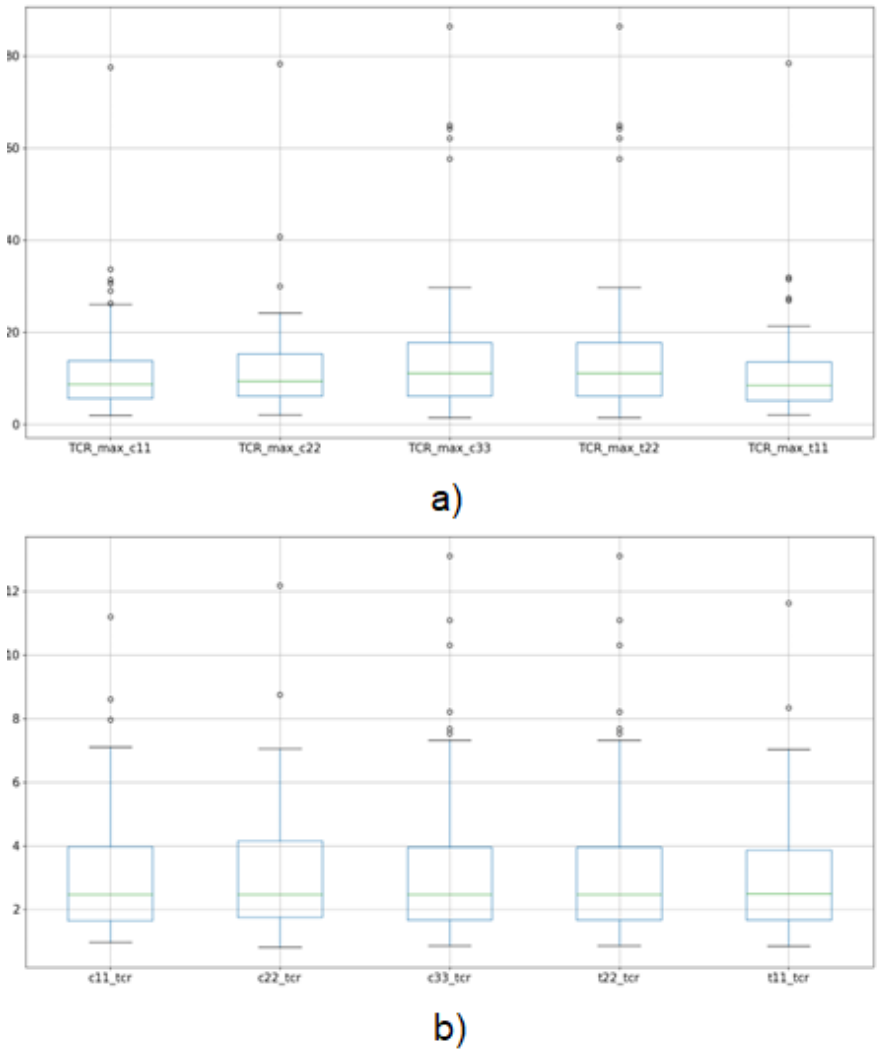

***Figure 6.17**: Satellite TCR mean and max boxplots 16th April, plots from left to right: C11 channel, C22 detector, C33 channel, PWF detector, OPD detector, T22 channel. Small circles indicate outliers, green line indicates average value, the box shows the interquartile range*

Figure 6.17 shows a similar outlook for mean TCR, while the max TCR has increased in range but remained constant across all channels. There are also less outliers for this date.

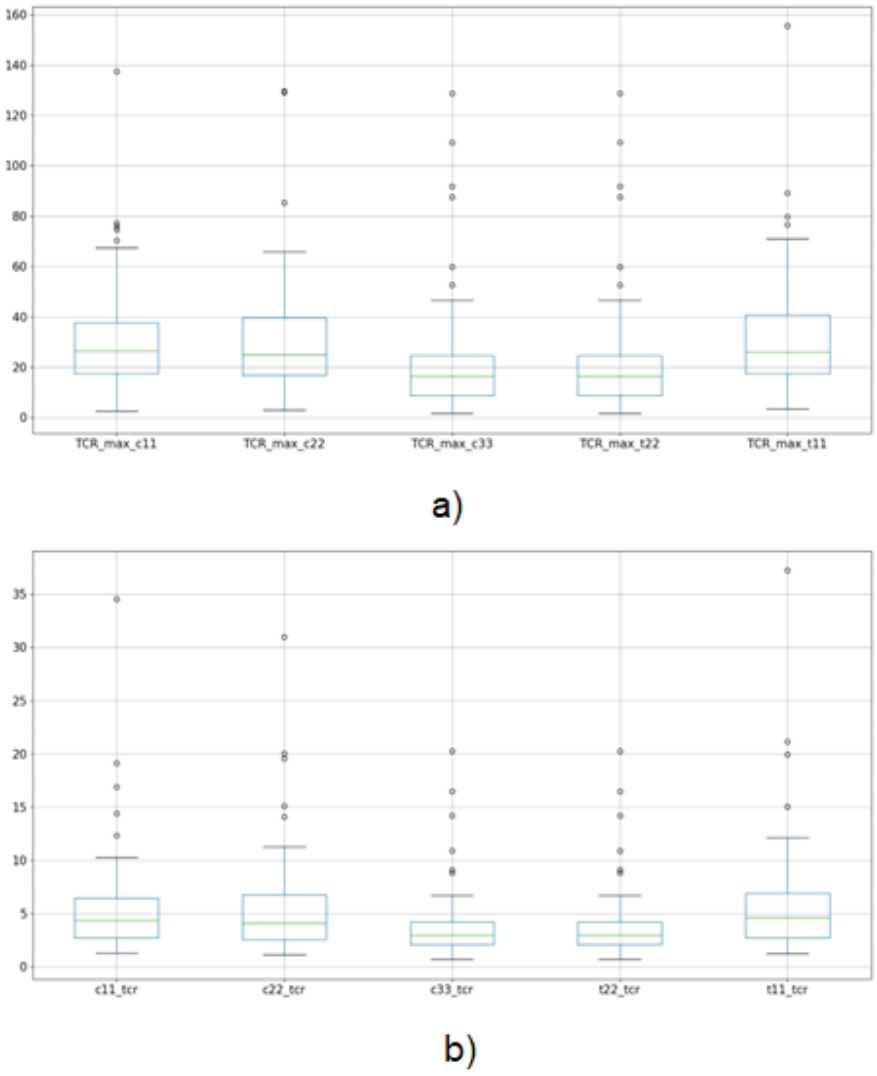

***Figure 6.18**: Satellite TCR mean and max boxplots 17th April, plots from left to right: C11 channel, C22 detector, C33 channel, PWF detector, OPD detector, T22 channel. Small circles indicate outliers, green line indicates average value, the box shows the interquartile range*

Figure 6.18 shows a variation in mean TCR, where the C33 and T22 channels have a lower range, while the other three channels are constant. The same pattern is found in the max TCR for this date. When compared to the satellite results, the ground-based results in Figure 6.19 show almost no range for mean TCR, and only a small range for max TCR as well as minimal outliers. This indicates that the ground data validation is consistent with the one of satellite data.

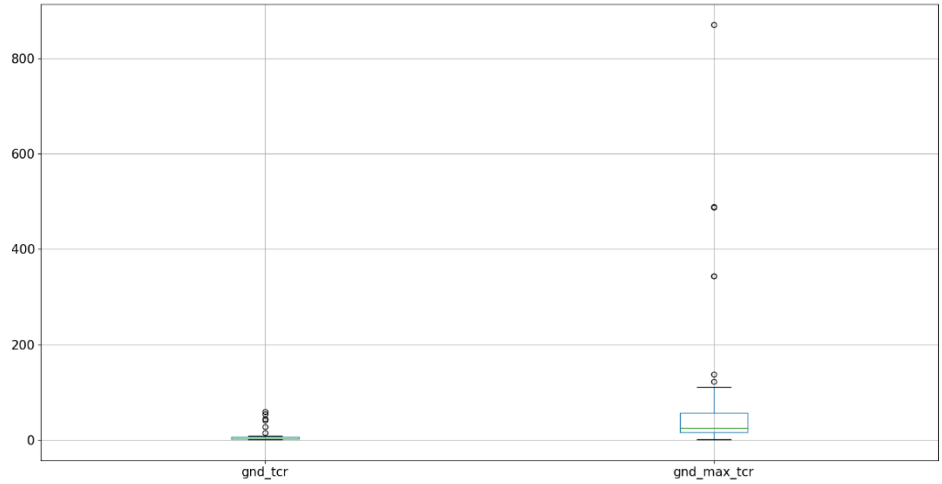

a)

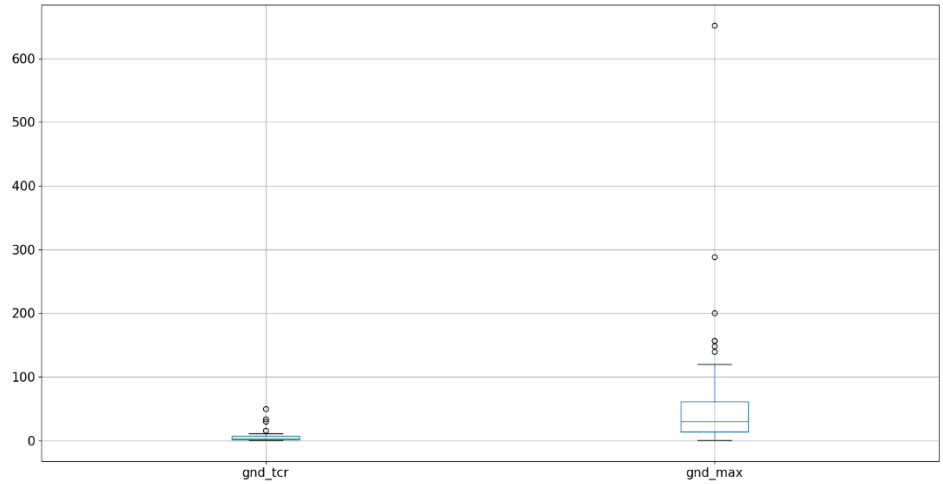

b)

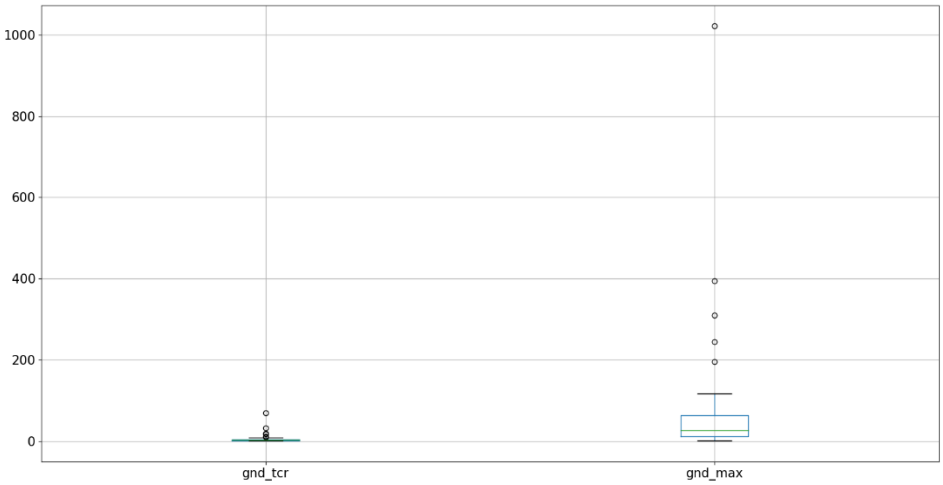

c)

Figure 6.19: *Ground TCR boxplot 15th April, from left to right: mean TCR, max TCR. Small circles indicate outliers, green line indicates average value, the box shows the interquartile range*

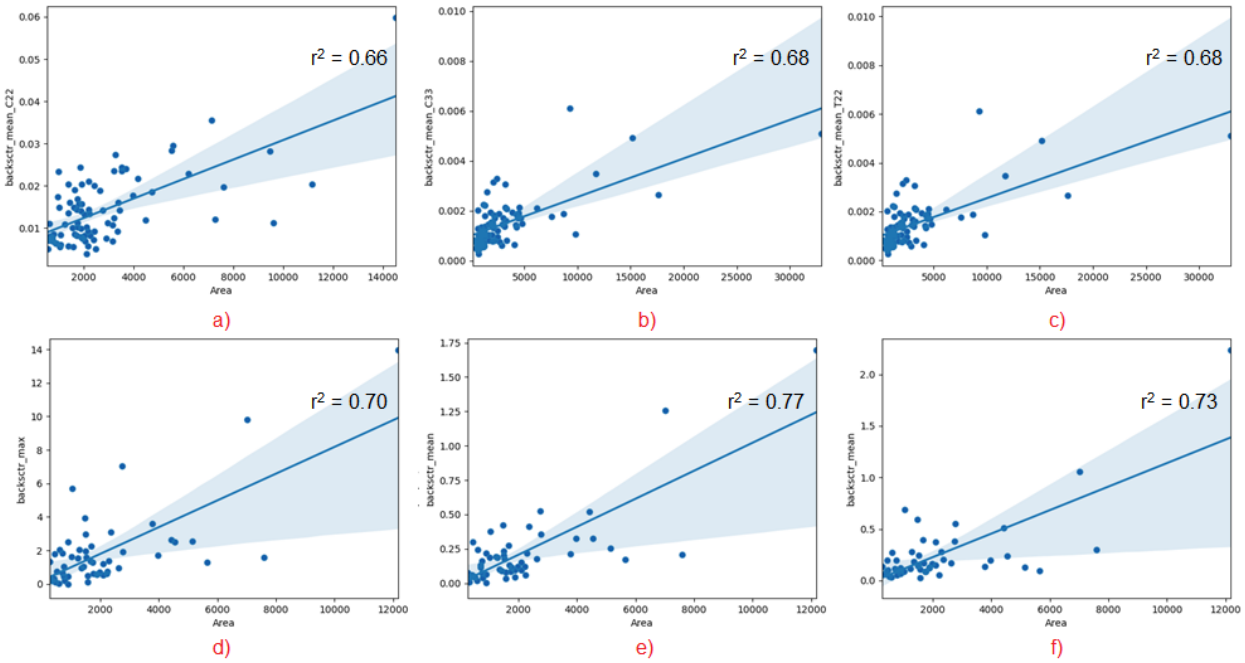

Figure 6.20: *Iceberg area versus backscatter plots a) mean satellite C22 channel 16th April, b) mean satellite C33 channel 16th April, c) mean satellite T22 channel 17th April, d) max ground 15th April, e) mean ground 15th April, f) mean ground 17th April, blue line indicates linear regression value, blue area indicates confidence interval with 95% significance level.*

6.5. Discussion:

6.5.1. Detection performance

In Figures 6.8-6.10, the best detection performance on 15th April is PWF and OPD with P_D = 0.5-0.7 for P_F = 0.01 and P_D = 0.75 for P_F = 0.05 on 16th April. The best detection performance on 17th April is the eig3 with P_D = 0.81 for P_F = 0.1 followed by the OPD with P_F = 0.7 for P_F = 0.1. One possible explanation for different performance during the dates is most likely the variation in meteorological and oceanographic conditions. Given that the scene collected on 16th April shows a relatively calmer sea-state, the detection is easier. Indeed, previous papers have documented the sea-state and the effect on detection performance (Akbari and Brekke, 2017b; Barbat *et al.*, 2019).

The entropy tends to be able to detect more icebergs when we relax the P_F to values that are completely unpracticable for use. Interestingly, we find that although the best detectors are the PWF and OPD, they cannot detect 20% of the icebergs. The only way to detect this remaining 20% is to use a detector like the entropy given a higher P_F value of 50%.

6.5.2. TCR

The results of TCR in Figures 6.16 to 6.19 provide an insight on the separability of target and clutter in backscattering images. The plots show that the majority of icebergs can be easily distinguished from the surrounding open water and sea-ice clutter background, particularly when the iceberg is within a cluster, or close to the archipelago in the centre part of the fjord. However, towards the far inner end of the fjord, icebergs start to meet sea-ice fields as well as smaller fragments of ice broken off the Kongsbreen and Kronebreen glaciers. This may contribute to the huge variation of TCR values seen within the fjord, particularly within the OPD and PWF plots.

When we compare the satellite results to the GPRI results, there are further increased values for the ground radar. A probable reason may be due to the incidence angle which increased iceberg double bounce and reduced surface scattering from sea and sea ice (Section 6.4.). We need also to keep in mind that the frequency is also different, although we would expect that the clutter would be enhanced in Ku-band by the same amount the icebergs would be.

Interestingly, we find that the TCR values differ depending on each of the polarimetric channels. For example, mean TCR values in the HV and HH channel are roughly similar on 15th April but HV values are higher on other dates This is in line with a previous finding which reported that the cross-polarisation channel HV is able to better distinguish icebergs than channels HH and VV due to a lower surface scattering from sea and sea ice found in HV (Bailey and Marino, 2020).

6.5.3. Correlation between backscattering and iceberg size

The results from the correlation graphs in Figure 6.20 and Table 6.3 also suggest that correlation with iceberg size is not straightforward. The linear fit is only for visual aid, and we are not proposing this as a valuable scattering model. The correlation using the mean over a small area of the icebergs is generally higher than the one using the maximum inside the same search window. This seems to corroborate the fact that the presence of single bright scatterers on icebergs may be not strongly correlated with the size. The overall size may not be impacting what we see in a small box over the iceberg. Considering averages is therefore suggested to improve correlation. Finally, the fact that the correlation is not very high suggests that algorithms to retrieve iceberg size may be better directed to extract dimensions using

some Computer Vision methodology rather than regressing based on backscattering values.

***Table 6.3**: TCR linear regression correlation values for satellite and ground images*

Satellite	**15/04**		**16/04**		**17/04**	
Backscatter	**Max**	**Mean**	**Max**	**Mean**	**Max**	**Mean**
C11	0.27	0.49	0.55	0.64	0.31	0.54
C22	0.25	0.47	0.55	0.66	0.28	0.57
C33	0.20	0.38	0.19	0.38	0.40	0.68
T11	0.30	0.49	0.56	0.65	0.31	0.55
T22	0.20	0.38	0.19	0.38	0.40	0.68
Ground						
TCR	0.70	0.77	0.17	0.50	0.65	0.73

Backscatter correlation with iceberg size is shown to be higher in ground images, as a result of a shallower incidence angle. Since the main scattering mechanism here is likely to be the double bounce a larger iceberg may imply a larger position above the water and therefore a bigger double bounce. This was less visible using satellite data due to the different incidence angle and the fact that icebergs appear mostly as surface scattering.

6.5.4. Limitations

The methods presented in this chapter are open to a few limitations. The calculation for iceberg area may not reflect actual surface area because of SAR distortions. The calculations for area may therefore not be fully accurate, and this may influence on TCR results. Previous work by Akbari and Brekke (2017a) shows that iceberg area is also calculated using the same approach. To avoid this problem, working with different incidence angles may be an option. It may be possible to identify the same iceberg in differing images that are acquired with different incidence angles, and then take the average area for each iceberg to account for various SAR distortions. However, this may not be practical. Another option would be including a step in image processing that corrects geometrical distortions caused by differing

incidence angles. Terrain correction is also not considered in Akbari and Brekke, (2017b) since the focus is on ocean regions. An increase in radar look angle direction may also increase the sea clutter, which may reduce the contrast between the clutter and icebergs.

The meteorological data obtained for this work is limited in that it was only available on an hourly basis. Wind speed and direction can change very quickly, and this can influence detection results, especially if the backscattering is closer to the noise floor. Nonetheless, Akbari and Brekke, (2017a) also use similar meteorological data for iceberg detection. However, no mention of limitations attributing to a lack of real time meteorological data are provided.

6.6. Conclusion:

In this work, we tested six state-of-the-art detectors with both a RADARSAT-2 and GPRI dataset on icebergs in Kongsfjorden, Svalbard. These detectors are the dual intensity polarisation ratio anomaly detector (iDPoLRAD and DPoLRAD), polarimetric notch filter (PNF), polarimetric match filter (PMF), reflection symmetry (sym), polarimetric whitening filter (PWF) and optimal polarimetric detector (OPD). Detection performance was estimated over three quad-polarimetric C-band RADARSAT-2 single look complex images, each collected between 15th and 17th April 2016. To validate the data, we also use three GPRI images of the same area, collected synchronously. We show that the OPD and PWF detectors provide the best detection performance, even when factors such as sea-ice cover, sea-state, and homogeneity are considered. P_D values range from 0.5-0.7 on 15th April during a choppy sea-state for a P_F of 0.01, to 0.75 on 16th for a P_F of 0.05. On 17th April where the sea is calmer, the eig3 shows the best performance with a P_D of 0.81 when the P_F is 0.1. TCR values showed major variation, because of factors such as polarimetric channels, window size of pixel area, and sea-ice activity towards the inner part of the fjord. Overall, this study contributes the potential of PolSAR data to identify icebergs in interchangeable and challenging conditions. Given that the limitations of this work include small incidence angles, future work could be focused on the use of higher incidence angles to compare multiple scattering mechanisms in the area.

Contributions

Conceptualisation, J.B., V.A., and A.M.

Methodology, J.B.

Software, A.M., J.B., and V.A.

Validation, J.B., A.M., and V.A.

Formal analysis, J.B.

Investigation, J.B

Resources, A.M., V.A.

Data curation, J.B.

Writing—original draft preparation, J.B.

Writing—review and editing, J.B, A.M, T.L., A.D, T.R., and V.A.

Visualisation, J.B.

Supervision, A.M and V.A.

Project administration, J.B.

7.0. DISCUSSION

7.1. General Discussion

A key major finding from this thesis is that target entropy, a parameter found from utilising the Cloude-Pottier eigenvalue/eigenvector decomposition, is not sufficient to be able to classify icebergs as single targets or partial targets. While there are no previous studies that use an entropy detector on icebergs, entropy was found to be adequate for ship detection (Touzi *et al.*, 2004). But in this thesis, we show that entropy is unsuitable and must be applied with caution because of multiple factors. Firstly, the window size of the image is important; this goes back to pre-processing steps during the multi-looking stage. An increasing window size introduces more image pixels, consequently, this will produce a better estimation as long as the target remains homogeneous. However, icebergs do not seem to follow this category since they are only homogeneous in patches. When the window size becomes larger, one could start including the nearby sea surface, which can be modelled using Bragg scattering. This surface scattering component may increase the entropy. On the other hand, the double bounce component is located in one area of the iceberg (at the corner). When this is included in the averaging window, the entropy is likely to rise. The icebergs analysed in this work seem to be homogeneous in patches and therefore the window size should be kept smaller than the size of these patches to prevent any bias of the polarimetric estimation. On the other hand, we cannot reduce the window too much or we will not filter out noise and the entropy will be biased toward one. For detection purposes, it is notable that false alarms are a lot higher. Results from Marino *et al.* (2013b) show that for ship detection, the entropy detector suffers from a high number of false alarms due to noise caused by low backscattering levels in seawater.

Additionally, environmental, and meteorological conditions may affect the entropy. This can happen when there is liquid water on top of the iceberg which may reduce the scattering from the iceberg, thus increasing the entropy due to noise floor issues. This may happen in the following ways: surface liquid water on the icebergs as a result of precipitation or a snow layer accumulated on top of the iceberg surface which has melted, choppy sea which can throw up spray and water onto smaller iceberg surfaces, the wind speed which can blow surface liquid water off an iceberg if strong enough, or simply the iceberg itself having toppled over so that the dielectric

constant of the iceberg surface is now increased. Any presence of surface liquid water could add specular scattering mechanisms.

The second major finding from this thesis is that when it comes to iceberg detection, the traditional detectors in our work perform relatively well for larger icebergs, but poorly when the icebergs are smaller and surrounded by sea ice floes. When the backscattering from icebergs is too weak (e.g., because they are too small) adding polarimetric information can boost detection performance and decrease the probability of false alarms. The reason is possibly linked to the fact that although surface scattering is often the dominant scattering mechanism for icebergs, there are more scattering mechanisms composing the final iceberg return. However, previous work also shows that polarimetric behaviour can make detectors unsuitable in the case of a high signal to noise ratio, particularly when values of backscattering are close to the noise floor (Dierking and Wesche, 2013; Marino *et al.*, 2013b; Marino *et al.*, 2016b). Adding additional polarimetric information should therefore consider potential effects on signal to noise ratio.

This is true for icebergs embedded in sea ice as well. Sea ice floes are mostly dominated by surface scattering. Because sea-ice does not form from glaciers it tends to be less irregular or jagged in shape and its dielectric constant is very high due to the presence of salt in water. This makes the penetration depth very small (Hajnsek *et al.*, 2021). Smaller sea ice floes such as slush and nilas tend to float with the ocean waves and therefore should have a higher surface scattering component whereas an iceberg trapped in an area of sea ice may have a second volume scattering component or double bounce component. Finally, if we have a scenario where icebergs are embedded within sea ice, if a volume scattering mechanism were to be present, this would help evaluate detection capabilities. Detecting icebergs embedded within sea-ice however is still currently very difficult, so this finding needs to be interpreted with caution. Better ground truth data of the area would help to validate such results.

Our results using ALOS-2 and RADARSAT-2 data show that the Optimal Polarimetric Detector and Polarimetric Whitening Filter are the best detectors in a scenario involving detecting icebergs in an open water setting. With ALOS-2 data, the P_D values for OPD and PWF are 0.99 when the P_F is set to 10^{-5}, and with RADARSAT-2 data, these values are 0.75 indicating that sea-state conditions or incidence angle did not have a notable effect on the ALOS-2 and RADARSAT-2 data

used. In icebergs embedded within sea ice, the results using ALOS-2 data degraded and OPD and PWF detectors showed P_D values of 0.71 and 0.69. In fact, eig3, the third eigenvalue of the Cloude-Pottier decomposition had the best performance (P_D = 0.90). It is likely that this eigenvalue is very low on targets predominantly characterised by surface scattering (ocean and sea ice), but it is still high on icebergs which are a composition of many different scattering mechanisms. Many powerful detectors that have been designed or tested on icebergs embedded within sea ice still have major difficulty with high false alarm rates (Marino and Hajnsek, 2012; Marino, 2013; Marino *et al.*, 2013b), suggesting that the combination of a detector and a polarimetric decomposition to determine scattering mechanisms, would be best for identifying icebergs in sea ice.

A third important finding of this work is related to the polarimetric mode employed. In Chapter 5, it was established that the quad-pol data obtained with ALOS-2 PALSAR contributed to the best detection performance. To evaluate different modes, we also compared with detectors using dual-pol modes. Overall, dual-pol data leads to a degraded performance compared to that of the quad-pol studies. This finding is backed up by Marino *et al.* (2016b). The authors proposed the iDPolRAD detector and tested it on dual-pol data using Sentinel-1. They concluded that performance would be better enhanced if the use of quad-pol data were added. For scenarios such as open ocean, the change in performance between quad-pol and dual-pol is very limited, suggesting that dual-pol data can be applied to scenarios involving open ocean for specifically this purpose. But when the scenario becomes more complex, discrimination capability is reduced because of a lack of polarimetric information. Thus, quad pol data is ideally preferred in terms of detection capabilities. However, situations in which dual-pol might be a better option include the capability to cover larger areas and smaller computational requirements. Until quad-pol technology with a large swath becomes available, it is impractical to use quad-pol for operational use. Currently the only available option for operational use with a large swath is dual pol.

Lastly, an important note is that results in Chapters 4 and 5 need to be taken with some caution compared to results in Chapter 6. This is due to a lack of good quality ground truth data for the Greenland study site, which is a limitation for this work. In contrast, in Kongsfjorden we were able to validate all icebergs situated in the

fjord due to availability of ground radar images. This has important implications for future work within this field, which we now turn to.

7.2. Implications

Iceberg detection and classification will continue to be developed as future satellite missions are launched. Some important questions that are necessary to answer include a) how should a future satellite system look like, and b) does the frequency band affect detection performance? In this section, we address these questions more broadly in terms of wider implications.

In previous work focusing on iceberg detection, we found that a common limitation is that multiple polarimetric imaging modes can only utilise a narrow swath width (Denbina and Collins, 2012; Marino *et al.*, 2016b). When mapping locations of icebergs, it is vital to image as large an area as possible. This provides a wider range of locations for shipping and ice forecasts. Currently, a quad-pol imaging mode on SAR instruments requires twice the repetition frequency, power, and data acquisition rate. The only way to keep power usage constant in quad-pol is to decrease the swath width, which in turn decreases the available coverage of data. For this reason, current spaceborne platforms offering data for iceberg services such as from the Canadian Ice Service use dual-pol SAR. The work presented in this thesis utilises ALOS PALSAR, and RADARSAT2, which each have swath widths 20-60 km, and 25 km respectively. While some of the detectors use a dual-pol system (iDPolRAD, notch filter, and reflection symmetry) the probability of false alarm is still too high for challenging environments such as icebergs embedded within sea ice. It is also notable that a narrow swath width means that for a SAR satellite acquiring a footprint over a particular ROI, the same satellite would not pass over for another few days. This information explains why several agencies and services that provide earth observation data are pushing towards future spaceborne platforms which have quad-pol with a larger swath width. Not only would this increase the coverage of data available but would also decrease the time taken for a satellite to acquire such data. Examples of such future satellites include ROSE-L (ESA) or Tandem-L (DLR).

Our iceberg detection results are obtained in two different frequency bands. We have used L-band for classification and detection, while we have used C-band while for detection only. Previous work which used C-band SAR found penetration depths within icebergs to be less than 15 m. This is supported by the fact that volume

scattering behaviour can occur within discontinuities of the top layer. Dierking and Wesche (2013) found that as long as icebergs have not toppled over, they exhibit a large volume scattering component. However, it should be noted that they selected two locations in Antarctica; their results are based on icebergs calving from ice shelves. The results of this thesis documented larger surface scattering contributions than other previous works. This is due to the nature of Arctic icebergs being much more irregular in shape and very prone to toppling over. Penetration depths in our work are much higher at L-band than at C-band. Comparatively, our results also show a high volume scattering contribution, but this is more likely due to less surface water in some locations. Future spaceborne platforms should consider an L-band wavelength for classification of Arctic based icebergs (like ROSE-L).

Detection performance in C-band and L-band revealed some interesting observations. RADARSAT-2 C-band results for PWF and OPD show P_D values of 0.75, compared to 0.99 for both detectors using ALOS-2 L-band. This suggests that L-band would also be better suited for detection work. Previous work supports this observation, as many results show higher false alarms at C-band. Karvonen *et al.* (2021) showed an average false alarm rate of 30.1% based on 2059 icebergs and three detectors. Comparatively, Marino *et al.* (2013b) showed an average false alarm rate of 2.6% based on 38 vessels and five detectors. It should be noted that while the detection targets were different in these studies, the false alarm rate using L-band SAR was clearly lower. Previous work on iceberg detection using L-band SAR and showing lower false alarm rates is not available because of no validation data (Marino *et al.*, 2016b). Based on these studies and the work of this thesis, a future recommendation for iceberg detection in non-challenging conditions such as open water would be more L-band spaceborne platforms. For challenging conditions, it is not possible to make a suitable recommendation.

7.3. Study limitations

This thesis presents a number of limitations in terms of the methods used. Here we explain some of these non-technical limitations.

It is notable that the number of images used in each data chapter is fundamentally small. This is due to two explanations. Firstly, the high spatial resolution of satellite SAR images requires a large CPU for processing. Secondly, the number of data acquisitions available in each study location is lacking. The data

processing stage therefore required a large amount of time to complete. One solution could be processing subsets of each image. However, this method may take up an even larger amount of time and it would not be practical to represent these subsets as separate images/scenes. A larger amount of storage space and CPU power is required to process these high-resolution SAR images more rapidly.

The overall visual identification of icebergs in all SAR images introduces the potential for human error. Sometimes it is not possible to identify a particular target as an iceberg, particularly in areas that also contain sea ice floes. The segmentation method described in Section 3.4.1 has not been automated in the same way as some studies on iceberg and ship detection use computer algorithms to fully automate the process. For example, Akbari and Brekke, (2017a) use an unsupervised automatic segmentation method through a finite mixture model which is produced from a computer algorithm. Thus, a more automated approach would eliminate erroneous iceberg identification. However, this also requires an increase in CPU for processing.

8.0. CONCLUSIONS AND FUTURE WORK

8.1. Summary and concluding remarks

Satellite Earth observation data has been utilised for cryosphere and oceanographic applications in both the Arctic and the Antarctic polar regions. The ability of SAR satellites to penetrate cloud cover and provide 24-hour quasi real time data makes remote sensing of these regions accessible for applications involving iceberg monitoring. Because of their small size, as well as the difficulty to detect them with ship instruments, icebergs are well-known as severe threats to Arctic maritime operations. Yet, the effects of climate change are evident: increased iceberg calving from glaciers in Greenland, Svalbard, and other areas in the Arctic region, which is leading to higher iceberg density, drifting of icebergs into warmer waters, and the grounding of icebergs in environments like Norwegian fjords. Similarly, as the Arctic economy begins to rely more on increased shipping operations, the hazardous nature of icebergs makes the work of remote sensing scientists essential for the safety, and longevity of these operations.

The work of this thesis contributes to current knowledge and methodologies for iceberg detection and classification using polarimetric data acquired from SAR satellites in Greenland, and Norway. As per the aims and objectives in Chapter 1, the following aspects have been achieved within this work:

a) Contribution to current knowledge on SAR polarimetry and its useful application in iceberg classification. It has been concluded that icebergs cannot be classified as single targets or partial targets, but a collection of single targets based on scattering mechanisms.

b) The use of polarimetric parameters to identify and classify icebergs. The Cloude-Pottier alpha/entropy decomposition exploits target entropy to determine the degree of randomness of multiple scattering mechanisms. In the case of iceberg classification, using entropy alone is not sufficient for this process.

c) The implementation of multiple state-of-the-art detection algorithms which have been tested on icebergs using ALOS-2 and RADARSAT-2 data for the first time. It has been shown that in two different scenarios: icebergs drifting in open

water, and icebergs embedded within sea ice, detection performance is highest in the Optimal Polarimetric Detector and Polarimetric Whitening Filter for icebergs in open water. However, for icebergs embedded within sea ice, the addition of polarimetric information on top of threshold detection will help classify icebergs and distinguish them from sea ice.

d) The use of quad-pol data is ideal in theory for iceberg classification and detection, but current spaceborne platforms that use a quad-pol SAR instrument do not utilise a wide enough swath width for future work to be considered viable and practical.

e) Backscatter conditions for icebergs are affected in the following ways. Meteorological conditions such as temperature, precipitation, and wind speed. Environmental conditions such as the sea-state and seawater salinity. Iceberg structural properties such as a rough or smooth surface, and various internal discontinuities. Finally, SAR system measurables such as a shallower or deeper incidence angle, and pixel size which may either remove or preserve polarimetric information

8.2. Future work

8.2.1. Technical methods

Given that SAR instruments still lack the ability to properly classify targets below a certain size, future research based on the findings of this thesis can be devised. The following section suggests paths for future work within the field of iceberg detection.

The application of other incoherent and coherent polarimetric decompositions may be utilised for classification of icebergs. Incoherent decompositions that were not tested may include the Freeman Durden decomposition, (Freeman and Durden, 1998) which is a model-based decomposition, that was later developed with a fourth scattering component by Yamaguchi *et al.* (2005). In contrast, examples of coherent decompositions include the Cameron decomposition which classifies targets based on ten physical scattering mechanisms, and the Touzi decomposition (Touzi, 2006) which has previously been applied to ships but was originally designed to solve for various ambiguities of the Cloude-Pottier incoherent eigenvector-based decomposition. It is only possible to utilise coherent decompositions if a target is single. Similarly, incoherent decompositions consider the second order statistics of

the scattering matrix. Since icebergs are in between these two categories (neither single nor partial), using coherent and incoherent together may help develop a conceptual model of iceberg backscatter physics and target characteristics. A completely new framework will need to be built in order to combine these two decomposition settings.

Secondly, it will be useful to increase the amount of SAR data utilised for this work. Using multiple SAR images will help analyse the effect of the incidence angle, in which the latter may influence backscattering behaviour on icebergs. Considered over the context of a larger time frame, it may be useful to employ time-series SAR data to better determine how scattering behaviour changes in time and space. For example, in Kongsfjorden, this thesis has only used three RADARSAT-2 images (Chapter 7). However, the addition of more images may help build a bigger conceptual idea. Time-series data can also be acquired for more regions in the Arctic, including in areas of higher iceberg activity i.e., where icebergs may be calving off glaciers more abundantly, the grounding of icebergs in various environments that may pose as hazards to local maritime operations, such as tourism in other Norwegian fjords or Greenland ice fields.

Ground-truthing satellite data for iceberg applications is an important part of data validation. Based on this concept, future work should consider a way of validating as for using ground-based radar or drones. In this thesis, we apply the use of GPRI for Kongsfjorden, and have been able to validate all iceberg targets as a result. However, ground truthing of iceberg data involves real time or near real time field applications, which are less likely in areas of lower iceberg activity as for offshore areas. Off-shore missions with sea ice are very costly and they only allow an extremely limited number of sightings. Grounded icebergs can also be used, since they do not move, and the validation can be done asynchronously to the vessel trip. Since grounding happens near the coast, in some situations this may also open the opportunity to use drones, or other high resolution multi-spectral satellite imagery.

Exploration of machine learning techniques will also be tested. Algorithms such as Random Forest may enhance the ability to classify icebergs. Such machine learning techniques may provide better accuracy and reduce computational burden and requirements. The advancement of artificial intelligence (AI) techniques is an innovative approach to remote sensing applications including iceberg detection.

Finally, the future launch of new satellites may enhance spatial resolution and availability of band frequencies which may allow for increased penetration of radar waves into iceberg bodies. Given that RADARSAT-2 uses C-band frequency, and ALOS-2 uses L-band, exploring frequencies such as P-band from future SAR missions as BIOMASS may help to enhance the findings of this thesis based on backscattering mechanisms and polarimetric behaviour. In particular, BIOMASS will be free-access quad-polarimetric and it will cover Antarctica.

8.2.2. Applied work

The improvement of technical methods can also increase the potential of future work looking into scientific questions that may impact iceberg production in the Arctic. For example, the retreat of glacier termini on the Greenland Ice Sheet could have an impact on iceberg production. This is work that may not have been explored under current detection methods. As the Greenland Ice Sheet loses ice each year due to climate change, it may be possible that as glacier termini retreats, the environment changes. One possibility is that a change from a tidewater terminus to an inland terminus may yield a higher number of icebergs, which could also be different in shape/ and size as a result of increased inland stresses on the ice, and the undulating nature of the landscape. Therefore, future work may consider monitoring of these glacier termini as the environment changes, as well as if the shape and size of icebergs change as a result.

There exist daily iceberg charts from the International Ice Patrol which are openly available. This resource provides excellent potential into future work that considers detection and classification of icebergs closer to the east North American coast. In particular, it could be a good source of validation data used to support future work looking into detection and classification of icebergs closer to the North Atlantic shipping lanes, rather than just a few kilometres from a glacier terminus.

References:

Akbari, V. and Brekke, C. (2017a) 'Iceberg detection in open and ice-infested waters using C-band polarimetric synthetic aperture radar', *IEEE Transactions on Geoscience and Remote Sensing,* 56(1), pp. 407-421.
Akbari, V. and Brekke, C. 'Iceberg detection in open water and sea ice using C-band radar polarimetry'. *2017 IEEE International Geoscience and Remote Sensing Symposium (IGARSS)*: IEEE, 2298-2301.
Akbari, V., Brekke, C., Doulgeris, A., Storvold, R. and Silvertsen, A. 'Quad-Polarimetric SAR for Detection and Characterization of Icebergs'. *Living Planet Symposium*, 50.
Akbari, V., Doulgeris, A. P. and Brekke, C. 'Subaperture analysis of polarimetric SAR data for iceberg detection'. *2016 IEEE International Geoscience and Remote Sensing Symposium (IGARSS)*: IEEE, 5666-5669.
Ardhuin, F., Tournadre, J., Queffeulou, P., Girard-Ardhuin, F. and Collard, F. (2011) 'Observation and parameterization of small icebergs: Drifting breakwaters in the southern ocean', *Ocean Modelling,* 39(3-4), pp. 405-410.
Bailey, J. and Marino, A. (2020) 'Quad-Polarimetric Multi-Scale Analysis of Icebergs in ALOS-2 SAR Data: A Comparison between Icebergs in West and East Greenland', *Remote Sensing,* 12(11), pp. 1864.
Bailey, J., Marino, A. and Akbari, V. (2021) 'Comparison of Target Detectors to Identify Icebergs in Quad-Polarimetric L-Band Synthetic Aperture Radar Data', *Remote Sensing,* 13(9), pp. 1753.
Barbat, M. M., Wesche, C., Werhli, A. V. and Mata, M. M. (2019) 'An adaptive machine learning approach to improve automatic iceberg detection from SAR images', *ISPRS Journal of Photogrammetry and Remote Sensing,* 156, pp. 247-259.
Barry, R. G. and Gan, T. Y. (2022) *The global cryosphere: past, present, and future.* Cambridge University Press.
Bassis, J. N. (2011) 'The statistical physics of iceberg calving and the emergence of universal calving laws', *Journal of Glaciology,* 57(201), pp. 3-16.
Bassis, J. N. and Walker, C. C. (2012) 'Upper and lower limits on the stability of calving glaciers from the yield strength envelope of ice', *Proceedings of the Royal Society A: Mathematical, Physical and Engineering Sciences,* 468(2140), pp. 913-931.

Bayer, T., Winter, R. and Schreier, G. (1991) 'Terrain influences in SAR backscatter and attempts to their correction', *IEEE Transactions on Geoscience and Remote Sensing,* 29(3), pp. 451-462.
Benn, D. and Evans, D. J. (2014) *Glaciers and glaciation.* Routledge.
Benn, D., Warren, C. R. and Mottram, R. H. (2007) 'Calving processes and the dynamics of calving glaciers', *Earth-Science Reviews,* 82(3-4), pp. 143-179.
Bigg, G. (2015) *Icebergs: their science and links to global change.* Cambridge University Press.
Bigg, G. and Billings, S. (2014) 'The iceberg risk in the Titanic year of 1912: Was it exceptional?', *Significance,* 11(3), pp. 6-10.
Bigg, G., Wadley, M. R., Stevens, D. P. and Johnson, J. A. (1997) 'Modelling the dynamics and thermodynamics of icebergs', *Cold Regions Science and Technology,* 26(2), pp. 113-135.
Bigg, G., Wei, H.-L., Wilton, D. J., Zhao, Y., Billings, S. A., Hanna, E. and Kadirkamanathan, V. (2014) 'A century of variation in the dependence of Greenland iceberg calving on ice sheet surface mass balance and regional climate change', *Proceedings of the Royal Society A: Mathematical, Physical and Engineering Sciences,* 470(2166), pp. 20130662.
Bigg, G., Zhao, Y. and Hanna, E. (2021) 'Forecasting the severity of the Newfoundland iceberg season using a control systems model', *Journal of Operational Oceanography,* 14(1), pp. 24-36.
Bjørk, A. A., Kruse, L. and Michaelsen, P. (2015) 'Brief communication: Getting Greenland’s glaciers right–a new data set of all official Greenlandic glacier names', *Cryosphere,* 9(6), pp. 2215-2218.
Brown, C. S., Meier, M. F. and Post, A. (1982) *Calving speed of Alaska tidewater glaciers, with application to Columbia Glacier*: U.S. Geological Survey.
Brusch, S., Lehner, S., Fritz, T., Soccorsi, M., Soloviev, A. and van Schie, B. (2010) 'Ship surveillance with TerraSAR-X', *IEEE transactions on geoscience and remote sensing,* 49(3), pp. 1092-1103.
Burgess, D. O., Sharp, M. J., Mair, D. W., Dowdeswell, J. A. and Benham, T. J. (2005) 'Flow dynamics and iceberg calving rates of Devon Ice Cap, Nunavut, Canada', *Journal of Glaciology,* 51(173), pp. 219-230.
Buus-Hinkler, J., Qvistgaard, K. and Krane, K. A. H. 'Iceberg number density—Reaching a full picture of the Greenland waters'. *2014 IEEE Geoscience and Remote Sensing Symposium*: IEEE, 270-273.

Campbell, J. B. and Wynne, R. H. (2011) *Introduction to remote sensing.* Guilford Press.
Chan, Y. K. and Lim, S. Y. (2008) 'Synthetic aperture radar (SAR) signal generation', *Progress In Electromagnetics Research B,* 1, pp. 269-290.
Chaney, R., Bud, M. and Novak, L. (1990) 'On the performance of polarimetric target detection algorithms', *IEEE Aerospace and Electronic Systems Magazine,* 5(11), pp. 10-15.
Chen, J. Y. and Reed, I. S. (1987) 'A detection algorithm for optical targets in clutter', *IEEE Transactions on Aerospace and Electronic Systems,* (1), pp. 46-59.
Christensen, E. and Luzader, J. (2012) 'From sea to air to space: a century of iceberg tracking technology', *Coast Guard Journal of Safety & Security at Sea, Proceedings of the Marine Safety & Security Council,* 69(2).
Cloude, S. (1985) 'Target decomposition theorems in radar scattering', *Electronics Letters,* 21(1), pp. 22-24.
Cloude, S. (1986) 'Group theory and polarization algebra', *Optik,* 75(1), pp. 26-36.
Cloude, S. 'Conditions for the physical realisability of matrix operators in polarimetry'. *Polarization Considerations for Optical Systems II*: International Society for Optics and Photonics, 177-187.
Cloude, S. (2010) *Polarisation: applications in remote sensing.* Oxford university press.
Cloude, S. and Pottier, E. (1996) 'A review of target decomposition theorems in radar polarimetry', *IEEE transactions on geoscience and remote sensing,* 34(2), pp. 498-518.
Crisp, D. J. (2004) *The state-of-the-art in ship detection in synthetic aperture radar imagery*: Defence Science And Technology Organisation Salisbury (Australia) Info … (DSTO-RR-0272.
Cristea, A., Doulgeris, A. P. and Eltoft, T. 'A filtering framework for SAR data based on nongaussian statistics and pixel clustering'. *Image and Signal Processing for Remote Sensing XXIII*: International Society for Optics and Photonics, 1042713.
Csatho, B., Schenk, T., Van Der Veen, C. J. and Krabill, W. B. (2008) 'Intermittent thinning of Jakobshavn Isbrae, West Greenland, since the little ice age', *Journal of Glaciology,* 54(184), pp. 131-144.
Delignon, Y. and Pieczynski, W. (2002) 'Modeling non-Rayleigh speckle distribution in SAR images', *IEEE Transactions on Geoscience and Remote sensing,* 40(6), pp. 1430-1435.

Denbina, M. and Collins, M. J. (2012) 'Iceberg detection using compact polarimetric synthetic aperture radar', *Atmosphere-ocean,* 50(4), pp. 437-446.
Dierking, W. and Wesche, C. (2013) 'C-band radar polarimetry—Useful for detection of icebergs in sea ice?', *IEEE Transactions on Geoscience and Remote Sensing,* 52(1), pp. 25-37.
Dowdeswell, J. A. (1989) 'On the nature of Svalbard icebergs', *Journal of Glaciology,* 35(120), pp. 224-234.
Dowdeswell, J. A. and Forsberg, C. F. (1992) 'The size and frequency of icebergs and bergy bits derived from tidewater glaciers in Kongsfjorden, northwest Spitsbergen', *Polar Research,* 11(2), pp. 81-91.
Dowdeswell, J. A. and Jeffries, M. O. (2017) 'Arctic ice shelves: An introduction', *Arctic ice shelves and ice islands*: Springer, pp. 3-21.
Eik, K. and Marchenko, A. (2010) 'Model tests of iceberg towing', *Cold regions science and technology,* 61(1), pp. 13-28.
Ferdous, M. S., Himi, U. H., McGuire, P., Power, D. T., Johnson, T. and Collins, M. J. (2020) 'C-Band Simulations of Melting Icebergs Using GRECOSAR and an EM Model: Varying Wind Conditions at Lower Beam Mode', *IEEE Journal of Selected Topics in Applied Earth Observations and Remote Sensing*.
Fettweis, X., Hanna, E., Huybrechts, P. and Erpicum, M. (2008) 'Estimation of the Greenland ice sheet surface mass balance for the 20th and 21st centuries', *Cryosphere,* 2(2), pp. 117-129.
Freeman, A. and Durden, S. (1998) 'A three-component scattering model for polarimetric SAR data', *IEEE Transactions on Geoscience and Remote Sensing,* 32, pp. 963-973.
Frost, A., Ressel, R. and Lehner, S. (2016) 'Automated iceberg detection using high-resolution X-band SAR images', *Canadian Journal of Remote Sensing,* 42(4), pp. 354-366.
Gammon, P. H., Gagnon, R. E., Bobby, W. and Russell, W. E. 'Physical and Mechanical Properties of Icebergs'. *Offshore Technology Conference*, Houston, Texas. OTC-4459-MS.
Gerland, S. and Renner, A. H. (2007) 'Sea-ice mass-balance monitoring in an Arctic fjord', *Annals of Glaciology,* 46, pp. 435-442.
Gill, R. (2001) 'Operational detection of sea ice edges and icebergs using SAR', *Canadian journal of remote sensing,* 27(5), pp. 411-432.

Gow, A. J. (1968) 'Bubbles and bubble pressures in Antarctic glacier ice', *Journal of Glaciology,* 7(50), pp. 167-182.
Gray, A. L. and Arsenault, L. D. (1991) 'Time-delayed reflections in L-band synthetic aperture radar imagery of icebergs', *IEEE Transactions on Geoscience and Remote Sensing,* 29(2), pp. 284-291.
Gutt, J. and Starmans, A. (2002) 'Quantification of iceberg impact and benthic recolonisation patterns in the Weddell Sea (Antarctica)', *Ecological studies in the Antarctic sea ice zone*: Springer, pp. 210-214.
Hajnsek, I., Parrella, G., Marino, A., Eltoft, T., Necsoiu, M., Eriksson, L. and Watanabe, M. (2021) 'Cryosphere Applications', in Hajnsek, I. and Desnos, Y.-L. (eds.) *Polarimetric Synthetic Aperture Radar: Principles and Application*. Cham: Springer International Publishing, pp. 179-213.
Hall, J. A., Bigg, G. R. and Hall, R. (2012) 'Identification and tracking of individual sea ice floes from ENVISAT wide swath SAR images: a case study from Fram Strait', *Remote sensing letters,* 3(4), pp. 295-304.
Hanna, E., Mernild, S. H., Cappelen, J. and Steffen, K. (2012) 'Recent warming in Greenland in a long-term instrumental (1881–2012) climatic context: I. Evaluation of surface air temperature records', *Environmental Research Letters,* 7(4), pp. 045404.
Hannevik, T. N. (2017) *Literature review on ship and ice discrimination*, Kjeller, Norway: Norwegian Defence Research Establishment (824642985X.
Hawkins, J. D., Abell Jr, F. and Ondrejik, D. (1993) *Antarctic Tabular Iceberg A-24 Movement and Decay Via Satellite Remote Sensing*: NAVAL RESEARCH LAB STENNIS SPACE CENTER MS.
Haykin, S., Lewis, E. O., Raney, R. K. and Rossiter, J. R. (1994) *Remote sensing of sea ice and icebergs.* John Wiley & Sons.
Herdes, E., Copland, L., Danielson, B. and Sharp, M. (2012) 'Relationships between iceberg plumes and sea-ice conditions on northeast Devon Ice Cap, Nunavut, Canada', *Annals of glaciology,* 53(60), pp. 1-9.
Hill, B. T. (2000) 'Database of Ship Collisions with Icebergs. Report of the International Ice Patrol Bulletin in the North Atlantic. 2000 Season', *Bulletin,* (86).
Hill, B. T. 'Ship collision with iceberg database'. *7th international conference and exhibition on performance of ships and structures in ice*, 16-19.
Himi, U. H., Ferdous, M. S., Power, D. T. and McGuire, P. (2021) 'Statistical Comparison of Melting Iceberg Backscatter Embedded in Sea Ice and Open Water

Using RADARSAT-2 Images of the Newfoundland Sea', *IEEE Transactions on Geoscience and Remote Sensing,* 60, pp. 1-13.
Hotzel, I. S. and Miller, J. D. (1983) 'Icebergs: their physical dimensions and the presentation and application of measured data', *Annals of Glaciology,* 4, pp. 116-123.
Howell, C., Youden, J., Lane, K., Power, D., Randell, C. and Flett, D. 'Iceberg and ship discrimination with ENVISAT multipolarization ASAR'. *IGARSS 2004. 2004 IEEE International Geoscience and Remote Sensing Symposium*: IEEE.
Iervolino, P., Guida, R. and Whittaker, P. 'A new GLRT-based ship detection technique in SAR images'. *2015 IEEE International Geoscience and Remote Sensing Symposium (IGARSS)*: IEEE, 3131-3134.
Ioannidis, G. and Hammers, D. (1979) 'Optimum antenna polarizations for target discrimination in clutter', *IEEE Transactions on Antennas and Propagation,* 27(3), pp. 357-363.
Jackson, C. and Apel, J. (2004) 'Synthetic aperture radar marine user's manual', *Chapter 2. SAR Imaging of Ocean Surface*: US Department of Commerce, pp. 53-54.
Jakeman, E. and Pusey, P. (1976) 'A model for non-Rayleigh sea echo', *IEEE Transactions on antennas and propagation,* 24(6), pp. 806-814.
Jansing, E. D. (2021) *Introduction to Synthetic Aperture Radar: Concepts and Practice.* McGraw-Hill Education.
Jin, R., Yin, J., Zhou, W. and Yang, J. (2017) 'Level set segmentation algorithm for high-resolution polarimetric SAR images based on a heterogeneous clutter model', *IEEE Journal of Selected Topics in Applied Earth Observations and Remote Sensing,* 10(10), pp. 4565-4579.
Jones, C., Minchew, B. and Holt, B. 'Polarimetric decomposition analysis of the Deepwater Horizon oil slick using L-band UAVSAR data'. *2011 IEEE International Geoscience and Remote Sensing Symposium*: IEEE, 2278-2281.
Karvonen, J., Gegiuc, A., Niskanen, T., Montonen, A., Buus-Hinkler, J. and Rinne, E. (2021) 'Iceberg Detection in Dual-Polarized C-Band SAR Imagery by Segmentation and Nonparametric CFAR (SnP-CFAR)', *IEEE Transactions on Geoscience and Remote Sensing,* 60, pp. 1-12.
Kay, S. M. (1993) *Fundamentals of statistical signal processing: estimation theory.* Prentice-Hall, Inc.

Khan, S. and Guida, R. (2013) 'On fractional moments of multilook polarimetric whitening filter for polarimetric SAR data', *IEEE Transactions on Geoscience and Remote Sensing,* 52(6), pp. 3502-3512.
Kirkham, J. D., Rosser, N. J., Wainwright, J., Jones, E. C. V., Dunning, S. A., Lane, V. S., Hawthorn, D. E., Strzelecki, M. C. and Szczuciński, W. (2017) 'Drift-dependent changes in iceberg size-frequency distributions', *Scientific reports,* 7(1), pp. 1-10.
Kristensen, M. (1983) 'Iceberg calving and deterioration in Antarctica', *Progress in Physical Geography,* 7(3), pp. 313-328.
Lee, J.-S., Grunes, M. R., Schuler, D. L., Pottier, E. and Ferro-Famil, L. (2005) 'Scattering-model-based speckle filtering of polarimetric SAR data', *IEEE Transactions on Geoscience and Remote Sensing,* 44(1), pp. 176-187.
Lee, J.-S., Jurkevich, L., Dewaele, P., Wambacq, P. and Oosterlinck, A. (1994) 'Speckle filtering of synthetic aperture radar images: A review', *Remote Sensing Reviews,* 8(4), pp. 313-340.
Lee, J.-S., Papathanassiou, K. P., Ainsworth, T. L., Grunes, M. R. and Reigber, A. (1998) 'A new technique for noise filtering of SAR interferometric phase images', *IEEE Transactions on Geoscience and Remote Sensing,* 36(5), pp. 1456-1465.
Lee, J.-S. and Pottier, E. (2017) *Polarimetric radar imaging: from basics to applications.* CRC press.
Lee, J.-S., Wen, J.-H., Ainsworth, T. L., Chen, K.-S. and Chen, A. J. (2008) 'Improved sigma filter for speckle filtering of SAR imagery', *IEEE Transactions on Geoscience and Remote Sensing,* 47(1), pp. 202-213.
Li, T., Peng, D., Chen, Z. and Guo, B. (2020) 'Superpixel-level CFAR detector based on truncated gamma distribution for SAR images', *IEEE Geoscience and Remote Sensing Letters,* 18(8), pp. 1421-1425.
Li, Y., Yang, Q. and Zhang, N. 'Ship detection with adaptive parameter based on detection background analysis'. *2009 International Conference on Microwave Technology and Computational Electromagnetics (ICMTCE 2009)*: IET, 486-489.
Liestøl, O. (1988) 'The glaciers in the Kongsfjorden area, Spitsbergen', *Norsk Geografisk Tidsskrift-Norwegian Journal of Geography,* 42(4), pp. 231-238.
Liu, G., Huang, S., Torre, A. and Rubertone, F. (1998) 'The multilook polarimetric whitening filter (MPWF) for intensity speckle reduction in polarimetric SAR images', *IEEE transactions on geoscience and remote sensing,* 36(3), pp. 1016-1020.

Liu, T., Yang, Z., Marino, A., Gao, G. and Yang, J. (2020) 'PolSAR ship detection based on neighborhood polarimetric covariance matrix', *IEEE Transactions on Geoscience and Remote Sensing,* 59(6), pp. 4874-4887.
Liu, T., Zhang, J., Gao, G., Yang, J. and Marino, A. (2019) 'CFAR ship detection in polarimetric synthetic aperture radar images based on whitening filter', *IEEE Transactions on Geoscience and Remote Sensing,* 58(1), pp. 58-81.
Livingstone, C., Sikaneta, I., Gierull, C., Chiu, S. and Beaulne, P. (2006) *RADARSAT-2 system and mode description*, Ottowa (Ontario): Defence Research and Development Canada (RTO-MP-SCI-150
Long, D. G. (2008) 'Microwave Sensors - Active and Passive', *Manual of Remote Sensing, Volume 1: Earth Observing Platforms and Sensors.* 4th ed. Bethesda, Maryland: American Society for Photogrammetry and Remote Sensing, pp. 119.
Lopes, A. and Séry, F. (1997) 'Optimal speckle reduction for the product model in multilook polarimetric SAR imagery and the Wishart distribution', *IEEE Transactions on Geoscience and Remote Sensing,* 35(3), pp. 632-647.
MacAyeal, D. R., Okal, E. A., Aster, R. C. and Bassis, J. (2008) 'Seismic and hydroacoustic tremor generated by colliding icebergs', *Journal of Geophysical Research: Earth Surface,* 113(F3).
Marino, A. (2012) *A new target detector based on geometrical perturbation filters for Polarimetric Synthetic Aperture Radar (POL-SAR).* Springer Science & Business Media.
Marino, A. (2013) 'A notch filter for ship detection with polarimetric SAR data', *IEEE Journal of Selected Topics in Applied Earth Observations and Remote Sensing,* 6(3), pp. 1219-1232.
Marino, A. 'Iceberg Detection with L-Band ALOS-2 Data Using the Dual-POL Ratio Anomaly Detector'. *IGARSS 2018-2018 IEEE International Geoscience and Remote Sensing Symposium*: IEEE, 6067-6070.
Marino, A., Cloude, S. R. and Woodhouse, I. H. (2010a) 'A polarimetric target detector using the Huynen fork', *IEEE Transactions on Geoscience and Remote Sensing,* 48(5), pp. 2357-2366.
Marino, A., Dierking, W. and Wesche, C. 'Contrast enhancement for an iceberg detector with a CFAR test using dual-polarized radar imagery'. *2016 European Radar Conference (EuRAD)*: IEEE, 73-76.

Marino, A., Dierking, W. and Wesche, C. (2016b) 'A depolarization ratio anomaly detector to identify icebergs in sea ice using dual-polarization SAR images', *IEEE Transactions on Geoscience and Remote Sensing,* 54(9), pp. 5602-5615.
Marino, A. and Hajnsek, I. 'Icebergs detection with TerraSAR-X data using a polarimetric notch filter'. *2012 IEEE International Geoscience and Remote Sensing Symposium*: IEEE, 3273-3276.
Marino, A. and Iervolino, P. 'Ship detection with Cosmo-SkyMed PINGPONG data using the dual-pol ratio anomaly detector'. *2017 IEEE International Geoscience and Remote Sensing Symposium (IGARSS)*: IEEE, 3897-3900.
Marino, A., Rulli, R., Wesche, C. and Hajnsek, I. 'A new algorithm for iceberg detection with dual-polarimetric SAR data'. *2015 IEEE International Geoscience and Remote Sensing Symposium (IGARSS)*: IEEE, 3446-3449.
Marino, A., Sanjuan-Ferrer, M. J., Hajnsek, I. and Ouchi, K. (2015b) 'Ship detection with spectral analysis of synthetic aperture radar: A comparison of new and well-known algorithms', *Remote Sensing,* 7(5), pp. 5416-5439.
Marino, A., Sugimoto, M., Nunziata, F., Hajnsek, I., Migliaccio, M. and Ouchi, K. 'Comparison of ship detectors using polarimetric alos data: Tokyo Bay'. *2013 IEEE International Geoscience and Remote Sensing Symposium-IGARSS*: IEEE, 2345-2348.
Marino, A., Sugimoto, M., Ouchi, K. and Hajnsek, I. (2013b) 'Validating a notch filter for detection of targets at sea with ALOS-PALSAR data: Tokyo Bay', *IEEE Journal of Selected Topics in Applied Earth Observations and Remote Sensing,* 7(12), pp. 4907-4918.
Marino, A. and Walker, N. 'Ship detection with quad polarimetric TerraSAR-X data: An adaptive notch filter'. *2011 IEEE International Geoscience and Remote Sensing Symposium*: IEEE, 245-248.
Marino, A., Walker, N. and Woodhouse, I. (2010b) 'Ship Detection Using SAR Polarimetry. The Development Of A New Algorithm Designed To Exploit New Satellite SAR Capabilities For Maritime Surveillance', *SeaSAR 2010,* 679, pp. 36.
Marino, A., Walker, N. and Woodhouse, I. 'Ship detection with RADARSAT-2 quad-pol SAR data using a notch filter based on perturbation analysis'. *2010 IEEE International Geoscience and Remote Sensing Symposium*: IEEE, 3704-3707.
Marsh, R., Ivchenko, V., Skliris, N., Alderson, S., Bigg, G. R., Madec, G., Blaker, A. T., Aksenov, Y., Sinha, B. and Coward, A. C. (2015) 'NEMO–ICB (v1. 0): interactive

icebergs in the NEMO ocean model globally configured at eddy-permitting resolution', *Geoscientific Model Development,* 8(5), pp. 1547-1562.
Mazur, A., Wåhlin, A. K. and Krężel, A. (2017) 'An object-based SAR image iceberg detection algorithm applied to the Amundsen Sea', *Remote Sensing of Environment,* 189, pp. 67-83.
Mugford, R. and Dowdeswell, J. (2010) 'Modeling iceberg-rafted sedimentation in high-latitude fjord environments', *Journal of Geophysical Research: Earth Surface,* 115(F3).
Murphy, D. L. (2014) 'Icebergs', *Encyclopedia of Remote Sensing. Encylopedia of Earth Sciences Series*. New York, NY: Springer, pp. 281-284.
Murphy, D. L. and Cass, J. L. (2012) 'The International Ice Patrol: safeguarding life and property at sea', *Coast Guard Journal of Safety & Security at Sea, Proceedings of the Marine Safety & Security Council,* 69(2).
Nick, F. M., Vieli, A., Andersen, M. L., Joughin, I., Payne, A., Edwards, T. L., Pattyn, F. and Van De Wal, R. S. (2013) 'Future sea-level rise from Greenland's main outlet glaciers in a warming climate', *Nature,* 497(7448), pp. 235-238.
Novak, L. M. and Burl, M. C. 'Optimal speckle reduction in POL-SAR imagery and its effect on target detection'. *Millimeter Wave and Synthetic Aperture Radar*: International Society for Optics and Photonics, 84-115.
Novak, L. M., Sechtin, M. B. and Cardullo, M. J. (1989) 'Studies of target detection algorithms that use polarimetric radar data', *IEEE Transactions on Aerospace and Electronic Systems,* 25(2), pp. 150-165.
Nunziata, F., Buono, A., Migliaccio, M., Moctezuma, M., Parmiggiani, F. and Aulicino, G. 'Multi-Frequency and Multi-Polarization Synthetic Aperture Radar for the Larsen-C A-68 Iceberg Monitoring'. *2018 IEEE 4th International Forum on Research and Technology for Society and Industry (RTSI)*: IEEE, 1-4.
Nunziata, F., Migliaccio, M. and Brown, C. E. 'A physically-based approach to observe man-made metallic objects in dual-polarized SAR data'. *2010 IEEE International Geoscience and Remote Sensing Symposium*: IEEE, 3007-3010.
Oliver, C. (1993) 'Optimum texture estimators for SAR clutter', *Journal of Physics D: Applied Physics,* 26(11), pp. 1824.
Oliver, C. and Quegan, S. (2004) *Understanding synthetic aperture radar images.* SciTech Publishing.

Parmiggiani, F., Moctezuma-Flores, M., Guerrieri, L. and Battagliere, M. (2018) 'SAR analysis of the Larsen-C A-68 iceberg displacements', *International Journal of Remote Sensing,* 39(18), pp. 5850-5858.
Plant, W. J. (1990) 'Bragg scattering of electromagnetic waves from the air/sea interface', *Surface waves and fluxes*: Springer, pp. 41-108.
Pottier, E. and Cloude, S. R. 'Application of the H/A/alpha polarimetric decomposition theorem for land classification'. *Wideband Interferometric Sensing and Imaging Polarimetry*: SPIE, 132-143.
Pottier, E., Lee, J.-S. and Ferro-Famil, L. (2005) *Advanced Concepts in Polarimetry. Part 1: Polarimetric Target Description, Speckle Filtering and Decomposition Theorems*: NAVAL RESEARCH LAB WASHINGTON DC.
Power, D., Youden, J., Lane, K., Randell, C. and Flett, D. (2001) 'Iceberg detection capabilities of RADARSAT synthetic aperture radar', *Canadian Journal of Remote Sensing,* 27(5), pp. 476-486.
Reeh, N. (1968) 'On the calving of ice from floating glaciers and ice shelves', *Journal of Glaciology,* 7(50), pp. 215-232.
Rignot, E., Velicogna, I., van den Broeke, M. R., Monaghan, A. and Lenaerts, J. (2011) 'Acceleration of the contribution of the Greenland and Antarctic ice sheets to sea level rise', *Geophysical Research Letters,* 38(5).
Robe, R. (1980) 'Iceberg drift and deterioration', *Dynamics of snow and ice masses,* 211, pp. 260.
Saini, O., Bhardwaj, A. and Chatterjee, R. 'Ship Detection from RISAT-1 and Radarsat-2 SAR Images using CFAR'. *MOL2NET, International Conference Series on Multidisciplinary Sciences USEDAT-08: USA-Europe Data Analysis Training Program Workshop, UPV/EHU, Bilbao-MDC, Miami, USA*, 8.
Salepci, N., Eckardt, R. and Richter, N. (2017) *Speckle filtering*. https://eo-college.org/resource/speckle/. Available at: https://eo-college.org/resource/speckle/.
Scharf, L. L. and Demeure, C. (1991) *Statistical signal processing: detection, estimation, and time series analysis.* Prentice Hall.
Scholander, P. and Nutt, D. (1960) 'Bubble pressure in Greenland icebergs', *Journal of Glaciology,* 3(28), pp. 671-678.
Shoshany, M., Svoray, T., Curran, P., Foody, G. M. and Perevolotsky, A. (2000) 'The relationship between ERS-2 SAR backscatter and soil moisture: generalization from a humid to semi-arid transect', *International Journal of Remote Sensing,* 21(11), pp. 2337-2343.

Silva, T. A. and Bigg, G. R. (2005) 'Computer-based identification and tracking of Antarctic icebergs in SAR images', *Remote sensing of environment,* 94(3), pp. 287-297.
Smith, S. D. (1993) 'Hindcasting iceberg drift using current profiles and winds', *Cold regions science and technology,* 22(1), pp. 33-45.
Soldal, I. H., Dierking, W., Korosov, A. and Marino, A. (2019) 'Automatic Detection of Small Icebergs in Fast Ice Using Satellite Wide-Swath SAR Images', *Remote Sensing,* 11(7), pp. 806.
Srikanth, P., Ramana, K., Deepika, U., Kalyan Chakravarthi, P. and Sesha Sai, M. (2016) 'Comparison of various polarimetric decomposition techniques for crop classification', *Journal of the Indian Society of Remote Sensing,* 44(4), pp. 635-642.
Straneo, F., Heimbach, P., Sergienko, O., Hamilton, G., Catania, G., Griffies, S., Hallberg, R., Jenkins, A., Joughin, I. and Motyka, R. (2013) 'Challenges to understanding the dynamic response of Greenland's marine terminating glaciers to oceanic and atmospheric forcing', *Bulletin of the American Meteorological Society,* 94(8), pp. 1131-1144.
Sudom, D., Timco, G. and Tivy, A. 'Iceberg sightings, shapes and management techniques for offshore Newfoundland and Labrador: Historical data and future applications'. *2014 Oceans-St. John's*: IEEE, 1-8.
Svendsen, H., Beszczynska-Møller, A., Hagen, J. O., Lefauconnier, B., Tverberg, V., Gerland, S., Børre Ørbæk, J., Bischof, K., Papucci, C. and Zajaczkowski, M. (2002) 'The physical environment of Kongsfjorden–Krossfjorden, an Arctic fjord system in Svalbard', *Polar research,* 21(1), pp. 133-166.
Szajnowski, W. (1977) 'Estimators of log-normal distribution parameters', *IEEE Transactions on Aerospace and Electronic Systems,* (5), pp. 533-536.
Tao, D., Anfinsen, S. N. and Brekke, C. (2015) 'Robust CFAR detector based on truncated statistics in multiple-target situations', *IEEE Transactions on Geoscience and Remote Sensing,* 54(1), pp. 117-134.
Tao, D., Doulgeris, A. P. and Brekke, C. (2016) 'A segmentation-based CFAR detection algorithm using truncated statistics', *IEEE Transactions on Geoscience and Remote Sensing,* 54(5), pp. 2887-2898.
Touzi, R. (2006) 'Target scattering decomposition in terms of roll-invariant target parameters', *IEEE Transactions on geoscience and remote sensing,* 45(1), pp. 73-84.

Touzi, R., Charbonneau, F., Hawkins, R. and Vachon, P. (2004) 'Ship detection and characterization using polarimetric SAR', *Canadian Journal of Remote Sensing,* 30(3), pp. 552-559.
Ultee, L. and Bassis, J. N. (2020) 'SERMeQ model produces realistic retreat of 155 Greenland outlet glaciers', *Earth and Space Science Open Archive*, pp. 15.
Vachon, P. W., Campbell, J., Bjerkelund, C., Dobson, F. and Rey, M. (1997) 'Ship detection by the RADARSAT SAR: Validation of detection model predictions', *Canadian Journal of Remote Sensing,* 23(1), pp. 48-59.
Valero, A., Botero, E. and Serra, L. 'The world's renewable water resources and ice sheets'. *Proceedings of the Conference on Sustainable Development of Energy, Water and Environmental Systems. Dubrovnik. Croatia. June*, 2-7.
Viehoff, T. and Li, A. (1995) 'Iceberg observations and estimation of submarine ridges in the western Weddell Sea', *International Journal of Remote Sensing,* 16(17), pp. 3391-3408.
Vincent, W. F. (2020) 'Arctic Climate Change: Local Impacts, Global Consequences, and Policy Implications', *The Palgrave Handbook of Arctic Policy and Politics*: Springer, pp. 507-526.
Wackerman, C. C., Friedman, K. S., Pichel, W. G., Clemente-Colón, P. and Li, X. (2001) 'Automatic detection of ships in RADARSAT-1 SAR imagery', *Canadian journal of remote sensing,* 27(5), pp. 568-577.
Wang, C., Liao, M. and Li, X. (2008) 'Ship detection in SAR image based on the alpha-stable distribution', *Sensors,* 8(8), pp. 4948-4960.
Weeks, W. F. and Mellor, M. (1978) 'Some elements of iceberg technology', *Iceberg utilization*: Elsevier, pp. 45-98.
Werner, C., Strozzi, T., Wiesmann, A. and Wegmüller, U. 'GAMMA's portable radar interferometer'. *Proc. 13th FIG Symp. Deform. Meas. Anal*, 1-10.
Werner, C., Wiesmann, A., Strozzi, T., Kos, A., Caduff, R. and Wegmiüler, U. 'The GPRI multi-mode differential interferometric radar for ground-based observations'. *EUSAR 2012; 9th European Conference on Synthetic Aperture Radar*: VDE, 304-307.
Wesche, C. and Dierking, W. (2012) 'Iceberg signatures and detection in SAR images in two test regions of the Weddell Sea, Antarctica', *Journal of Glaciology,* 58(208), pp. 325-339.

Wesche, C. and Dierking, W. (2015) 'Near-coastal circum-Antarctic iceberg size distributions determined from Synthetic Aperture Radar images', *Remote Sensing of Environment,* 156, pp. 561-569.
Wiley, C. A. (1985) 'Synthetic aperture radars', *IEEE Transactions on Aerospace and Electronic Systems,* (3), pp. 440-443.
Williams, R., Rees, W. and Young, N. (1999) 'A technique for the identification and analysis of icebergs in synthetic aperture radar images of Antarctica', *International Journal of Remote Sensing,* 20(15-16), pp. 3183-3199.
Willis, C., Macklin, J., Partington, K., Teleki, K., Rees, W. and Williams, R. (1996) 'Iceberg detection using ERS-1 synthetic aperture radar', *International Journal of Remote Sensing,* 17(9), pp. 1777-1795.
Wilton, D. J., Bigg, G. R. and Hanna, E. (2015) 'Modelling twentieth century global ocean circulation and iceberg flux at 48 N: implications for west Greenland iceberg discharge', *Progress in Oceanography,* 138, pp. 194-210.
Winkelmann, R., Levermann, A., Martin, M. A. and Frieler, K. (2012) 'Increased future ice discharge from Antarctica owing to higher snowfall', *Nature,* 492(7428), pp. 239-242.
WMO (2014) *Sea ice nomenclature* (259. Available at: https://library.wmo.int/doc_num.php?explnum_id=4651.
Woodhouse, I. H. (2005) *Introduction to microwave remote sensing.* CRC press.
Xie, S., Dixon, T. H., Holland, D. M., Voytenko, D. and Vaňková, I. (2019) 'Rapid iceberg calving following removal of tightly packed pro-glacial mélange', *Nature communications,* 10(1), pp. 1-15.
Xu, J., Li, G., Peng, Y.-N., Xia, X.-G. and Wang, Y.-L. (2008) 'Parametric velocity synthetic aperture radar: Multilook processing and its applications', *IEEE transactions on geoscience and remote sensing,* 46(11), pp. 3488-3502.
Yamaguchi, Y., Moriyama, T., Ishido, M. and Yamada, H. (2005) 'Four-component scattering model for polarimetric SAR image decomposition', *IEEE Transactions on Geoscience and Remote Sensing,* 43(8), pp. 1699-1706.
Young, N., Turner, D., Hyland, G. and Williams, R. (1998) 'Near-coastal iceberg distributions in East Antarctica, 50-145 E', *Annals of Glaciology,* 27, pp. 68-74.
Zakharov, I., Power, D., Bobby, P. and Randell, C. 'Multi-resolution SAR data analysis for automated retrieval of sea ice and iceberg parameters'. *ESA Living Planet Symposium*.

Zhai, P., Pirani, A., Connors, S., Péan, C., Berger, S., Caud, N., Chen, Y., Goldfarb, L., Gomis, M. and Huang, M. 2021. IPCC 2021: Climate Change 2021: The Physical Science Basis. Contribution of Working Group I to the Sixth Assessment Report of the Intergovernmental Panel on Climate Change. Cambridge University Press.
Zhao, Y., Bigg, G. R., Billings, S. A., Hanna, E., Sole, A. J., Wei, H.-l., Kadirkamanathan, V. and Wilton, D. J. (2016) 'Inferring the variation of climatic and glaciological contributions to West Greenland iceberg discharge in the twentieth century', *Cold Regions Science and Technology,* 121, pp. 167-178.